# Predicting Longshore Sediment Transport and Coastline Dynamics using Satellite-derived Shoreline data

L.J.O. Beiboer

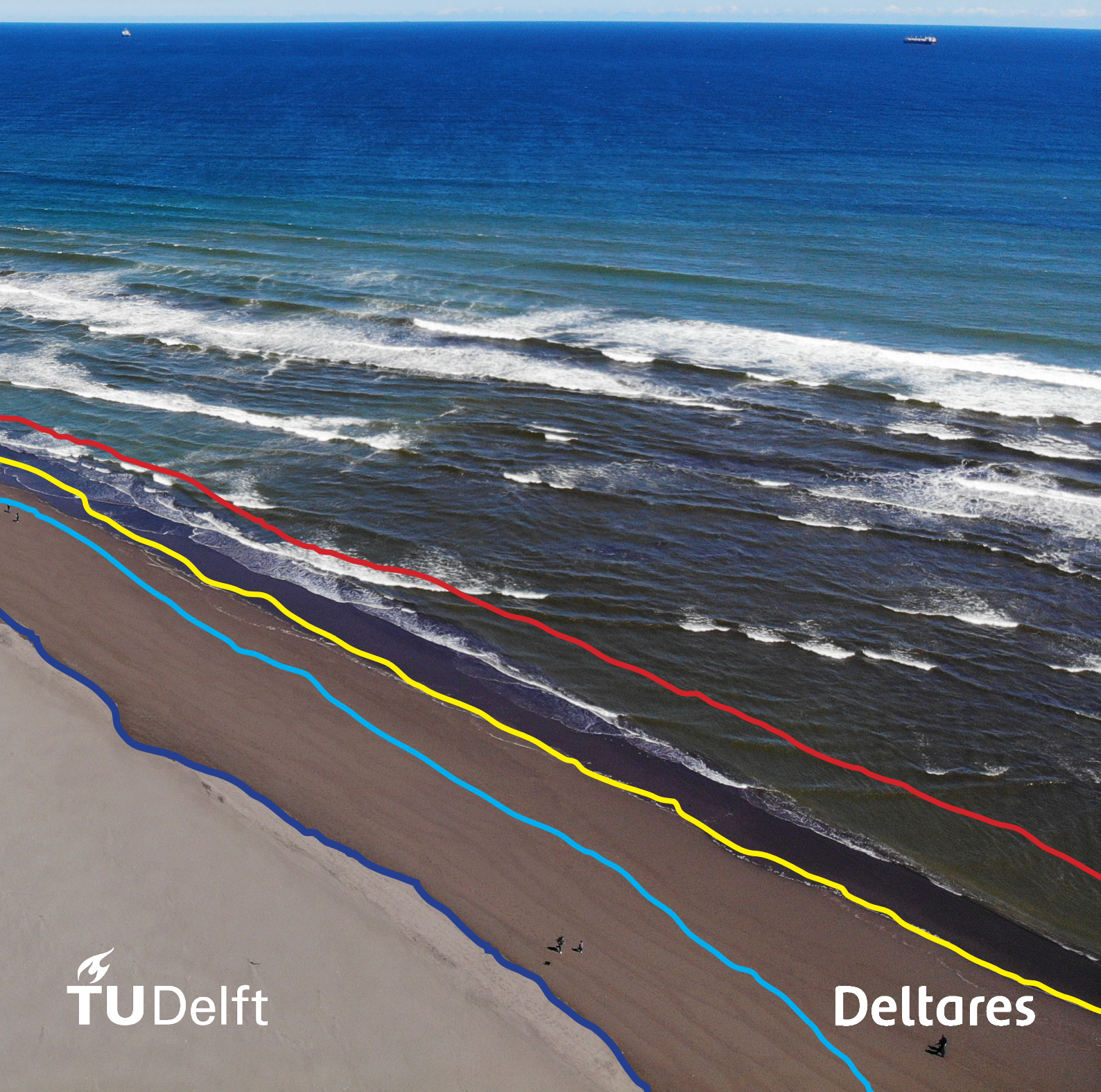

TU Delft

Deltares

# Predicting Longshore Sediment Transport and Coastline Dynamics using Satellite-derived Shoreline data

Determining the Longshore Sediment Transport using a littoral barrier combined with shoreline orientations to extend into the future

by

**L.J.O. (Luitzen-Jan) Beiboer**

to obtain the degree of Master of Science

at the Delft University of Technology,

to be defended publicly on Thursday 4 July, 2024 at 14:00.

| | | |
|---|---|---|
| Student number: | 5409640 | |
| Project duration: | September, 2023 – July, 2024 | |
| Thesis committee: | Dr. M.A. de Schipper, | TU Delft (Chair) |
| | Dr. Ir. A.P. Luijendijk, | TU Delft / Deltares |
| | Ir. F. Scheel, | Deltares |
| | Dr. J.E.A Storms, | TU Delft |

An electronic version of this thesis is available at `http://repository.tudelft.nl/`.

Cover photo: Drone image from the coastline of San Antonio, Chile (Beiboer, 2022)

TU Delft

Deltares

# Preface

Once, I attended a guest lecture on morphology at Hanze University of Applied Sciences, which sparked my interest in the subject. As I pursued my master's at Technical University Delft, my passion for the topic only grew stronger. Taking courses like Coastal Dynamics I and II solidified my direction. A lecture by Arjen Luijendijk (TU Delft/Deltares) introduced me to innovative aspects of coastal dynamics, like Satellite-derived Shorelines.

In addition to my interest in morphology, I developed a keen interest in programming and learned various languages. Thanks to Arjen Luijendijk, I discovered an excellent graduation topic at Deltares that allowed me to apply my knowledge of coastal dynamics and Python. Collaborating with Freek Scheel (Deltares), I successfully executed an engaging master's thesis study. I am grateful to Freek and Arjen for their guidance and support throughout the research. Additionally, I appreciate Matthieu de Schipper and Joep Storms (TU Delft) for their valuable contributions during our meetings. Lastly, I would like to express my heartfelt thanks to my girlfriend, Emma Marioni, for her valuable feedback and advice on my report, as well as to my parents for their unwavering support throughout my entire master's program at TU Delft and their valuable input and advice on my report.

Throughout my master's program, I had the pleasure of forming numerous friendships through my involvement in the Student Ice Skating Association (ELS). My unforgettable journey to Chile for a Multi-Disciplinary Project strengthened these connections. I am grateful to my friends from ELS, the MDP Chile group (Dick, Menno, Jesper, and Alessia), as well as my colleagues at Deltares (Tom, Celine, Prayla, Bernice and Sofie) for their unwavering support. Furthermore, I want to thank my colleagues from Shore Monitoring and Research. They provided invaluable assistance during my thesis. Lastly, I would like to conclude with a meaningful quote by Hincks (2022).

***"Sand, leads me to the shores of new discoveries"***

*L.J.O. Beiboer*
*Delft, June 2024*

# Abstract

Coastal regions, particularly beaches, are vital and dynamic areas for human activities. They serve various functions and are crucial barriers safeguarding coastal cities. However, the beach faces an increase in population and natural hazards caused by climate change. This creates new challenges that coastal engineers are working to address.

This study focuses on developing a new technique as an add-on to the Satellite-derived Shoreline (SDS) to estimate the shoreline dynamics in front of the shoreline and predict shoreline positions globally. This method aims to provide a quick and accessible alternative to the existing models for predicting shorelines based on bathymetry and wave data as inputs, which may not be readily accessible in underdeveloped areas. Therefore, the study's primary objective is to employ shoreline position data obtained from SDS to estimate Longshore Sediment Transport (LST) and predict shoreline position quickly and effortlessly as an alternative to existing models.

To achieve the study's objective, a tool called SHORECAST (Satellite-derived Historical and future Orientation-based Relation for Estimating Coastline Adjustments and Sediment Transport) is developed and adapted into a multi-step framework using the annual dataset from the Shoreline Monitor of Luijendijk et al. (2018). The dataset assesses sandy and non-sandy beaches and their historical shoreline position at transects every 500 meters along the coast for the last 37 years. Only sandy shoreline evolutions are considered for the development of this new tool. First, a routine is developed to find coastal cells to which the research's aim could be applied. Secondly, multiple algorithms were deployed on the coastal cells, such as detecting nourishments, outliers and linear interpolation. Next, the historical shoreline orientation and the Longshore Sediment Transport were calculated and combined to find a correlation for predicting shorelines.

Out of all the coastal cells studies, three have been chosen: Nouakchott (Mauritania), Aveiro (Portugal) and Delfland (the Netherlands). The Nouakchott cell was split into a north and south side. These cells have in common that they all have a littoral barrier at one of the boundaries of the coastal cell with the assumption that there is no sediment transport. Due to this assumption, the Longshore Sediment Transport could be calculated for each coastal cell. Nouakchott North experienced an annual sediment transport of 0.66 million $m^3$ between 1985 and 2020, resulting in a volume increase of 23.01 million $m^3$. Conversely, Nouakchott South experienced an erosion rate of 0.92 million $m^3$ per year, resulting in a total loss of 32.36 million $m^3$ over 35 years. In this same period, the Aveiro shoreline has accumulated a volume of 17.83 million $m^3$ of sediment. In addition, the Aveiro shoreline displayed significant fluctuations compared to Nouakchott.

The Delfland coastal cell is the most complex coastal area among the three selected cases due to two littoral barriers at the boundaries and the anthropogenic measures in the past 37 years. This results in a volume increase of 45.55 million $m^3$, similar to the beach nourishment volume of 46.51 million $m^3$. As a result, it can be concluded that only the beach nourishment is visible in the SDS data, even though shoreface and dune nourishments have also been carried out during this period.

The findings indicate that the SHORECAST model, which incorporates the "Single-line theory" and specific boundary conditions, can generate multiple predictions. This makes it a universal tool for estimating sediment transport over time, even with future anthropogenic measures. It is important to note that not all assumed zero boundaries in sediment transport are zero in reality. Apart from SDS data, other shoreline position data can be integrated into the model to achieve similar results. The model can be applied to any shoreline with an annual change rate of at least 1 meter. Further research is needed to explore the possibilities of improving the understanding of different boundary conditions, thereby enhancing the obtained outcomes and the practicality of this study. An important suggestion is to explore the feasibility of identifying littoral barriers and other boundary conditions. This would make the developed model more robust and widely applicable.

# Contents

# Acronyms

| Notation | Description |
|---|---|
| CM | Configuration and Management. 92 |
| CST | Cross-shore Sediment Transport. 6 |
| ENSO | El Niño-Southern Oscillation. 28 |
| EPSG | European Petroleum Survey Group. 10 |
| ESA | European Space Agency. 9, 10 |
| GEBCO | General Bathymetric Chart of the Oceans. 8 |
| GEE | Google Earth Engine. 4, 9, 10, 12 |
| LST | Longshore Sediment Transport. iv, vi, 3, 4, 6–8, 15–19, 23, 24, 27, 34–36, 39–43, 45, 47, 48, 50, 52–54, 57, 58, 61, 63, 65, 66, 68, 70, 74–76, 78–82, 97, 99, 102, 103, 106–108, 113, 115, 117–119, 122, 126–128, 130, 131, 136, 138–140, 142, 143, 145, 148 |
| MNDWI | Modified Normalized Difference Water Index. 13 |
| NAO | North Atlantic Oscillation. 1 |
| NASA | National Aeronautics and Space Administration. 9, 10 |
| NDWI | Normalized Difference Water Index. 12, 13 |
| NIR | Near-InfraRed. 12 |
| OLI | Operational Landsat Imager. 9 |
| OSM | OpenStreetMap. 10, 11, 29 |
| RMSE | Root Mean Squared Error. 20, 37, 38, 62, 63, 72, 107, 118, 130, 143 |
| SDS | Satellite-derived Shoreline. iv, vi, 4–6, 9–27, 32, 40, 42–45, 48, 49, 53, 57, 60, 63, 65–68, 71, 73, 75, 76, 78, 79, 93–95, 97, 98, 103, 109, 110, 121, 122, 132–135, 150, 152 |
| SLR | Sea Level Rise. 14 |
| TM | Thematic Mapper. 9 |
| TM | Transverse Mercator. 92 |
| TOA | Top of Atmosphere. 11, 12 |
| UTM | Universal Transverse Mercator. 91–93 |
| WGS | World Geodetic Systems. 10, 91 |

# 1

# Introduction

Coastal areas, particularly beaches, are vibrant and active regions that serve diverse purposes and are essential for human activities. According to estimates, more than two-thirds of people on Earth reside 100 kilometres or less from a shore (Adebisi et al., 2021; Roelvink et al., 2020; Vousdoukas et al., 2020; Toure et al., 2019). In addition, beaches are essential as a barrier, keeping coastal cities safe in the present and future. The threads of the coastal area are natural hazards and anthropogenic activities. Natural hazards, like storms and rising sea levels (Harley et al., 2019; Hagenaars et al., 2018). Anthropogenic activities include constructing groynes along the coast and sediment-holding river dams (Van Rijn, 2011; Kahl et al., 2024). These threads can cause significant coastal erosion. In other words, the shoreline gets squeezed according to Pontee (2013). Therefore, shoreline protection is a critical aspect of coastal management.

As stated by Vitousek, Barnard, & Limber (2017), marine and geological processes cause shoreline changes on various geographical and temporal scales. Five processes alter the shoreline response. These include phenomena that occur temporarily, such as (1) tides and currents, (2) as well as storms of a specific magnitude, frequency, direction and length. (3) Sea level rise, (4) climate cycles like El Niño and La Niña, the North Atlantic Oscillation (NAO), and (5) tectonic processes that induce coastline uplift or subsidence are all long-term effects.

According to Luijendijk et al. (2018), the coastal region is characterised by notable spatial differences and various coastal landforms, including barrier islands, sea cliffs, tidal flats, and river deltas. Since sandy coastlines show more evident spatial changes along their shores, the main focus of this study will be on sandy shorelines. The area of interest for these sandy shorelines is from the transition between the dune and beach up to and including the closure depth, as shown in Figure 1.1. This area is also called the “active coastal zone”.

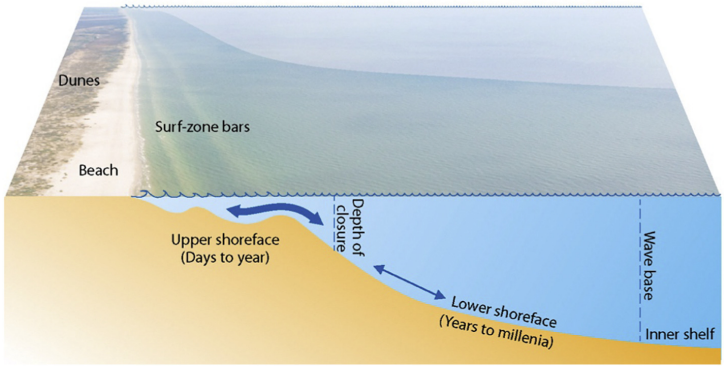


Figure 1.1: An illustration of the active coastal zone. The active coastal zone is from the transition between the dune and beach up to and including the closure depth. Arrows show the relative magnitudes of the sediment transport rates in cross-shore direction. Source: Anthony & Aagaard (2020).

## 1.1 Coastal Cells

According to Boak & Turner (2005), the definition of the coastline is expressed as follows: "the shoreline is the point where the physical boundary between land and water coincides". In addition, Boak & Turner (2005) stated that the position of the shoreline is in constant instability due to the movement of sediment both across and along the shore, mainly influenced by the dynamic fluctuations in water levels along the coastal boundary.

This study focuses on the sediment flowing along the beach in the active coastal zone (Figure 1.1). This sediment transport provides information on how the shoreline develops over time. To better clarify the sediment transport in the active coastal zone, a framework is used "coastal cells", also known as littoral cells or sediment cells (Figure 1.2). These cells reflect sections of the shoreline where sediment transport and coastal morphodynamics can be better understood because natural processes are contained mainly within them (Sedrati & Anthony, 2014; Marchand et al., 2009; Van Rijn, 2011). Figure 1.2 illustrates these processes, with longshore sediment transport referring to sediment flowing along the shoreline. Combining all of the components results in a sediment balance. Predicting whether the shoreline would erode or accumulate is feasible with this sediment balance.

The sediment balance of a coastal system can be influenced not only by its components but also by the time of occurrence of specific mechanisms. For instance, dune erosion from storms can happen in hours, while the sediment outflow from a river can take decades. These two time moments are within the scope of the engineering time scale. Engineering time scales vary from a few hours to several decades (Bosboom & Stive, 2021). Events within the engineering time scale impact the active coastal zone, also known as the engineering region.

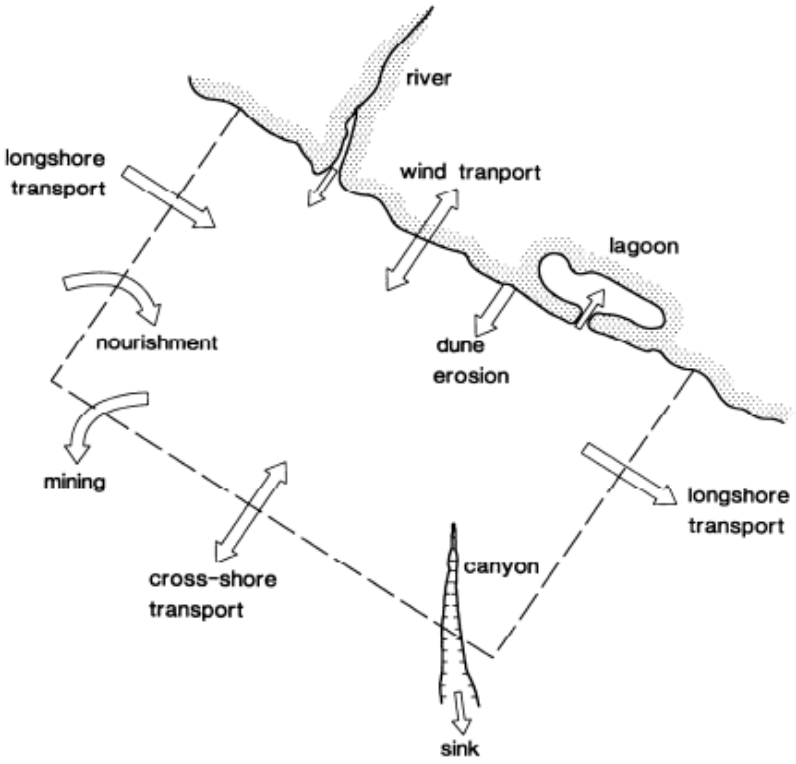


Figure 1.2: An example of a coastal cell. It shows the sediment fluxes which can appear in a sediment cell. All the components together give the sediment balance to the given coastal cell. Source: Marchand et al. (2009).

## 1.2 Research objective and scope

As described in the previous section, the coastal zone is dynamic and threaded by natural hazards and anthropogenic activities. Therefore, it is crucial to monitor these shoreline changes to determine the spatial variations on a yearly, decadal and century scale. Examples of processes that can occur within these time scales are natural and artificial sediment supply (nourishment), relative sea level changes, aeolian transport, land use, gradients in alongshore sediment transport and climatic variations. According to Vitousek, Barnard, Limber, Erikson, & Cole (2017) are these processes responsible for regular coastal change. Engineers have tried to understand coastal dynamics in specific coastal areas by understanding the current processes and making predictions for the future. The sediment transport in front of the shoreline is crucial for these processes. Sediment transport primarily occurs within the upper shoreface domain and is often referred to as Longshore Sediment Transport (LST), also referred to as littoral transport. In many cases, especially in models, sediment transport is expressed in bulk transport (Güner et al., 2013; Bosboom & Stive, 2021). As a result, it is normal to describe the sediment transport rate ($S$) in units of $m^3/s$, which stands for volumes of sand per second.

Different models and formulas are created to forecast sediment movement throughout the years. These models offer valuable information on the short- and long-term dynamics. Numerical software programs such as Delft3D and Unibest-CL+ represent these models (Deltares, 2023a,b). They are commonly referred to as the "existing method". In Delft3D, shallow equations will be solved numerically. Unibest-CL+ calculates wave height offshore to nearshore and shoreline position based on coast orientation and longshore sediment transport. The advantage of using these models is that they can accurately predict shoreline movement in short- and long-term scenarios. The short-term ranges from daily to a few years, while the long-term ranges from a few years to decades (Vitousek, Barnard, & Limber, 2017). However, the accuracy of the results produced by these models relies on the accuracy of the input data. This level of reliable data is a significant issue in many regions of the world (Vitousek, Buscombe, et al., 2023). In addition, employing physical-based models is costly due to their extensive processing time (Vitousek, Barnard, & Limber, 2017).

New tools have emerged that enable monitoring and providing insights into historical shoreline positions (Vos et al., 2019; Luijendijk et al., 2018; Do et al., 2019; Hagenaars et al., 2017; Vitousek, Buscombe, et al., 2023). These tools use satellite imagery (remote sensing) to extract the shoreline and track its evolution. According to Thyrsted (1986), remote sensing is collecting information about an object without making physical contact with it. The resulting set of historic shoreline positions can be referred to as Satellite-derived Shoreline (SDS). This tool is easily deployed globally, and the Google Earth Engine (GEE) provides access to global satellite imagery at no cost. The SDS provides historic shoreline positions for the past 40 years. However, for future shoreline predictions, wave data (regional wave climate) is still required to determine littoral transport (Vitousek, Vos, et al., 2023; Castelle et al., 2022). According to Vitousek, Buscombe, et al. (2023), these new tools convert the so-called "data-poor" areas into "data-rich" fields.

## 1.3 Research questions

In conclusion, the existing methods (the numerical models and equations) need accurate input data to calculate the littoral transport and the corresponding shoreline changes. This accurate input data can take time to collect. On the other hand, the new tools developed to extract the shoreline from satellite imagery offer the historical shoreline positions. They are available at no cost (Luijendijk et al., 2018; Vos et al., 2019). Unfortunately, these new tools cannot predict future shorelines or provide littoral transport. Would it not be an opportunity to derive the Longshore Sediment Transport, shoreline direction and make shoreline predictions using the data from Satellite-derived Shoreline? This satellite data can provide valuable insights about shoreline migration, reducing processing times significantly and being used globally. This opportunity may also be outlined as the main subject of research, which is represented as follows:

---

***"How can various shoreline predictions be established using Satellite-derived Shorelines to estimate alongshore sediment transport and orientation?"***

---

In order to answer this opportunity, the main question needs to be broken down into smaller pieces. These minor components are also the steps in this study that must be completed to answer the primary research question. First, use the obtained shoreline evolution from the SDS to estimate the annual accretion and erosion. This shoreline evolution is visualised as a one-dimensional line per year. To calculate the LST, transform the one-dimensional shoreline movement to a three-dimensional volume. The next step is using the sediment-orientation relationship to predict the shoreline. However, a boundary condition is required, which must be located along the coastline. These smaller steps can be expressed as the following sub-questions:

1. ***How can a one-dimensional shoreline shift between two transects be converted into a sediment volume gradient?***
2. ***Which boundary conditions can be applied to estimate Longshore Sediment Transport from a sediment volume gradient across transects in a selected area?***
3. ***How can the Satellite-Derived Shoreline historical Longshore Sediment Transport data and shoreline orientation be used to make future shoreline predictions?***
4. ***How can the proposed method be adapted to be applicable globally?***

## 1.4 Study approach

When addressing the research question, the initial steps involve enhancing our understanding of what existing methods can compute compared to the new innovative tool called SDS. To achieve this, relevant literature will be consulted. Additionally, exploring any existing examples that could serve as a solid starting point for this research. Next, the possibilities hidden in the data will be examined through the SDS examination. This is followed by identifying the essential parameters while keeping the central question in mind, which is crucial. In order to determine the volume gradient, the data must be analysed, validated, and adjusted, if necessary by establishing the boundary conditions and calculating the

longitudinal sediment transport. Moreover, investigating potential relationships between transport and shoreline orientation to make predictions based on this correlation. Finally, if all the steps are successful, the developed tool can be considered a valuable addition to Satellite-derived Shoreline.

## 1.5 Report structure

This report consists of seven main chapters. Chapter 2 will provide background information relevant to this study, focusing on existing and new innovative methods for deriving shoreline changes and longshore sediment transport. Furthermore, this chapter gives special attention to the Shoreline Monitor by Luijendijk et al. (2018) as it forms the basis of this study. The research methods will be explained in Chapter 3, along with the corresponding steps. Chapter 4 presents the results from the derived method at different locations, which were selected based on the methodology's initial part. In Chapter 5, the results of the various cases will be compared and validated. In addition, the limitations of the developed method will be explained in this chapter. Chapter 6 will reflect on the research questions as outlined in Section 1.3, while Chapter 7 will provide recommendations for future studies.

# 2

# Background information

This chapter will provide an overview of the existing knowledge concerning the research objective described in Section 1.2. First, Section 2.1 will give more information about sediment transport because this is an essential element in this study. Knowing the sediment transport rate along the shoreline provides information on how the shoreline will change over time. Will the shoreline erode or accrete for example. The Longshore Sediment Transport is determined with existing methods, these are numerical models and equations as outlined in Section 2.2. Besides the existing methods, new methods do rise up, such as Satellite-derived Shoreline (SDS) and will be described in Section 2.3. This section will explain the Shoreline Monitor, which is the main driver for this study. Therefore, the third section thoroughly describes its underlying hypotheses and findings. In addition, three attempts to derive the littoral transport using SDS are presented in Section 2.4. All the previously gathered information is consolidated and transformed into a main research question and several sub-questions, as described in Section 2.5, the last section.

## 2.1 Sediment transport

The term "coastal cells", or "littoral cells", was introduced in Section 1.1 and is examined in more detail in this section. This section will elaborate more on the coastal cell's sediment transport. The sediment transport gradient determines coastal accretion and erosion. In other words, there should be a difference in sediment input and output at a specific site. Sediment can be transported in two directions: cross-shore and longshore, as displayed in Figure 2.1. Sediment transport in a cross-shore direction moves sediment from the shoreline to deeper sections of the sea and the other way around. Storms typically generate high wave energy, the principal source of Cross-shore Sediment Transport (CST) (Oh et al., 2020). According to Bosboom & Stive (2021), the volume of sediment in the cross-shore direction remains constant over several years, assuming no sediment transport in the longshore direction. Bruun (1962), shows that this process in cross-shore direction is in a dynamic equilibrium.

Wave direction angle relative to the coast influences sediment flowing in the longshore direction, particularly the interaction between currents and waves. The sediment migrating in the longshore direction is referred to as Longshore Sediment Transport (LST). Although the CST of powerful storm waves can cause beaches to erode abruptly, they can also gradually rebound under mild wave conditions following the storm. On the other hand, LST gradients are primarily responsible for the permanent loss of sediment, highlighting the importance of monitoring this process (Bosboom & Stive, 2021).

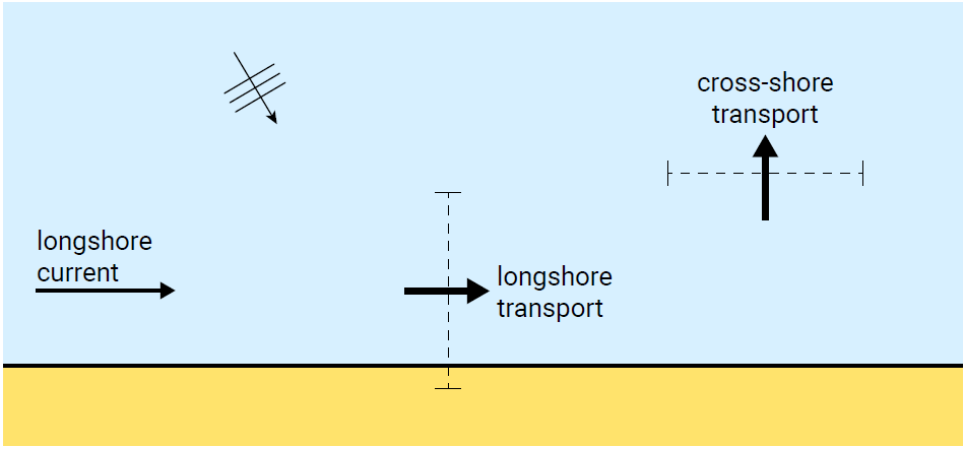


Figure 2.1: The two primary types of sediment transport along the coast: longshore transport and cross-shore transport. Whereby the coast is shown in yellow and the sea in blue. Source: Bosboom & Stive (2021).

### 2.1.1 Longshore Sediment Transport

Bosboom & Stive (2021) define Longshore Sediment Transport as the net movement of sediment particles along a fixed vertical plane perpendicular to the shoreline. This transport runs parallel to the beach and depth contour lines. According to Bosboom & Stive (2021), coastal change happens when there are spatial sediment transport gradients, sediment sinks, or sources. Understanding LST is crucial for coastal engineering and management since it helps forecast shoreline changes and create effective coastal protection measures. Longshore transport gradients lead to long-term shoreline alterations (Bosboom & Stive, 2021). The LST depends on available movable sediment in a particular place. If the bottom is fixed, erosion is prevented. The sediment transport may be lower than the local transport capacity based on hydrodynamics (Bosboom & Stive, 2021). Unless otherwise specified, LST refers to total or bulk transport in $m^3$. Equation 2.1 relates the displacement of the shoreline per unit time and the volume change (Longshore Sediment Transport rate, $Q$) derived from sediment continuity in one-line theory (Oh et al., 2020). This means that the shoreline is migrating horizontally without changing shape.

$$\frac{\partial y}{\partial t} = -\frac{1}{h}\frac{\partial Q}{\partial x} \tag{2.1}$$

#### Sediment Balance

The LST gradient can be followed along the shoreline to gain further insight into the shoreline development. One way to accomplish this is to measure the amount of sediment that enters and exits a certain location. Figure 2.2 demonstrates the input and output concept at a certain site. If $S_{in}$ equals $S_{out}$, the shoreline will not change. In other words, the shoreline remains stable. Erosion occurs when $S_{out} > S_{in}$ ($\frac{dS}{dx} > 0$), and accretion when $S_{out} < S_{in}$ ($\frac{dS}{dx} < 0$) (Bosboom & Stive, 2021).

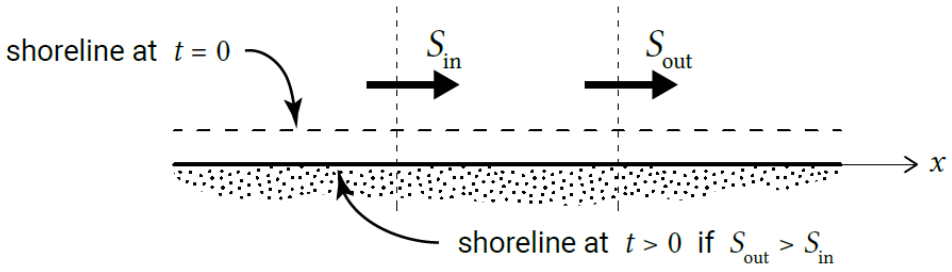


Figure 2.2: The net yearly Longshore Sediment Transport in a specific area with sediment intake $S_{in}$ and output $S_{out}$. The shoreline will alter depending on the difference between these input and output values. Source: Bosboom & Stive (2021).

The main direction and amount of net sediment transport can be determined by measuring the LST gradients in the spatial domain, for example, between a river mouth and a littoral drift barrier (a breakwater or groyne orthogonal to the shoreline) and collecting data every year for the past ten years (Kunte et al., 2013). The direction in which sediments are moved along the shore over several years is known as the net sediment transport. A Longshore Sediment Transport can be performed from the various sediment transport gradients by presuming that the sediment rate at a littoral drift barrier is zero. The various sediment transport gradients from this zero point can be added to determine the LST along the beach at different locations.

## 2.2 Existing Methods

The existing methods are the ones engineers have created in the last century to determine the Longshore Sediment Transport along the beach and the associated shoreline movements. These methods include numerical models and empirical equations. Engineers tried to determine how the shoreline will appear tomorrow, next week, next year or next decade using models and equations (Miller & Dean, 2004). In other words, it is essential to understand the current condition to ensure that new human interventions are effective. The LST is determined using various numerical models and empirical equations. An example is the Bruun rule determines the impact of sea level rise on coastline profile Bruun (1962). The fact that the empirical models are constructed with the idea that there is always an equilibrium is a crucial component (Miller & Dean, 2004).

#### Numerical models

Numerical models have been created to determine the LST associated with the shoreline position. Numerical models can solve various equations, including sediment conservation, shallow water equations and mass-momentum. Furthermore, this also applies to the hydrodynamical equations, which include the effects of tides and currents, waves, sediment movement and morphology. Examples of these models include Delft3D (Deltares, 2023a; Tonnon et al., 2018; Miranda et al., 2022), Unibest-CL+ (Deltares, 2023b; Tonnon et al., 2018) and Xbeach (Deltares, 2023c; Bolle et al., 2011).

Unibest-CL+ (Deltares, 2023b) is a numerical model used widely in different studies. This model has been applied in coastal engineering to model erosion and accretion rates, the life span of the coastline and maintenance volumes of mega-nourishments (Tonnon et al., 2018). This model can be used to determine LST and the position of the coastline over decades and centuries, especially at a large scale.

A more complex numerical model is Delft3D, which can run multi-dimensional hydrodynamic and transport simulations, considering non-steady flow and transport phenomena driven by tidal and meteorological forces. Delft3D is a model used to solve the shallow water equations and advection-diffusion equation for sediment in coastal areas (Tonnon et al., 2018). It has been widely used to simulate the Longshore Sediment Transport and related morphodynamics (Miranda et al., 2022). The model is complex due to the number of options that can be added, such as wind and wave-induced circulations for the sediment transport. Delft3D is used for short-term scales, which span a few days to a few years (Deltares, 2023a).

#### Advantages and disadvantages

The advantage of using numerical models is the ability to predict LST over varying time and spatial scales in the most comprehensive approaches. The time scale can be in the order of days to centuries. This information is valuable for decision-making concerning human interventions, providing insights into how the coastal system behaves. It is possible to create various scenarios of human interventions with these numerical models. Optimizing the best scenario can minimize adverse effects on the shoreline.

However, these models require various input values, such as offshore wave data, bathymetry data and offshore tide data. The accuracy of these inputs is crucial, as inaccuracies in input can lead to inaccurate model outputs (Vitousek, Vos, et al., 2023; Miller & Dean, 2004). Offshore wave data can be obtained from buoys or the ERA5 wave data (ECMWF, 2023), with buoys being the most accurate source. Bathymetry data can be challenging to obtain due to limited survey data that is accessible. In regions with limited surveys, the General Bathymetric Chart of the Oceans (GEBCO) dataset is a valuable resource (Centre, 2023; Wölfl et al., 2019). GEBCO is an international project dedicated to mapping and providing comprehensive bathymetric data essential for coastal engineering studies and ocean-related

research. In addition, sediment transport can be computed using various formulas, where the size and type of the sediment are important parameters (Vitousek, Barnard, & Limber, 2017).

Furthermore, it is necessary to note that numerical models are computationally intensive (Vitousek, Barnard, Limber, Erikson, & Cole, 2017). Setting up the base model can be time-consuming and running the model to assess the impact of different scenarios also requires significant computational resources, depending on the model applications.

## 2.3 Satellited Derived Shorelines

In recent years, innovative methods and techniques have been developed to monitor shoreline changes, extract shoreline positions and analyse shoreline dynamics, relying on remote sensing. Remote sensing involves obtaining information about objects or areas from a distance, typically using aircraft or satellites (Toure et al., 2019; Boak & Turner, 2005; Thyrsted, 1986). Analysing the acquired satellite images gives a comprehensive and constant perspective of coastal zones over time. This new technique brings more information about the coastal dynamics in different time scales. It can visualise the coastline change around the world (Hagenaars et al., 2017; Vitousek, Buscombe, et al., 2023). Various remote sensing methods have been used to detect shorelines, including photogrammetry, airborne Synthetic-Aperture Radar (SAR), airborne Light Detection and Ranging Technology (LiDAR) and video imaging from drones and human-crewed aircraft (McAllister et al., 2022; Aarninkhof et al., 2003; Harley et al., 2019). However, these approaches can be expensive and cover only a limited time and space.

Another remote sensing option relies on satellite images, such as those used by Luijendijk et al. (2018); Vos et al. (2019); Randazzo et al. (2020) to determine coastline positions. An example of these new methods is CoastSat, created by Vos et al. (2019). CoastSat is a specialised tool and platform for satellite images to track and analyse shorelines and their dynamic changes. Researchers, coastal managers and environmental professionals can gain valuable information from this platform, which was specifically built to study the evolution of sandy beaches. One of the critical advantages of CoastSat is its user-friendly interface, which enables users to select the most suitable images for coastal analysis. On the other hand, in the approach presented by Luijendijk et al. (2018), the Satellite-derived Shoreline (SDS) detection process is fully automated, using an algorithm to determine which (part of) satellite images are suitable for shoreline detection. The results are distributed through the Shoreline Monitor and the technique is outlined in Section 2.3.2.

### 2.3.1 Google Earth Engine

Both shoreline extraction tools (CoastSat by Vos et al. (2019) and the Shoreline Monitor by Luijendijk et al. (2018)) make use of the Google Earth Engine (GEE). The GEE is a cloud-based platform for large-scale geospatial analysis with significant computational capabilities. It primarily distributes satellite images from National Aeronautics and Space Administration (NASA) and European Space Agency (ESA). The SDS uses this cloud-based platform to analyse satellite imagery and extract shorelines (Gorelick et al., 2017). However, it is essential to note that not all satellite images are usable. Some images may be marred by excessive cloud cover, making shoreline detection difficult. Additionally, the choice of satellite also plays a crucial role. The shoreline extraction tools CoastSat and Shoreline Monitor use the Landsat series from number 4 to number 8 and the Sentinel-2. Table 2.1 overviews when a particular satellite is active, the revisit period and the pixel resolution.

Table 2.1: An overview of the satellites used for shoreline extraction in the tools CoastSat and Shoreline Monitor (Hagenaars et al., 2018; Vos et al., 2019; Luijendijk et al., 2018; Do et al., 2019). The Landsat satellites have been launched by NASA (2023a,b,c) and the Sentinel-2 has been launched by ESA (2023).

| Satellite Mission | Time coverage | Revisit period | Pixel resolution [m] |
|---|---|---|---|
| Landsat 5 (TM) | 1984 - 2013 | 16 days | 30 x 30 |
| Landsat 7 (ETM+) | 1999 - present | 16 days | 30 x 30 |
| Landsat 8 (OLI) | 2013 - present | 16 days | 30 x 30 |
| Sentinel-2 | 2015 - present | 5 days | 10 x 10 |

GEE was officially launched in 2010 as a cloud computing platform with significant computational capabilities, allowing users to run algorithms on a planetary scale (Gorelick et al., 2017; Zhao et al.,

2021; Hagenaars et al., 2018; Almeida et al., 2021). GEE enables cloud computing and is a valuable tool for geospatial big data analysis on a global scale. In addition, it is a free access platform which provides a large amount of remote sensing data from the earth's surface. Another advantage is that GEE has its own cloud computing infrastructure. This means the user does not have to download the large datasets (Gorelick et al., 2017). This feature frees users from the load of managing and storing large quantities of data. It allows them to concentrate on data interpretation and decision-making.

### 2.3.2 Shoreline detection - Shoreline Monitor

**Transect system**

For the shoreline detection, satellite images provided by GEE were used to extract the shoreline. Table 2.1 shows that the revisit time is approximately every 5 - 16 days. Thereby, the NASA Landsat satellites have a moderate spatial resolution of ∼30 m, while the ESA Sentinel-2 (ESA, 2023) has a more accurate spatial resolution. The Shoreline Monitor uses Landsat imagery (Landsat 5, 7 and 8 (Luijendijk et al., 2018; NASA, 2023a,b,c)) and Sentinel-2. Images from Sentinel-2 are used to detect sandy beaches around the world. In contrast, Landsat pictures are utilised to extract shoreline positions because they have a more extended history.

Determining the shoreline's location is crucial before extracting the shoreline's annual position from the satellite images. This is why the OpenStreetMap (OSM) of 2016, which includes the coastline feature, is used. OSM is a free collaborative tool which lets people access, modify and use geographic data from anywhere. The maps are displayed in reference systems World Geodetic Systems (WGS) 84 (EPSG 4326) (OpenStreetMap, 2024).

The first step is to place orthogonal transects at 500-meter intervals worldwide on the shoreline of OSM 2016. Each transect is 1 km long (500 meters of land and seawards, starting from the land side), as shown in Figure 2.3. It is important to note that only ice-free locations can be detected. According to a study by Luijendijk et al. (2018), the total length of the world's ice-free shoreline is 1.11 million km. Each transect is then assigned a unique ID based on its global location, including its starting and ending points in longitude and latitude. In total, there are 1.8 million transects within the ice-free area, which spans between latitudes 60°N and 50°S. Figure 2.4 shows the steps to develop a Satellite-derived Shoreline algorithm.

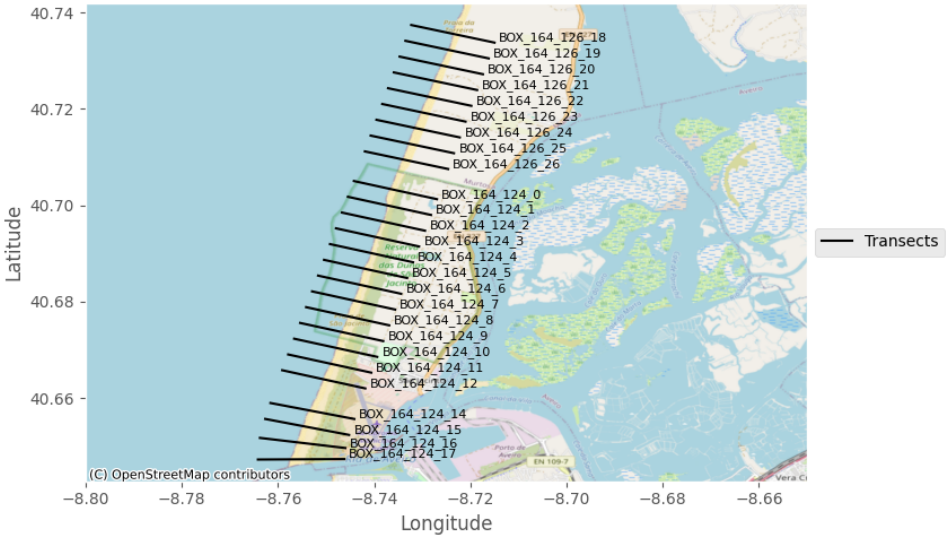


Figure 2.3: An illustration of different transects along the shoreline. Each transect is 1 km long (500 meters of land and seawards, starting from the land side).

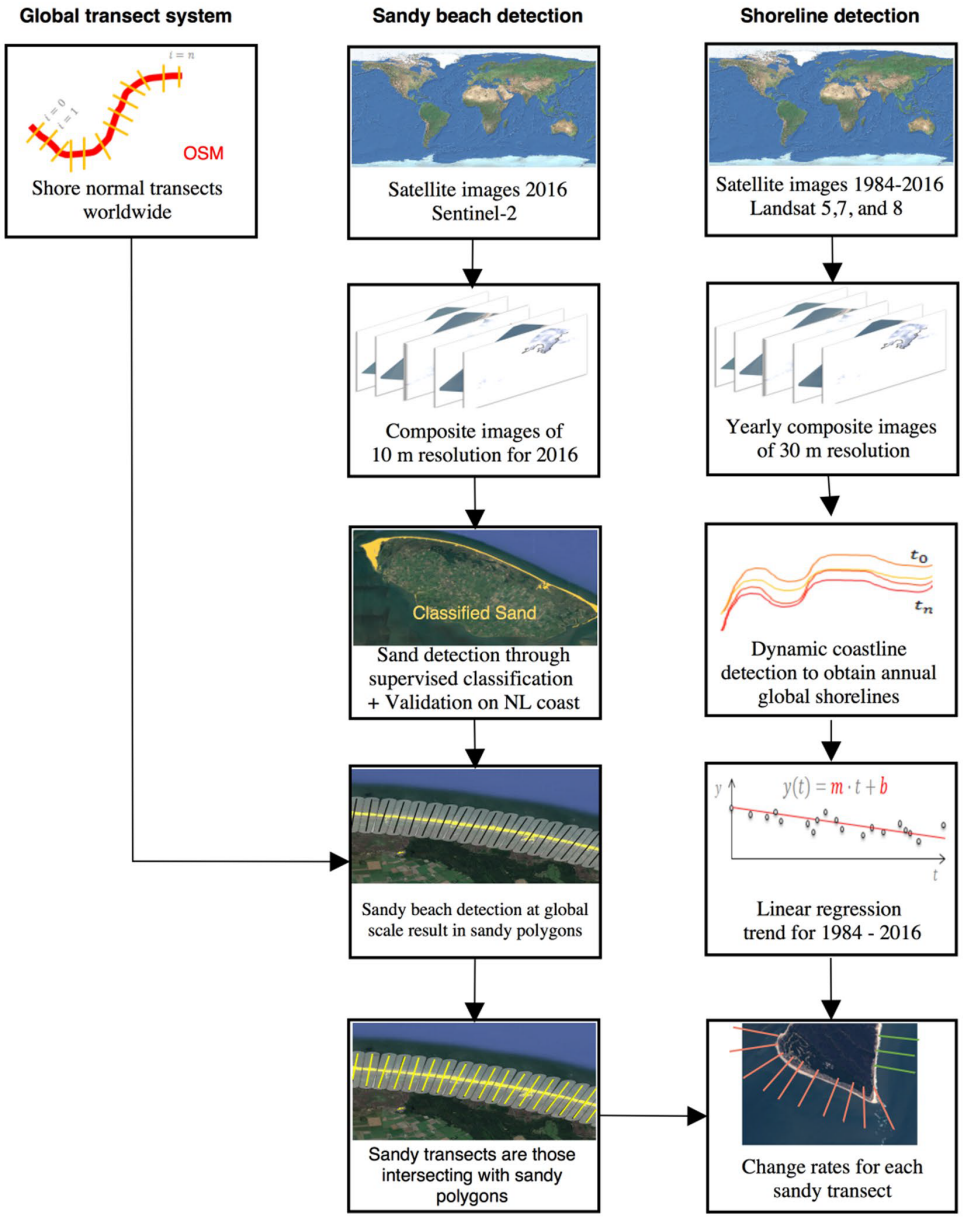


Figure 2.4: The three processes for the Shoreline Monitor: the global transect system, sandy beach and shoreline detection. Using the Global Transect system from OSM and the Sandy beach detection, it is feasible to extract shorelines worldwide and generate a Satellite-derived Shoreline database of 33 years of shoreline positions. Source: Luijendijk et al. (2018).

### Sandy beaches

After laying the transects along the shorelines worldwide, it is feasible to determine whether the shoreline is a sandy beach. Luijendijk et al. (2018) states that a sandy beach consists of carbonate sand, quartz and gravel. The detection is accomplished by doing a pixel-based supervised classification on a global Top of Atmosphere (TOA) brightness percentile composite image for 2016 using all available Sentinel-2 images. As a result, the earth has been divided into 20 km $\times$ 20 km boxes, with only the boxes overlapping with the OSM shoreline 2016 being used. This creates 24,000 boxes in total (Luijendijk et al., 2018).

The supervised classifier was trained on data from the Dutch Texel island to detect various land use types. The findings were compared to the sandy beach feature in OSM to determine the most promising categorization algorithm. The study by Luijendijk et al. (2018) found that the Classification and Regression Tree (CART) classifier had the highest actual positive percentage (97%) and the lowest omission error in a 100 km section of sandy beaches along the Dutch coast. Next, the trained supervised classification algorithm was applied to all boxes to detect sandy beaches on a global scale. Therefore, the

Sentinel-2 imagery was used to find more sandy beaches. As a result, the transects laying on a sandy beach are indexed as “sand” and others as “non-sand”. Transects without sand categorization due to no cloud-free Sentinel-2 images are annotated as “undermined sediment composition”. With this sandy beach detection, it is possible to display sites where the coastline consists of sand worldwide. This is visible in Figure 2.5.

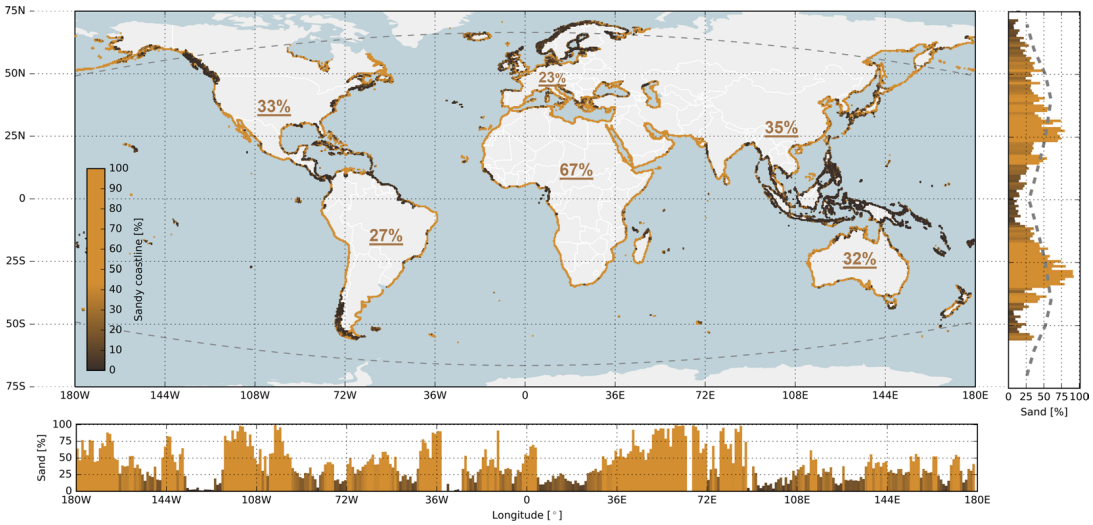


Figure 2.5: The coloured dots along the world’s coastline show the local percentage of sandy shorelines (yellow is sand, dark brown is non-sand). Source: Luijendijk et al. (2018).

### Satellite-derived Shoreline algorithm

After detecting sandy beaches, the next step is to extract shorelines. The GEE platform offered a 33-year collection of LandSat satellite photos for shoreline detection. The first step in the process is identifying clean satellite pictures. There should not be too many clouds, shadows, snow, or ice in the image. The 15% TOA reflectance percentiles per pixel were examined to identify global shoreline positions, resulting in the elimination of clouds and shadows (Hagenaars et al., 2018; Luijendijk et al., 2018). Figure 2.6 displays each pixel’s reflectance percentiles of 15%. Satellite images pixels that met the 15% TOA reflectance criteria were combined to create a composite for each year. According to Luijendijk et al. (2018), yearly composite images have the advantage of significantly reducing the influence of tidal stage on detected coastline positions and averaging out seasonal variations in wave and beach characteristics. Nonetheless, in areas with extensive swell conditions, wave-induced foam from wave breaking may cause a seaward offset in detected shoreline positions.

The next step in the process is to extract the waterline position using an unsupervised threshold algorithm. Therefore, the Normalized Difference Water Index (NDWI) method is used, Equation 2.2. With the radiance value in the Green and Near-InfraRed (NIR) band, the waterline position can be determined (Hagenaars et al., 2017, 2018; Do et al., 2019; Luijendijk et al., 2018; Almeida et al., 2021).

$$NDWI = \frac{\lambda_{NIR} - \lambda_{GREEN}}{\lambda_{NIR} + \lambda_{GREEN}} \tag{2.2}$$

in which $\lambda_{NIR}$ denotes the TOA radiance value in the Near-InfraRed and $\lambda_{GREEN}$ the TOA value in the Green band per pixel. Calculating the NDWI value per pixel gives a greyscale image ranging from $-1$ to 1. The Otsu (1979) threshold technique determines the ideal threshold value based on the statistical features of the NDWI histogram (Luijendijk et al., 2018; Hagenaars et al., 2017). The detected water lines at the edge of the water mask are smoothed with a 1D Gaussian smoothing operation to provide a progressive shoreline that avoids the pixel-induced staircase effect. As a result, 33 annual worldwide shorelines (1984–2016) with an alongshore resolution of less than 30 metres are produced using the automated shoreline detection approach. Following up, the shoreline change rate (m/yr) is calculated for each transect by running a linear regression on all the shoreline positions. Several SDS places, however, may be constrained by cloud cover and the accessibility of satellite imagery. Figure 2.4 displays the entire SDS procedure.

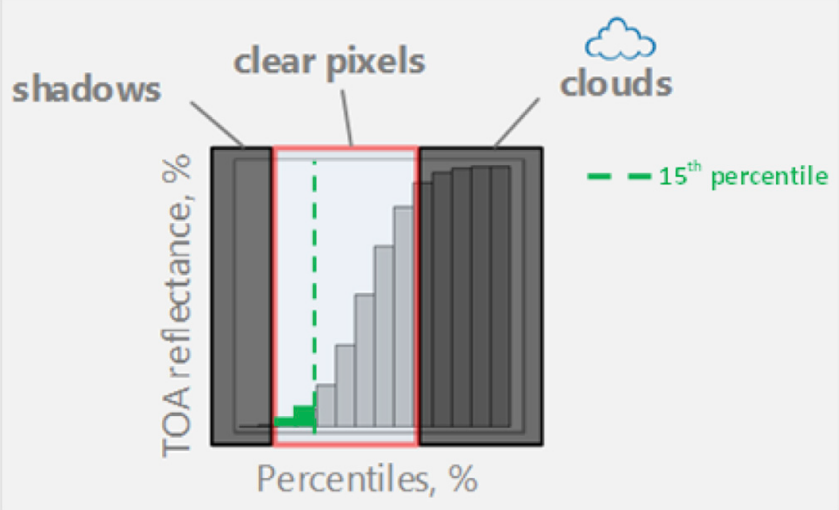


Figure 2.6: The image composite technique's principle is based on the per-pixel distribution of all TOA reflectance values inside the image composite time window. Source: Hagenaars et al. (2018).

Besides the NDWI, there is also a possibility to use the MNDWI, which is used by Vos (2019) and is as follows (Equation 2.3):

$$MNDWI = \frac{SWIR1 - G}{SWIR1 + G} \tag{2.3}$$

where $SWIR1$ and $G$ represent the pixel intensities in the short-wave infrared and green bands, respectively. Similarly to the NDWI, the MNDWI ranges from $-1$ to 1. The Otsu (1979) threshold technique can be used here to find the MNDWI value that maximises inter-class variance between the "sand" and "water" distribution, excluding upfront pixels belonging to the "white-water" and "other land features" class (Vos et al., 2019). This "white-water" can generate inaccuracies in the shoreline detecting approach (Hagenaars et al., 2018). According to McAllister et al. (2022), the Shoreline Monitor (Luijendijk et al., 2018) offers a global shoreline extraction approach, whereas CoastSat (Vos et al., 2019) focuses on regional and local methods. As stated by McAllister et al. (2022), the most common shoreline extraction strategies for the instantaneous waterline shoreline indicator are the indexing approach, including the NDWI and MNDWI.

Comparing the methods of Vos et al. (2019), Luijendijk et al. (2018) and Hagenaars et al. (2017) reveals that they can be arranged in the same category group according to Toure et al. (2019), namely group three. There are various automated methods for extracting shorelines from satellite images. Toure et al. (2019) divided the methods into three categories:

1. Edge detection: This method considers the shoreline extraction an edge detection problem.
2. Band thresholding: In this approach, a thresholding value is selected by man-machine interaction or a local adaptive strategy.
3. Classification: This method separates the image into land and water components and then takes the boundary line between them as the shoreline.

However, it is essential to note that the data obtained from SDS has some uncertainties due to tidal range in certain areas around the world (Castelle et al., 2022). At micro tidal beaches ($< 2$ m), this inaccuracy is typically under 10 meters. However, examining the meso (2 - 4 m) to macro ($> 4$ m) tidal range, the errors of the obtained SDS surpass 30 meters due to the breaking waves increasing the overall water level at the coast and blurring the dry sand/water limit (Castelle et al., 2022).

## 2.4 Example Satellite-derived Shoreline

Satellite-derived Shoreline is becoming a valuable resource for researching coastal processes (Vitousek, Buscombe, et al., 2023). Examples of research done by Luijendijk et al. (2018); Vos et al. (2019) demonstrate how the shoreline position has moved over time (Section 2.3). Besides determining the shoreline

position with SDS, some studies have tried to make shoreline predictions using the historical shoreline positions obtained by SDS. An example is the study by Vitousek, Vos, et al. (2023) "A model integrating satellite-derived shoreline observations for predicting fine-scale shoreline response to waves and sea-level rise across large coastal regions". This study uses the CoSMoS-COAST model to make shoreline projections using historical shoreline positioning data acquired by CoastSat (Vos et al., 2019), wave data and expected SLR. The predictions were made for the shoreline at Ocean Beach, San Fransico as shown in Figure 2.7.

### CoSMoS-COAST model

The CoSMoS-COAST model is a transect-based, one-line model that predicts short-term and long-term shoreline response to climate change in the 21st century. Where CoSMoS stands for, "Coastal Storm Modeling System", and COAST for "Coastal One-line Assimilated Simulation Tool" (Vitousek, Barnard, Limber, Erikson, & Cole, 2017). This model was initially developed and applied as a part of the larger USGS Coastal Storm Modeling System (Barnard et al., 2014). The model was created to help researchers assess the consequences of shoreline changes on future flooding caused by waves and sea level rise. The model uses partial differential equations: a sea level-driven shoreline recession model, a cross-shore equilibrium shoreline model and a longshore transport one-line model. It also contains a long-term rate parameter coming from unresolved processes. Hence, the following formula can be created (Vitousek, Barnard, Limber, Erikson, & Cole, 2017), Equation 2.4.

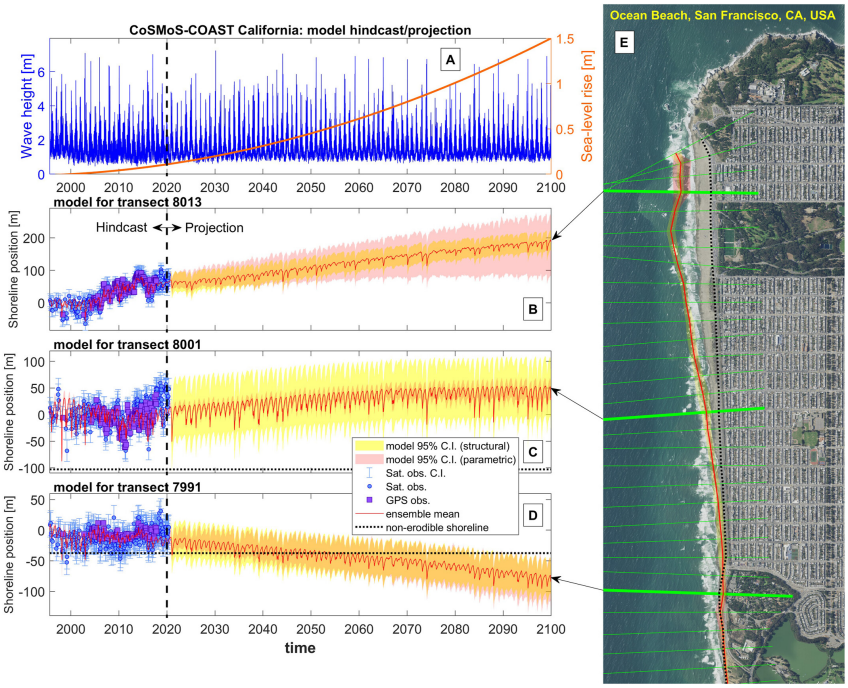


Figure 2.7: The shoreline prediction along Ocean Beach in San Francisco. The CoSMoS-COAST model is utilised for these projections, with input values including historical shoreline positions, expected wave conditions and a SLR of 1.5 metres. Source: Vitousek, Vos, et al. (2023).

$$\underbrace{\frac{\partial Y}{\partial t}}_{\text{shoreline change}} = \underbrace{\frac{-1}{d}\frac{\partial Q}{\partial X}}_{\text{longshore transport}} + \underbrace{CE^{1/2}\Delta E}_{\text{Cross-shore transport}} - \underbrace{\frac{c}{\tan\beta}\frac{\partial S}{\partial t}}_{\substack{\text{shoreline migration} \\ \text{due to sea-level rise}}} + \underbrace{v_{It}}_{\substack{\text{Long-term shoreline trend;} \\ \text{unresolved processes}}} \tag{2.4}$$

where $t$ is the time and $Y$ is the shoreline location as indicated by the distance from the onshore end of the transect along a shore-normal transect. According to Vitousek, Barnard, Limber, Erikson, & Cole

(2017), the alongshore gradient in the Longshore Sediment Transport (LST) rate $Q$ is represented by the first term of Equation 2.4. The LST is obtained as a function of wave and sediment characteristics (Vitousek, Barnard, Limber, Erikson, & Cole, 2017; Vitousek, Vos, et al., 2023). The unit is bulk sediment transport in $m^3$. $X$ denotes the alongshore coordinate and $d$ is the depth of closure. The second term is the equilibrium shoreline model, which models irregular beach erosion and recovery at high and low wave energy. Assuming that the beach slope, tan $\beta$, will remain approximately constant over time, the third term expresses the coastline recession caused by passive flooding due to sea level rise. The last term is the long-term coastal trend, which stands for unresolved processes, including sand mining, cliff collapse, nourishments, aeolian transport, sources, sediment sinks and rivers sediment output (Vitousek, Barnard, Limber, Erikson, & Cole, 2017).

**North Holland Coastline**

The study "The Estimation and Evaluation of Shoreline Locations, Shoreline-Change Rates, and Coastal Volume Changes Derived from Landsat Images" by Do et al. (2019) is another study that uses the shoreline generated from satellite data. This study evaluates sediment volumes derived from JARKUS profiles using the volume gradient provided by SDS (Do et al., 2019). The sediment transport gradient from SDS is ($\Delta V$) in $m^3$/year. The study area covered the North Holland coastline from Wijk aan Zee to Den Helder. The shoreline position was extracted using the same technique as the Shoreline Monitor, as described in Section 2.3. Using SDS to determine shoreline position, the volume change rate was computed between two transects and two years, multiplied by the active height (Do et al., 2019). To calculate sediment volume gradient, use the formula 2.5 (Do et al., 2019):

$$\Delta V = A_D \Delta_y \Delta_x \tag{2.5}$$

where, for every transect, $A_D$ is the active height (m), $\Delta_y$ is the shoreline-change rate in meters per year, and $\Delta_x$ is the transect spacing in meters. This way, it is possible to see how the beach profile erodes or accumulates over a certain period. In the calculations, the active height $A_D$ is the sum of the closure depth, $D_C$, and the berm crest or dune elevation, $D_B$, as shown in equation 2.6. The depth of closure, $D_C$, can be determined using active beach profile measurements or an analytical approach provided by Hallermeier (n.d.).

$$A_D = D_B + D_C \tag{2.6}$$

According to Do et al. (2019), it states that the volume $\Delta V$ ($m^3$/y) was computed using the shoreline-change rates under the assumption that the coastline is migrates horizontally over an active height ($A_D$) without altering shape, see Equation 2.5. Figure 2.8 illustrates this process.

The validation method for Satellite-derived Shoreline uses JARKUS data to validate shoreline changes and calculate sediment volume gradient. JARKUS data are field measurements taken annually across the same transect (Do et al., 2019). The volume change for each transect from the JARKUS profiles, $\Delta V_{profile}$ ($m^3$/y), was determined using linear regression. To compare volume changes, $\Delta V_{SDS}$ ($m^3$/y) and $\Delta V_{profile}$ ($m^3$/y) values were calculated for various times. Do et al. (2019) analysed five, ten, twenty, and twenty-five-year periods. According to Do et al. (2019), the results of the shoreline-change rates indicate a better agreement between the JARKUS and the SDS over more extended periods (20-25 years) compared to shorter periods (5-10 years). Likewise, the same holds for the sediment volume derived from the SDS.

**Nouvelle-Aquitaine Coastline**

A related study to Do et al. (2019) is the study from Castelle et al. (2022), "Primary drivers of multi-decadal spatial and temporal patterns of shoreline change derived from optical satellite imagery", which investigated the relationship between long-term shoreline change rate and longshore drift gradient. The study was done in the Nouvelle-Aquitaine region of southwest France, which has a large sandy shoreline. The shoreline in the study of Castelle et al. (2022) is more exposed than that of Do et al. (2019). Because of the continental shelf, the Nouvelle-Aquitaine region's shoreline experiences meso-macrotidal conditions, with the tidal range spreading northward. Furthermore, extratropical cyclones that track eastward in the North Atlantic Ocean subject the beach to extreme wave conditions.

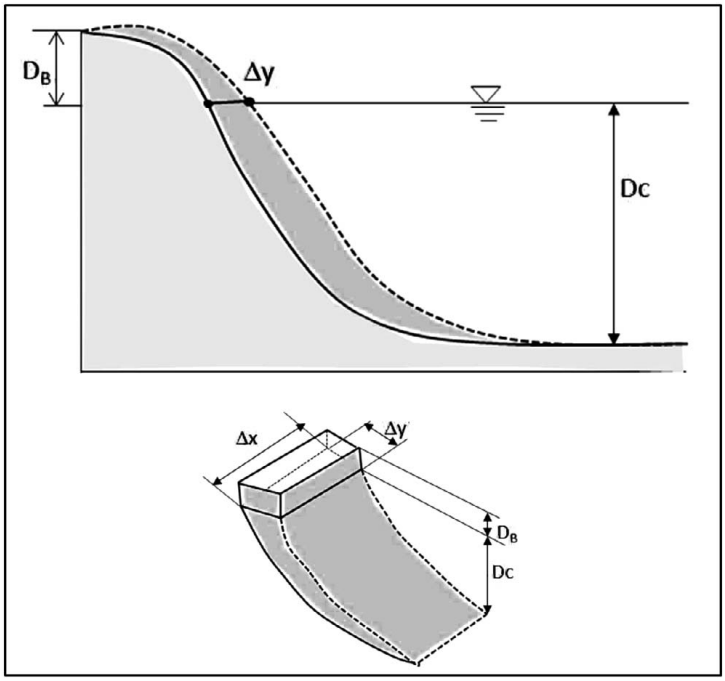


Figure 2.8: Illustration of the calculation to compute the sediment transport volume gradient by using the changes from the shoreline between two years and two transects. Source: Do et al. (2019).

The long-term rate of change of the shoreline was determined using CoastSat (Vos et al., 2019). In addition, the change rate trend obtained with SDS was compared with the field change rate trend, and the two trends were consistent. To calculate the longshore drift, a time series of wave conditions was retrieved hourly in front of the coast (Castelle et al., 2022). The offshore significant wave height $H_s$, peak period $T_p$, and angle of incident $\theta$ were converted into wave conditions at breaking $H_sb$, $T_pb$, and $\theta_b$ (Castelle et al., 2022). Equation 2.7 (Castelle et al., 2022) calculates the longshore sand transport $Q_{lst}$ at each wave time step based on the breaking wave circumstances. $V$ represents the longshore current, as seen in Equation 2.8.

$$\begin{aligned} Q_{lst} &= 0.23 H_{sb}^2 V, \text{ if } H_{sb}^2 V < 0.15 \\ Q_{lst} &= 0.2300225 + 0.008 H_{sb}^2 V, \text{ if } H_{sb}^2 V > 0.15 \end{aligned} \tag{2.7}$$

$$V = 0.25 k_v \sqrt{\gamma g H_{sb}} \sin 2\alpha_b \tag{2.8}$$

According to Castelle et al. (2022), $g$ represents gravity acceleration, $\gamma = 0.78$ is the breaker parameter, and $k_v$ is a free parameter valued at 2.9. To shift from longshore sand transport $Q_{lst}$ to longshore drift $Q_s$, $Q_{lst}$ is averaged across time for each transect. Castelle et al. (2022) found a strong correlation between long-term shoreline changes and estimated longshore drift gradients. Using the one-line assumption that, in the long term, the profile shifts parallel to itself with changing shape and with longshore sand transport taking place uniformly over the entire beach profile from the depth of closure to the top of the dune, the conservation of sediment gives $dS/dt = \frac{1}{h} dQ_s/dx$, where $h$ is the height of the active profile (Castelle et al., 2022).

## 2.5 Bridging the known and unknown

Comparing the existing method stated in Section 2.2 to the new innovative method described in 2.3 reveals that both ways aim to achieve the same goal, which is understanding a specific place's coastal systems and specifically its shoreline dynamics. Existing methods can calculate the Longshore Sediment Transport and determine past and future shoreline movements. For this calculation, wave and bathymetry data are required to estimate shoreline alteration using standard methods. In contrast, The

Shoreline Monitor can only display historical shoreline movements and forecasts using extrapolation, not including climate change or human intervention scenarios. However, the data input does not need to be the same as that of existing methods.

In comparison to existing methods for determining shoreline position from the past, the Shoreline Monitor produces faster results (Sections 2.2 and 2.3). However, comparing shoreline predictions made with the Shoreline Monitor to existing methods reveals that this is not currently feasible, according to existing literature. Section 2.4 provides examples that try to fill the gap in the literature, such as the research of Do et al. (2019). The research of Do et al. (2019) is an excellent attempt to determine sediment movement along the coast using the Shoreline Monitor. In contrast to the studies of Vitousek, Vos, et al. (2023); Castelle et al. (2022), the study from Do et al. (2019) does not predict shorelines. Nonetheless, wave data has been utilised in these two other investigations to determine littoral transport.

**Conclusion**

In conclusion, there is a vacuum in the literature when using the Shoreline Monitor to predict the shoreline when insufficient time or correct data is available to develop a model according to the existing methods. Thus, this research aims to create a technique that determines the Longshore Sediment Transport to predict shoreline positions using Satellite-derived Shoreline. This goal could serve as the study's primary research question. The main research question is formulated as follows:

---

***"How can various shoreline predictions be established using Satellite-derived Shorelines to estimate alongshore sediment transport and orientation?"***

---

The main research question can be broken down into smaller components in order to provide an answer to this primary research issue. First, a technique to convert 1D SDS data with X and Y coordinates into a volume gradient and LST. Thus, the following is the first sub-question that arises:

> ***How can a one-dimensional shoreline shift between two transects be converted into a sediment volume gradient?***

The next step would be to calculate the sediment transport at a specific place when the gradual littoral transport has been established, as shown in Figure 2.2 in Section 2.1. Therefore, boundary conditions are required to determine the sediment transport per transect because only the gradual LST is known. Littoral drift barriers can be employed as a boundary condition. Thus, the second sub-question is formulated as follows:

> ***Which boundary conditions can be applied to estimate Longshore Sediment Transport from a sediment volume gradient across transects in a selected area?***

Making predictions from the sediment transport per transect requires a crucial step. A sediment-orientation relationship is required to anticipate shorelines and provide insight into the shoreline's behaviour throughout time. Consequently, each transects shoreline direction is required. The third sub-research topic is therefore raised, and it is phrased as follows:

> ***How can the Satellite-Derived Shoreline historical Longshore Sediment Transport data and shoreline orientation be used to make future shoreline predictions?***

Given that Luijendijk et al. (2018)'s Shoreline Monitor offers shoreline positions globally, it would be beneficial to use the build method globally to obtain the shoreline movements both historically and in the future. Thus, the fifth sub-question is expressed as follows:

> ***How can the proposed method be adapted to be applicable globally?***

# 3

# Methodology

This study aims to build a methodology to derive the Longshore Sediment Transport using Satellite-derived Shoreline dataset and to make shoreline predictions, as mentioned in the introduction (Sections 1.2 and 1.3). The previous chapter outlines information on sediment transport (Section 2.1), existing methods (Section 2.2) and the Shoreline Monitor (Section 2.3). The research methods created and used to accomplish the research objective (Section 1.3) are contained in this chapter, which is divided into four sections, as shown in Figure 3.1 and will be elaborated in the Sections 3.2, 3.3, 3.4 and 3.5.

## 3.1 Methodology overview

The methodology consists of four primary themes, which area "Potential Case Studies", "Littoral Transport", "S-$\varphi$ Relation" and "Future Shorelines". The combination of the last three components forms the SHORECAST model, which is the main part of the study. SHORECAST stands for "Satellite-derived Historical and future Orientation-based Relation for Estimating Coastline Adjustments and Sediment Transport". Figure 3.1 illustrates how to proceed with these topics and the elements of the SHORECAST model. All these procedures employ data from the Shoreline Monitor by Luijendijk et al. (2018) to address the research questions in Section 1.3.

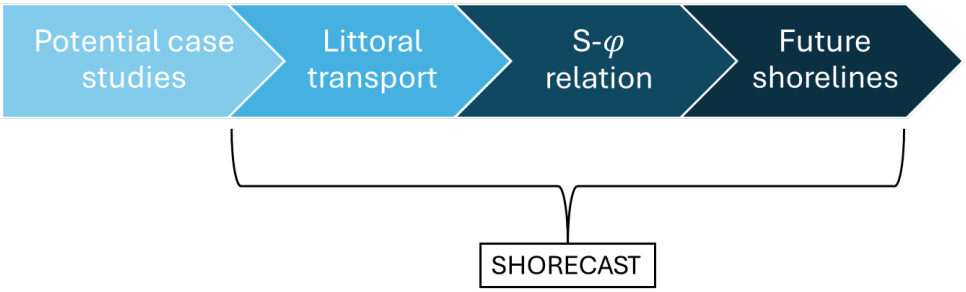


Figure 3.1: An overview of all four major methodology components, the four major themes in this study, and the last three components form the SHORECAST model. Obtaining an unprocessed SDS dataset to build a model for future shorelines.

Following the sequence of the four themes from left to right is essential, as shown in Figure 3.1. However, the "Potential case studies" stage is conducted only once as it provides multiple potential case studies. After choosing a case study, a new model can be developed to determine littoral transport from SDS. From this, shoreline prediction can be made. After completing this procedure once, the developed method

can be tested on one or more cases discovered in the first theme. The other three primary components of the SHORECAST model will be discussed in detail in the following sections. Section 3.3 explains how to derive the littoral transport (LST) from Satellite-derived Shoreline. Section 3.4 builds a relationship between the LST and the shoreline orientation. Section 3.5 demonstrates how this relationship predicts future shorelines.

Python is used to implement the methodologies outlined in the following sections. For more information, visit `https://www.python.org/`

## 3.2 Potential case studies

The methodology component "Potential case studies" identifies potential case studies based on specific criteria introduced in Section 3.2.2. The Potential case studies stage can be divided into three smaller steps, as shown in Figure 3.2. It is important to note that the pre-processing stage is only required once because the large dataset and the established filter criteria for future cases result in a wide range of examples worldwide. This stage aims to filter the data to include only places that align with specific filter criteria, as introduced in Section 3.2.2.


Figure 3.2: The step inside the Potential Case studies phase to find potential case studies that can derive the littoral transport from the SDS dataset and make shoreline predictions.

### 3.2.1 Satellite-derived Shoreline data collection

In this study, the dataset that will be used is created and provided by Luijendijk et al. (2018). A more detailed explanation of the Satellite-derived Shoreline dataset is provided in Section 2.3. This study uses version 1.5 of the SDS dataset. Handling this data is the first step in the potential case studie process.

### 3.2.2 Filter criteria

To be able to find potential cases to develop the new method, the large SDS dataset needs to be filtered based on specific criteria. These criteria identify places with less noise in the data. In order to create the model, the data used should be relatively noise-free. In other words, the data from a transect should perfectly fit the estimated regression line, as will be elaborated on in Section 3.2.3. A specific erosion and accretion rate is required to ensure considerable coastline change, as discussed more in Section 3.2.4. The final criterion applies to ensure many years with a coastline position. In other words, the transects do not have too many empty spaces, as will be explained in section 3.2.5. In summary, cases must satisfy three conditions on each transect to identify case locations with lower noise. These criteria include:

1. The data must fit the regression line, with an R-square value of 0.75 or higher
2. A minimum of five meters of erosion or accretion must occur annually.
3. Availability of at least 25 years of trustworthy data, excluding outliers, that align with the regression line.

Applying these three criteria to the SDS data produces various examples for developing a new method to derive the Longshore Sediment Transport from SDS and predict future shorelines. These cases can be used for both developing and testing the new method.

### 3.2.3 Regression Line Fit

The first criterion relates to the fit of the regression line. The data from a transect should fit perfectly with the fitted regression line. The regression line fit can be evaluated with two different statistical

measures. These are the "coefficient of determination", the so-called R-squared ($R^2$), and the Root Mean Squared Error (RMSE). The R-squared (Equation 3.1) indicates how much of the variance in the dependent variable in a regression model can be explained by the independent variables (Nakagawa & Schielzeth, 2013). The R-squared value goes from 0 to 1, with one indicating that the data is fully aligned with the regression line. While 0 indicates no fit at all. A number closer to one, or a larger R-squared, suggests a better model fit to the data and a more vital ability of the independent variables to explain the variance in the dependent variable.

$$R^2 = 1 - \frac{\sum_{i=1}^{n}(y_i - \hat{y}_i)^2}{\sum_{i=1}^{n}(y_i - \bar{y})^2} \tag{3.1}$$

where $n$ is the number of observations, $y_i$ the observed value of the dependent variable for observation $i$, $\hat{y}_i$ the predicted value of the dependent variable for observation $i$ from the regression model, and $\bar{y}$ the mean of the observed values of the dependent variable (Nakagawa & Schielzeth, 2013).

In contrast, RMSE (Equation 3.2) measures the average size of errors between anticipated and actual values. Vafaei et al. (2018) presents a single number representing the sample standard deviation of the differences between expected and observed values. The RMSE evaluates the variation of model error. A lower RMSE suggests a better regression model.

$$RMSE = \sqrt{\frac{1}{n}\sum_{i=1}^{n}(y_i - \hat{y}_i)^2} \tag{3.2}$$

Where $n$ is the number of observations, $y_i$ is the observed value of the dependent variable for observation $i$, and $\hat{y}_i$ is the regression model's predicted value of the dependent variable for observation $i$. Since the focus in the potential case studies process is to see if the regression line is in line with the data, the R-squared value will be used instead of the RMSE.

An example is illustrated in Figure 3.3. The data along the transect in the left image fits the fitted regression almost perfectly because the R-squared value is 0.94. On the other hand, the right image shows an R-squared value of 0.09, which indicates that the fitted regression line is not a decent fit through the data. In addition, the regression line and an approximate outlier detection are supplied by the SDS dataset. Luijendijk et al. (2018) defines the outliers as SDS points that deviate by more than three times the standard deviation.

#### R-squared value

Analysing Figure 3.3 reveals that a thighter R-squared value corresponds to less noise than a lower one. This makes it one of the three requirements for identifying possible case studies for the method's development and testing. The R-squared value must be greater than or equal to 0.75 ($R^2 \geq 0.75$) to filter properly (Nakagawa & Schielzeth, 2013).

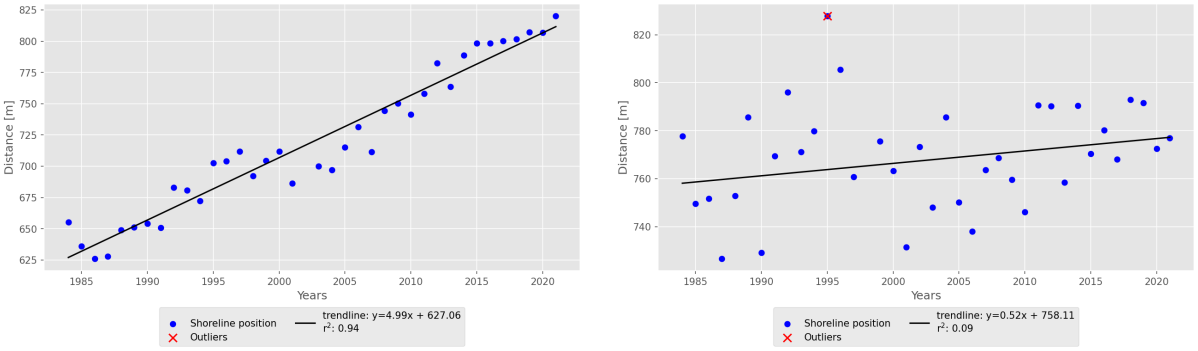


(a) (b)

Figure 3.3: Both graphs display the location of the coastline along a certain transect. The annual shoreline position along a certain transect is determined with Satellite-derived Shoreline. The result of these positions are the blue spots. Figure (b) is far from a perfect fit because of the R-squared value, but figure (a) demonstrates nearly perfect fit with the regression line. The red cross through the blue dot in figure (b) is classified as an outlier since the SDS point differs more than three times the standard deviation (as set by Luijendijk et al. (2018)).

### 3.2.4 Significant erosion or accretion rate per year

In Figure 3.3, besides the R-square number, the regression line value is also important. The shoreline line position in the left image in Figure 3.3 is roughly 625 metres in 1984 and 825 metres in 2021. This corresponds to an annual accretion rate of roughly 5 metres. It is clear from the right image that there has not been much of a shift in the location of the shoreline between 1984 and 2021. According to Luijendijk et al. (2018), shoreline erosion and accretion can be classified into six classifications as illustrated in Table 3.1.

Table 3.1: The table displays the classification of a specific change rate. There is just one classification for accretion and stability, although several classifications for erosion exist. Source: Luijendijk et al. (2018).

| **Accretion / Erosion Classification** | **Range** |
|---|---|
| Accretion | $> 0.5$ m/yr |
| Stable | $-0.5$ to $0.5$ m/yr |
| Erosion | $-1$ to $-0.5$ m/yr |
| Intense erosion | $-3$ to $-1$ m/yr |
| Severe erosion | $-5$ to $-3$ m/yr |
| Extreme erosion | $< -5$ m/yr |

To detect a significant annual rate of erosion or accretion, the extreme erosion rate will be utilised for erosion and the same rate for accretion, but positive ($> 5$ m/yr). As a result, the second requirement requires an absolute rate of at least 5 metres each year. In other words, the slope ($a \geq 5$ and $a \leq -5$) of the regression line ($y = ax + b$) (Hagenaars et al., 2018).

### 3.2.5 Trustworthy data availability

Last but not least, there is a need of reliable data availability. This indicates that there should be a sufficient number of years available which the SDS does not identify as outliers. Since the years in the SDS dataset span from 1984 to 2021, data should be available for 38 years in the best-case scenario. Obtaining a good satellite image over 38 years is not always feasible due to cloud cover in some areas or other considerations. An elaborate explanation of these clear satellite images is found in Section 2.3. Figure 3.4 shows the number of available years after all transects are examined and the years identified as outliers are removed. To ensure that the data contains enough data points, the minimum number of available data is 25 years or more.

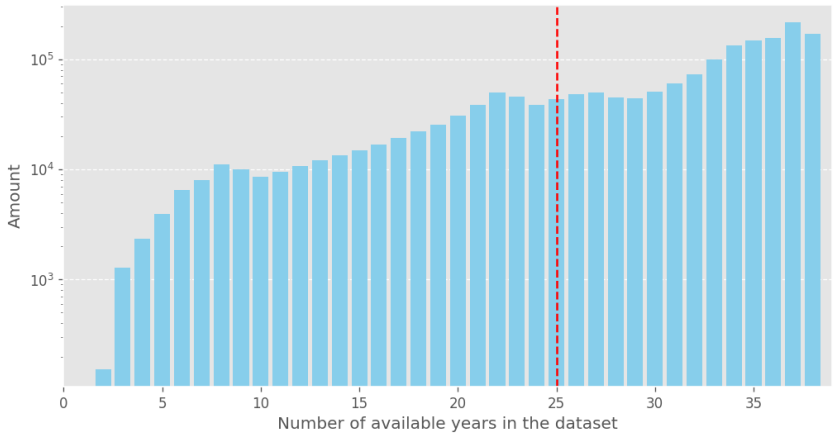


Figure 3.4: This figure displays a specific number of usable years per transect. The years detected as outliers by SDS have been eliminated.

## 3.3 Littoral Transport

After the Potential case studies process, a case study is selected to produce a strategy to determine the littoral transport and predict shorelines. Figure 3.5 illustrates the necessary steps. Essential steps are Outlier Detection, Interpolation, Smoothing, Determining $\Delta A$, Determining $\Delta V$ and the Longshore Sediment Transport. The bold boxes represent the primary steps in the littoral transport building block and the dashed boxes represent necessary assumptions.

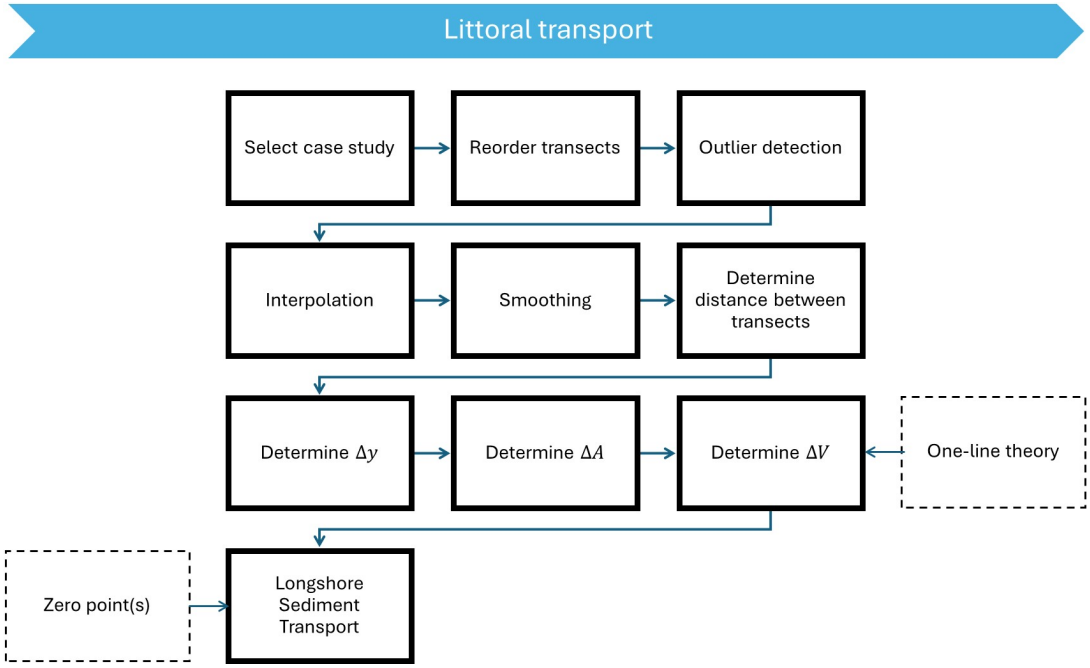


Figure 3.5: The steps to derive littoral transport along the shoreline starting from the SDS dataset and shoreline position. In addition to the data from the SDS, the active height and zero point location should be provided. The primary steps in the littoral transport building block are represented by bold boxes and dashed boxes represent the necessary assumptions.

### Reorder transects

After selecting a case study, a quick check is performed to ensure all transects are properly put one after the other in the data frame. First, find the southernmost transect's Easting and Northing coordinates to align the transects. Appendix A.1 explains utilizing Easting and Northing coordinates instead of latitude and longitude. Once the southern transect is determined, the distance between the southern transect and the remaining transects is computed. Appendix A.2 provides a more detailed explanation. The transects are reordered according to the distances between the start and other transects. As a result, the data frame's transect will be arranged from south to north. It is important to note that the most southern point in Easting and Northing corresponds to the origin in the $x$-$y$ coordinate system. The $x$-$y$ coordinate system is used in the following steps to derive the littoral transport. Figure 3.6 shows this $x$-$y$ coordinate system.

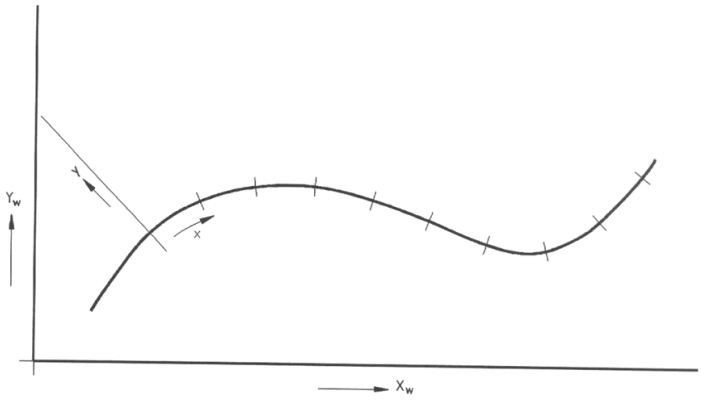


Figure 3.6: The shoreline presented in $x$ and $y$ coordinates. The solid curved line is the shoreline. The perpendicular lines on the shoreline are the transect. The transect closest to the origin is the southern transect. Source: Huisman & Dagalaki (2020).

### 3.3.1 Outliers

Once a case has been chosen and the transects have been rearranged, the subsequent task involves verifying whether the shoreline positions align with the trend for each transect in a natural way. Figure 3.3 in Section 3.2.3 illustrates shoreline positions that match the regression line (Figure 3.3a) and those that do not (Figure 3.3b). An outlier detection method is employed to identify whether a shoreline position is unusual. Outlier identification represents the common practice of deleting unusual occurrences from data. According to Hodge & Austin (2004), mechanical failures can cause outliers, as well changes in system behaviour, fraud, human mistakes, instrument errors, or natural population variances. Outliers can occur in this study due to system behaviour and instrument error due to the SDS resolution (Section 2.3). In this study, two outlier methods are applied, which are:

1. Standardised Residuals Outliers
2. Shoreline Shift Detection

Figure 3.7 displays the results of these two strategies. The top graph in Figure 3.7 is used for the Standardised Residuals outlier method. The bottom graph represents the difference between two shoreline positions used for the Shoreline Shift Detection.

#### Nourishment

Numerous anthropogenic measures have been implemented in various coastal regions worldwide to protect inland areas from flooding and prevent shoreline erosion. One such measure involves the placement of nourishment along the coastline. Nourishment is a massive sand accumulation spread across the coast, whereby the sand is acquired from dredging in the deep sea. Four types of nourishment exist: on the inner slope of dunes, on the outer slopes of dunes, on a dry beach or directly on the shoreline (Bosboom & Stive, 2021). As mentioned earlier, the presence of nourishment in the SDS dataset is the most significant matter as it impacts the process of obtaining the Longshore Sediment Transport. In a year when nourishment is present, the LST will be significantly higher compared to previous years. Without proper identification, the relationship between S-$\varphi$ becomes invalid since the orientation of the shoreline no longer aligns with the LST as observed in earlier years without nourishment.

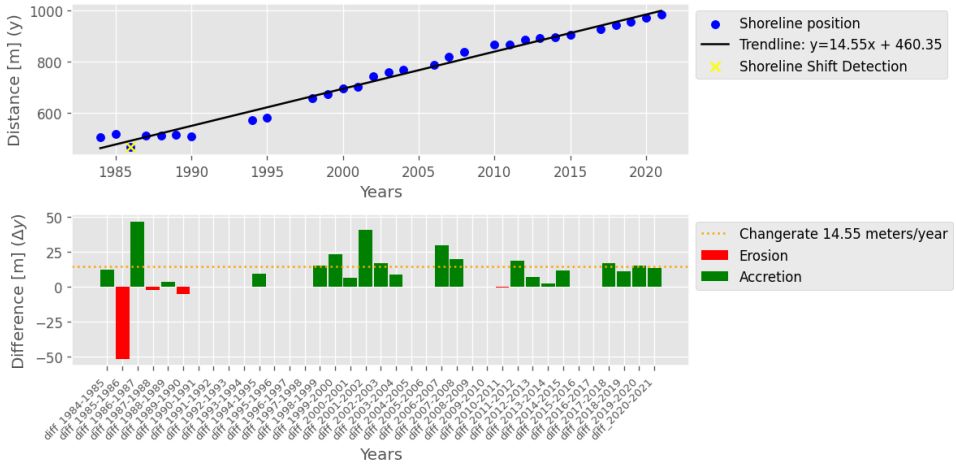


Figure 3.7: This figure contains two graphs. The top graph depicts the shoreline position (blue dots) in metres yearly. The solid black line represents the regression line for this particular transect. The bottom graph displays the difference between every two successive coastline positions. Green indicates accretion, whereas red represents erosion, both in meters. The orange line represents the annual change rate based on the slope of the regression line from the SDS dataset Luijendijk et al. (2018). Finally, the yellow cross at the blue dot in the top graph indicates that this place has been discovered as an outlier and will be removed from the dataset..

To identify the nourishments in the dataset, it is necessary to understand their function. Figure 3.8 shows the shoreline position significantly shifts further seawards when nourishment is placed along the shoreline. Furthermore, the shoreline location movement occurs across numerous transects, not just one. Therefore, nourishment is recognised as a substantial rise, where the shoreline position shifts by at least 40 metres between two years and is distributed over at least 5 SDS transects. An elaboration on the nourishment detection can be found in Appendix A.3.

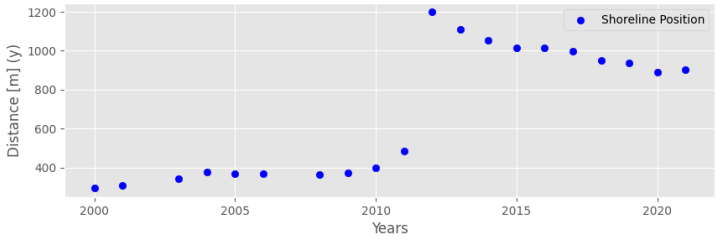


Figure 3.8: A time-series of shoreline positions along a SDS transect. Between 2011 and 2012, nourishment was placed along the shoreline. This is noticeable due to a large shift in shoreline position.

### Standardised Residuals Outliers

The shoreline position has been retreating and recovering over the years. Because of this fluctuation, the Satellite-derived Shoreline may make an error when extracting the shoreline position. To detect the extreme errors, Luijendijk et al. (2018) makes use of the "Standardised Residuals" method (Blatná, 2006). Luijendijk et al. (2018) defines an outlier as a shoreline position along a transect three times or greater than the standard deviation. This method is consistent with Blatná (2006). According to Blatná (2006), Standardised Residuals of |3| or greater can be defined as outliers. Thus, the outlier identified by Luijendijk et al. (2018) are deleted from the SDS dataset. Figure 3.9 depicts the steps of the Standardised Residuals Outliers Method. However, not all outliers are genuine outliers, as shown in Figure 3.9. An identified outlier can also serve as a source of nourishment if it meets the nourishment criteria. If this is the case, the coastline position will not be removed from the dataset.

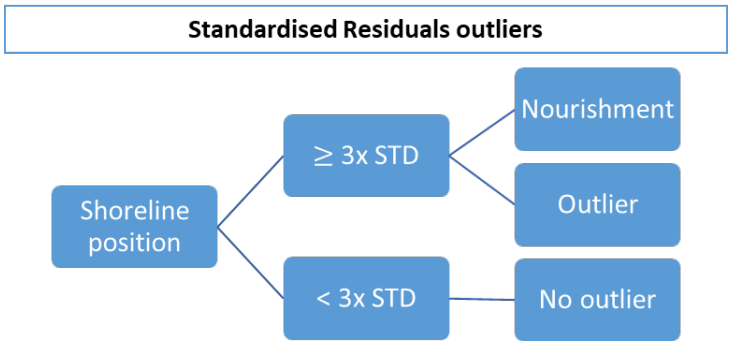


Figure 3.9: The stages for determining whether a shoreline position is an outlier, nourishment, or simply a natural shoreline position.

### Shoreline Shift Detection

Another outlier method is "Shoreline Shift Detection". This method determines if a shoreline shifts landward and returns roughly to the same position the following year or vice versa. Poor satellite picture clarity or many high or low tide photographs in the annual imagery compilation may cause the shoreline to shift (Castelle et al., 2022). As a result, a different procedure will be applied to the SDS data.

To identify these small errors, it is necessary to determine the difference between two shoreline points using a technique similar to the "Euclidean Distance" method (Knorr et al., 2000), which is illustrated in Equation 3.3. with $P_n$ shoreline position year 1 and $P_{n+1}$ shoreline position year 2. $d$ gives the difference between shoreline positions from 1984 till 2021, which is represented as $n$.

$$d(P_n, P_{n+1}) = P_{n+1} - P_n \tag{3.3}$$

A mistake can be identified if it fits three requirements. The first rule states that two successive differences in the series $D = d_1, d_2, \ldots, d_{n-1}$ should have opposite signs. Searching for the opposite sign ensures accretion between years one and two and erosion between years two and three. Or vice versa. Next, the absolute value difference ($d_k$ and $d_{k+1}$) should be greater than two times the standard deviation of the difference between the shoreline location and the trendline. Equation 3.4 calculates the standard deviation by summing the difference between the shoreline location and the regression line of a single transect.

$$\begin{aligned} W(n) &= P_n - (a \cdot n + b) \\ \sigma &= \text{std}(W) \end{aligned} \tag{3.4}$$

Where $P_n$ represents the shoreline location of a particular year $n$, $a$ is the regression line's change rate and $b$ is the intercept. $W$ is an array with the difference between shoreline position and trendline.

As last, the ratio $R$ between the two differences should be found (Equation 3.5), with a $1/1.25 \leq R \leq 1.25$ range. The explanation for determining this ratio is to ensure accretion and erosion are connected. In other words, there was a correction since the shoreline location differed significantly from the other shoreline positions around it. The reason for choosing a range of $1/1.25$ to $1.25$ is to eliminate differences in shoreline length. The value of 25% was chosen because even after adjusting for shifts, the shoreline may have undergone erosion or accretion. In other words, the difference between two shoreline positions includes the actual shift and the deviation error. Therefore, 25% is considered an appropriate value for these factors. A new pattern appears if the ratio is tiny or more significant than this deviation. Equation 3.6 summarises all three criteria.

$$R = \frac{|d_k|}{|d_{k+1}|} \tag{3.5}$$

$$\begin{cases} \text{Criteria 1, opposite sign:} & \text{if } d_k \times d_{k+1} < 0 \\ \text{Criteria 2, two times std:} & \text{if } |d_k| + |d_{k+1}| \geq 2\text{std(shoreline - trendline)} \\ \text{Criteria 3, ratio:} & \text{if } 1/1.25 \leq R \leq 1.25 \end{cases} \tag{3.6}$$

As with the Standardised Residuals Outliers technique, particular coastline places may be recognised as outliers despite being part of a nourishment. That is why the nourishment check is incorporated in this outlier method. If a shoreline position is determined as an outlier and not as a nourishment or a regular shoreline position, it will be eliminated from the SDS dataset.

### 3.3.2 Interpolation

After applying the outlier, the shoreline positions that did not meet the outlier criteria were eliminated from the dataset, resulting in missing values in the dataset. Besides the empty spots created by the outlier methods, the SDS dataset is also incomplete. There are years where no annual shoreline could be found due to insufficient clear satellite pictures to estimate an annual shoreline position, as stated in Sections 2.3 and 3.2. To derive littoral transport from the Satellite-derived Shoreline, the missing data points need to be filled using a particular method.

Linear interpolation along the transect is a method to fill up these empty spots because each transect can be seen as a time series and the empty spots are very brief gaps (Salgado et al., 2016). Time series can benefit from linear interpolation, which computes a missing value by interpolating the values of the previous and next accessible coastline position. When using linear interpolation, missing data are replaced with predicted values that underestimate variance and ignore uncertainty. This is equivalent to "single-value imputation" (Salgado et al., 2016). Filling up the empty spots will be done in three steps. These are:

1. Spatial boundaries
2. Spatial Intersections
3. Linear interpolation

#### Spatial boundaries

The initial step in the interpolation process is ensuring the boundary cells contain a value. The boundary cells refer to the four cells located at the corners of the matrix. Specifically, the first and last transects must be inspected during the initial year to ensure they contain a value. This same process must be repeated for the final year. If any of these cells lack a value, the shoreline position from the subsequent or previous year will be utilized. Consequently, two consecutive years within the same transect will share the same shoreline position. Filling in these boundaries provides the benefit of expanding the number of shoreline positions in the next steps of the interpolation process. More shoreline positions will make determining the Longshore Sediment Transport easier.

#### Spatial Intersections

The next step is to check whether the initial and last year's shoreline positions are known across all transects. If this is not the case, these positions should be extracted via spatial interpolation. In other words, the shoreline position at the missing transect will be determined using the shoreline positions from the transects adjacent to it. This step is required to be able to perform a linear interpolation between all missing points on each transect between the first and last years. Otherwise, only the empty cell between the known points will be interpolated.

This missing shoreline position can be obtained by drawing a line between transects where the shoreline has been known. The intersection of the shoreline and the transect with the missing shoreline position produces the new shoreline position. Figure 3.10 illustrates three transects. The two solid black lines represent transects where the coastline position from the first year is known. The dashed line represents a transect where the shoreline position is unknown. The intersection's coordinates are Easting and Northing. First, the SDS shoreline position provided in metres from the start of the transects (starting from inland) needs to be converted into a $X$ and $Y$ coordinate to know where the shoreline position is in space. Therefore, Pythagoras will be used as illustrated in Equation 3.7.

$$\begin{aligned} x_{length} &= |A.x - B.x| \\ y_{length} &= |A.y - B - y| \\ D &= \sqrt{x_{length}^2 + y_{length}^2} \end{aligned} \tag{3.7}$$

The starting point of the transect is $A$, the intersection point is $B$, and the distance between the two points is $D$, as shown in Figure 3.10.

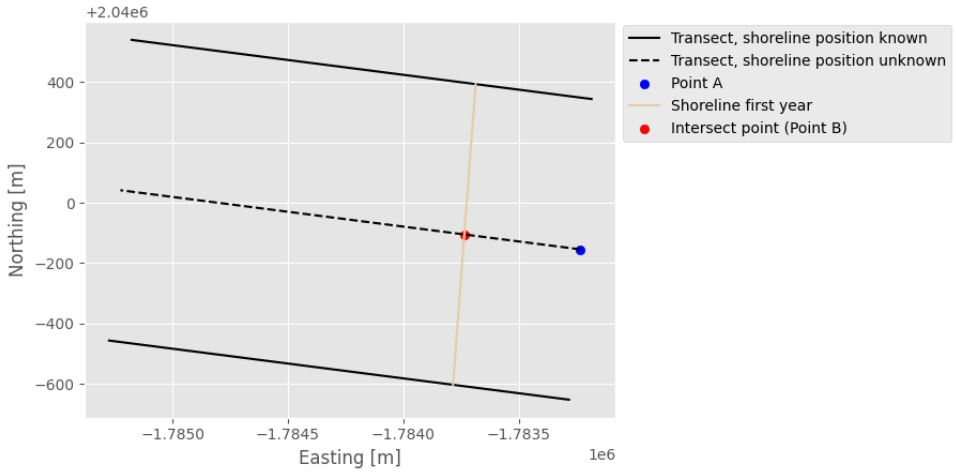


Figure 3.10: The two solid black lines represent the transects where the shoreline position is known. The dashed black line in the middle is the transect where the shoreline position is unknown. The intersection of the shoreline and the dotted line reveals the shoreline position for that transect.

#### Linear interpolation

Now that the shoreline positions for the first and last years of the dataset are known per transect, the missing data point in the centre can be filled in using linear interpolation. The reason for filling empty spots with linear interpolation is to have a yearly shoreline position at each transect. The absence of a shoreline position per transect would complicate the surface area and volume calculation. However, comparing the surface and volume values with those of another transect would be more challenging. Additionally, linear interpolation is valid because the shoreline positions are per year. Therefore, seasonal shoreline changes will be minimized (Bosboom & Stive, 2021; Luijendijk et al., 2018).

Linear interpolation will be applied to the empty places in each transect. In other words, the missing data points are estimated using the values of neighbouring data points. These neighbouring data points represent the years before and after the empty spot where the shoreline is known. Equation 3.8 illustrates the linear interpolation method.

$$y = y_0 + (x - x_0) \cdot \frac{y_1 - y_0}{x_1 - x_0} \tag{3.8}$$

where $x$ represents the year in which the shoreline position $y$ is unknown. $y_0$ is the last known shoreline position before $y$ in year $x_0$, while $y_1$ is the first known shoreline position following $y$ in year $x_1$.

### 3.3.3 Smoothing

The next step in determining the littoral transport process is smoothing the data after the outlier detection and interpolation. Smoothing the data is needed to lower the noise and raise the signal-to-noise ratio (Duncan & Mengersen, 2020). The data is smoothed using a variant of the moving average, with a $N$ value of five. According to Ibaceta et al. (2023), a five-year timeframe can catch significant coastline patterns. This was applied to the coast of Australia where the El Niño-Southern Oscillation (ENSO) plays an important role. However, this ENSO affects other coastal locations globally. As a

result, the smoothing factor $N = 5$ might be applied in a variety of locations around the world. Other $N$ variables were tested, including 3, 7, and 9. A higher value provides a better signal-to-noise ratio. However, the number of years available for further research is decreasing. As a result, the $N$ value is set at 5 and is used further in this study.

Equation 3.9 illustrates the rolling window mean function, where $P$ is the shoreline location and $N$ is the rolling window size. However, with $N = 5$, the moving average calculates a value after three years. In other words, this indicates no value for the first two years. The mean of the first four distances is computed for year two with N=5 to calculate an extra value at the start. The same procedure is followed in the conclusion, where the average distance for the last four years is calculated to provide an extra distance value.

$$\text{Moving average}(P_i, N) = \frac{1}{N} \sum_{i=n-N+1}^{n} P_i \tag{3.9}$$

### 3.3.4 Mean distance transects

As Section 2.3 mentioned, the transects along the shoreline are placed perpendicular to the shoreline from OSM 2016, with an interval of 500 metres. Since the shoreline changes yearly, the distance between two transects may be greater or less than 500 metres. Because of these annual fluctuations, comparing shorelines that are not in the same location is more complicated. To address this issue, the average distance between transects must be computed using the shoreline length from all years. This distance can also be used for visualization purposes. With the mean distance transects the shoreline difference ($\Delta y$), surface gradient ($\Delta A$) and volume gradient ($\Delta V$) for all years can be placed at the same $X$ value.

The mean distance is determined using Easting and Northing coordinates (Appendix A.1 gives more information on this coordinate system). The calculation starts the most southern point in $X$ and $Y$ space. At this point, the first transect will be set to $x = 0$ meters. For the next point $x_1$, two perpendicular lines are drawn from the transect to the middle point of the shoreline as illustrated in Figure 3.11. The first line is from the first transect (the green dashed line) and the second line from the second transect to the middle point of the shoreline (the blue dashed line). The length of these blue and green lines represents the shoreline's distance for a given year. Equation 3.10 illustrates how to calculate the mean distance between these two transects by collecting distances for all available years.

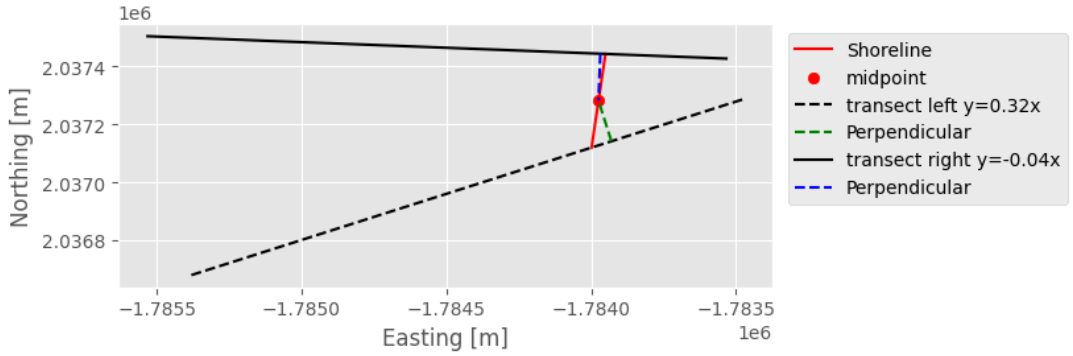


Figure 3.11: The steps to calculate the shoreline distance between two transects. The red line represents the shoreline for a specific year, the black dashed lines represent the transect, and the blue and green lines represent the distance from the shoreline's midway point perpendicular to the transect.

$$\overline{x} = \frac{1}{n} \sum_{i=1}^{n} x_i \tag{3.10}$$

Where $\overline{x}$ represents the average distance between two transects, $n$ is the total number of years available, and $x_i$ is the distance between each year's blue and green lines. In order to calculate the distance between all the transects, this process needs to be repeated for each transect.

### 3.3.5 Determining $\Delta y$ and $\Delta A$

To gain insight into the behaviour of the shoreline over time, the difference between years ($\Delta y$) is computed. This difference provides information on how much the shoreline erodes or accretes over the years. These eroding and accreting processes can occur naturally due to storms but can also be artificial. An artificial accumulation is a nourishment. It is possible to detect whether the nourishment is spreading, degrading at the top and accumulating at the sides (Arriaga et al., 2017). Additionally, knowing the shoreline annual difference can help determine whether coastline structures, such as a groyne, are along the shoreline. Because of accretion at one side and on the other side erosion.

To better understand how much the shoreline has migrated horizontally over time, $\Delta A$ is established. $\Delta A$ provides information on the amount of coastal erosion or accretion in $m^2$ each year. Thus, the surface gradient provides more details regarding nourishment (in two dimensions space). It indicates how much the nourishment degrades and accumulates along the sides.

To determine if $\Delta A$ is accurately calculated, the lines in a $\Delta A$ - $X$ plot should look similar to a $\Delta y$ - $X$ plot. Nonetheless, the values on the $Y$-axis are different, but the values of $X$ are the mean distance values.

#### Determining $\Delta y$

Determining $\Delta y$ is just the difference in shoreline position of two years. This difference can be calculated with a simple equation as illustrated in Equation 3.11. The shoreline positions are provided as a set, $P = \{P_1, P_2, \ldots, P_i\}$, after the smoothing process with $i$ the number of years after smoothing.

$$\Delta y = P_{i+1} - P_i \tag{3.11}$$

#### Determining $\Delta A$

To calculate the surface gradient ($\Delta A$) the time difference ($\Delta y$) is multiplied by the difference between two transects ($\Delta x$). Equation 3.12 shows the formula for calculating the surface area between two years and two transects in simple terms. It is important to note that the calculation of $\Delta x$ does not involve the mean distance transects, as the goal is to determine the yearly difference. Therefore, the $x$ component of the shoreline between two transects is used since the domain is in $x$ and $y$ space.

$$\Delta A = \Delta y \times \Delta x \tag{3.12}$$

Figure 3.12 illustrates how the surface gradient between two transects is calculated. The points $A$ and $B$ are from year one, whereas the points $C$ and $D$ are from year two. Using the "Schoelace formula", also known as the "Surveyor's formula" Equation 3.13 (Windarni et al., 2023), the surface of the polygon can be determined.

$$\Delta A = \frac{1}{2}\left|\sum_{i=1}^{n-1}(x_i y_{i+1} - x_{i+1} y_i) + x_n y_1 - x_1 y_n\right| \tag{3.13}$$

The polygon's area is represented by $\Delta A$, as shown in Figure 3.12. $(x_1, y_1), (x_2, y_2), \ldots (x_n, y_n)$ represent the coordinates of the polygon's vertices in anticlockwise order. The summation sign $\sum$ adds the terms for each successive pair of vertices. The phrase $x_i y_{i+1} - x_{i+1} y_i$ computes the "cross-product" between each pair of subsequent vertices. Finally, compute the cross-product of the last and first vertices, $x_n y_1 - x_1 y_n$, and take the absolute value to guarantee the area is positive. The full summation is divided by two to get the area gradient.

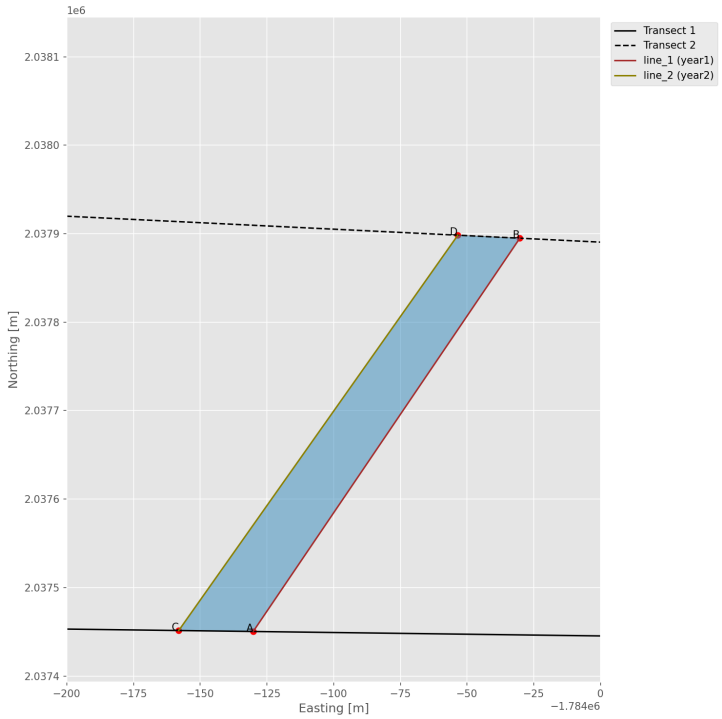


Figure 3.12: The surface is calculated based on the position of the points $A, B, C$ and $D$. Each point has a $x$ and $y$ coordinate.

If the lines from the years do not cross, the "Schoelace formula" can be applied. Suppose the lines intersect (Figure 3.13), then an additional approach is required to compute the surface area. This is $0.5|x \bullet y_{\perp}|$. Equation 3.14 demonstrates how to calculate the surface of a triangle.

$$\begin{aligned} \Delta A =& \frac{1}{2} \left| \begin{bmatrix} x_1 \\ x_2 \\ x_3 \end{bmatrix} \cdot \begin{bmatrix} (y_2 - y_3) \\ (y_3 - y_1) \\ (y_1 - y_2) \end{bmatrix} \right| \\ =& \frac{1}{2} \text{ abs} \left( x_1 \times (y_2 - y_3) + x_2 \times (y_3 - y_1) + x_3 \times (y_1 - y_2) \right) \end{aligned} \tag{3.14}$$

The Schoelace formula determines whether the surface is positive or negative. If the shoreline from year 2 is to the left of the shoreline from year 1, it is positive (Figure 3.12). If the shoreline from year two is on the right, it is negative. The triangle depends on which area is the largest to see if the sign is positive or negative.

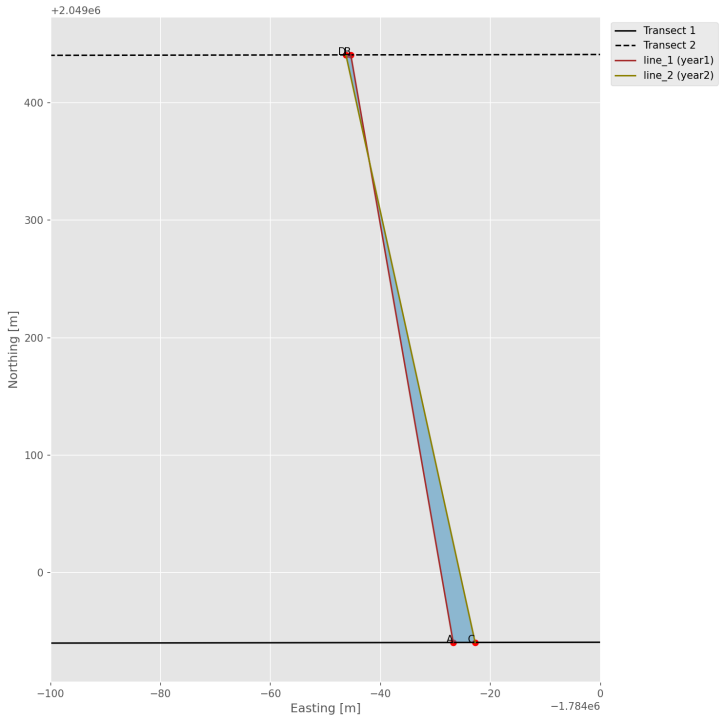


Figure 3.13: The surface is calculated based on the surface areas of both triangles. Therefore, the intersection point will also be used in the calculation.

### 3.3.6 Determining $\Delta V$

The volume gradient ($\Delta V$) should be determined to better understand the sediment transport gradient along the shoreline. The volume gradient can provide additional information about whether nourishment is carried out as planned.

To determine the volume gradient, first multiply the surface gradient by the change in bathymetry. Since the annual change in bathymetry is unknown in most regions worldwide, another approach must be utilised to compute the volume gradient. This alternative method is based on the assumptions of one-line theory (or single-line theory) and active height. Equation 3.15 gives the formula for calculating the volume gradient using these assumptions. In summary, the one-line hypothesis states that the shoreline moves horizontally while the coastline profile remains constant. Figure 3.14 illustrates the calculation of the volume gradient. However, $S_x$ remains unknown and will be determined in the following step (Section 3.3.7). Important to note is that the visualisation of $\Delta V$ along the $X$-axis should look similar to the ones of $\Delta A$ - $X$ and $\Delta y$ - $X$, where $X$ is the mean distance between transects.

$$\Delta V = \Delta A \cdot H \tag{3.15}$$

$$H = d_c + \text{tidal range} \tag{3.16}$$

where $H$ is the active height and $d_c$ the closure depth.

#### Single-line theory

The nearshore zone (the coastal zone) changes over time. However, SDS data does not provide the height of the beach, nor does it give it the shoreline profile. Therefore, another way must be found to calculate the volume. This is possible when it is assumed that the coast does not change in shape. The coast moves seaward or landward direction, but the shoreline profile remains. This is also called the "Single-line theory". The single-line theory assumes that the cross-shore profile's form remains constant, resulting in an equilibrium profile with any shape (Bosboom & Stive, 2021; Larson et al., 1987; Oh et al., 2020). Figure 3.15 and Figure 2.8 in Section 2.4 show that when the coast erodes or accretes, the entire profile moves seawards or landwards by a horizontal distance ($\Delta A$).

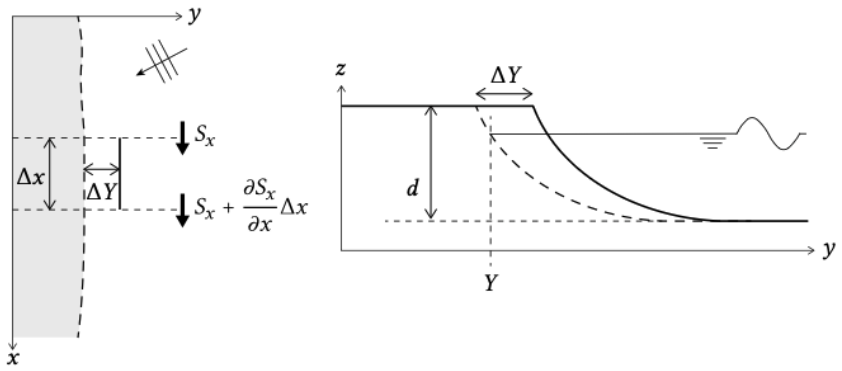


Figure 3.14: The sediment transport along the coast with a shoreline change of $\Delta Y$, assuming the Single-line theory. Source: Bosboom & Stive (2021).

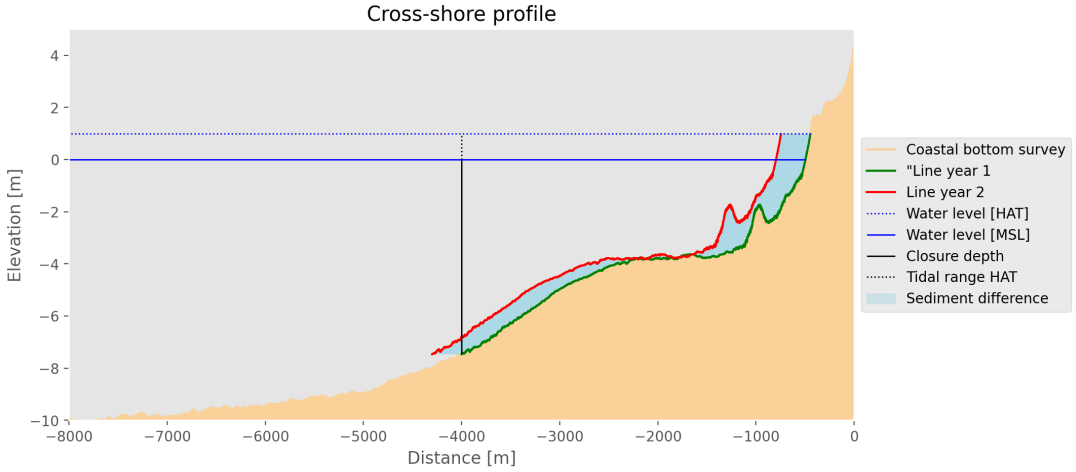


Figure 3.15: A cross-shore profile of a transects. The one-year change in the shoreline is shown by the blue line's transition from green to red. The active height, fixed at one point, is shown by the black line and consists of the closure depth and Highest Astronomical Tide (HAT). Shifting the green to the red line shows a small gap between -8 meters and the coast profile. This small error will be made by applying the shifting method. Shore Monitoring & Research (2023) provides the coastline profile data for this image.

### Active height

The active height consists of two elements. These are the closure depth and the mean spring tidal range (Valiente et al., 2019) as illustrated in Equation 3.16. Both depend on the area of interest. Coastal Engineers express that the most seaward point where the shoreline profile will not change anymore is the so-called closure depth, or depth of closure, shown in Figure 3.15 (Bosboom & Stive, 2021; Athanasiou et al., 2019) According to Kraus et al. (1998), the definition of the closure depth is as follows: "The depth of closure for a given or characteristic time interval is the most landward depth seaward of which there is no significant change in bottom elevation and no significant net sediment transport between the nearshore and offshore". The closure depth is based on an empirical formula where $d_c$ relates to wave parameters. The most common closure depth formula is Equation 3.17 (Athanasiou et al., 2019).

$$d_c = 2.28H_{e,t} - 68.5\left(\frac{H_{e,t}^2}{gT_{e,t}^2}\right) \tag{3.17}$$

Here, $H_{e,t}$ represents the significant wave height in meters exceeding only 12 hours per $t$ years, $T_{e,t}$ denotes the associated wave period in seconds, and $g$ represents gravitational acceleration ($m/s^2$). The variable $d_c$ provides the closure depth in meters influenced by wave dynamics.

Athanasiou et al. (2019) looked into the depth of closure worldwide. Figure 3.16 shows the research results of Athanasiou et al. (2019). Consequently, he employed the identical transect created for the study conducted by Luijendijk et al. (2018). Using the Bruun rule, the elevation profile was utilised to find the cross-shore location of the closure depth $d_c$ in order to ascertain the closure depth. The next step was to find the first point shallower than $d_c$ to determine the depth of closure. Therefore, they started offshore and moved in the direction of land. The shoreline (MSL) point's cross-shore location was then estimated using a similar technique. The cross-shore distance between these two locations was used to compute the nearshore area $L$'s horizontal length. The nearshore slope $\tan(\beta)$ was then calculated using the ratio $\frac{d_c}{L}$.

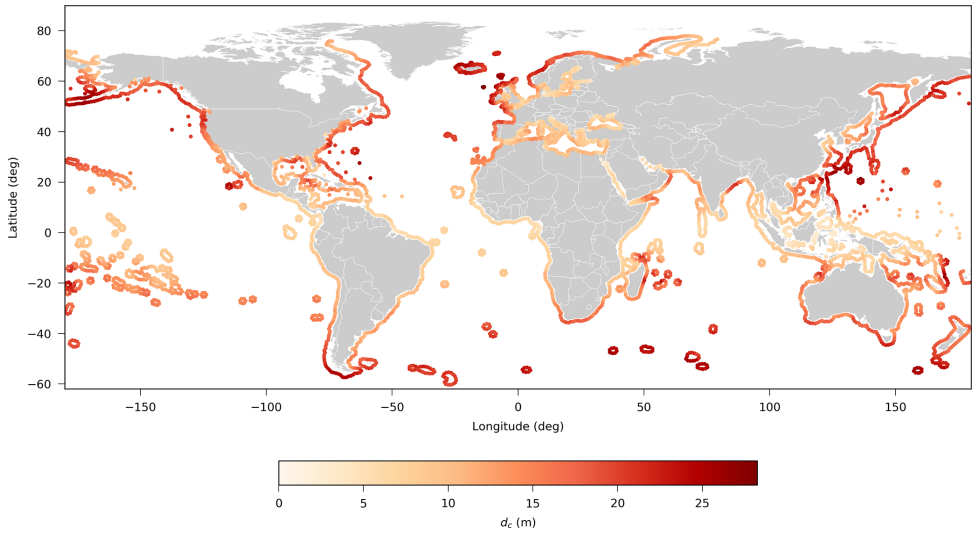


Figure 3.16: Depth of closure $d_c$ along the global coastline. Source: Athanasiou et al. (2019).

Over the past forty years, various methods have been used to determine the morphological depth of closure (Valiente et al., 2019), which was established on wave dynamics. In addition to the closure depth, the tidal range significantly affects several regions across the world (Egbert & Erofeeva, 2002). As a result, the mean spring tidal range must also be considered, otherwise, some volume will be lost in the volume gradient.

### 3.3.7 Longshore Sediment Transport

The Longshore Sediment Transport is the final stage in the littoral transport building stone, as shown in Figure 3.5. The LST indicates how much sediment flows in and out of a coastal cell (Section 1.1). Certain boundary conditions are required to compute sediment transport per transect, as shown in Figure 3.17. One example of a boundary condition is the amount of sediment that flows into or out of the system (Figure 3.17a). However, this value is not always known. Another boundary condition is zero sediment transport at a given place ($S = 0$) (Figure 3.17b). This boundary condition can be achieved with a groyne or breakwater when there is no bypassing of sediment.

Since the $S_{in}$ and $S_{out}$ are usually unknown, the Longshore Sediment Transport is solved with the $S = 0$ boundary condition. It is important to note that $S = 0$ is also the starting point for the calculations. This means that if the boundary $S = 0$ is not at the origin but at some distant from it, the calculation happens backwards, from $X = L$ to $X = 0$. Nonetheless, the result is always projected with the origin on the left, and the $X$-axis numbers represent the mean distance.

The calculation of the sediment balance starts at the transect with the zero-point ($S = 0$). From $S = 0$, the other sediment transport values can be calculated using the $\Delta V$ as established in the previous section. To go from $S_0$ to $S_1$, the volume gradient between these two transects can be used as shown in Equation 3.18. Where $S$ is the Longshore Sediment Transport and $\Delta V$ is the volume.

$$S_1 = S_0 + \Delta V_i \tag{3.18}$$

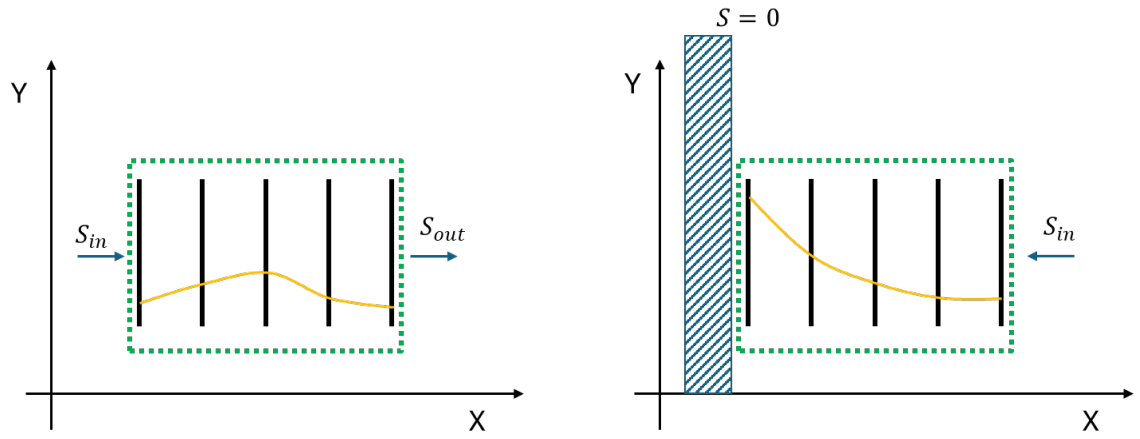


(a) (b)

Figure 3.17: These two figures illustrate two types of boundary conditions. (a) The boundary condition is known at $S_{in}$ or $S_{out}$. (b) The boundary condition near the origin is known, which is $S = 0$. Transects are represented by black vertical lines, the shoreline by the yellow line and littoral cells by a green dotted line.

### Longshore Sediment Transport visualisation

As demonstrated in Figure 3.17, the graph's origin is always on the left. This signifies sediment transport occurs from left to right while looking from land into the sea. When sediment transport moves from left to right, it produces a positive signal. If sediment transport runs from right to left, it will have a negative sign. This is done to maintain consistency and allow for comparisons between different locations.

### Littoral drift barriers

When the breakwaters or groynes are long enough in such a way that there is no bypassing of sediment, this gives a zero-point in the LST. They can be called Littoral drift barriers. Groynes, for example, are the preferred option for beaches that are exposed to significant littoral drift, according to Barkwith et al. (2014). This shows that littoral drift affects the design and placement of barrier structures that control sediment flow and coastal erosion. As a result, these obstacles influence coastal morphology and sediment movement significantly. Adding a barrier in the shoreline will lead to sediment accretion on the up-drift side and erosion on the down-drift side (Barkwith et al., 2014; Bulleri & Chapman, 2010). Figure 3.18 illustrates up-drift accretion and down-drift erosion.

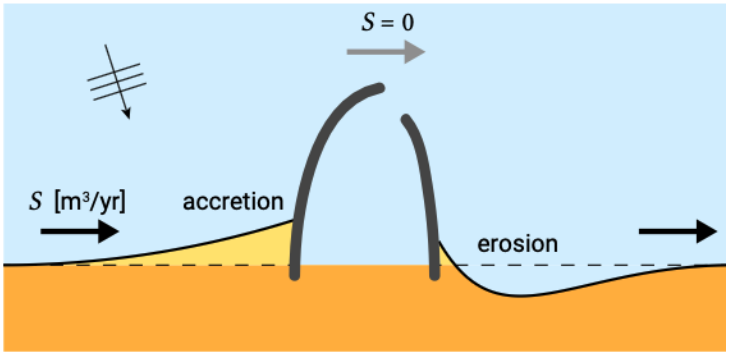


Figure 3.18: Typical structural down-drift erosion and up-drift accretion. Source: Bosboom & Stive (2021).

To determine whether the assumption that there is no bypassing of sediment is correct, the amount of accretion should be equal to the amount of erosion on the other side of the barrier at a certain length. Assuming that the beach was stable before the seawall was built. If there is no sediment bypass, it is feasible to conclude that the end-point of the littoral drift barrier was sufficiently far into the sea.

## 3.4 S-$\varphi$ relation

To accurately shoreline predictions, it is crucial to establish a relationship between littoral transport and shoreline orientation. Such a relation describes the LST given the shoreline angle. Figure 3.19 illustrates the necessary stages. As illustrated in the images, the littoral sediment transport and the shoreline orientation can form a relationship called a Sediment ($S$) - Orientation ($\varphi$) relation. The first step is littoral transport, which involves sediment transport along transects. Given that the transect at one of the boundaries is near a massive breakwater, it can be assumed that there is no sediment transport ($S = 0$).

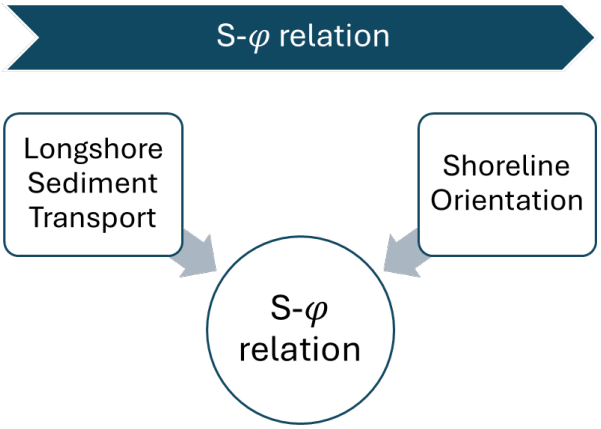


Figure 3.19: The procedures required to establish a Sediment-orientation relation.

### 3.4.1 Shoreline Orientation

Shoreline orientation refers to the direction a coast faces. The coastline direction is significant because it affects the littoral transport gradient, which affects erosion and accretion rates. Deepwater waves approaching the coast at an angle result in a specific LST gradient (Ashton & Murray, 2006b,a). As a result, it depends on whether these waves approach the beach at a small or high angle. At a small wave angle ($0 < \theta < 45$ degrees), the coastline diffuses more, whereas at a high angle ($45 < \theta < 90$ degrees), the beach becomes unstable and spits form (Ashton & Murray, 2006b).

Unfortunately, wave data is not always accessible. However, the shoreline can still be tracked. The tracking can be done to determine the shoreline's direction relative to the north. Collecting shoreline orientation over time can provide insight into how the shoreline rotates. The diffusing principle indicates if the shoreline is stable or unstable (Ashton et al., 2016). In other words, there is no difference in the gradient when entering and departing an area. This information might help make predictions because it makes it easier for prediction models to predict the shoreline position.

#### Determining $\varphi$

Deriving the shoreline orientation of the shoreline is the reference point North. In this way, all the shoreline orientations can be compared because the direction North will not change. In Figure 3.20 the north direction, the north line is presented as a red dotted line. First, the shoreline (orange line) is drawn between the two transects (black lines). A middle line is drawn between the two transects. This red dashed line is in the middle of the two black lines. Since the orientation is calculated for each transect, the approach is divided into three numerical schemes. These schemes are Upward, Midpoint, and Backward. Identify a beach midpoint (Quarter point in Figure 3.20) between the lowest transect and the red line for the upward scheme. From this point, a perpendicular line (blue line) is drawn towards the seashore. In Figure 3.20, the beachside is on the right while the seaside is on the left, indicating that the green line represents the coastline angle in degrees.

The backward scheme technique is similar to the upward scheme, except now the direction for the top transect is established, as shown in Figure 3.21b. The middle scheme will have two orientations, comparable to the upward and backward schemes. The orientation is computed using the mean of the

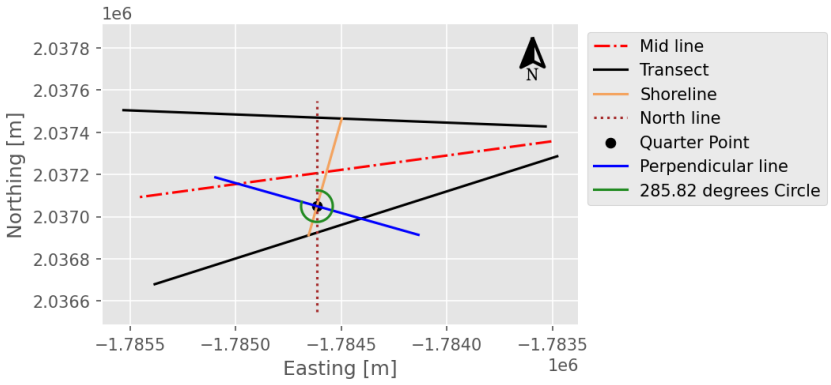


Figure 3.20: A visualisation of deriving the shoreline orientation. The black lines represent the transects. The orange line represents the beachfront between two transects, the blue line is perpendicular to the shoreline, and the green circle represents the shoreline's angle in degrees.

two orientations below and above the transect, as shown in Figure 3.21a. The method described above is similar to the method in the "COCOONED" model. This model is created by Antolínez et al. (2019) and is a hybrid shoreline change foredune erosion model (A COupled CrOss-shOre, loNg-shorE, and foreDune evolution model, COCOONED). Determining the coastline orientation for all transects and all years provides information about the shoreline orientation over time.

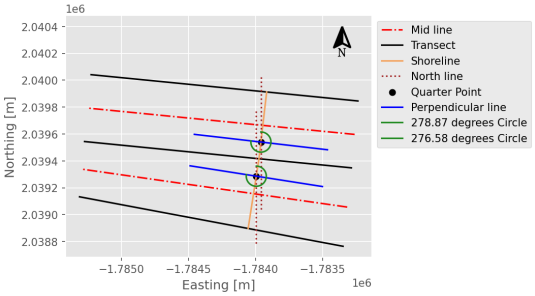


(a) Midpoint scheme

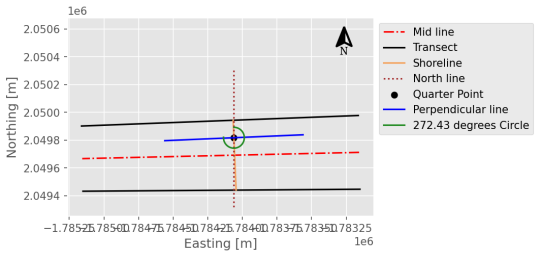


(b) Backward scheme

Figure 3.21: A visualisation of deriving the shoreline orientation for a midpoint (a) and backwards (b). The black lines indicate the transects. The orange line depicts the beachfront between two transects, the blue line is perpendicular to the shoreline, and the green circle shows the shoreline's angle in degrees.

### 3.4.2 Littoral Drift Rose

The S-$\varphi$ relation is the so-called "Littoral Drift Rose" concept. This concept is used to analyse coastal stability by compiling wave metrics and computing sediment transport for various shoreline orientations (Walton & Dean, 2010, 1973; Huisman & Dagalaki, 2020). It provides information about the sediment movement along the coastline, considering factors like wave climate, shoreline orientation and sediment transport rates. Ashton & Murray (2006b), show the effect on the wave direction to the shoreline and what kind of sediment transports this will give, as illustrated in Figure 3.22.

Nevertheless, in this research, the wave angle is not provided. Conversely, the coastline orientation and sediment transport are known, as computed in Section 3.3.7. As a result, a relationship can be established between sediment transport and shoreline orientation. Equation 3.19 describes the analytical function used in Unibest-Cl+ to derive this relation (Huisman & Dagalaki, 2020).

$$\begin{aligned} Q_s(\theta) &= c_1 \theta_r e^{-(c_2 \theta_r)^2} \\ \theta_r &= \theta - \theta_{eq} \end{aligned} \tag{3.19}$$

Where $Q_s$ is the sediment transport, $c_1$ and $c_2$ coefficients will be determined by the lowest RMSE. $\theta$ is

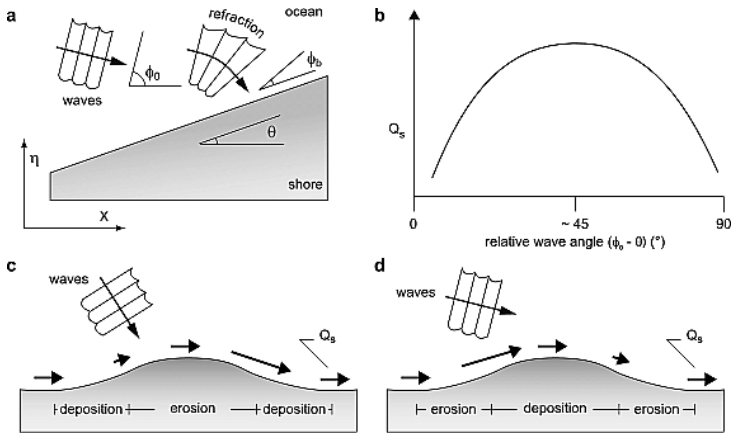


Figure 3.22: A visualisation of how waves affect the shoreline. (a) shows a wave approaching the beach and how the shoreline can erode or accrete depending on the wave angle (c and d). The link between sediment transport and wave angle is defined in (b). Source: Ashton & Murray (2006b).

the shoreline orientation and $\theta_{eq}$ is the equilibrium angle where the sediment transport is zero ($S = 0$). An example of fitting this analytical function in a scatter plot of sediment transport and orientation is illustrated in Figure 3.23

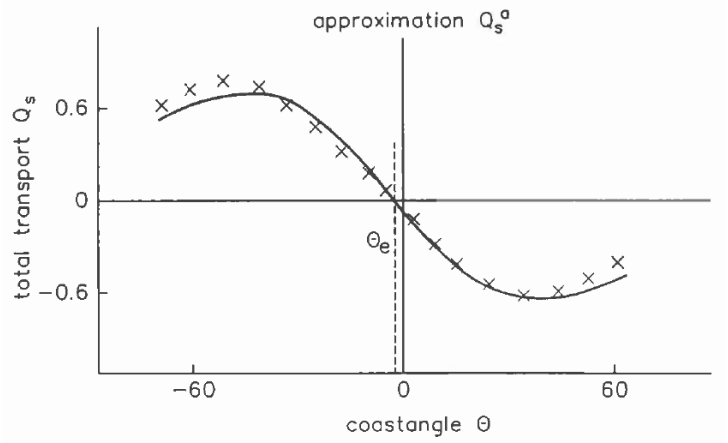


Figure 3.23: A schematic S-$\varphi$ relationship (littoral drift rose) between sediment movement and shoreline orientation. Source: Huisman & Dagalaki (2020).

For each year an S-$\varphi$ is fitted with all the sediment and orientation data from all the transects to determine the values for the coefficients $c_1$, $c_2$ and $\theta_{eq}$. Furthermore, the ideal fit depends on the lowest RMSE. Another condition is that sediment transport is zero at 90 and -90 degrees and will remain so. The maximum sediment transport is between $43 \sim 45$ and $-43 \sim -45$ degrees. To achieve these conditions, $c_2$ is limited from 0.0157 to 0.0177, and $c_1$ from 0 to 1. To establish the averaged S-$\varphi$ relation, calculate the mean of all coefficients at the chosen location after obtaining the $c_1$, $c_2$, and $\theta_{eq}$ values for all years.

## 3.5 Future shorelines

Future Shorelines is the final stage of the process, as shown in Figure 3.1. With the obtained S-$\varphi$ relation in the previous section, it gives the possibility to make shoreline predictions based on the recent shoreline orientation. As shown in Figure 3.24, the future shorelines stage is essentially a loop that uses previous data to predict a new coastline for the upcoming year. For instance, this loop requires ten completions to predict ten years.

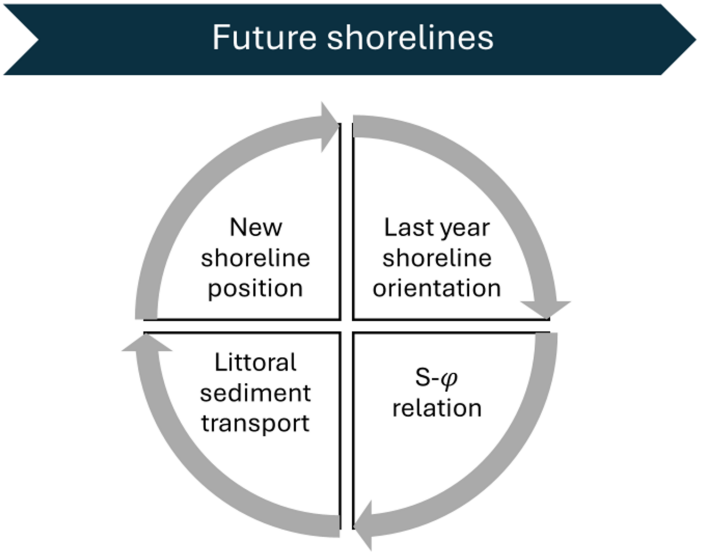


Figure 3.24: An overview of the loop process to predict a shoreline position based on the latest shoreline orientation as input.

#### Staggered Grid

The circle in Figure 3.24 suggests four processes to anticipate the new shoreline positions for the next year. The steps will be detailed in the following sections. Before beginning the cycle, a certain grid is picked to make the prediction. This is a staggered grid, which is also used by Unibest-CL+ to make shoreline position predictions (Huisman & Dagalaki, 2020). This grid separates sediment transport ($S$) and orientation ($\varphi$) from shoreline position ($y$), as illustrated in Figure 3.25. An advantage is that a staggered grid offers more stability and dispersive abilities than a grid where the shoreline position and LST are at the same point (Uh Zapata et al., 2018).

Two types of boundary conditions are used to forecast the coastline position quantitatively to make a shoreline prediction. These boundary conditions include zero sediment transport ($S = 0$) and a stable shoreline position ($\Delta y = 0$). These can be placed in various positions, as seen in Table 3.2.

Table 3.2: The different boundary conditions that could occur when predicting the new shoreline position

| Option | Location | Boundary |
|---|---|---|
| 1 | At x=0 | $S = 0$ |
| | At x=L | $\Delta y = 0$ |
| 2 | At x=0 | $\Delta y = 0$ |
| | At x=L | $S = 0$ |
| 3 | At x=0 | $S = 0$ |
| | At x=L | $S = 0$ |

### 3.5.1 Orientation to littoral transport

The initial stage in the cycle is to collect the shoreline orientation from the current year. The method used to determine the shoreline orientation is similar to the method in Section 3.4.1. However, in this

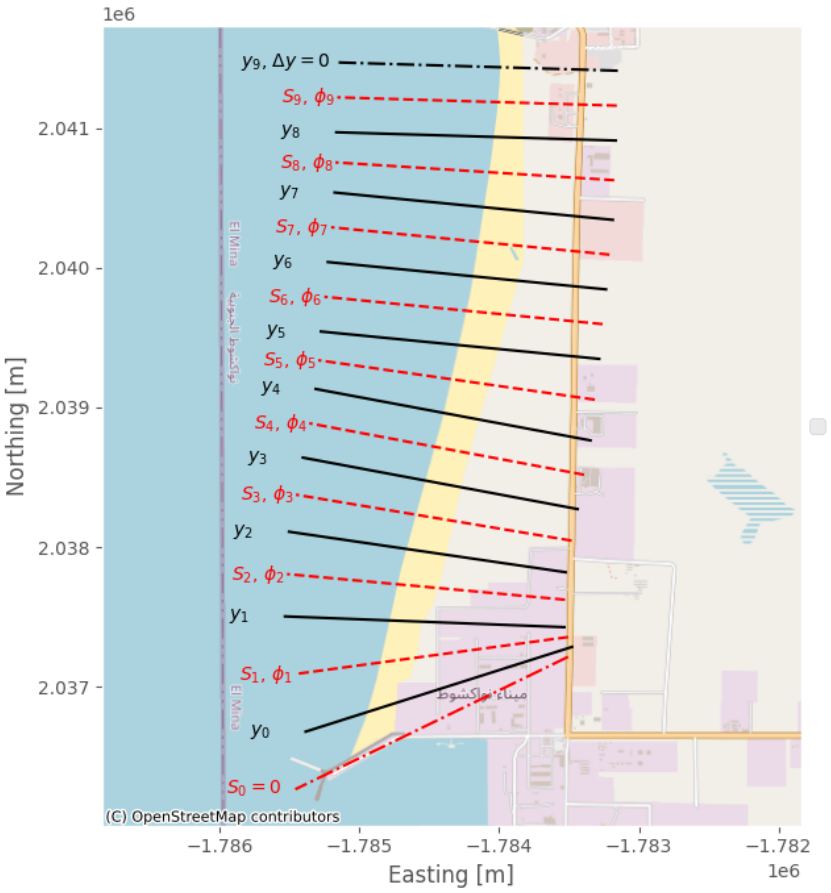


Figure 3.25: An illustration of a staggered grid along the shoreline line. The black lines represent the transects from SDS for the shoreline position ($y$), whereas the red line marks the midway point of the transect showing the shoreline orientation ($\varphi$) and sediment transport ($S$) on this line. Furthermore, the bounds in this scheme are $S_0 = 0$ at the bottom and $y_9, \Delta y = 0$ at the top.

case, the orientation is obtained between the transect and the red line, as illustrated in Figure 3.25. As a result, no upward, middle or backward schemes are required.

The obtained shoreline orientations will be filled in the littoral drift rose (the S-$\varphi$ relation) with the values $c_1$, $c_2$ and $\theta_{eq}$ to get the Longshore Sediment Transport. The values of $c_1$, $c_2$ and $\theta_{eq}$ are obtained from the historical data in Section 3.4. The output will provide the LST for the points $S = [1, 2, \ldots, n]$ at $\varphi = [1, 2, \ldots, n]$.

### 3.5.2 New shoreline position

Once the predicted sediment transport and current shoreline position are known, the new shoreline position can be determined using the continuity equation, Equation 3.20. This equation is similar to the one used in Unibest-CL+ (Huisman & Dagalaki, 2020) to calculate the new shoreline position. It is crucial to notice that the scheme always starts with the boundary condition $S = 0$ because the input or output of the system is unknown.

$$\begin{aligned} H \cdot \frac{y_{n+1} - y^n}{\Delta t} + \frac{S^{n+1} - S^{n+1}}{\Delta x} &= 0 \\ y^{n+1} &= -\left(\frac{S^{n+1} - S^{n+1}}{\Delta x}\right) \cdot \frac{\Delta t}{H} \end{aligned} \tag{3.20}$$

where $H$ is the active height, $y^n$ is the shoreline position this year, and $y^{n+1}$ next year. The sediment transport is given by $S^{n+1}$, with $\Delta x$ chosen between the two red lines (Figure 3.25). The distance

between $S_0$ and $S_1$ is two times the distance between $y_0$ and $S_1$. $\Delta t$ represents the time step in years. In this study, the shoreline is forecasted for one year per cycle. To ensure a reliable prediction model, it must be checked if the model is stable enough. The stability check can be done with the Courant number ($C$) as shown in Equation 3.21 and the value must be smaller than 1 to be stable. The Courant number is sometimes called the Courant-Friedrichs-Lewy (CFL). According to (Bhattacharyya et al., 2021), the model is stable if the fluid's local velocity multiplied by the time step is smaller than the element size. As a result, $\Delta t$ is set to 1/2, indicating two steps in a one-year.

$$C = v\frac{\Delta t}{\Delta x} \leq 1 \tag{3.21}$$

where $\Delta x$ is the distance between the red lines in Figure 3.25, $v$ is the Longshore Sediment Transport.

# 4

# Model results

Chapter 3 explains how to derive littoral transport from Satellite-derived Shoreline and predict future shorelines. Section 3.2 outline the methodology's initial step: identifying examples where the method can be implemented. These findings are presented in Section 4.1. On these presented cases, the SHORECAST model will be applied as described in Chapter 3 and shown in Figure 3.1. This chapter presents the results of the method and will provide an answer for the first three sub-research questions stated in Section 1.3. The results are reported for each case study. Section 4.2 shall present the first case, which is also the case on which the method was developed. The second and third cases are tests to see if the developed method works and are outlined in Sections 4.3 and 4.4. Each section of the three case studies is divided into two parts. The last case (number three) has some extra elements compared to the first two cases, such as two points where the sediment transport is assumed zero and anthropological measures. Section 4.5 will reflect on all these presented cases.

In Section 1.1, the definition of coastal cells was introduced. This chapter will also present the case result as a coastal cell, where the boundary conditions discussed in Section 3.3.7 will be applied on the coastal cell. Considering the case as a coastal cell, a sediment balance can be established, which is also evident in the results.

## 4.1 Potential cases

As outlined in Section 3.1, the first step is to find cases that can be used to derive the littoral transport and to make shoreline position predictions. In Section 3.2 three criteria are formulated. Applying these criteria on the Satellite-derived Shoreline dataset from Luijendijk et al. (2018) gives nine potential cases to investigate further as illustrated in Table 4.1 and Figure 4.1.

As discussed in Section 3.3, the littoral transport is derived by assuming that one of the boundaries from the area of interest satisfies a boundary condition wherein the LST is zero (Section 3.3.7). Due to this condition, the cases that can be utilised to derive and test the technique are those with one or more zero points. In addition, several of these selected situations, as presented in Table 4.1, are also nominated by Luijendijk et al. (2018). The proposed cases are Nouakchott, Aveiro and Delfland. The Delfland case determines whether the SHORECAST method may also be applied to a case with two zero points.

Table 4.1: An illustration of a part of the possible case studies that can be used to build and test SHORECAST model

| Case | Geographical location | Number of zero points | Use |
|---|---|---|---|
| Nouakchott | Mauritania | 1 | Development |
| Aveiro | Portugal | 1 | Test |
| Sulina | Romenia | 1 | - |
| Delfland | The Netherlands | 2 | Test |
| IJmuiden | The Netherlands | 1 | - |
| Puerto Chiapas | Mexico | 1 | - |
| Lafayette | United States | 0 | - |
| Bhitarkanika | India | 0 | - |
| Gành Hào | Vietnam | 0 | - |

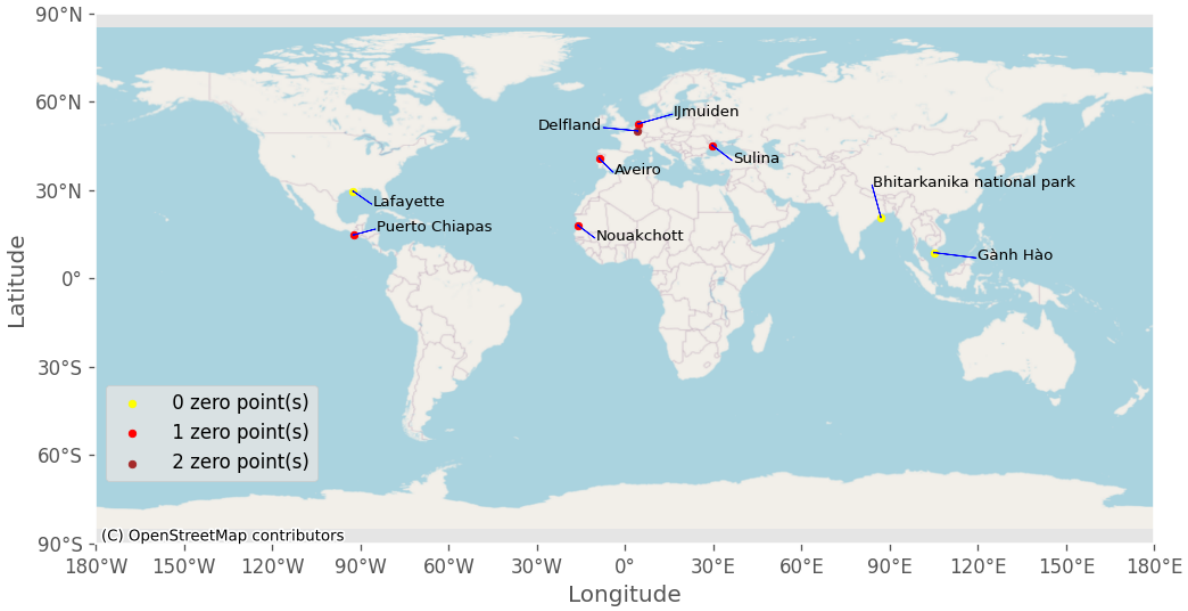


Figure 4.1: A world map whereby a selection of the potential locations are shown to derive the littoral transport using data from SDS. The number of zero points indicates that the Longshore Sediment Transport is zero, for example, near a harbour.

## 4.2 Case study: Nouakchott - Mauritania

### 4.2.1 Introduction

Nouakchott, Mauritania's capital city, is on Africa's west coast, facing the Atlantic Ocean. Mauritania is located between latitudes 15°N and 26°N and has a coastline of 750 km (Elmoustapha et al., 2007). Figure 4.2 shows the Nouakchott Shoreline. According to Elmoustapha et al. (2007), a linear, dry and windy beach characterises the coastline around Nouakchott. This sandy beach is surrounded by a 5- to 10-meter-high sand dune that protects large low-lying saltwater depressions (Elmoustapha et al., 2007).

To create the new method to derive the littoral transport from SDS and to make a prediction, the Nouakchott case will be split into two separate coastal cells as shown in Figure 4.3. A north side (Figure 4.3a) with the harbour at the bottom and a south side (Figure 4.3b) with the harbour at the top. The north side is the case that will be used to develop the full method from deriving the littoral transport from Satellite-derived Shoreline to make shoreline prediction. The south side will be used to test the created method.

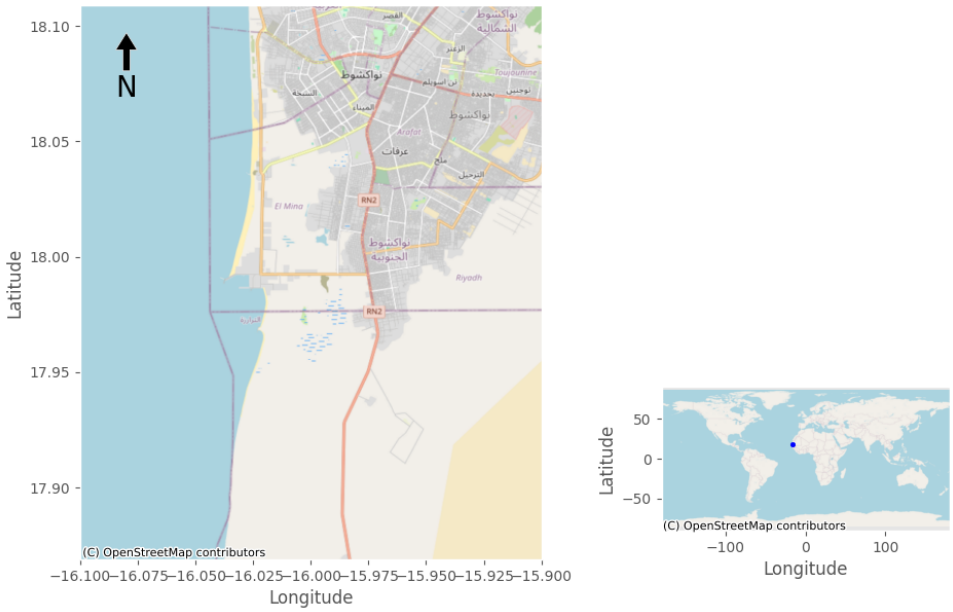


Figure 4.2: The shoreline of Nouakchott and the harbour is located at latitude 18 degrees. The small image represents the locations in the world.

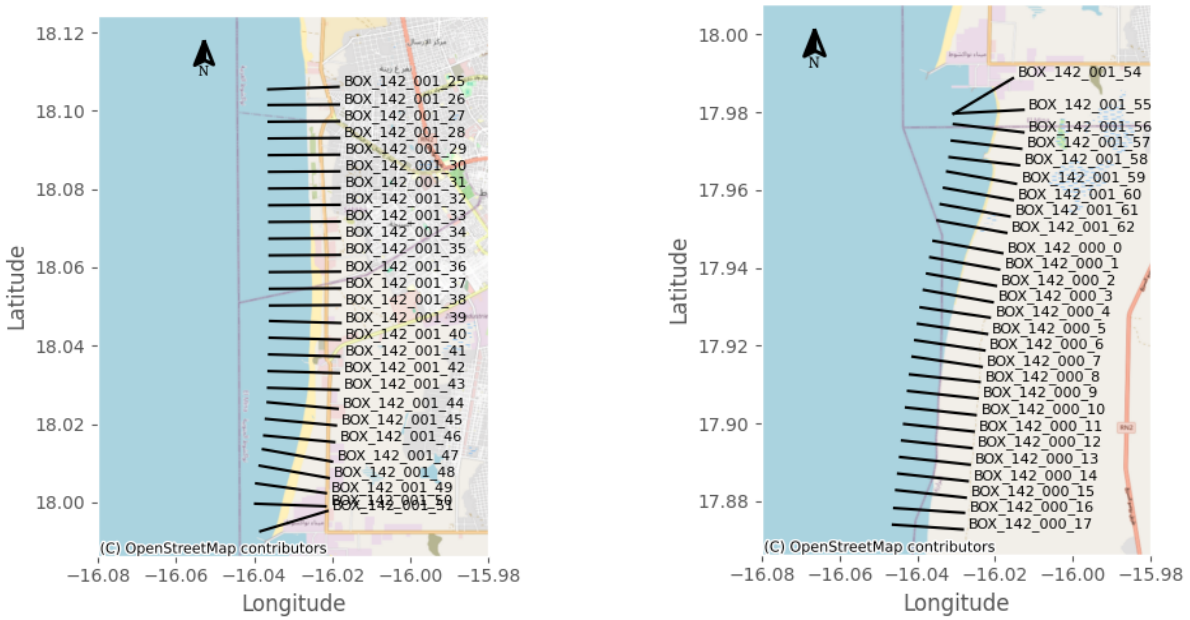


(a) Nouakchott north side

(b) Nouakchott south side

Figure 4.3: These two images display two areas of interest for creating a method to derive littoral transport from SDS and make forecasts. The left image depicts the north side, whereas the right image depicts the south. The black lines represent the SDS transects used in the process.

### 4.2.2 Results - Nouakchott North

The coastal cell of Nouakchott North was initially studied as a coastal cell. This particular cell consists of 27 transects, with transect IDs ranging from *BOX_142_001_51* to *BOX_142_001_25*, extending from the southern harbour to the north. The distance between the southernmost and northernmost transects is approximately 13 kilometres, calculated based on the average distance between transects detailed in Section 3.3.4. Figure 4.3a illustrates the Nouakchott North coastal cell layout under the assumption of no bypassing of sediment at the harbour. Additionally, the dataset was not entirely complete, as 16.76%

of it contained empty values before conducting the outlier detection process.

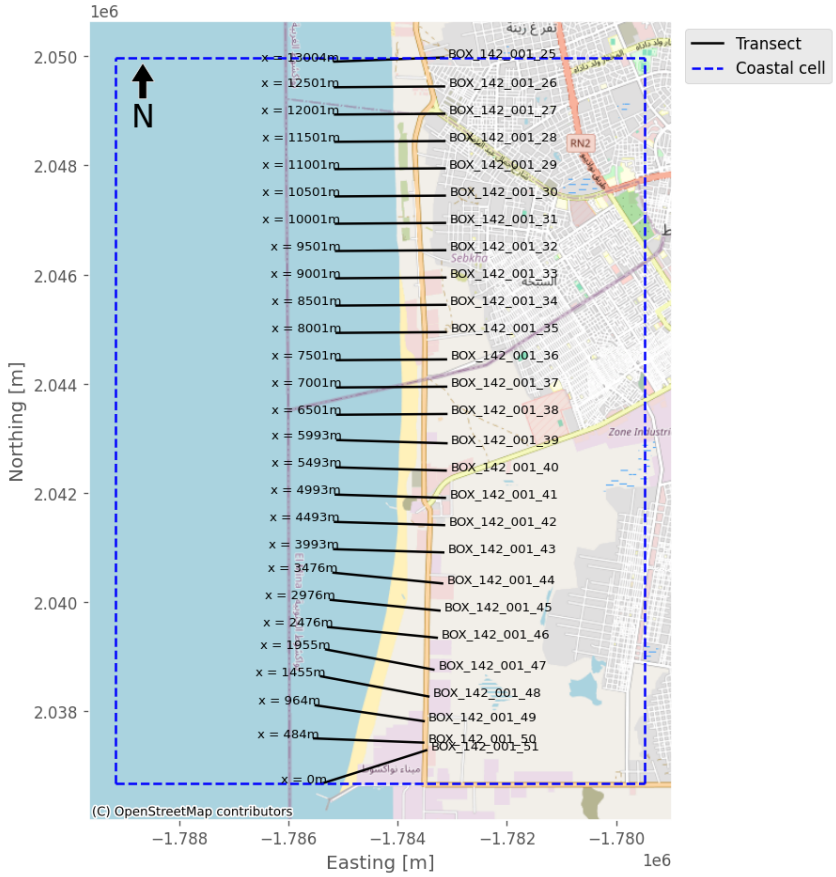


Figure 4.4: Coastal cell for Nouakchott case. Inside the blue dashed line, the transects can be found as provided by the SDS dataset. Aside from the transect ID, the average measured distance from the south (the harbour) to the most northern transect is provided.

As a result of the construction of the harbour in approximately 1980, the shoreline to the north of the harbour experienced significant accumulation and migration towards the sea. This phenomenon can be observed in Figure 4.5, which displays the shoreline's position over the past 35 years. There has been a significant accumulation of the shoreline close to the harbour. Over 35 years, the shoreline has migrated nearly 1 kilometre. Furthermore, the shoreline in the northern part of the coastal area has remained relatively stable in the same period, indicating a stable shoreline position.

Figure 4.5 provides a visual representation of the historical shoreline position after undergoing assessments for nourishment and outliers. The dataset does not include any nourishments, but 48 shoreline positions from the SDS dataset have been labelled as outliers. Consequently, 48 shoreline positions have been removed besides the already blank ones (Appendix B.1). By employing linear interpolation and smoothing techniques with a smoothing factor of 5, the surface gradient for the past 35 years could be estimated. Multiplying this surface gradient by the active height (8.71 metres) and utilizing the breakwater of Nouakchott's harbour as a boundary, the Longshore Sediment Transport is determined. The active height includes the closure depth (7.76 metres) as obtained from Athanasiou et al. (2019) and the mean spring tidal range is 0.95 metres (Micro-tidal range) (Egbert & Erofeeva, 2002).

Over the last 35 years, the mean annual Longshore Sediment Transport stands at around 0.66 million $m^3$ (Appendix B.1). This value corresponds to the yearly sediment import calculated from the sediment balance, as illustrated in Figure 4.6. The sediment balance is computed by assessing the surface alteration between the shoreline positions of 1985 and 2020, then multiplying by the active height. Consequently, the shoreline has expanded by 23.01 million $m^3$ over 35 years.

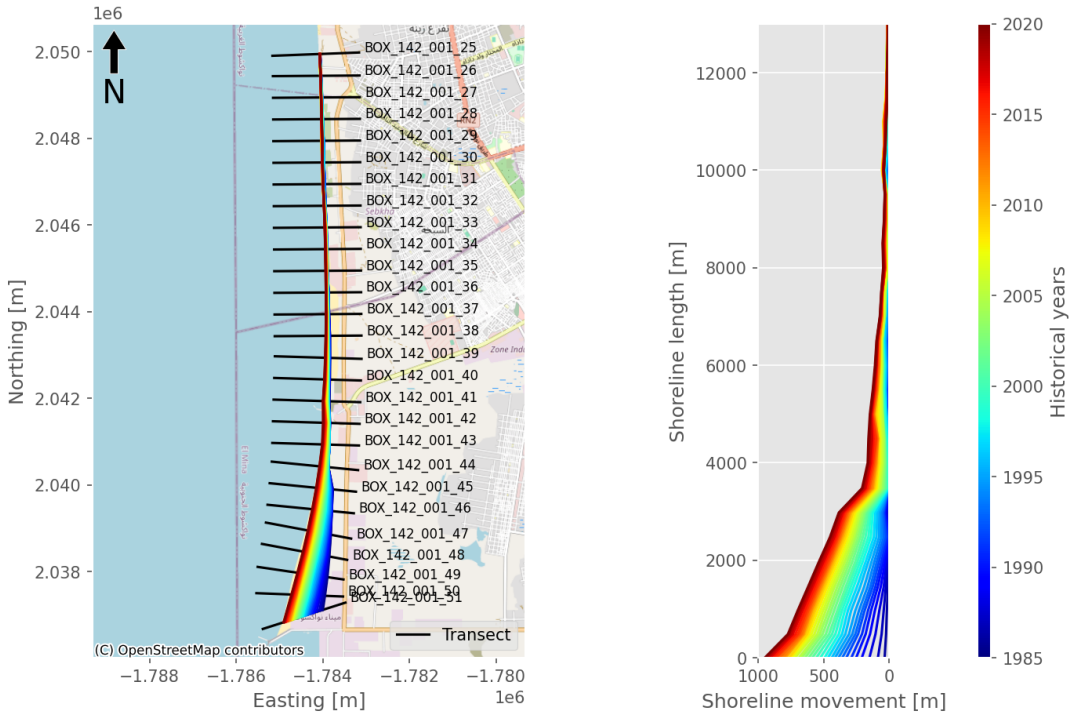


Figure 4.5: The result of the smoothing procedure along the Nouakchott coastline, where blue represents the oldest year (1985) and red represents the most recent year (2020).

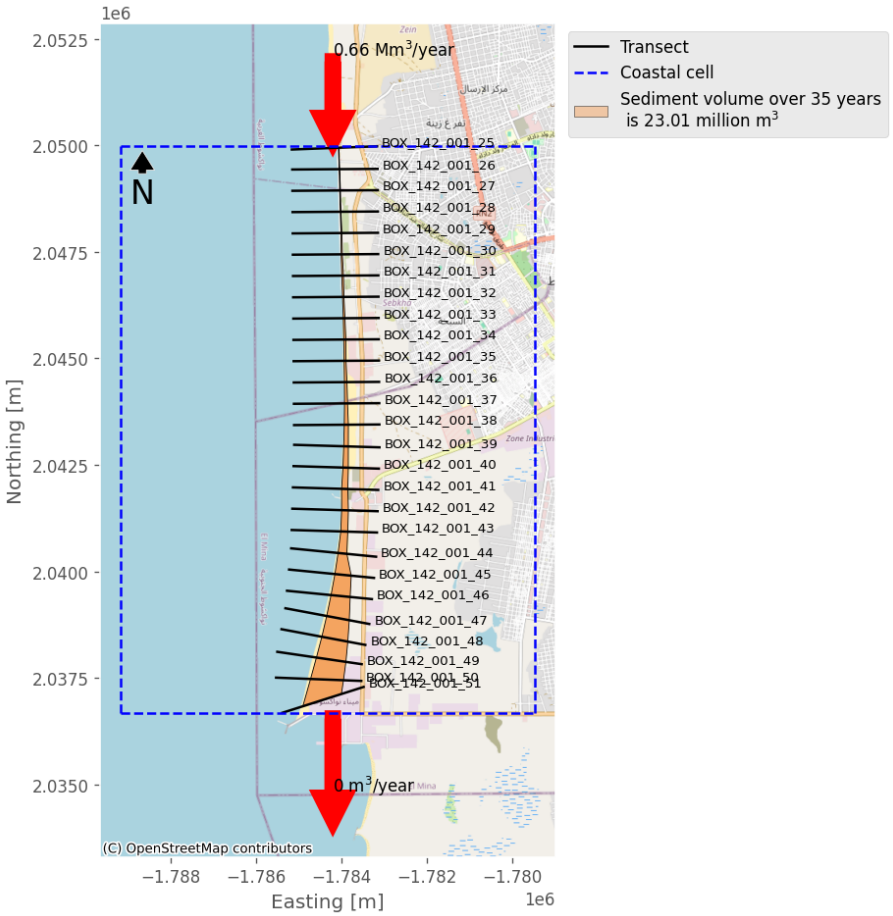


Figure 4.6: The result of the sediment balance of the Nouakchott north coastal cell. The assumption is that there is no sediment transport at the bottom.

The relationship between the LST and the orientation of the shoreline at a specific location can be established by fitting a S-$\varphi$ relation. An observation is that the sediment transport along the shoreline decreases as the shoreline angle increases. Figure 4.7 shows the shoreline orientation with the corresponding LST and the fitted S-$\varphi$ relation per year. The solid black line represents the mean S-$\varphi$ value, while the black dashed lines indicate the 95% confidence interval. Equation 4.1 presents the mean S-$\varphi$ relation in equation form. It is noteworthy that the confidence interval closely follows the mean S-$\varphi$ relation. By averaging the orientation of the last three transects in the northern region over the past 35 years, a Longshore Sediment Transport of 0.65 million $m^3$ is calculated with an average orientation of 267.96 degrees. This aligns with the derived LST and the annual sediment transport input derived from the sediment balance. So, the S-$\varphi$ relation is a good representative of the historical shoreline evolution.

$$\begin{aligned} S(\theta_r) &= 0.0390 \cdot \theta_r e^{-(0.0169 \cdot \theta_r)^2} \\ \theta_r &= \theta - 286.18 \end{aligned} \tag{4.1}$$

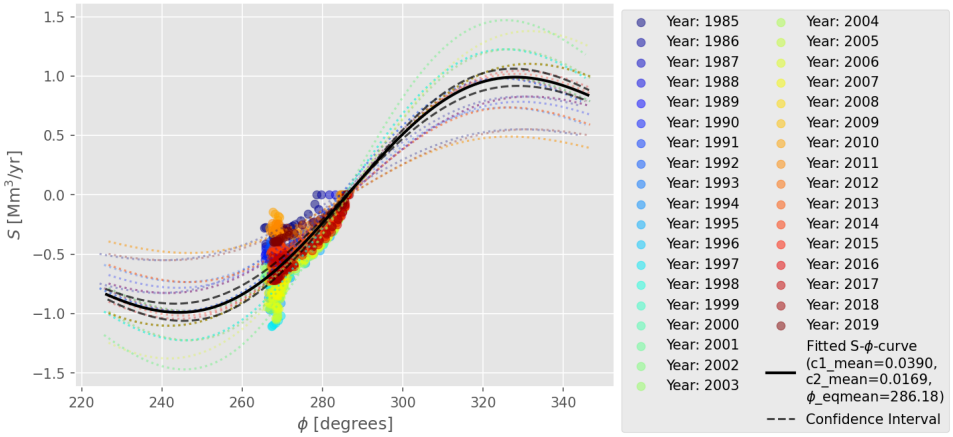


Figure 4.7: The S-$\varphi$ relation with a 95% confidence interval (black dashed lines).

Using the most recent shoreline orientation and Equation 4.1, it is possible to predict the shoreline position for the next two decades starting from 2020, as illustrated in Figure 4.8. The shoreline is expected to accrete further towards the north over this period and seawards. Specifically, there will be more accretion in a few transects north of the harbour compared to the transect adjacent to the harbour. The shoreline prediction indicates a narrow 95% confidence interval, suggesting a more precise range of the shoreline prediction, as illustrated in Figure 4.8. Furthermore, the shoreline position at the northern transect is predicted to remain constant. A more comprehensive prediction analysis can be found in Appendix B.1. It is essential to highlight that the prediction is made with the assumption of no bypassing of sediment at the harbour.

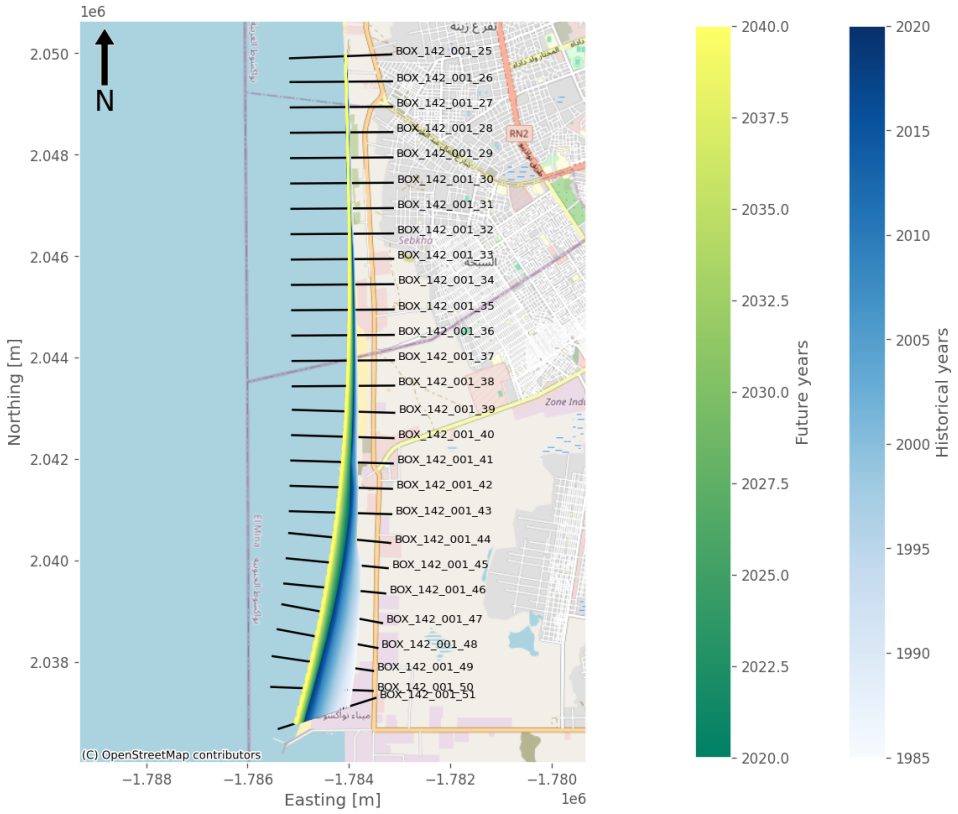


Figure 4.8: The prediction of the Nouakchott North shoreline for the next 20 years. The historical movement (white to blue range) and predicted shoreline position (green to yellow range). The yellow dashed lines is the 95% confidence interval.

### 4.2.3 Results - Nouakchott South

The southern coastal cell, known as Nouakchott South, matches the length of the North coastal cell. Nouakchott South coastal cell is comprised of 27 transects ranging from *BOX_142_000_17* to *BOX_142_001_54*, with a shoreline length of 13 kilometres which is the same for the coastal cell of Nouakchott North. Figure 4.9 shows the coastal cell of Nouakchott South. Similar to Nouakchott North, sediment transport at Nouakchott's harbour is assumed to be negligible and the Nouakchott South dataset is also not complete. 21.15% of the dataset is empty values before conducting the outlier detection process.

The shoreline south of the harbour has experienced significant retreat over the past 35 years, from 1985 to 2020. Due to the construction of the harbour. A small revetment was constructed a few kilometres south of the harbour to address this erosion, stabilizing the shoreline between the revetment and the harbour. In the SDS data analysis detailed in Appendix B.2, 16 shoreline positions were identified as outliers and excluded. By applying linear interpolation and a smoothing factor of N=5, the Longshore Sediment Transport was calculated, revealing an annual sediment loss of 0.92 million $m^3$. This sediment loss over 35 years correlates to a volume of 32.36 million $m^3$ determined by the shoreline surface migration between 1985 and 2020 multiplied by the active height of 8.71 metres as shown in Figure 4.11.

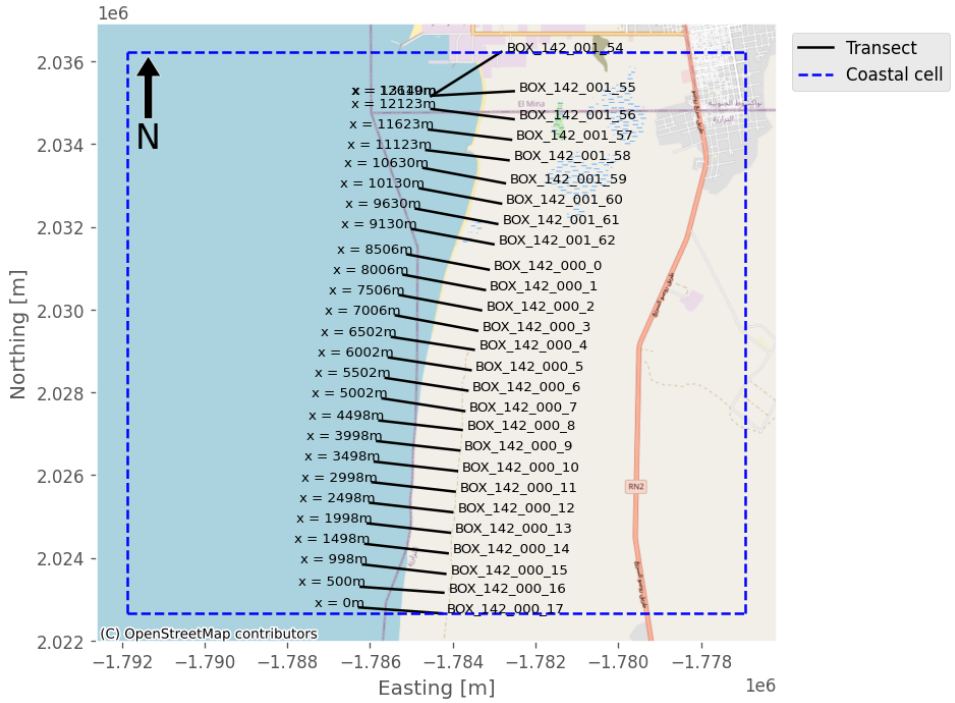


Figure 4.9: A visualisation of the Nouakchott south coastal cell with the transects provided by the SDS dataset inside the cell. Aside from the transect ID, the average distance from the south to the most northern transect (the harbour) is provided.

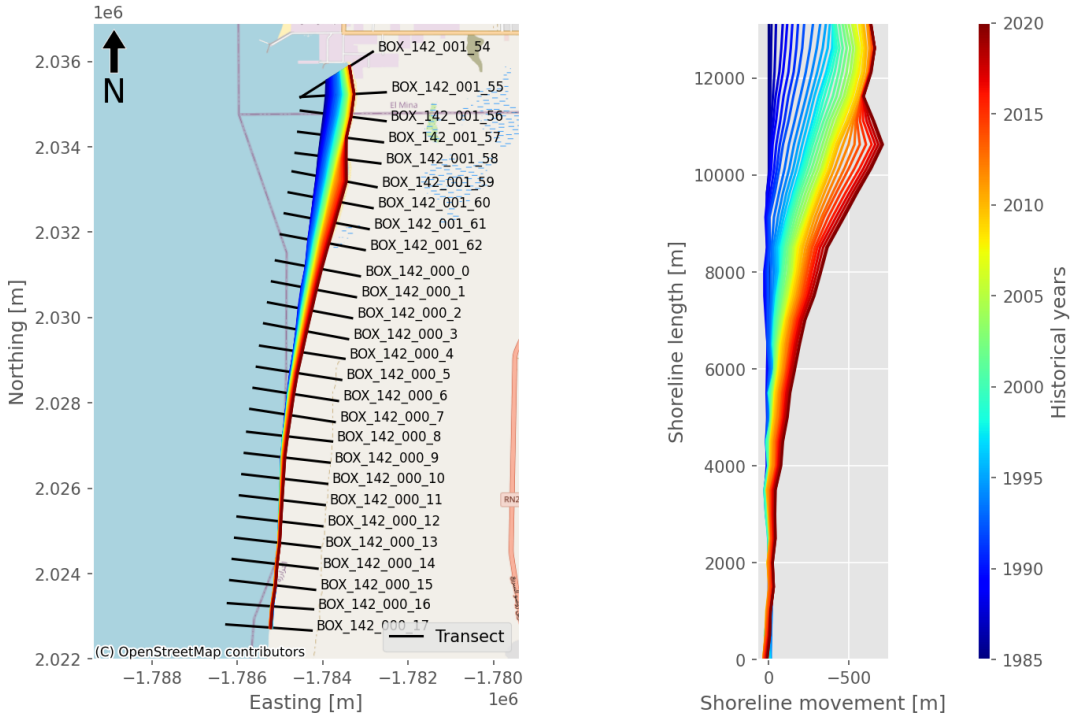


Figure 4.10: The result of the smoothing procedure may be seen along the Nouakchott coastline, where blue represents the oldest year (1985) and red represents the most recent (2020).

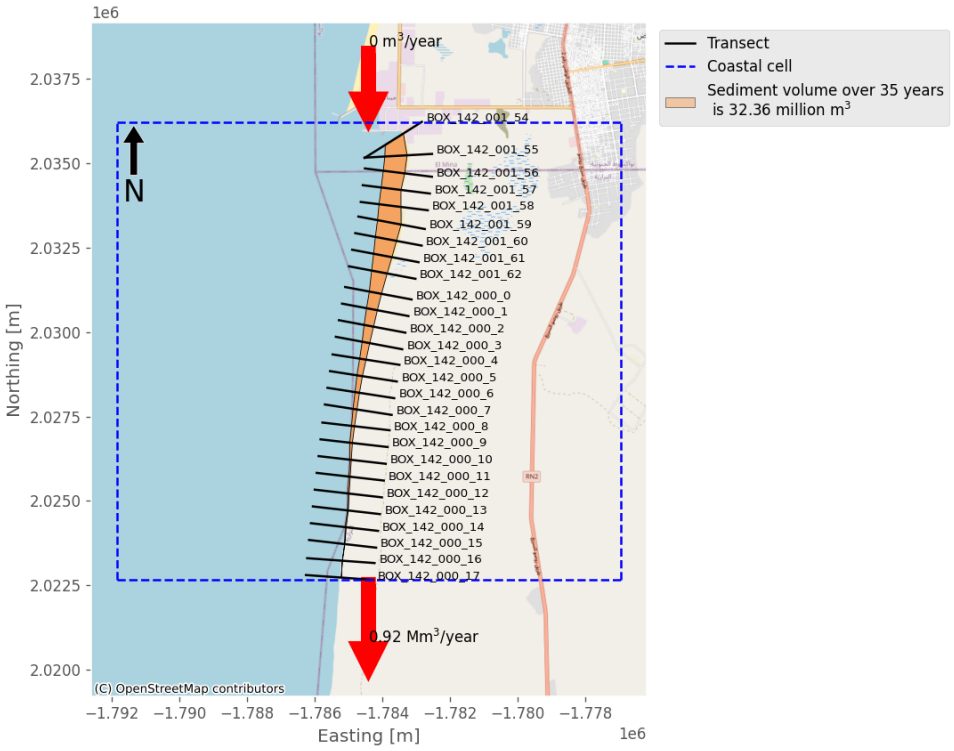


Figure 4.11: The sediment balance of the Nouakchott South coastal cell assumes no sediment transport at the top.

The S-$\varphi$ relation is derived along with the acquired shoreline orientation and Longshore Sediment Transport. However, it is worth noting that the orientations and LST between the revetment and the harbour have not been used in the derivation since 2012. Consequently, Equation 4.2 and Figure 4.12 illustrate the S-$\varphi$ relation. By filling in the mean orientation of the last three transects in the south, a Longshore Sediment Transport of 0.81 million m$^3$ is obtained. This value is lower than the LST derived from the historical shoreline positions.

$$\begin{aligned} S(\theta_r) &= 0.0392 \cdot \theta_r e^{-(0.0171 \cdot \theta_r)^2} \\ \theta_r &= \theta - 299.49 \end{aligned} \tag{4.2}$$

The shoreline prediction from 2020 to 2040, as illustrated in Figure 4.13, is determined using the above equation and the latest shoreline orientation. Over the next 20 years, the shoreline is expected to retreat south of the revetment. However, it is expected to remain stable between the harbour and the revetment. The 95% confidence interval shown in Figure 4.12 indicates that the shoreline prediction will not experience significant changes. This information can be found in Appendix B.2. Furthermore, the shoreline prediction suggests that there will not be substantial further retreat close to the revetment, but more erosion will occur in the southern part of the coastal cell.

According to Bosboom & Stive (2021), various approaches are available to combat structural erosion, including hard and soft solutions. In Appendix C.1, a soft solution in the form of a mega-nourishment, is executed along the shoreline in 2025 to combat shoreline erosion effectively. Furthermore, as part of a hard solution, two groynes are strategically positioned to reduce erosion in Appendix C.2.

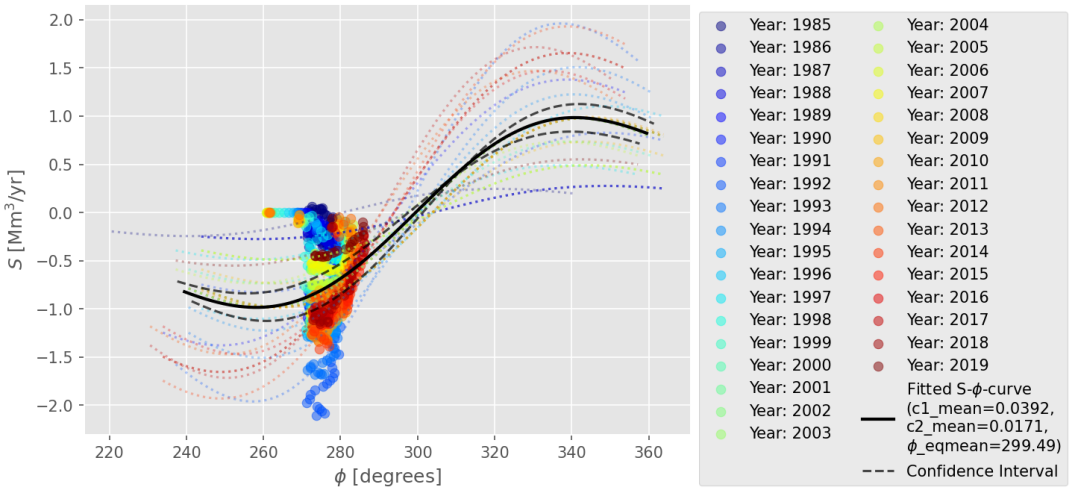


Figure 4.12: The S-$\varphi$ relation with a 95% confidence interval (black dashed lines).

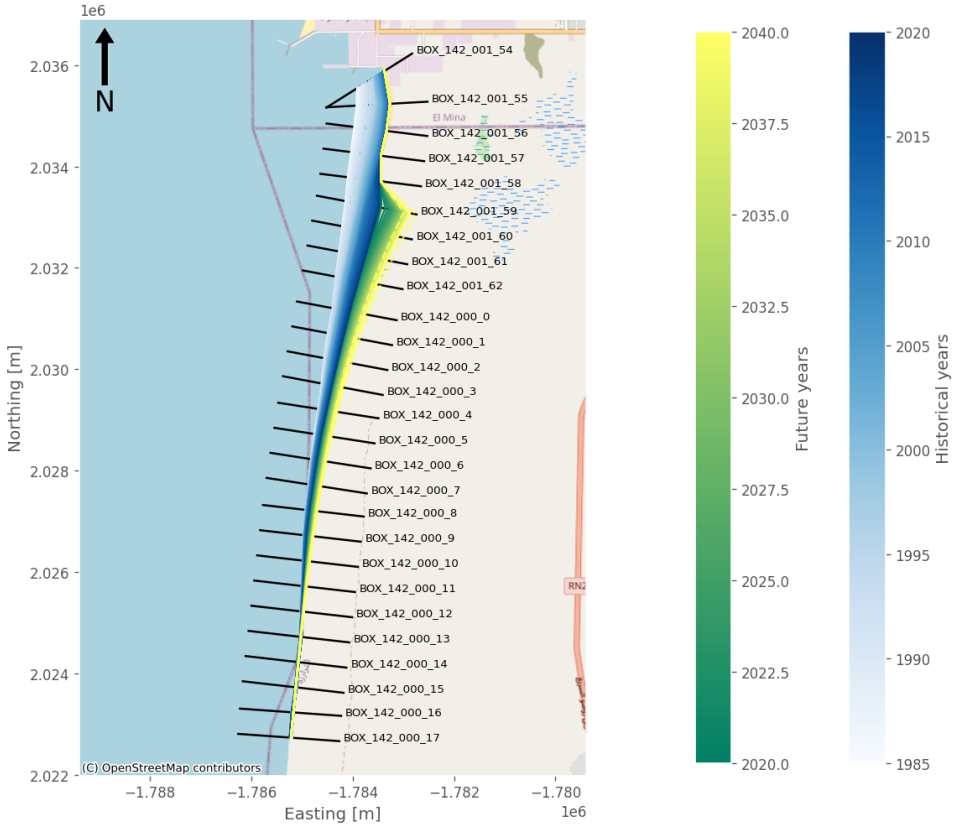


Figure 4.13: The prediction of the Nouakchott South shoreline for the next 20 years. The historical movement (white to blue range) and predicted shoreline position (green to yellow range). The yellow dashed line is the 95% confidence interval.

## 4.3 Case study: Aveiro - Portugal

### 4.3.1 Introduction

Following the development of the SHORECAST model on the Nouakchott shorelines, a different case study is being utilized to validate this innovative model. This new location is the shoreline of Aveiro (Portugal), as shown in Figure 4.14, above the Ria de Aveiro. According to F. Silva & Duck (2001), the

beginning and evolution of the Ria de Aveiro are related to the southward extension of the leading sand spit that encloses the lagoon from the Atlantic Ocean. The littoral transport is primarily from north to south, while winds shift sand piled on the beach southward, generating dunes. According to Pinto et al. (2022), the shoreline has a high-energy wave-dominated climate. In 1808, a new inlet/outlet channel for the lagoon was built, which is still the current outlet of the river.

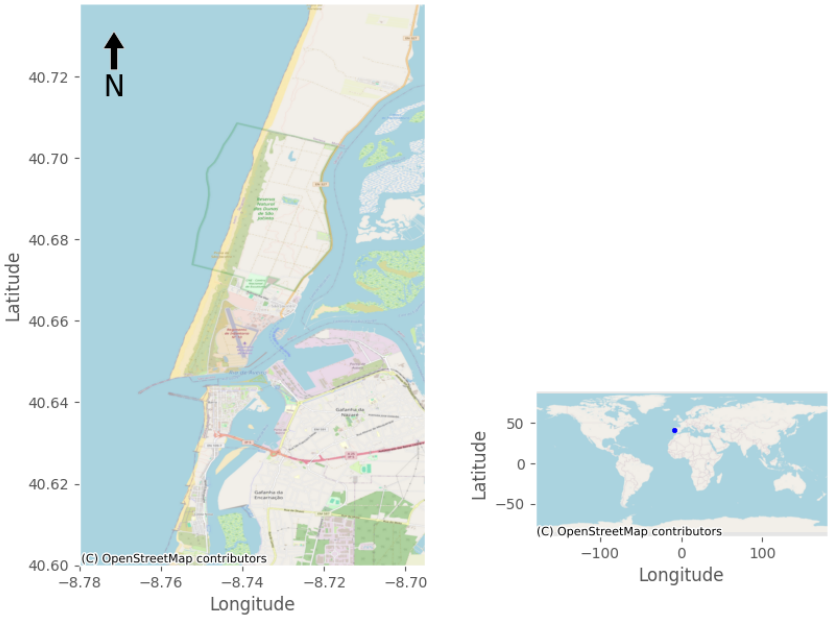


Figure 4.14: The shoreline of Aveiro and the lagoon behind the beach. The seawall at the Ria de Aveiro causes sand to build in the north and erode in the south of the river. The right world map shows the location of Aveiro on the map.

The new exit disrupted the north-south Longshore Sediment Transport (F. Silva & Duck, 2001). In 1936, the inlet/outlet canal was upgraded with a jetty to provide a better direction to incoming tidal flows (i.e. closer to parallel) and a breakwater built on the north embankment F. Silva & Duck (2001). As a result, sand began to accumulate on the north side of the Ria de Aveiro while the south side eroded. Between 1947 and 1954, Pinto et al. (2022) reported an annual erosion rate of 15 metres. Since 1965, various beach fills have been carried out on the southern side (Pinto et al., 2022). This study will employ only the north side above the Ria de Aveiro.

### 4.3.2 Results - Aveiro

The Aveiro coastal cell, illustrated in Figure 4.15, consists of 26 transects covering a distance of around 10 kilometres. Although the transects should be placed 500 meters apart (Section 2.3), Figure 4.15 reveals that this is not consistently followed. The transects in the Aveiro coastal cell start at the southern port with transect *BOX_164_124_17* and end at *BOX_164_126_18* in the north. Like the Nouakchott datasets, the Aveiro dataset is not fully complete. Before the outlier detection, 19.64% of the dataset was empty. Moreover, 44 shoreline positions were eliminated during the outlier detection process. These blank cells are subsequently filled through linear interpolation.

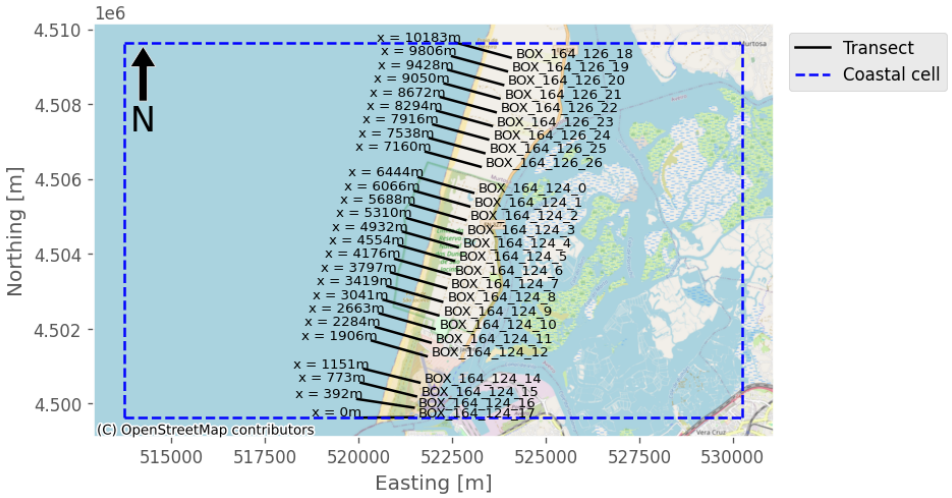


Figure 4.15: A visualisation of the coastal cell of Aveiro with the transect inside the cell provided by the SDS dataset. Aside from the transect ID, the average measured distance from the south (the harbour) to the most northern transect is provided.

Over the past 35 years (1985-2020), the shoreline has experienced landward and seaward migration, with accretion the most dominant. The shoreline has accumulated significantly in the last 20 years, as shown in Figure 4.16. As mentioned earlier, the Aveiro shoreline features a littoral barrier in the coastal cell's southern part. At this barrier, the assumption is that the LST is zero. Consequently, the annual Longshore Sediment Transport entering the cell from the north is estimated to be 0.51 million $m^3$ per year (Appendix B.3). Using an active height of 17.66 metres, including a closure depth of 15.43 metres and a mean spring tidal range of 2.23 metres (Meso-tidal regime) (Egbert & Erofeeva, 2002). The derived annual Longshore Sediment Transport does align with the volume change following the sediment balance. Over the past 35 years, the coastal cell collect a volume of 17.83 million $m^3$ sand, as illustrated in Figure 4.17 (Appendix B.3).

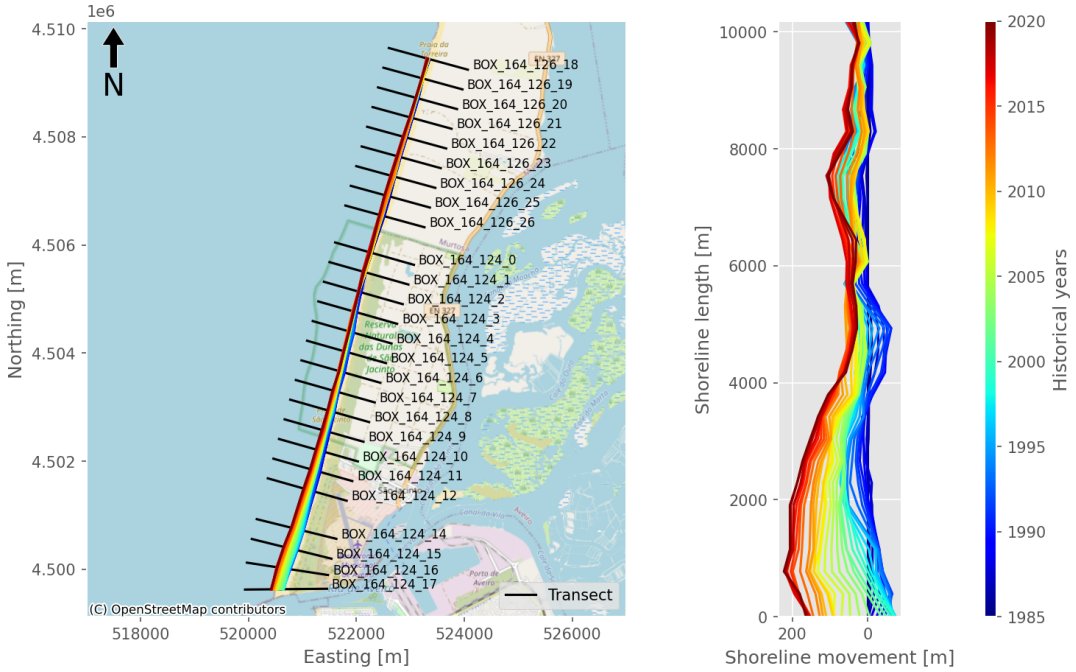


Figure 4.16: The result of the smoothing procedure along the Aveiro coastline, where blue represents the oldest year (1985) and red represents the most recent (2020).

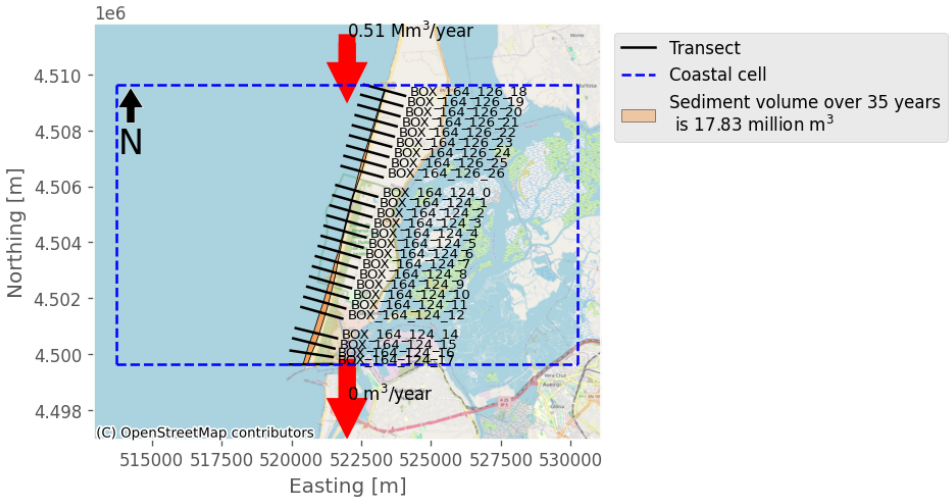


Figure 4.17: The sediment balance of the Aveiro coastal cell assumes no sediment transport at the bottom.

A relation can be established by combining the derived Longshore Sediment Transport with the corresponding shoreline orientation, namely the S-$\varphi$ relation. Figure 4.18 shows the result of this relation whereby Equation 3.19 has been fitted through the data, leading to the following equation (Equation 4.3).

$$\begin{aligned} S(\theta_r) &= 0.0612 \cdot \theta_r e^{-(0.0175 \cdot \theta_r)^2} \\ \theta_r &= \theta - 290.30 \end{aligned} \tag{4.3}$$

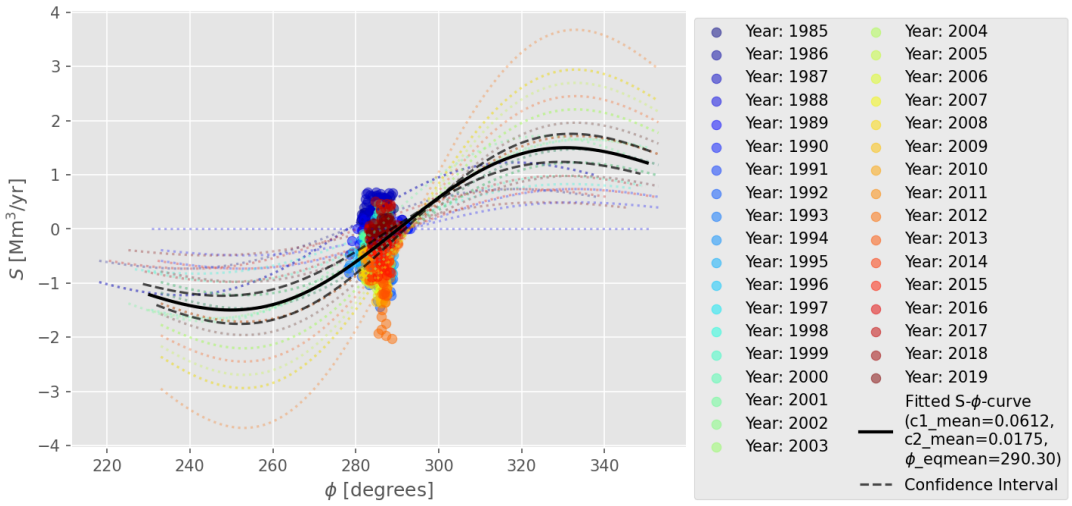


Figure 4.18: The S-$\varphi$ relation with a 95% confidence interval (black dashed lines).

The mean shoreline orientation of the last three northern transects of the coastal cell is 286.11 degrees and results in a Longshore Sediment Transport of 0.25 million m$^3$ that enters the coastal cell from the north. In comparison with the derived LST, this value is significantly lower, as well as compared to the volume change over the past 35 years. The substantial difference can be attributed to the fluctuations in shoreline orientation. The north's shoreline orientation of the last three transects is unstable and fluctuates excessively. Additionally, the 95% confidence interval is broader than that of the Nouakchott case.

Consequently, the shoreline prediction for the next 20 years has a broader range, as shown in Figure 4.20 and Figure 4.19. With a larger confidence interval, the shoreline could migrate faster or slower towards

the sea than initially predicted. This is particularly noticeable at the barrier compared to the predicted shoreline position further away from the barrier. Overall, the shoreline of Aveiro is expected to expand in the next 20 years. Taking into account that there is no bypassing of sediment in the south.

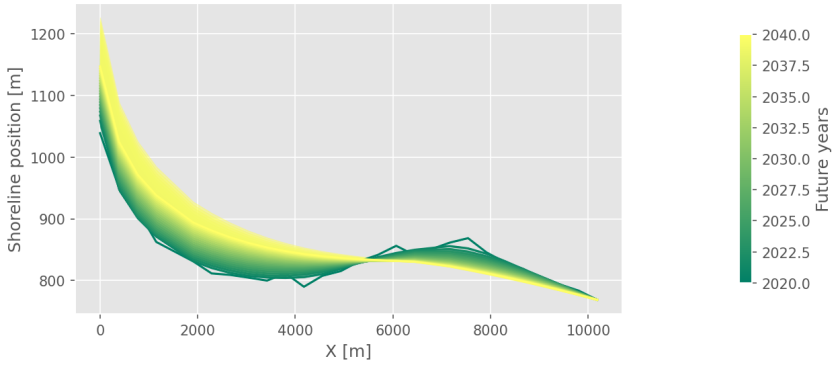


Figure 4.19: Shoreline prediction from 2020 to 2040 with a 95% confidence interval spreading, the filling between the lines. At $X$ is zero at the breakwater. The distance $X$ is the mean distance between the transects.

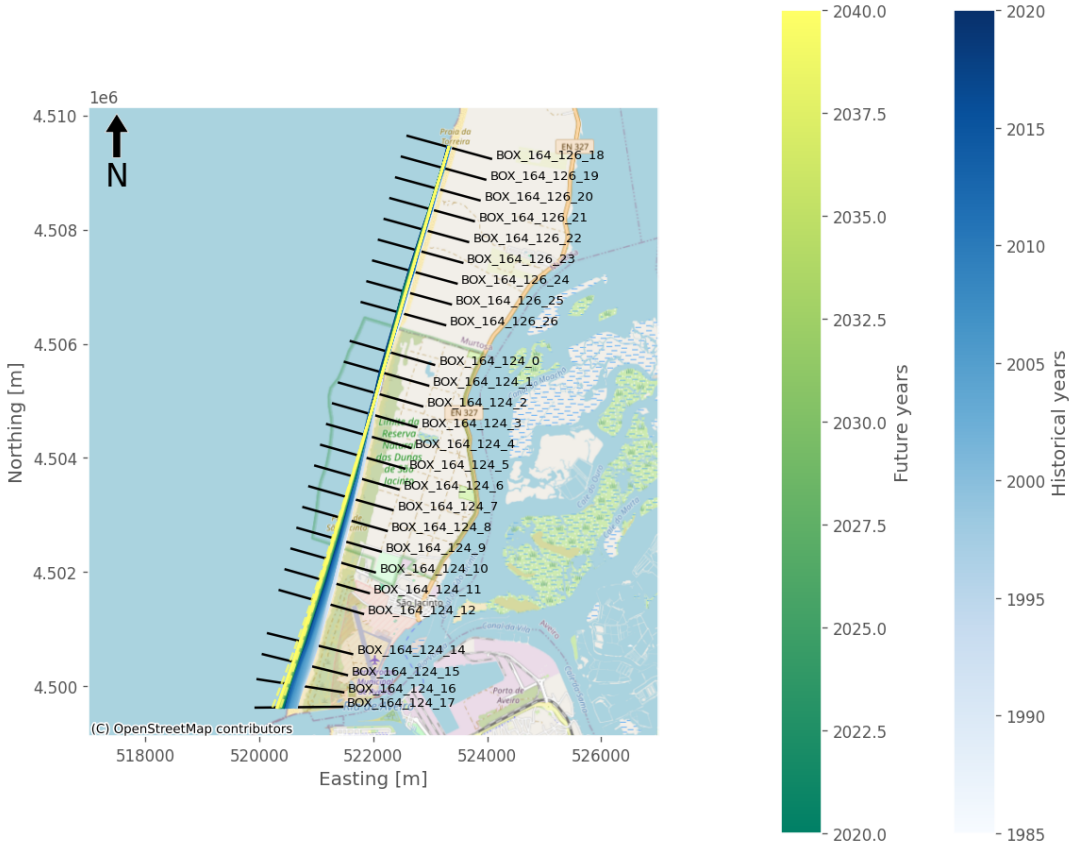


Figure 4.20: The prediction of the Aveiro shoreline for the next 20 years. The historical movement (white to blue range) and predicted shoreline position (green to yellow range).

## 4.4 Case study: Delfland - The Netherlands

The cases discussed above have one thing in common: they all had only one location where sediment transport was assumed to be zero. Table 4.1 shows that the Delfland case has two locations with zero sediment transport. The zero sediment transport is assumed at both boundaries of the coastal cell. This

coastal cell can be considered as closed because of the two border requirements that imply negligible sediment transport.

### 4.4.1 Introduction

Figure 4.21 shows the Delftland shoreline, a 17-kilometer-long part of the Dutch North Sea coast stretching from Hoek van Holland to Scheveningen. It has been the focus of extensive research due to its history of coastal erosion and mitigating efforts. The Delfland shoreline has been examined in the last 20 years to explore the impact of frequent sand nourishments and the presence of groynes for coastal protection (Radermacher et al., 2018; Wijnberg, 2002). In 2011, a new sand nourishment, called a "mega-nourishment," was deployed to defend the Delfland coastline. This mega-nourishment, also known as the Sand Engine (in Dutch "De Zandmotor"), comprises 21 million cubic metres of sediment (Luijendijk et al., 2017; de Schipper et al., 2016).

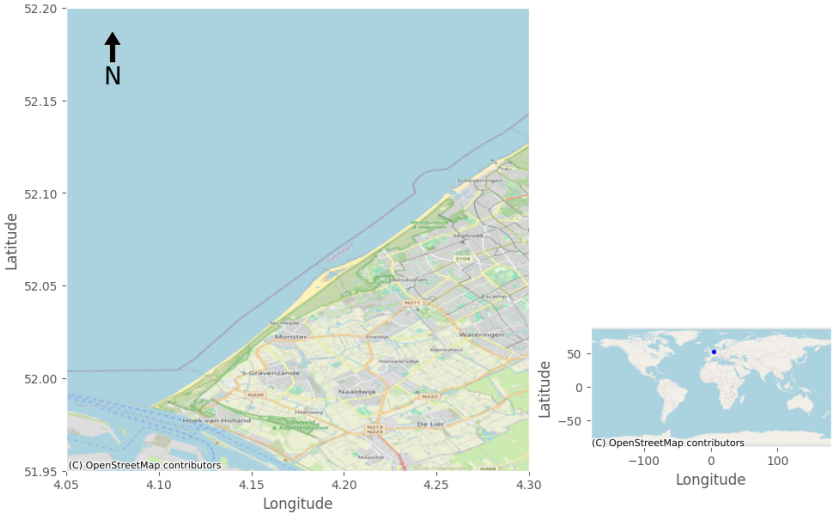


Figure 4.21: The Delfland shoreline with the Rotterdam harbour entrance is on the south and Scheveningen harbour entrance is on the north.

Other anthropogenic activities were implemented before the mega-nourishment was placed along the Delfland coast in 2011. In 2009, three Sand Groynes were built near Ter Heijde village (Hoekstra et al., 2012). These were placed as pathways in the "Delfland Coast Restoration Programme" (Hoekstra et al., 2012). The Sand Groynes serve the same purpose as the Sand Engine. Both strategies are so-called "soft solutions". The advantage is that a soft solution leaves the shoreline more natural than a permanent one (Bosboom & Stive, 2021). Therefore, these solutions fit into the category of Building with Nature (van Slobbe et al., 2013).

### 4.4.2 Results - Delfland

The Delfland coastal cell includes 53 transects spanning a 16.5-kilometer distance. Two barriers enclose this coastal cell, the breakwater of Rotterdam harbour at the south and the Scheveningen harbour at the north, creating a closed system. The transects within this coastal area run from south to north, starting at *BOX_187_084_39* and ending at *BOX_187_087_64* as illustrated in Figure 4.22. Similar to the Nouakchott datasets, the Delfland dataset is not fully complete. Before conducting outlier detection, 6.6% of the dataset contained empty values. Additionally, 49 shoreline positions were removed during the outlier detection process. The empty cells were then filled through linear interpolation.

As mentioned in the introduction of Delfland, the coastal area has undergone various anthropogenic interventions over the past 37 years. Among these, the construction of the mega-nourishment in 2011 stands out as the most recent and largest nourishment (Appendix D). The evolution of the shoreline over the last 37 years can be seen in Figure 4.23. The nourishment, particularly the mega-nourishment, has led to the exclusion of smoothing. This decision was made to prevent an unrealistic increase in shoreline position before the mega-nourishment. Figure 4.23 displays the erosion process of the Sand Engine in a Gaussian format (Arriaga et al., 2017).

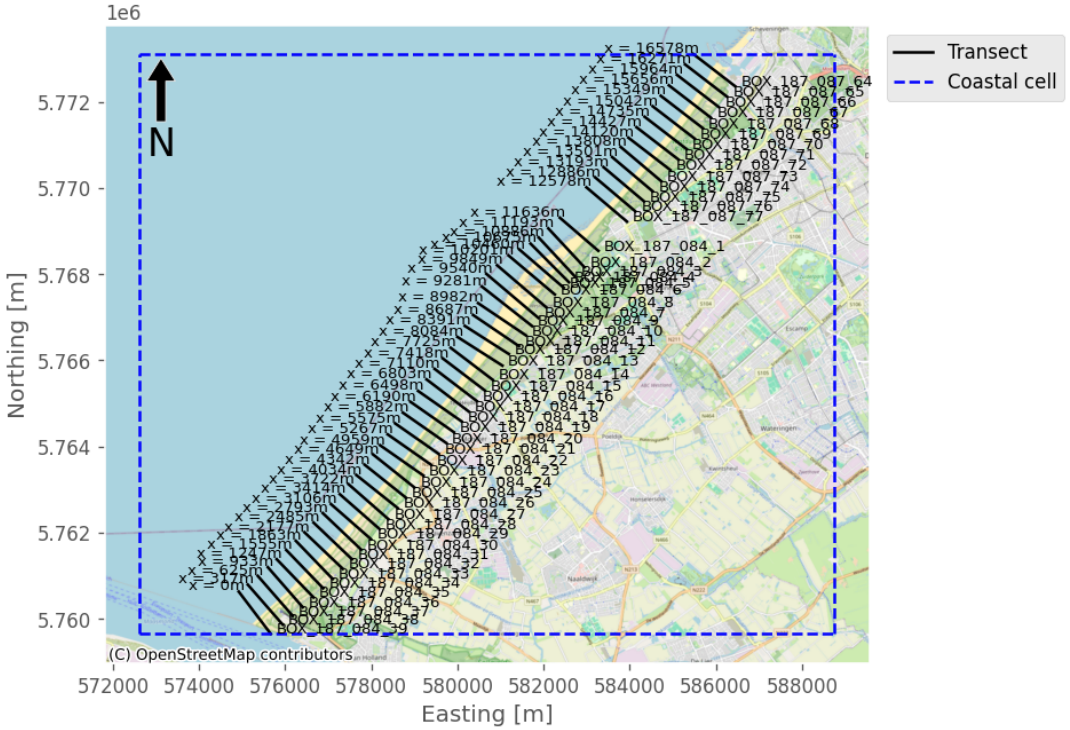


Figure 4.22: The visualisation of the Delfland's coast cell with inside the position of the transects along the shore provided by the SDS dataset. Aside from the transect ID, the average measured distance from the south to the most northern transect is provided.

The nourishment detection algorithm, outlined in Section 3.3.1 successfully identified the large mega-nourishment and several smaller nourishments, as detailed in Table 4.2.

Table 4.2: The detected nourishment along the Delfland coast using the nourishment algorithm explained in Section 3.3.1.

| **Years** | **Start transect** | **End transect** |
|---|---|---|
| 1984 - 1985 | BOX_187_084_23 | BOX_187_084_19 |
| 1996 - 1997 | BOX_187_084_30 | BOX_187_084_26 |
| 2000 - 2001 | BOX_187_084_26 | BOX_187_084_16 |
| 2003 - 2004 | BOX_187_084_19 | BOX_187_084_10 |
| 2008 - 2009 | BOX_187_084_29 | BOX_187_084_21 |
| 2009 - 2010 | BOX_187_084_18 | BOX_187_084_8 |
| 2009 - 2010 | BOX_187_084_1 | BOX_187_087_74 |
| 2010 - 2011 | BOX_187_084_11 | BOX_187_084_2 |
| 2010 - 2011 | BOX_187_087_71 | BOX_187_087_66 |
| 2011 - 2012 | BOX_187_084_13 | BOX_187_084_2 |

Based on the historical evolution of the shoreline position and the presence of two littoral barriers, the Longshore Sediment Transport can be calculated. The two barriers are located at Hoek van Holland and Scheveningen, assuming no bypassing of sediment occurs at these points. In addition, the nourishments detected years in Table 4.2 will be excluded from the sediment transport analysis due to the additional sand they introduce, impacting the S-$\varphi$ relation and shoreline predictions.

The sediment volume gradient is obtained by multiplying the surface gradient by the active height, which contains the closure depth and mean spring tidal range. With a closure depth of 9.07 meters and a mean spring tidal range of 1.56 meters (Micro-tidal regime) and semi-durnal (Wijnberg, 2002; Egbert & Erofeeva, 2002), the active height is calculated as 10.63 meters. As the Delfland coast has two

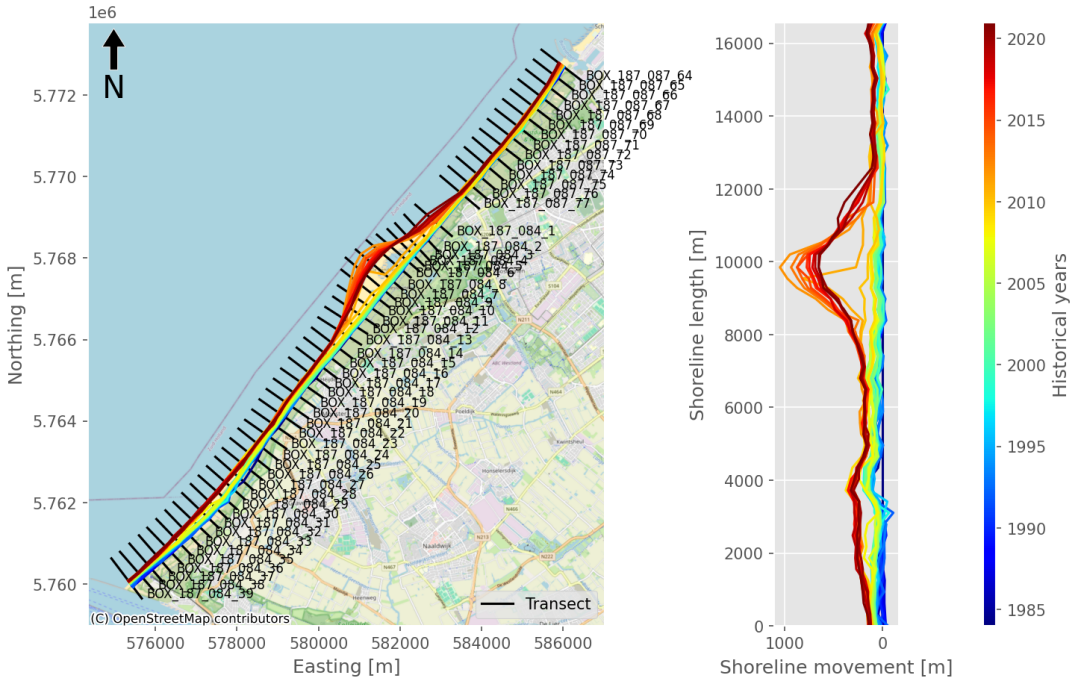


Figure 4.23: The result of the interpolation procedure along the Delfland coastline, where blue represents the oldest year (1984), and red represents the most recent (2021).

boundaries with zero sediment transport, the LST is determined by averaging the sediment transport between Hoek van Holland and Scheveningen. The highest sediment transport recorded was 0.75 million $m^3$ from 1999 to 2004 from Hoek van Holland (at 0 km) to Scheveningen (at 16.5 km). Between 2019 and 2021, sediment transport from Scheveningen to Hoek van Holland also reached 0.75 million $m^3$, attributed to erosion at the Sand Engine (Appendix B.4).

Over 37 years, the shoreline volume has increased by 45.55 million $m^3$, assuming no sediment bypassing. This growth is displayed in a sediment balance shown in Figure 4.24, where the volume increase at the Sand Engine is particularly visible. It is essential to highlight that all nourishments conducted are accounted for in this sediment balance, with the volume calculated based on the coastline position difference between 1984 and 2021, multiplied by the active height.

A correlation can be established by combining the total years of the Longshore Sediment Transport without nourishments with the calculated shoreline orientation over 37 years. The graph in Figure 4.25 illustrates the average S-$\varphi$ relationship for the remaining years (represented by the black line), Equation 4.4. The black dashed lines represent the 95% confidence interval, which is wider compared to the scenarios discussed in Sections 4.2 and 4.3. Consequently, even $\theta_{eq}$ produces a broader distribution. This indicates the challenge of fitting the Delfland coastline into an S-$\varphi$ relationship, as evident from the visual representation. The yearly relationships display a significant spread across the orientation spectrum.

$$\begin{aligned} S(\theta_r) &= 0.0261 \cdot \theta_r \cdot e^{-(0.0170 \cdot \theta_r)^2} \\ \theta_r &= \theta - 304.18 \end{aligned} \tag{4.4}$$

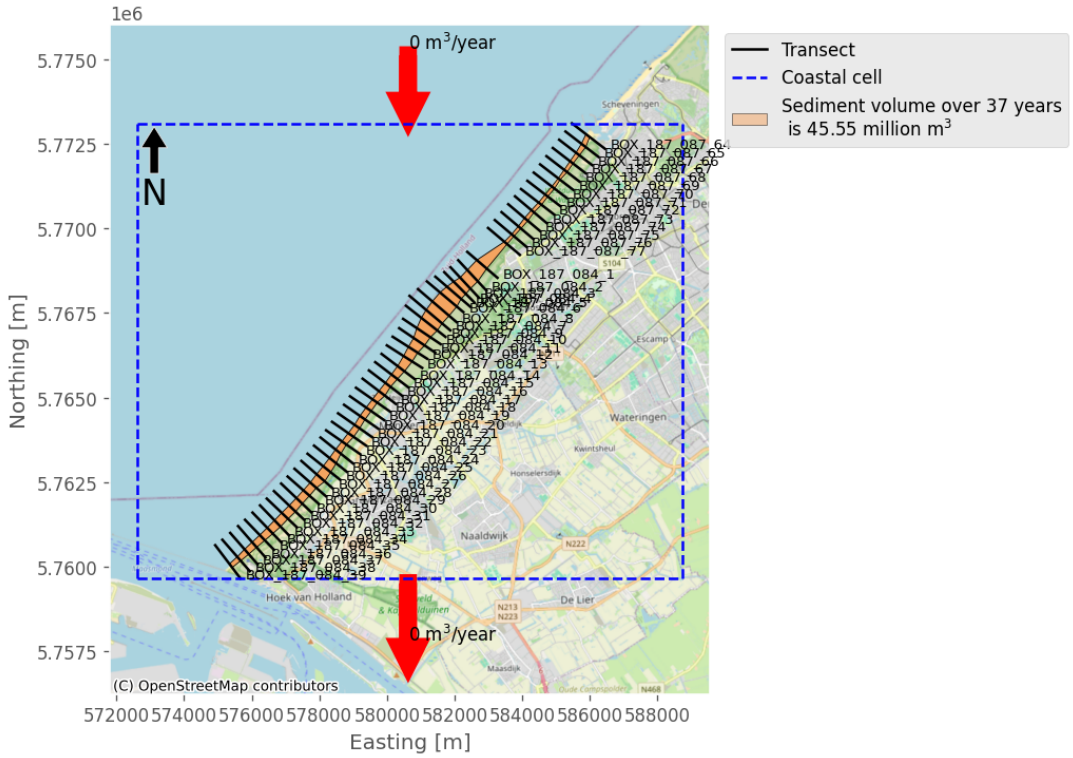


Figure 4.24: The sediment balance in the selected coastal cell of the Delfland. The assumption is that there is no sediment transport at both sides.

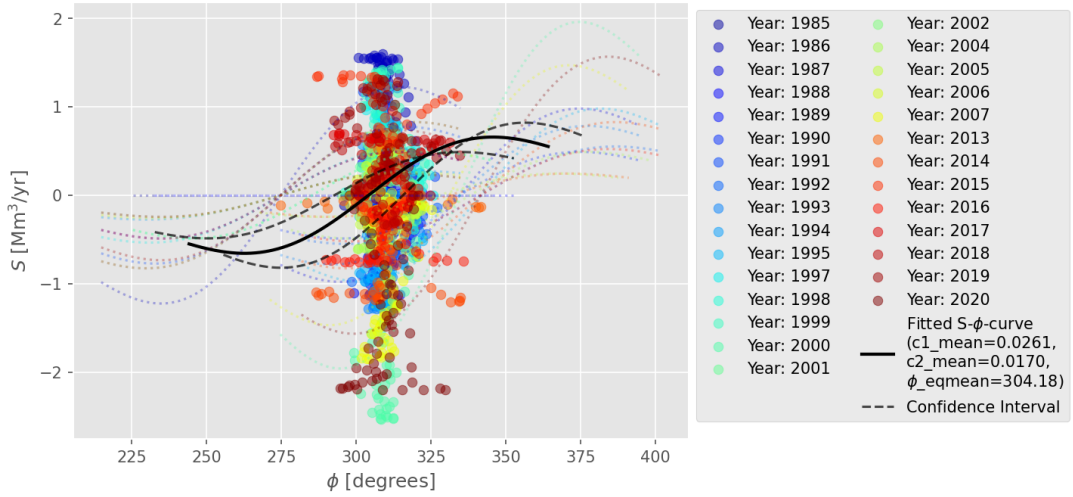


Figure 4.25: The S-$\varphi$ relation of the years where no nourishment was detected by the nourishment detection algorithm. The black dashed line is the 95% confidence interval.

Due to the wide range of the equilibrium shoreline orientation ($\theta_{eq}$), the shoreline prediction will also reveal a broader range, as illustrated in Figure 4.26. This figure displays the shoreline position from Hoek van Holland to Scheveningen along the mean distance between transects. From this visualisation, it is evident that there is significant uncertainty regarding the boundaries. It is plausible that the shoreline near Hoek van Holland may experience minimal movement or substantial retreat. The average prediction indicates considerable erosion near Hoek van Holland. This extensive range could be attributed to the littoral barrier, which hinders waves from the southwest direction from impacting the shoreline at Hoek van Holland.

As a result, an alternative equilibrium orientation may be identified in this area next to the Hoek van Holland breakwater. Regarding Scheveningen, the shoreline may shift significantly seaward or retreat. Nevertheless, the average prediction suggests a seaward migration of the shoreline. Figure 4.27 presents the same shoreline prediction with a confidence interval along the Delfland coast (Appendix B.4).

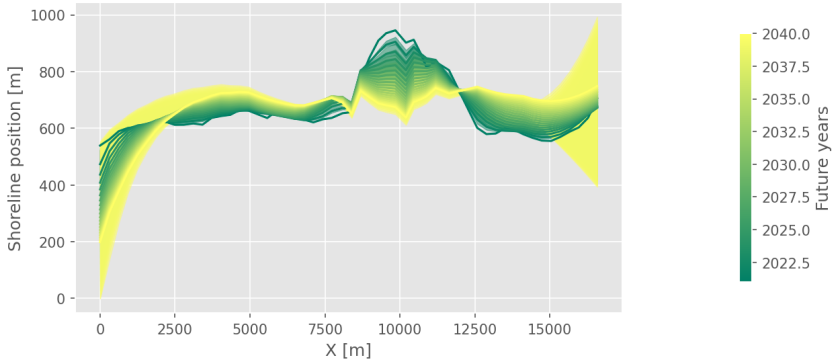


Figure 4.26: Shoreline prediction from 2020 to 2040 with a 95% confidence interval spreading, the filling between the lines. At $X$ is zero is the harbour of Rotterdam, and at $X$ is 16.5 kilometres is the harbour of Scheveningen. The distance $X$ is the mean distance between the transects.

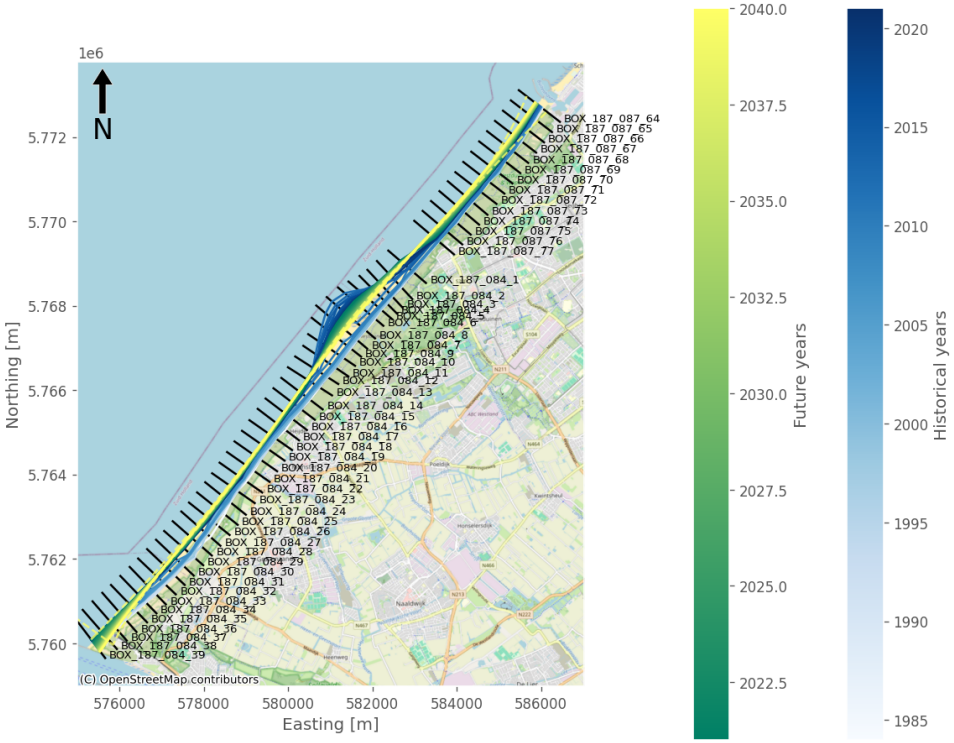


Figure 4.27: The prediction of the Delfland shoreline for the next 20 years. The historical movement (white to blue range) and predicted shoreline position (green to yellow range). The yellow dashed line is the 95% confidence interval.

## 4.5 Case Comparison

After reviewing the data from the SDS based on the criteria outlined in Section 4.1, various cases were presented in Table 4.1. Along with the findings of Luijendijk et al. (2018), the selected cases include Nouakchott - Mauritania (Section 4.2), Aveiro - Portugal (Section 4.3), and Delfland - the Netherlands (Section 4.4). The Nouakchott coastal cell was further divided into northern and southern areas due to the city's harbour in the centre. This division allows for examining how the SHORECAST model

would react in each coastal cell and whether they align. Consequently, there are now four cases available for comparison. The Delfland coastline was specifically selected due to the presence of breakwaters at Rotterdam and Scheveningen harbour, where sediment bypassing is considered unfeasible.

In addition, the Delfland coast incorporates specific anthropogenic interventions like nourishments. Numerous pilot projects have focused on this coastal region to mitigate structural erosion (de Schipper et al., 2016; Hoekstra et al., 2012). As a result of these initiatives, the Delfland coast stands out as one of the most extensively documented and monitored shorelines among the cases, offering valuable opportunities for validating the model outcomes (Vitousek, Buscombe, et al., 2023).

The chosen locations, Aveiro and Nouakchott, are both situated along the Atlantic Ocean, with Aveiro positioned at approximately 40.64 degrees North latitude and Nouakchott at around 18.07 degrees North latitude (Figure 3.2). On the other hand, the Delfland coast faces the North Sea, located between the Netherlands and Great Britain, at about 52.06 degrees North latitude. Moreover, all three cases experience a semi-diurnal tidal pattern, with Aveiro having a meso-tidal regime (F. Silva & Duck, 2001; Coelho et al., 2011), and Nouakchott and Delfland having a micro-tidal regime (Elmoustapha et al., 2007; Wijnberg, 2002). As noted by Pinto et al. (2022), high-energy waves are dominant along the Aveiro coast, in contrast to the Delfland coast, which features a medium wave energy environment (de Schipper et al., 2016; Luijendijk et al., 2017). Additionally, the Delfland coast is exposed to significant storm surges when storm winds push seawater from the North Sea into the narrow channel, referred to as the Canal, between the Netherlands and Great Britain (Weisse et al., 2012; Kew et al., 2013).

Upon examining the initial three coastal cells, namely Nouakchott North, Nouakchott South and Aveiro, it is evident that these cases all share a common boundary condition. This condition assumes that there is no sediment transport at one of the boundaries of the coastal cell. In Nouakchott's case, this condition was generated by a breakwater at the harbour. Similarly, a breakwater was constructed in Aveiro, but this one was intended to increase the outflow of Ria de Aveiro. Both breakwaters were designed to stretch far enough into the sea to block sediment from bypassing. The validity of these breakwaters will be discussed in Section 5.2.

The Nouakchott coastal cell was an excellent example of implementing the new methodology described in Chapter 3 and testing the developed approach. Over the first thirty years, the Nouakchott cases demonstrated a consistent increase in accretion for Nouakchott North and a steady erosion for Nouakchott South without human intervention. Consequently, a clear Longshore Sediment Transport difference was observed, as illustrated in Figures 4.6 and 4.11. Resulting in an accumulation of 23.01 million $m^3$ and an erosion of 32.36 million $m^3$ over 35 years.

Comparing the smooth accumulation and erosion outcomes of the Aveiro coastal system, it is evident that Aveiro's historical shoreline experiences more fluctuations compared to Nouakchott. The shoreline in Aveiro undergoes years of erosion followed by years of accretion, as shown in Figure B.43. Due to these fluctuations, it is more challenging to observe a clear general pattern, as seen in the Nouakchott cases. Figures 4.16 and B.42 indicate that the trend along the Aveiro coast leans towards accretion. The comparison of S-$\varphi$ connections between Nouakchott and Aveiro cases reveals that the significant fluctuations in Aveiro's shoreline positions challenge establishing a solid relationship. In Nouakchott cases, the mean S-$\varphi$ relation closely reaches the yearly fitter S-$\varphi$ relation. However, the equilibrium orientations in Aveiro have diverged notably over the past 38 years. This fluctuation can also be traced back to a larger 95% confidence interval by Aveiro (Figures 4.7 and 4.18).

**Nouakchott**

Examining the relationship between sediment transport and orientation in Nouakchott's coastal cells using the data presented in Figures B.15a and B.31a, a slight trend is observed. The complex S-$\varphi$ plots in the Aveiro scenario may be attributed to the temporal variability of the offshore wave regime (A. N. Silva et al., 2012). Despite being in the same ocean as Aveiro but closer to the equator, the Nouakchott coast is not exposed to high wave regime (Samou et al., 2023).

Nouakchott's north and south coastal cells reveal a significant difference in Longshore Sediment Transport. In the north coastal cell there is sediment transport of 0.66 million $m^3$ entering the cell at the top per year, while in the southern cell 0.92 million $m^3$ per year is leaving the coastal cell. Figure 4.28a shows both regions' sediment transport and coastline orientations. Crosses denote Nouakchott North, while triangles represent Nouakchott South. The shoreline orientation of most of Nouakchott North

ranges between 265 and 270 degrees north, gradually increasing to 290 degrees where sediment transport reduces. Conversely, Nouakchott South exhibits a broader range. The orientation falls between 270 and 290 degrees, similar to the north, but sediment transport is more pronounced in Nouakchott South, leading to increased sediment transport. Important to note is that the data from the transect between the harbour and revetment are not taken into account from 2012 to 2020.

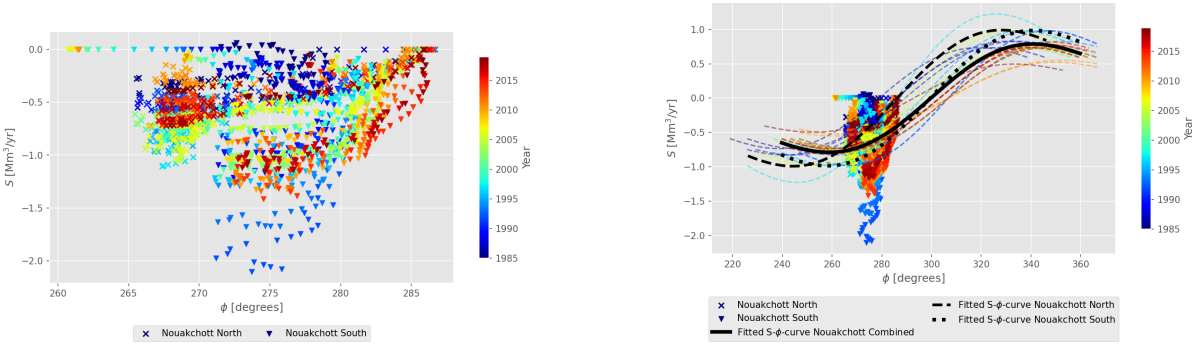


(a) (b)

Figure 4.28: The combined shoreline orientation and sediment transport of the Nouakchott coastal cell in (a). In (b) the S-$\varphi$ relation per coastal cell is presented and the combined relation.

Figure 4.28b illustrates the average S-$\varphi$ relationship of all data with a black line, while the dashed black line represents the S-$\varphi$ relationship for Nouakchott North, and the dotted black line represents the Nouakchott South instance. Table 4.3 presents the variables derived from the S-$\varphi$ relationship for Nouakchott North, South, and combined. The table indicates that the equilibrium orientation ($\theta_{eq}$) is 299.75 degrees when combining the north and south data. This value is slightly larger than the south equilibrium orientation. In addition, the RMSE is higher than the Nouakchott North case, but lower for the South case. As a result, the derived combined S-$\varphi$ relation at Nouakchott should be applied at both coastal cells.

Table 4.3: The presented variables from Equation 3.19 along with the values obtained from the cases of Nouakchott North and South and their combined data.

| Variables | North | South | Combined |
|---|---|---|---|
| $C_1$ | 0.0390 | 0.0392 | 0.0317 |
| $C_2$ | 0.0169 | 0.0171 | 0.0173 |
| $\theta_{eq}$ | 286.18 | 299.49 | 299.75 |
| RMSE | 0.06 | 0.09 | 0.08 |

However, the southern case may experience some wave reduction due to the breakwater of Nouakchott, assuming the dominant wave direction is from the northwest (Elmoustapha et al., 2007). The influence of this breakwater will be elaborated in Section 5.3. Besides the varying S-$\varphi$ relationship, the shoreline's curvature is another factor contributing to the differences in sediment transport. When observed from a greater distance, the shoreline appears to rotate slightly. As a result of this rotation, there is a higher amount of sediment movement in the south compared to the north. These findings align with the research conducted by Elmoustapha et al. (2007).

### Delfland

In Section 4.4, the last coastal cell analysed is the Delfland coast, which strongly differs from the previously analysed cases. Firstly, it has two boundary conditions, unlike the other cases. As mentioned earlier, the Delfland coast is known for its numerous anthropogenic interventions. These anthropogenic measures offer a unique opportunity for the model to validate the reliability of the developed model.

Due to the nourishments along the Delfland shore, some data could not be utilized for the analysis to establish a suitable S-$\varphi$ relationship. Consequently, the computation of S-$\varphi$ for the Delfland coastal

cell relies on fewer data points than the other cases because the nourishment years are removed. Even after removing these years, the Sand Engine nourishment may still impact the S-$\varphi$ relationship. The S-$\varphi$ relationship was computed with data before and after the Sand Engine nourishment to determine the impact of this mega-nourishment as shown in Table 4.4. Comparing the results of Table 4.4 and Figures 4.29a and 4.29b shows that the S-$\varphi$ relation for the complete dataset is significant different in comparison with the data before and after the nourishment. Furthermore, the S-$\varphi$ relation before and after the Sand Engine does not change significantly. However, the confidence interval for the S-$\varphi$ relation after constructing the Sand Engine is much broader than before the Sand Engine. In other words, this construction of the Sand Engine significantly impacts the S-$\varphi$ relationship.

Table 4.4: The presented variables from Equation 3.19 along with the values obtained from the Delfland coastal cell containing the parameters before (1984 - 2010) and after (2013 - 2021) the Sand Engine and the complete dataset (1984 - 2021).

| Variables | Before | After | Completely |
|---|---|---|---|
| $C_1$ | 0.0366 | 0.0265 | 0.0261 |
| $C_2$ | 0.0175 | 0.0169 | 0.0170 |
| $\theta_{eq}$ | 309.77 | 306.92 | 304.18 |
| RMSE | 0.54 | 0.73 | 0.73 |

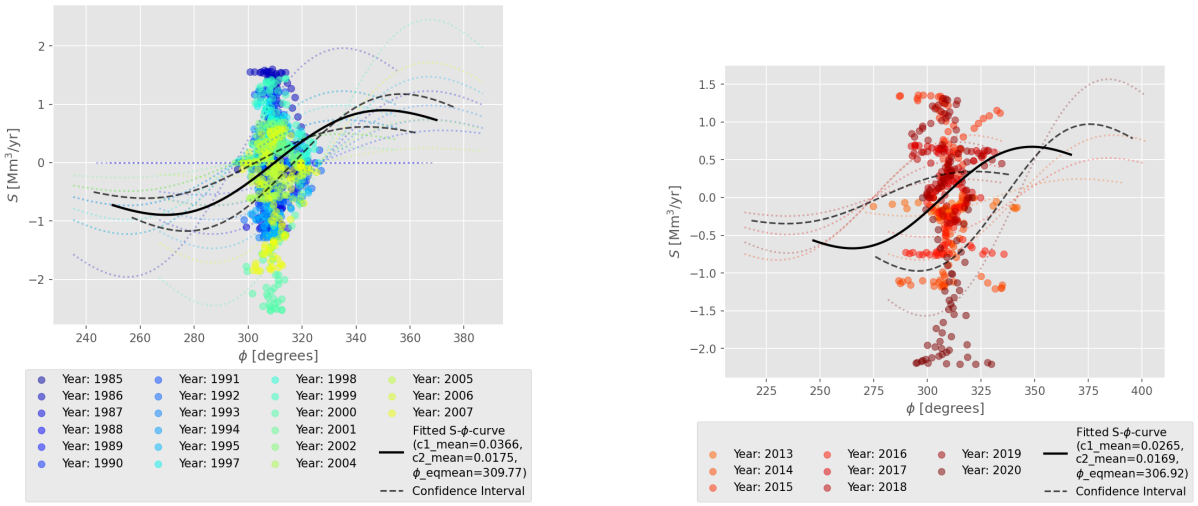


(a) (b)

Figure 4.29: These two images display the computed S-$\varphi$ relation for the mega-nourishment constructed at the Delfland coast (figure a) and after (figure b). The scatter in the plot represents the obtained shoreline orientations with the corresponding Longshore Sediment Transport. The black dashed lines in both plots represent the 95% confidence interval.

The comparison of the results from the nourishment detection at the Delfland coast with the actual placed nourishments, as presented in Appendix D reveals that not all nourishments are visible in the SDS data. From 1984 to 2021, a total of 36 nourishments were carried out. Among these, only three types of nourishment were implemented along the Delfland coast: Beach, Shoreface, and Dune nourishment. The Dune nourishment was conducted only once in 1986, while during the same period, 28 beach nourishments and seven shoreface nourishments were completed. The SDS focuses on detecting changes in the shoreline position where land meets water along a two-dimensional plane whereby the volume is estimated based on the One-line theory (Sections 3.3.6 and 5.3.2). Consequently, the Shoreface and Dune nourishments remain undetected by the SDS.

The combined volume of all nourishments amounts to 55.99 million $m^3$, with beach nourishment accounting for 46.51 million $m^3$ and Shoreface nourishment for 9.49 million $m^3$. When comparing the volume of Beach nourishments with the value derived from the sediment balance in Figure 4.24, which is 45.55 million $m^3$, it is evident that the volumes are nearly identical. This suggests that some beach

nourishment may have exited the coastal cell due to bypassing or moving under the water line. However, the coastal cell was assumed to be fully enclosed on both sides. Section 5.2 will examine this hypothesis further.

It is worth mentioning that in all the cases presented in Chapter 4, the equilibrium angles are close to each other. This can be attributed, at least partially, to the fact that the shorelines are approximately parallel to each other, only lying far apart. However, there is difference in sediment transport between the Nouakchott and Aveiro cases, where the transport is from north to south and the Delfland case from south to north. This difference can be primarily attributed to the primary wave direction. In the Nouakchott and Aveiro cases, the primary wave direction is North-West (Elmoustapha et al., 2007; A. N. Silva et al., 2012), while along the Delfland shore, it is from the southwest (de Schipper et al., 2016).

# 5

# Discussion

This chapter reviews the findings of Chapter 4 and the developed method as explained in Chapter 3. Therefore, this chapter is divided into three sections. Section 5.1 looks briefly into other shoreline prediction techniques to argue why the model SHORECAST would be a better method to predict the shoreline position. Next, the developed technique behind SHORECAST will be validated using the model results compared to the real-world data as elaborated in Section 5.2. Lastly, Section 5.3 reflects on the limitations associated with the developed method.

## 5.1 Prediction techniques

Besides the developed SHORECAST model, there are other methods to predict the shoreline position in the future. One of these methods is following the linear trend of the collected SDS data. Extrapolating the regression line would produce accurate results in areas unaffected by external factors and with no limitations on sediment availability. This strategy could be implemented for shoreline analysis in Lafayette, United States (Section 4.1). Due to significant retreat at this site, the shoreline position can be predicted, but the Longshore Sediment Transport cannot be predicted as with the method described in Chapter 3.

Applying this approach to the case of Nouakchott North and Aveiro would result in an infinite accretion of the shoreline. However, this is not feasible in reality due to sediment bypassing at a certain moment, which causes the coast to grow slower. It is crucial to notice that the shoreline cannot grow beyond the breakwater. Likewise, the SHORECAST model from Chapter 3 also assumes no sediment bypassing, which is a limitation of the model discussed in Section 5.3. On the other hand, applying the extrapolation of the trend line to Nouakchott South would lead to infinite erosion. Figure 4.13 demonstrates that the erosion force decreases over the years near the revetment, and the shoreline remains stable between the harbour and the revetment.

A more illustrative example is the Delfland coast, where linear extrapolation of the derived regression lines from the Satellite-derived Shoreline data cannot be used. Figure 5.1 illustrates the shoreline prediction using linear extrapolation of the obtained regression lines and the derived S-$\varphi$ relation prediction. This figure clearly shows that the shoreline position predicted by the linear extrapolation method will continue to migrate further into the sea. This is partially true due to the erosion and accretion occurring at the Sand Engine. The sides of the Sand Engine will accrete, while the top of the Sand Engine will erode. However, the accretion predicted by the extrapolation is significantly more than would happen in reality. The prediction by the SHORECAST model provides a more realistic result. As expected, the model indicates erosion at the top of the Sand Engine nourishment. Therefore, the SHORECAST model is much more reliable than linear extrapolation.

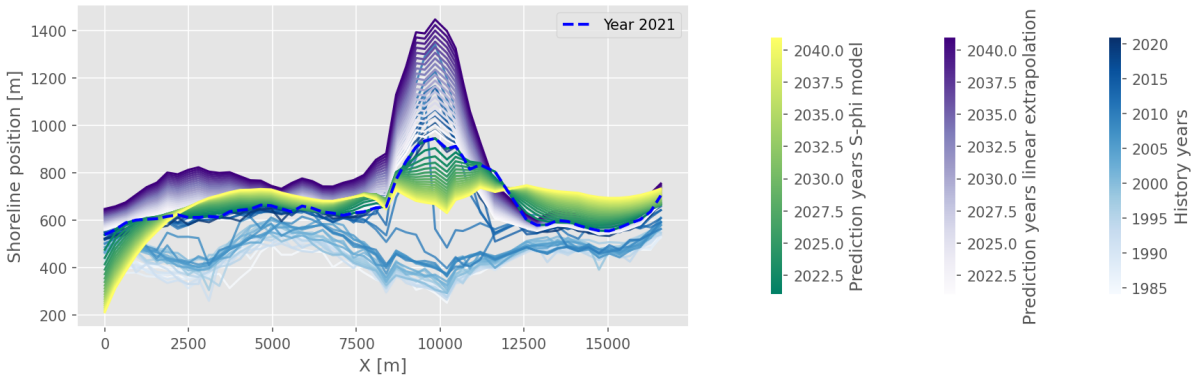


Figure 5.1: An illustration of two shoreline prediction techniques: linear extrapolation (purple) and S-$\varphi$ method (green to yellow). The white-to-blue colour gradient represents the historical shoreline position.

The expected rise in sea levels has not yet been taken into account for predicting shorelines by the SHORECAST model. Incorporating this value could result in a lower accretion rate but a higher erosion rate. However, it is not ruled out that with a significant rise in seawater level, accretion may change to erosion, following Bruun rule (Bruun, 1962). Furthermore, the method developed in Chapter 3 offers the advantage of being resilient to future coastal changes. The model can adapt to various scenarios, such as nourishment or building a groyne along an eroding coast (Appendix C), which are more difficult for linear extrapolation methods. The SHORECAST model is dynamic and can withstand alterations, providing a sense of reassurance about its future relevance.

The comparison between the developed and existing methods, as discussed in Section 2.2, reveals that the new method resembles the Unibest-CL+ numerical model. Unibest-CL+ is designed to simulate shoreline changes caused by gradients in longshore sediment transport. These longshore transports are influenced by tide and wave-driven longshore currents (Huisman & Dagalaki, 2020). The similarity between the two methods arises from their shared utilization of the single-line theory (One-line theory). However, while Unibest-CL+ incorporates waves, tides, bathymetry and sediment characteristics data, the new method outlined in Chapter 3 only depends on Satellite-derived Shoreline data. This unique characteristic of the new method allows for its application in locations where limited research has been conducted (Vitousek, Buscombe, et al., 2023).

## 5.2 Validation

In order to confirm the reliability of the methodology described in Chapter 3, it is crucial to validate the findings using real-world data. The validation process will include evaluating the critical stages of the SHORECAST model, starting with the nourishment and outlier techniques (Section 5.2.1). The effectiveness of breakwaters in preventing sediment bypassing, as discussed in Chapter 4 will also be verified to determine its accuracy in Section 5.2.2. Additionally, the accuracy of shoreline prediction will be cross-checked with the existing shoreline to ensure precise predictions are generated, utilizing the derived S-$\varphi$ relationship (Section 5.2.3).

### 5.2.1 Littoral transport gradient

#### Nourishment

In Section 4.5, it is outlined that only the Delfland case contains nourishment data. Detecting these nourishments is important because they significantly impact the estimated Longshore Sediment Transport and can result in an inaccurate shoreline prediction by affecting the S-$\varphi$ relation. Hence, it is crucial to develop a robust nourishment detection system. Along the Delfland coast, Rijkswaterstaat (Appendix D) records the nourishment activities, including the nourishments' location, volume and placement time. By comparing the actual placed nourishment (Figure 5.2a) with the SDS dataset shown in Figure 5.2b, the challenges in capturing all nourishments when calculating the difference between years using SDS data become evident. As mentioned in Section 4.5, only the beach nourishment is visible in the data. Figure 5.2a illustrates that most nourishments are of small scale.

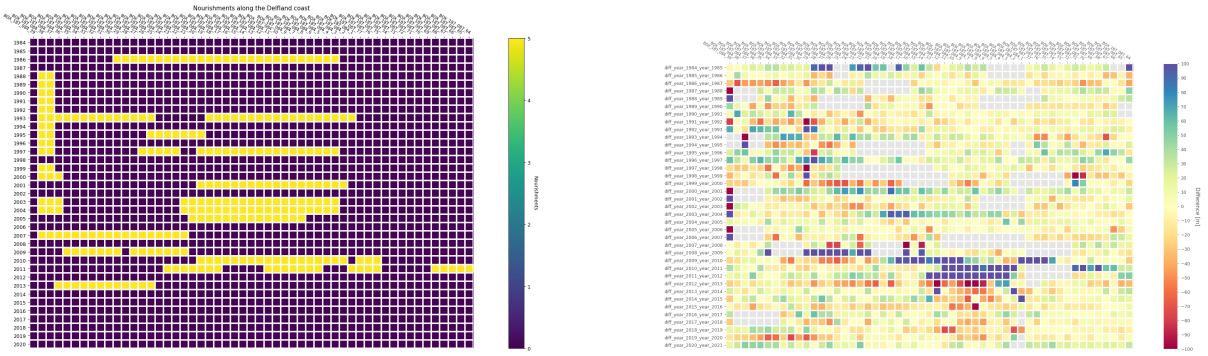


(a) Nourishment RWS

(b) Shoreline difference

Figure 5.2: Figure (a) displays the documented nourishment according to de Boer & den Heijer (2016) and Appendix D. Figure (b) shows the difference in shoreline position for the Delfland case. The white spots are cells with no data. Blue means an increase, and red means a decrease between the shoreline positions.

Comparing Figure 5.2a with 5.2b shows that not all nourishments are visible in the Satellite-derived Shoreline dataset (Figure 5.2b), which raises the question of how to detect the most significant nourishment from the Satellite-derived Shoreline data. Table 5.1 displays the largest beach nourishments. The first row in the table is the Sand Engine nourishment.

The nourishment detection algorithm, detailed in Section 3.3.1, identifies nourishment if the shoreline has shifted by 40 meters or more along five or more transects (Figure B.54). The recognised nourishment in the SDS data aligns with the largest nourishments. In Appendix A.3, various shoreline migrations were tested to determine which one would detect the most nourishments from the SDS data. The 40 meters shoreline shift has proven to be the most effective, marking a significant step forward in this research, with the results presented in Table 4.2 corresponding to the top 10 largest nourishments listed in Table 5.1. As a result, the nourishment detection algorithm is functioning effectively, indicating that it is operating as intended.

Table 5.1: The largest beach nourishment based on the data from Appendix D. The first largest nourishment is the Sand Engine.

| Date start | Date end | Volume $Mm^3$ |
|---|---|---|
| 2011-03-01 | 2011-10-31 | 17.00 |
| 2009-07-01 | 2010-12-31 | 5.00 |
| 2008-06-01 | 2009-10-31 | 4.50 |
| 2009-07-01 | 2010-01-31 | 3.00 |
| 2008-06-01 | 2009-01-31 | 3.00 |
| 2010-01-01 | 2011-07-31 | 2.50 |
| 1986-05-01 | 1986-10-31 | 1.90 |
| 2003-09-01 | 2003-11-30 | 1.25 |
| 2004-05-01 | 2004-06-30 | 1.16 |
| 1993-06-01 | 1993-07-31 | 1.14 |

Other methods of identifying nourishment involve assessing the initiation of a new trend. In the event of structural erosion along the shoreline, a downward trend line will be observed in a time series. Following the addition of nourishment, the shoreline will extend further into the sea before eroding once more. As a result, two distinct slopes are visible in the time series data: one before nourishment and one after. However, indicating these regression lines within a fluctuating time series can be challenging.

Nevertheless, it is important to note that the spatial requirement for detecting nourishment is typically set at five transects, although this value can be adjusted higher or lower depending on the specific conditions. Figure 5.2a illustrates instances where nourishments are distributed across two or three sections. This demonstrates the adaptability of the method to different scenarios. Since these nourishments are not

shown in Figure 5.2b, the spatial domain value of five transects remains unchanged, highlighting the consistent application of the method.

#### Outliers

Upon detecting the nourishments, the SDS data undergoes analysis for outliers using the two methods outlined in Section 3.3.1. Examination of the shoreline position along the transects indicates significant variability. However, this variability is a common feature of a sandy coastline. Due to these natural fluctuations, not all shoreline positions should be labelled as outliers. It is, therefore, essential to differentiate between natural shoreline changes and outliers. Fortunately, outliers can be distinguished based on irregular coastline patterns. For instance, a sudden significant movement towards the sea or land could indicate an outlier or the initiation of nourishment. Consequently, the shoreline should retreat or advance in relatively equal measures. Both outlier detection methods can identify these abrupt changes, but only the extreme cases are pinpointed.

Alternative techniques for identifying outliers in time series involve assessing whether the overall trend shifts upon removing specific data points. If shoreline positions do not impact the general regression line, they may be outliers. Instead of focusing only on outliers, the outlier detection process could be skipped. This would allow for more shoreline positions to be examined, and the significance of outliers would decline due to smoothing after linear interpolation with a smoothing factor of $N = 5$. If outliers are situated near gaps, these spaces will be filled, considering the presence of the outlier. The shoreline will expand or contract before and after the outlier point, or vice versa. Therefore, identifying outliers is crucial. The process should be approached with moderation as coastlines naturally undergo fluctuations.

### 5.2.2 Zero-points

Section 3.3.7 explained how several boundaries were implemented to convert the sediment transport gradient into Longshore Sediment Transport. In the coastal cells discussed in Chapter 4, the boundaries were set so that sediment transport is assumed to be zero on at least one side of the coastal cell. In the case of the Delfland instance, both sides of the coastal cell have no sediment transport. However, it is critical to determine whether this assumption holds in all circumstances or if there is any sediment bypassing.

#### Nouakchott

In Section 4.2, the Nouakchott case was divided into a northern and southern case with Nouakchott's harbour in between, where the assumption is of no bypassing of sediment shown in Figure 5.3. The north coastal cell has experienced an increase of approximately 23.01 million $m^3$, while the South coastal cell has eroded a 32.36 million $m^3$ over 35 years. In the overall coastal cell, the blue dashed line indicates that more material is leaving the cell from the south than entering it in the north.

With the overall coastal cell, it is possible to see whether the assumption at Nouakchott's harbour holds. The equation presented in 5.1 suggests that the north sediment input should match the south output. However, the sediment bypassing is lower than the calculated value because of the single-line assumption. When the shoreline retreats, the active height is lower than assumed. Additionally, the erosion volume estimated by the S-$\varphi$ in Section 4.2.3 at the end of the coastal cell is approximate 0.81 million $m^3$. Which is closer to the input value in the north. Consequently, it can be affirmed that sediment bypassing occurs, although not to the extent indicated in Equation 5.1.

$$\begin{aligned} \text{input}_{\text{sediment}} - \text{output}_{\text{sediment}} &= 0 \\ 0.66 \cdot 10^6 \text{ m}^3 - 0.92 \cdot 10^6 \text{ m}^3 &= -0.26 \cdot 10^6 \text{ m}^3 \end{aligned} \tag{5.1}$$

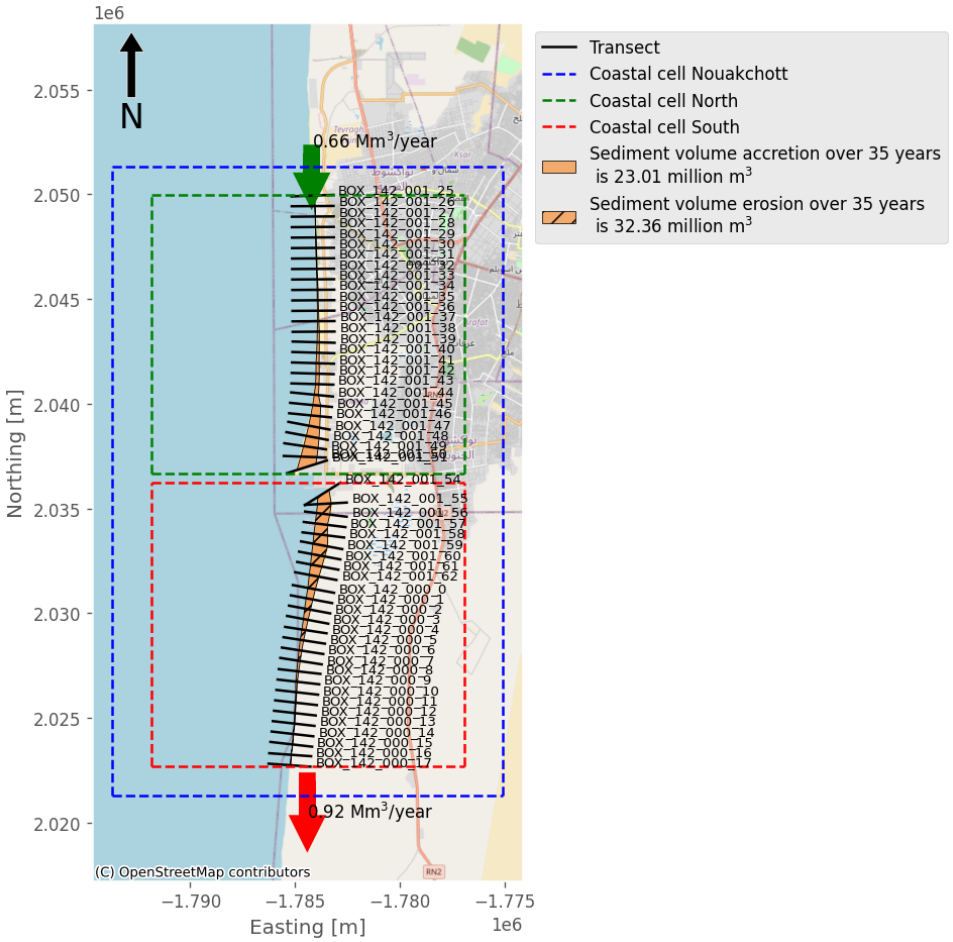


Figure 5.3: The combined coastal cells of Nouakchott North and South to provide a sediment balance for the original Nouakchott case.

Additionally, satellite images can be used to validate whether or not sediment bypassing occurs. The figures 5.4a and 5.4b show the breakwaters in Nouakchott before and after 2015. There might have been various factors behind the decision to extend the breakwater. Nonetheless, one possible reason could be to avoid the ongoing sediment bypassing, thus minimizing the sand flow into the harbour's entrance channel.

(a) (b)

Figure 5.4: Two satellite photos depict the breakwater of Nouakchott's port. The left image is from March 2014, while the right is from December 2015. Source: Google (2024)

As a result, sediment transport at Nouakchott's breakwater cannot be considered zero. However, due to a significant main channel entering the harbour, the sediment is directed towards this channel. Therefore, not much sediment will reach the other side. According to the study conducted by Elmoustapha et

al. (2007), sediment bypassing is predicted to occur from 2015 to 2025. However, Figure 5.4 indicate sediment bypassing occurred earlier than anticipated.

In addition, the sediment volume over the past 35 years assumes that the active height has remained constant. However, this does not have to be the case. The active height can be smaller with erosion, leading to a smaller erosion volume in the Nouakchott South coastal cell. This assumption of the active height and the sand falling into the entrance channel supports the validity of the Nouakchott littoral barrier assumption.

Analysing the breakwater at Aveiro presents a slightly more intricate challenge because only the northern side of the Aveiro case has been evaluated. Based on satellite images, the breakwater in Aveiro remained unchanged from 1984 to 2021. According to Pinto et al. (2022), there is a bypassing of sediment at this breakwater. Part of the sediment will fall into the entrance channel, but a part reaches the other southern side. However, the amount is so small that it can be ignored. Hence, the assumption that no sediment bypassing is held in the Aveiro scenario.

#### Delfland

The Delfland coast has two breakwaters, one near Rotterdam and the other at Scheveningen. The breakwater at Rotterdam is considerably more prominent than the one at Scheveningen. According to a study by Luijendijk et al. (2017), the Longshore Sediment Transport is completely blocked due to the massive breakwater at Hoek van Holland (called the Noorderdam). In contrast, sediment bypassing is present at the breakwater in Scheveningen, as mentioned in the same study by Luijendijk et al. (2017). Figure 5.5 shows satellite images of the breakwater at Scheveningen, revealing that sand is collected at the harbour's entrance as indicated by the red arrow. Whether this material originated from Scheveningen's southern or northern side is still being determined.

Due to sediment bypassing at Scheveningen, the coastal cell could be split into two scenarios. In the first scenario, the Delfland coast is subject to no sediment transport at Hoek Van Holland and complete sediment transport at Scheveningen. The second scenario involves two boundary conditions, with the Scheveningen boundary allowing some sediment transport, although the precise quantity cannot be determined.

Figure 5.5: The breakwaters of Scheveningen's port. The red arrow shows the buildup of sediment. This means that there is a bypass. Source: Google (2024)

### 5.2.3 Historical prediction

As outlined in Section 3.5, the shoreline predictions rely on the most recent shoreline orientation of the coastal cell to calculate sediment transport using the S-$\varphi$ relation. Typically, historical data spanning the past 38 years establishes the S-$\varphi$ relationship. However, would the obtained SHORECAST model be able to predict the same historical shoreline positions when starting at different moments in history? These starting points are 1985, 1990, 2000 and 2010 to predict the shoreline position of 2020.

### Nouakchott

Figure 5.6 shows the shoreline prediction from 1985 (A), 1990 (B), 2000 (C) and 2010 (D). A closer look at the image shows that the period of the last years is the most accurate with actual shoreline position compared to the other graphs. Therefore, it can be stated that the SHORECAST model may be suitable for predicting shoreline changes in the upcoming decade starting from 2020 using the Satellite-derived Shoreline data.

However, the model will likely underperform beyond that timeframe based on the observed differences between the predicted and actual shoreline positions of the other shoreline prediction in Figure 5.6. The colour gradient from white to blue indicates the historical shoreline position derived from Satellite-derived Shoreline, while green to yellow represents the predicted shoreline position. The red line denotes the actual coastline position in 2020 by SDS.

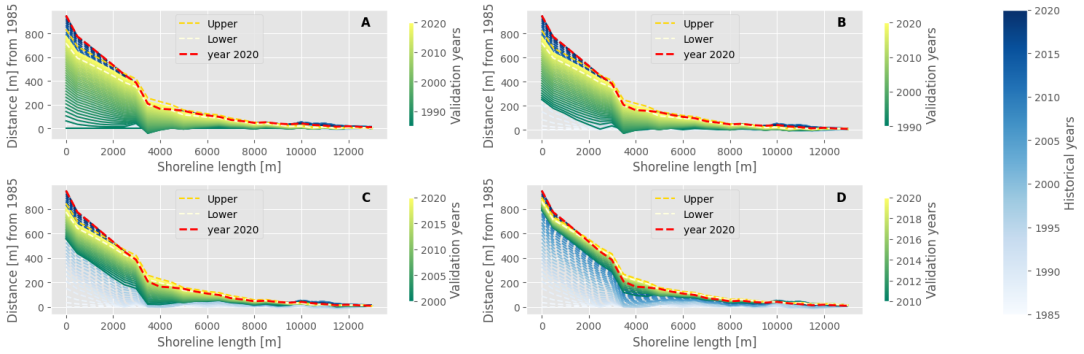


Figure 5.6: Four shoreline predictions for the Nouakchott North case compared to the historical shoreline location. The white-to-blue spectrum represents the historical shoreline, while the green-to-yellow spectrum shows the predicted shoreline. The red dashed line indicates the most recent historical shoreline position. The upper and lower bounds refer to the upper and lower limits of the 95% confidence interval. Shoreline positions are calculated with the 1985 shoreline position.

Upon sediment accumulation on the north side of the Nouakchott harbour, visible erosion was observed on the south side. In 2012, a small barrier was built below the harbour to fight the erosion. The shoreline between the barrier and the harbour stabilised while erosion accelerated south of the revetment. For the SHORECAST model validation the year 2010 is replaced for 2013, with 2013 being chosen due to the clear presence of the built revetment in the SDS dataset. Figure 5.7 illustrates the model's predictions compared to the actual conditions for these years.

An in-depth analysis reveals that the model SHORECAST struggles to predict erosion levels accurately. It tends to underestimate erosion compared to the actual erosion observed. However, the prediction from 2013 to 2020 indicates increased erosion just behind the revetment. The shoreline predictions from 1985, 1990, and 2000 reveal significant erosion near the harbour (at $X$ is 13 kilometres). Several factors influenced this anticipated erosion. One reason is the model's limitation due to grid dependency, particularly with the transects represented by black lines. The transect near the harbour differs significantly from the previous transects, leading to inaccuracies in computation due to the staggered grid. Another contributing factor is the breakwater located north of the harbour, which blocks a significant portion of the waves, causing a shoreline orientation equilibrium that deviates from the surrounding area. This will be verified in Section 5.3.3.

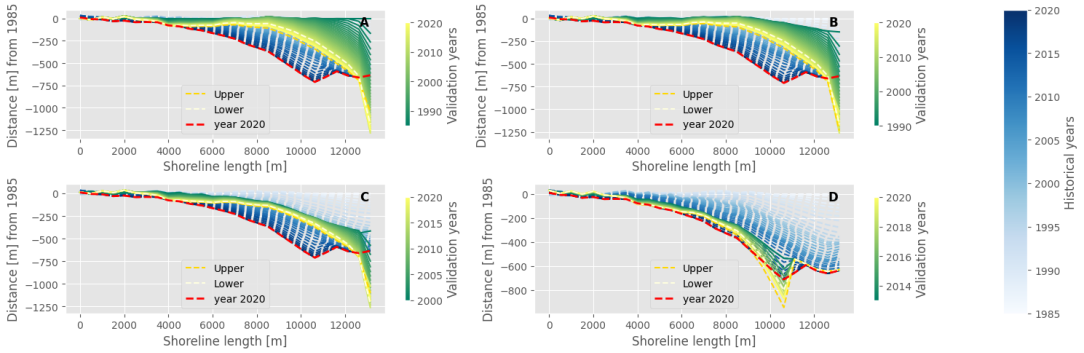


Figure 5.7: Four shoreline predictions for the Nouakchott South case compared to the historical shoreline location. The white-to-blue spectrum represents the historical shoreline, while the green-to-yellow spectrum shows the predicted shoreline. The red dashed line indicates the most recent historical shoreline position. The upper and lower bounds refer to the upper and lower limits of the 95% confidence interval. Shoreline positions are calculated with the 1985 shoreline position.

### Aveiro

The Aveiro shoreline experiences extensive shoreline migration in both directions, as mentioned in Section 4.3. Over the years, periods of erosion and accretion have made it challenging to predict the shoreline due to these significant fluctuations. Nevertheless, the historical data's concluded S-$\varphi$ relations exhibit a low RMSE, suggesting the potential for generating high-quality prediction. Similar to the Nouakchott case, four shoreline predictions of the SHORECAST model were made and compared with the current shoreline position for 1985, 1990, 2000, and 2010. The results, as shown in Figure 5.8, indicate that the predictions in Figure 5.8C and D are the most in line with the reality.

All predictions show a good sediment accumulation between $X$ is 0 and 2000 metres near the Ria de Aveiro breakwater. It is worth noting that sometimes, the upper bound predicts more accretion than in reality. Additionally, predicting the shoreline position between 2 and 11 kilometres is particularly challenging. This difficulty may be attributed to sand wave migrations along the coast observed by satellite images, which significantly impact the model based on shoreline orientation. Nevertheless, predictions from the previous decade align well with the actual shoreline, suggesting that the SHORECAST model can accurately predict the shoreline for the next decade.

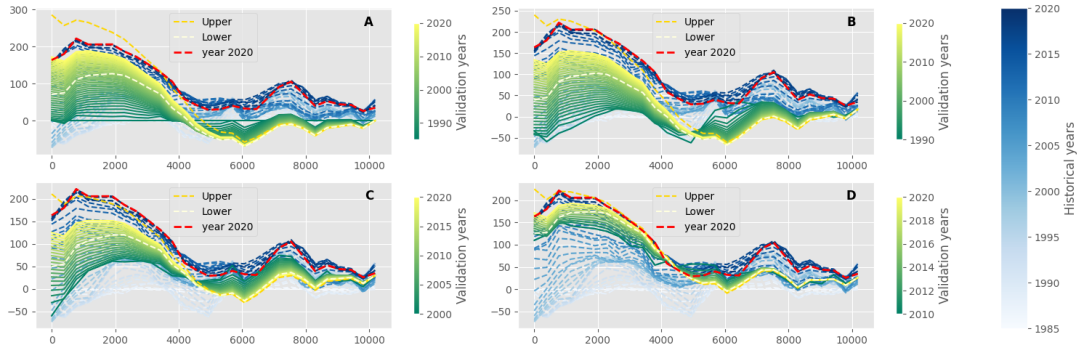


Figure 5.8: Four shoreline predictions for the Aveiro case compared to the historical shoreline location. The white-to-blue spectrum represents the historical shoreline, while the green-to-yellow spectrum shows the predicted shoreline. The red dashed line indicates the most recent historical shoreline position. The upper and lower bounds refer to the upper and lower limits of the 95% confidence interval. Shoreline positions are calculated with the 1985 shoreline position.

### Delfland

Validating the S-$\varphi$ relationship derived for the Delfland case in Section 4.4 is difficult due to the artificial measures along the Delfland shore (Hoekstra et al., 2012). The largest measure was the mega-nourishment

in 2011, the Sand Engine. The 2013 SDS data clearly shows this nourishment. Therefore, the most important validation of the SHORECAST model is between 2013 and 2021. Figure 5.9D displays the entire result along the Delfland shore, whereas Figure 5.10 displays the outcome around the Sand Engine. Nonetheless, shoreline predictions are also made from 1985, 1990 and 2000 and shown in Figure 5.9 A to C.

The view for the shoreline prediction between 2013 and 2021 is that the shoreline position is consistent with reality. In addition, the placement of the Sand Engine has been well distributed throughout the years, which also happened with the actual shoreline position. However, at two locations, the shoreline does not match the truth. These locations are in Hoek van Holland and near the Sand Engine. The predicted shoreline does not align at Hoek van Holland because of the enormous littoral barrier that limits the domain's wave direction from the southwest. As a result, the shoreline orientation equilibrium could differ from that of the obtained equilibrium for the entire coastal area (Section 5.3.3). Furthermore, the upper and lower bounds also have difficulty predicting the Delfland boundaries. The upper and lower bounds are the 95% confidence interval.

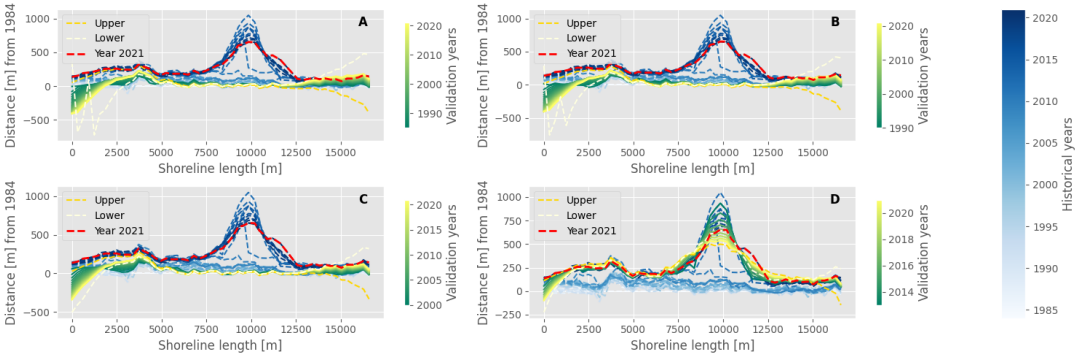


Figure 5.9: Four shoreline predictions for the Delfland case compared to the historical shoreline location. The white-to-blue spectrum represents the historical shoreline, while the green-to-yellow spectrum shows the predicted shoreline. The red dashed line indicates the most recent historical shoreline position. The upper and lower bounds refer to the upper and lower limits of the 95% confidence interval. Shoreline positions are calculated with the 1985 shoreline position.

Figure 5.10 illustrates a detailed view of the Sand Engine from 2013 to 2021. The predicted shoreline erosion is faster compared to the current state. Additionally, sediment accretion of the Sand Engine is mainly concentrated on the northern side of the mega-nourishment, indicated by the higher red line in contrast to the yellow line. Conversely, the yellow line is more seawards on the southern side than the red line, suggesting a higher sediment transport towards the south. This difference is due to the shoreline orientation equilibrium and the difference in active height on the north and south sides of the Sand Engine in reality. Despite this difference, the variance between the predicted and actual observations is minor. Therefore, the S-$\varphi$ obtained in Section 4.4 can be employed for predicting the next two decades.

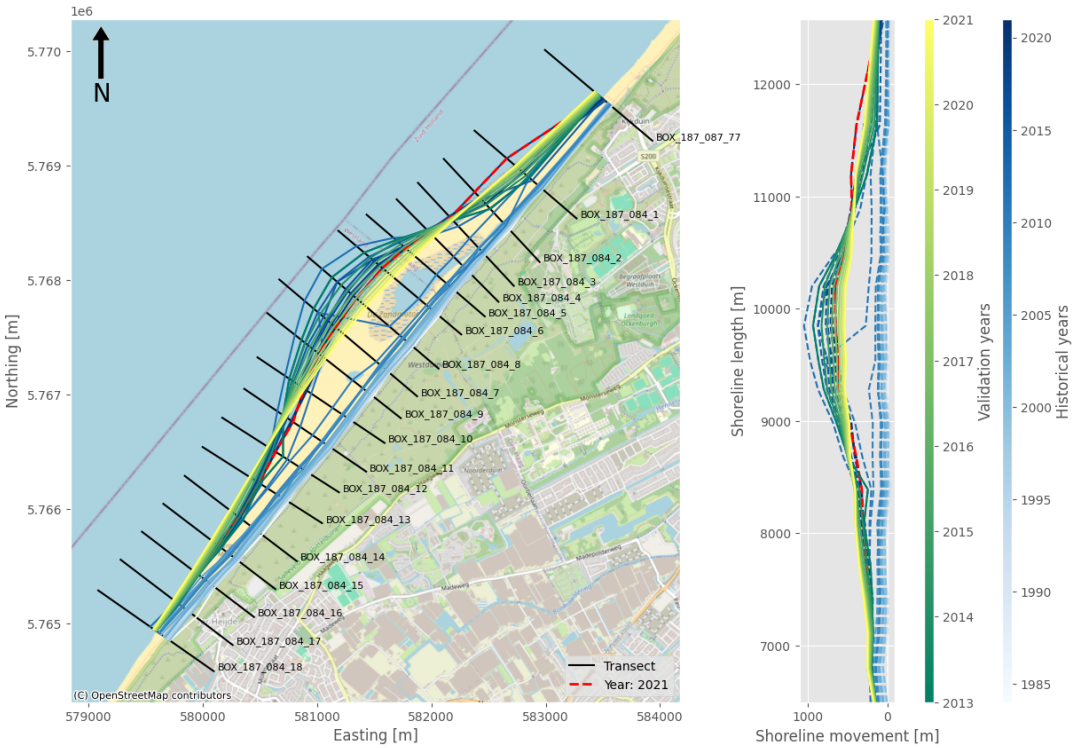


Figure 5.10: The historical shoreline position (white to blue) where the red line is the last surveyed shoreline position around the Sand Engine. The green to yellow colour is the predicted shoreline starting in 2013 to 2021.

## 5.3 Limitations

The developed model described in Chapter 3 is developed on various assumptions. These assumptions made it easier to do the calculations such as the volume gradient and the LST. The used assumptions are presented in Table 5.2, which provides information on the assumption's name, its corresponding calculation, and the methodology section where it is elaborated upon.

Table 5.2: Presented all the used assumptions for deriving the method as described in Section 3.

| Name assumption | Brief description | Use for | Explained Section |
|---|---|---|---|
| Shoreline movement | Significant Erosion / Accretion | LST | 3.2.4 |
| Single line theory | Coast remains shape<br>Horizontal movement | $\Delta V$ | 3.3.6 |
| Active height | Constant depth | $\Delta V$ | 3.3.6 |
| Littoral drift barriers | No bypassing of sediment | LST | 3.3.7 |

### 5.3.1 Shoreline movement

The SHORECAST model is a tool used to predict the shoreline positions based on historical data. It uses a correlation between shoreline orientation and sediment transport to estimate the future Longshore Sediment Transport and shoreline position. However, determining sediment transport gradients over time becomes challenging for unchanged shorelines, such as a cliff or dyke. Therefore, it is crucial that any input data consistently reflect changes in the shoreline position. From a broader viewpoint, any shoreline position data that fluctuates along the same transect and is measured for many years can be used as input in the SHORECAST model.

The cases in Chapter 4 were selected based on specific criteria outlined in Section 3.2.2. Two crucial criteria were an R-squared value set at 0.75 and a mean accretion/erosion rate over 38 years set at five in

absolute value. However, the model shows promising results with transects containing a lower R-squared value, as shown in Table 5.3. As a result, a mean R-squared value should be used, which should be 0.5 or higher. In this way, the SHORECAST model can deliver reasonable results. The R-squared value should be reasonable because a value that is too low would result in more shoreline positions being labelled as outliers. In addition, excessive fluctuation in the shoreline also results in significant fluctuations in the Longshore Sediment Transport

Table 5.3: The $R^2$ value for each coastal cell is calculated, including the average, maximum, and minimum $R^2$ values.

| Coastal cell | R2 mean | R2 max | R2 min |
|---|---|---|---|
| **Nouakchott North** | 0,725 | 0,989 | -0,045 |
| **Nouakchott South** | 0,643 | 0,981 | -0,012 |
| **Aveiro** | 0,525 | 0,939 | 0,035 |
| **Delfland** | 0,681 | 0,889 | 0,085 |

The second criterion is the absolute average rate of change, set at five meters per year. Value five says that at least extreme erosion or accretion is necessary to derive the Longshore Sediment Transport as shown in Table 3.1 (Luijendijk et al., 2018). This table states that the lowest obtained erosion and accretion rate is between |0.5| and |1| metres per year. It is recommended to have a change rate greater than the resolution error to ensure an accurate Longshore Sediment Transport. The mean of all change rates in the coastal cell should fall within the severe erosion and severe accretion classification (|3| to |1| m/yr). This way, a shoreline movement will be detected, and the shoreline will migrate in one direction over the years.

In addition, only some of the coastal cells' transect met the five metre per year requirement. Therefore, it can be concluded that the SHORECAST model can effectively estimate the Longshore Sediment Transport and shoreline prediction with lower erosion and accretion values than five metres per year.

Looking at the data source itself, whereby now SDS data is used, it would also be possible to use different data sources as long the shoreline is migrating. For example, data from a field measurement. As long as the specific transects where the measurements were taken are identified, the methodology outlined in Section 3 can be employed to determine littoral transport and shoreline prediction. However, establishing a boundary condition is necessary to calculate littoral transport, such as having zero sediment transport on one side of the coastal cell.

### 5.3.2 Single-line theory and Active height

One of the key hypotheses for obtaining Longshore Sediment Transport, as detailed in Section 3.3.6, is the One-line theory, often known as the Single-line theory. This hypothesis suggests that the shape of the shoreline remains constant over time while migrating horizontally (Larson et al., 1987). The coastal profile should always be in equilibrium, as indicated by the equilibrium profile from Bruun (1962). However, in reality, the coastal profile changes over time. The coastline profile changes due to waves from different directions, varying strengths and fluctuations in water levels (Bosboom & Stive, 2021). These threads ensure that the shoreline is continually reshaping. Regardless, these fluctuations lead to a stable dynamic equilibrium profile when looking at the shoreline for a longer period (Bosboom & Stive, 2021). Therefore, this assumption can be used to derive the LST because the time span is large.

Another essential hypothesis for computing the LST is the Depth of Closure (or Closure Depth) $d_c$ (Figure 3.15) (Athanasiou et al., 2019; Larson et al., 1987; Bosboom & Stive, 2021). Outlined in Section 3.3.6, the closure depth is a number that applies to the entire coastal cell and is mixed with the mean spring tidal range. These two values combined are the active height. The mean spring tidal range is included to ensure that the whole beach profile, high tide to mean sea level is used. It becomes increasingly significant when the mean spring tidal range surpasses the depth of closure.

Due to the active height assumption, the developed model can be considered two-dimensional. However, various closure depths can be applied at different transects. Including bathymetry data in the model enhances the accuracy of the shoreline evolution representation. Unfortunately, bathymetry data may not always be readily available or precise enough (Wölfl et al., 2019). Consequently, a single fixed value is employed as the active height, leading to a slight difference with actual conditions.

It is crucial to highlight that for the assumptions discussed in this section to be applicable, the shoreline must be uniform. A shoreline is considered homogeneous when its characteristics, such as slope, sediment composition, and vegetation cover, remain consistent throughout a coastal cell. The three coastal cells presented in Chapter 4, which focus on model results, all have a homogeneous shoreline.

### 5.3.3 Littoral drift barrier

Apart from blocking the sediment transport (Section 5.2.2), these breakwaters also reduce wave force along a short part of the shoreline. When deriving the S-$\varphi$ relation, all Longshore Sediment Transport are considered along the shoreline. However, there are areas where the shoreline is not fully exposed to all the waves. In areas with less exposure, the shaded side of the drift barrier may produce a unique S-$\varphi$ correlation, leading to varied shoreline predictions compared to the entire exposed shoreline.

Looking at the significant annual wave direction, the Nouakchott South and Delfland shorelines have an area where the shoreline is less exposed to waves than the rest of the coast due to the littoral barrier. A revetment was built along the shoreline of Nouakchott south in 2012, offering a glimpse of what is to come. Due to this revetment, the shoreline stabilised between the harbour and the revetment. Since the revetment was small, it would suggest that there is another shoreline orientation equilibrium. Figure 5.11 displays the S-$\varphi$ relationship of the transects between the harbour and the revetment, resulting in an equilibrium angle of 295.50 degrees, which is smaller than the equilibrium obtained from the entire coastal cell (299.49 degrees). This equilibrium is based on the years before the revetment is constructed otherwise the S-$\varphi$ would be influenced by the stable shoreline. The difference between the two equilibria is only four degrees and with the large confidence interval, it could be argued that the effect of the littoral barrier on the shoreline is insignificant based on the numerical calculations.

Figure 5.12 displays the predicted shoreline from 2013 to 2020, showing minimal changes. It seems that the orientation of the shoreline is stable across the coastal area, particularly between the harbour and the revetment. Although the calculations do not indicate a significant shoreline equilibrium for these five transects, the SDS data suggests the presence of another equilibrium, as otherwise, the revetment would not effectively stabilise the shoreline between the harbour and the revetment. Therefore, it can be concluded that the littoral barrier impacts the shoreline immediately behind it.

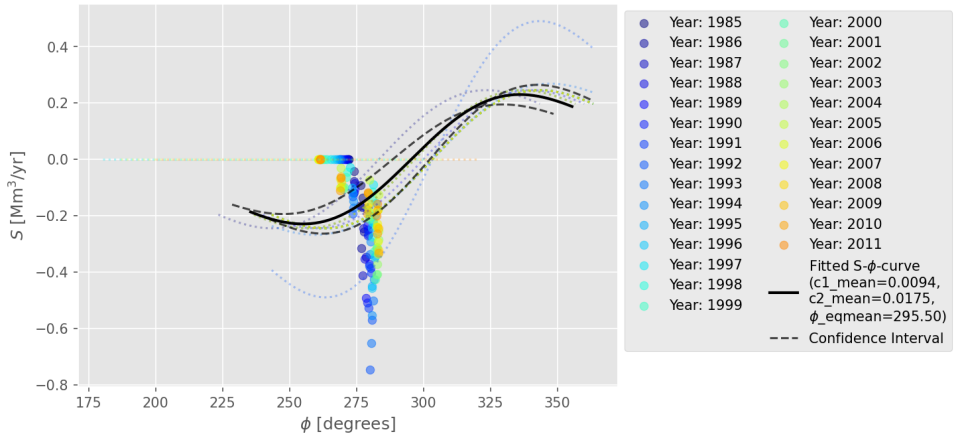


Figure 5.11: The S-$\varphi$ relation from the transect in the leeward side of Nouakchott's harbour.

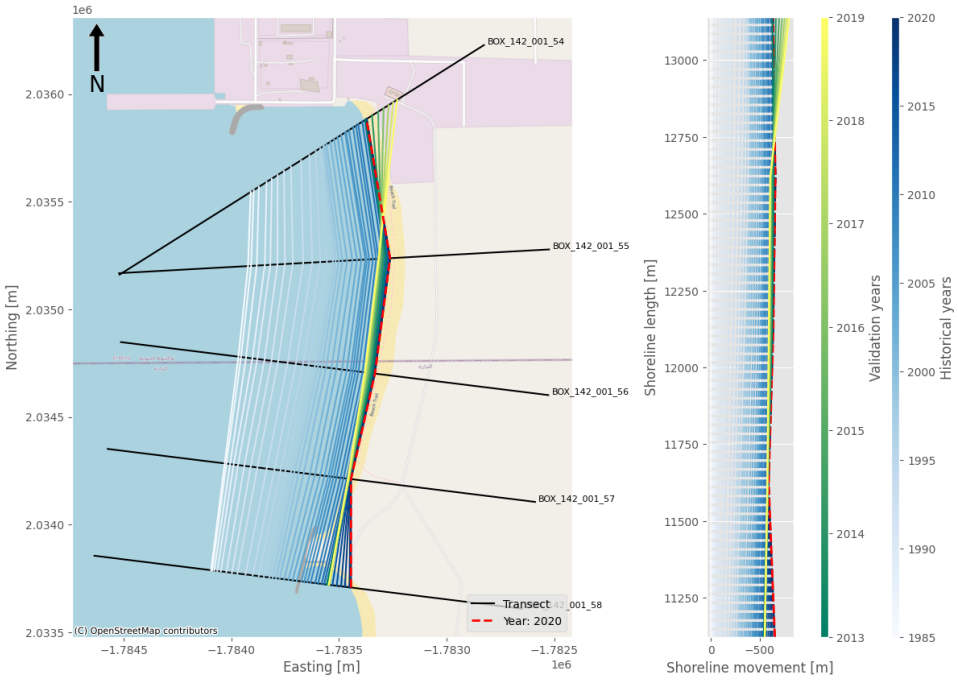


Figure 5.12: The historical shoreline position (white to blue) where the red line is the last surveyed shoreline position. The green to yellow colour is the predicted shoreline starting in 2013 to 2021.

In the coastal cell of Delfland, the breakwater located at Hoek van Holland serves the purpose of reducing the impact of waves coming from the southwest, as stated by (Wijnberg, 2002). The revised S-$\varphi$ relation for this specific location is illustrated in Figure 5.13. The orientation equilibrium of the nine transects adjacent to the Hoek van Holland breakwater is 314.07 degrees. This value is considerably higher than the equilibrium orientation for the entire coastal cell, which is 304.18 degrees (Figure 4.25). The new equilibrium aligns more closely with the current shoreline position behind the breakwater shown in Figure 5.14 than Figure 5.9. However, the 95% confidence interval also has a significant spread. Consequently, the breakwater at Hoek van Holland significantly influences the shoreline's evolution, although the impact may vary in different years.

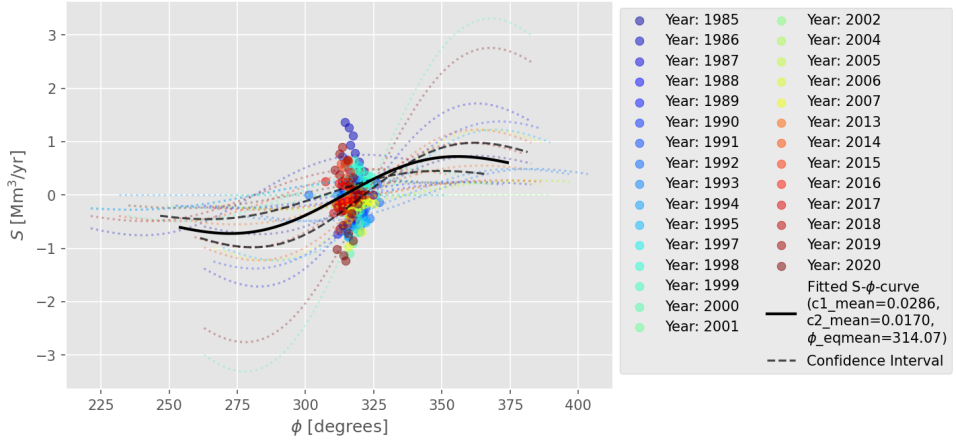


Figure 5.13: The S-$\varphi$ relation from the transect in the leeward side of the breakwater at Hoek van Holland. The dashed black line is the 95 % confidence interval.

All in all, the effects of diffraction due to the barriers give another shoreline equilibrium in the shadow region. However, the current model, as presented in Chapter 3, does not consider these effects because the relation between sediment transport and shoreline orientation is derived, whereby this effect is limited with the whole dataset.

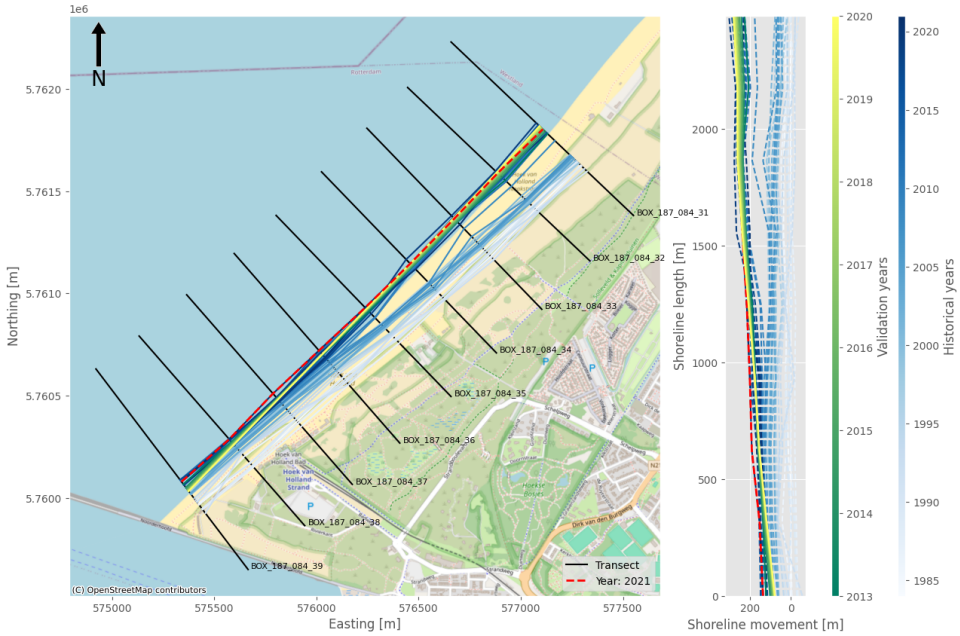


Figure 5.14: The historical shoreline position (white to blue) where the red line is the last surveyed shoreline position. The green to yellow colour is the predicted shoreline starting in 2013 to 2021.

#### Detection barriers

The cases presented in Chapter 4 share a common feature. They all used the same boundary condition, specifically a littoral barrier at one end of their coastal cell. Currently the user chooses these littoral barriers, which are assumed to be zero. An improvement could be achieved by implementing an algorithm that automatically can detect these barriers or boundary conditions from within the coastal cell. This method would resemble the one used for nourishment detection, as explained in Sections 3.3.1 and 5.2.1.

### 5.3.4 Coastal cell and Grid

In Section 1.1, the definition of coastal cells was introduced. The coastal cells serve as a framework for understanding coastal morphodynamics influenced by natural processes, as illustrated in Figure 1.2. While various processes are at play within these coastal cells, this study focuses on four specific processes: longshore transport, nourishment, dune erosion, and cross-shore transport. However, these last two processes were assumed to be steady due to the single-line hypothesis and the active height, detailed in 5.3.2 to be able to derive the Longshore Sediment Transport. Consequently, the model restricts natural fluctuations. The coastal cells that were presented in Chapter 4 did also not contain any sources or sinks. These could be added to the model. Introducing sinks is easier than sources, requiring certain assumptions and offering opportunities to enhance the model's generality.

Apart from the elements of the coastal cell, the coastal cell is also presented as a grid over the shoreline. The existing Satellite-derived Shoreline data for generating the Longshore Sediment Transport and shoreline prediction relies on transects spaced 500 metres apart (Luijendijk et al., 2018). These transects were used as the current grid because it made the model faster, and these transects were located at fixed locations in the 37 years. Reducing the distance between the transects, as the current method treats them as a grid, could enhance the accuracy of shoreline positioning. The closer the transects are placed, the more precise the prediction will be. Alternatively, a customizable grid allowing users to choose their grid size could also improve accuracy. However, this would lead to a slower model because the time step must also be smaller according to the Courant equation, Equation 3.21.

# 6

# Conclusion

New techniques have emerged in recent years for determining the positions of shorelines, such as Satellite-derived Shoreline (SDS), that have enabled the determination of the historical shoreline position worldwide. The Shoreline Monitor by Luijendijk et al. (2018) provided a comprehensive coastal observation dataset for the past 36 years. As a result, the SDS method has expanded global shoreline data, allowing for analysis in previously unmonitored locations (Vitousek, Buscombe, et al., 2023). This provides an opportunity to use SDS data to calculate Longshore Sediment Transport (LST), anticipate shoreline directions, and predict changes in the shoreline position. This led to the main research question, as illustrated below:

---

***"How can various shoreline predictions be established using Satellite-derived Shorelines to estimate alongshore sediment transport and orientation?"***

---

A method called SHORECAST (Satellite-derived Historical and future Orientation-based Relation for Estimating Coastline Adjustments and Sediment Transport) was developed and implemented in three different locations worldwide to address the research question. The model was developed on the Nouakchott case because it provided two distinct cases under optimal conditions. Using the technique of Do et al. (2019) with the one-line hypothesis, it is possible to estimate the Longshore Sediment Transport gradient. Using Nouakchott's breakwater as a boundary in the coastal cell where sediment transport is zero and a stable shoreline on the other side, an accretion volume of 23.01 million $m^3$ and an erosion volume of 32.36 million $m^3$ were calculated based on the shoreline change between the first and last year multiplied by the active height over 35 years. The SHORECAST model has been verified by applying to two additional scenarios, Aveiro and the Delfland coast, leading to a volume increase of 17.83 million $m^3$ for Aveiro over 35 years.

In Section 5.2.2, it was observed that not all boundaries satisfied the assumption of no sediment bypassing, which was used to calculate the Longshore Sediment Transport. Only the breakwater at Hoek van Holland in the Delfland Coastal cell confirmed the no bypassing of sediment. The cases presented considered only zero sediment transport and stable shoreline boundary conditions for estimating the Longshore Sediment Transport. Other boundary conditions are discussed in Section 3.3.7, including when the Longshore Sediment Transport is known at one of the coastal cell boundaries. However, this was impossible with current cases presented in Chapter 4 due to the unknown LST value at the sides.

As mentioned earlier, the Delfland coastal cell contains significant human intervention. By applying the two zero boundary conditions, sediment volume could be estimated between 1984 and 2021, resulting

in an accretion of 45.55 million $m^3$, slightly lower than the total beach nourishment in the same period (46.51 million $m^3$). The difference could be attributed to the assumption of active height and the zero-boundary condition at the Scheveningen breakwater. Additionally, the nourishment detection algorithm successfully identified the ten largest nourishments to have a more accurate S-$\varphi$ relation, because the nourishment years were removed from the S-$\varphi$ relation as they involved artificial sand addition rather than natural processes.

Altogether, it can be concluded that the SHORECAST model can estimate the past Longshore Sediment Transport by employing a zero boundary condition. It is evident that the sub-queries "*How can a one-dimensional shoreline shift between two transects be converted into a sediment volume gradient?*" and "*Which boundary conditions can be applied to estimate Longshore Sediment Transport from a sediment volume gradient across transects in a selected area?*" have been addressed sufficiently.

The SHORECAST model uses historical Longshore Sediment Transport data and shoreline orientation correlation to make accurate shoreline predictions. This correlation, known as the S-$\varphi$ relation, is the basis for the groundbreaking shoreline prediction method, eliminating the need for bathymetry and wave data. The S-$\varphi$ relationship is similar to the one in the numerical model Unibest-CL+. By iterating the three variables, the optimal annual correlation can be obtained. These correlations are averaged to establish an S-$\varphi$ relation, which can be used for shoreline prediction by taking the latest shoreline orientation as input. In addition, the correlation also offers insights into the magnitude of LST and whether a specific shoreline location can be considered stable.

As described in Section 5.2.3, the SHORECAST model can sufficiently predict for at least ten years by confirming the anticipated last decade with the actual coastline location of the previous decade. The model performs better regarding accretion predictions when comparing Nouakchott Noth and South validation. In addition, the model can handle both accretion and erosion within the same coastal cell, as demonstrated in the Delfland coastal cell. The model can anticipate more than a decade into the future. Still, it will get more accurate on the erosion side using another equilibrium orientation at the slate side of a breakwater. Overall, this demonstrates that predictions can be made based on the relationship between orientation and sediment transport, thus addressing the third sub-question "*How can the Satellite-Derived Shoreline historical Longshore Sediment Transport data and shoreline orientation be used to make future shoreline predictions?*".

In conclusion, the SHORECAST model, as described and developed in Chapter 3 has shown how to deal with easy (Nouakchott) and complex cases (Delfland), which is heavily influenced by human activities. This indicates that SHORECAST can accurately analyse the Longshore Sediment Transport and make predictions. Consequently, it can be concluded that the designed generic model can be incorporated into the Shoreline Monitor to estimate the sediment volume gradient at an uniform coast in a selected coastal cell. In conjunction with a boundary condition, shoreline prediction can be made. Altogether, it can be asserted that the final sub-research question, referred to as "*How can the proposed method be adapted to be applicable globally?*", has been successfully addressed. As a result, the main research question has also been answered.

As an additional step, it can also predict the effects of anthropogenic interventions to reduce erosion. For instance, a nourishment or a Groyne along the coast of Nouakchott as illustrated in Appendix C. Moreover, the SHORECAST model can be divided into three distinct components only to examine the Longshore Sediment Transport or enable a straightforward and fast prediction of shoreline alterations. Likewise, the model can incorporate data which is not obtained from satellites, such as JARKUSRaai data (de Boer & den Heijer, 2016). Consequently, these modules offer valuable perspectives into unmonitored regions across the globe or can be employed with local historical survey data to promptly and effortlessly predict fluctuations in the shoreline position.

# 7

# Future directions

This chapter offers an overview of recommendations for future research directions, primarily based on the limitations and potential outcomes discussed in Chapter 5 and the conclusion of Chapter 6. The list below presents six concrete and feasible recommendations, prioritized from top to bottom. The first four recommendations present excellent opportunities to enhance the model's generality for other coastal areas. The remaining two recommendations serve as valuable studies to complement the developed method and provide additional insights.

1. The developed SHORECAST model operates with different boundary conditions, such as littoral drift barriers, under the assumption of zero sediment transport. Section 5.2.3 discussed that this assumption may only sometimes be valid. To improve the accuracy of the prediction module, a certain amount or percentage of bypassing should be included to prevent shoreline accretion from growing indefinitely. Therefore, the breakwater length can be essential in knowing when sediment bypassing will occur. Furthermore, formulae from the Unibest-CL+ model can also help estimate this amount. In addition to the length, the type of barrier should also be considered. The impact of poles on increasing accretion is a factor that should be considered when making predictions.

2. Given the significant role that littoral barriers play in deriving the Longshore Sediment Transport, it presents a favourable prospect to develop an algorithm similar to the nourishment algorithm for identifying these structures inside a coastal cell. In addition to detection, it would be beneficial to incorporate this algorithm as an add-on in the existing model of this study and assess whether the barrier allows sediment bypassing.

3. Another factor that has yet to be considered is the shadow effect of coastal barriers. This phenomenon has been observed in locations such as Nouakchott South and Delfland, as documented in Section 5.3.3, where a part of the shoreline is impacted by these barriers, causing wave diffraction. Consequently, a different shoreline orientation will be reflected in the S-$\varphi$ relation. The extent of the shadow shoreline remains unclear, presenting an exciting opportunity for further exploration and integration into the methodology of this research.

4. The presented model can currently only be applied in locations where it can be assumed that sediment transport is zero or where the alongshore sediment transport is known at the boundaries of the coastal cell. As discussed in Section 4.1, there are also areas around the world that are experiencing rapid erosion, but the boundary conditions are unknown. To enhance the abilities of the existing tool to provide alongshore sediment transport values and shoreline predictions, an alternative method needs to be added to make shoreline predictions for shorelines in areas with no barriers. An example of a potential study location for conducting such research is along the coast of Texas in the United States.

5. During the introduction (Section 1.1), the coastal cells were introduced and exposed to several factors that influenced them. For this particular study, the components employed were longshore transport and nourishment. Cross-shore transport and dune erosion were disregarded based on the one-line theory. The remaining elements were not taken into consideration. Additional elements that can be included in the existing generic model are sinks and sources, such as a canyon where sediment is lost or sediment output from a river within the coastal cell. This inclusion provides more opportunities for the application of the developed method.
6. Existing methods use sediment formulas to estimate the Longshore Sediment Transport in coastal cells. A common feature among all these different formulas is that grain size is one of the input parameters. Since this model provides Longshore Sediment Transport data, the equation can be modified so that the LST becomes an input parameter and the grain size an output. In addition, determining the beach slope might also be feasible by using the grain size. This could benefit the horizontal shoreline migration within the developed approach.

# Bibliography

Aarninkhof, S. G., Turner, I. L., Dronkers, T. D., Caljouw, M., & Nipius, L. (2003, 10). A video-based technique for mapping intertidal beach bathymetry. *Coastal Engineering*, *49*, 275-289. doi: 10.1016/S0378-3839(03)00064-4

Adebisi, N., Balogun, A.-L., Mahdianpari, M., & Min, T. H. (2021, 9). Assessing the impacts of rising sea level on coastal morpho-dynamics with automated high-frequency shoreline mapping using multi-sensor optical satellites. *Remote Sensing*, *13*. doi: 10.3390/rs13183587

Almeida, L. P., Efraim de Oliveira, I., Lyra, R., Scaranto Dazzi, R. L., Martins, V. G., & Henrique da Fontoura Klein, A. (2021). Coastal analyst system from space imagery engine (cassie): Shoreline management module. *Environmental Modelling and Software*, *140*, 105033. Retrieved from `https://www.sciencedirect.com/science/article/pii/S1364815221000761` doi: https://doi.org/10.1016/j.envsoft.2021.105033

Anthony, E. J., & Aagaard, T. (2020, 11). The lower shoreface: Morphodynamics and sediment connectivity with the upper shoreface and beach. *Earth-Science Reviews*, *210*, 103334. Retrieved from `https://www.sciencedirect.com/science/article/pii/S0012825220303809` doi: https://doi.org/10.1016/j.earscirev.2020.103334

Antolínez, J. A. A., Méndez, F. J., Anderson, D., Ruggiero, P., & Kaminsky, G. M. (2019, jun). Predicting climate-driven coastlines with a simple and efficient multiscale model. *Journal of Geophysical Research: Earth Surface*, *124*(6), 1596–1624. Retrieved from `http://dx.doi.org/10.1029/2018JF004790` doi: 10.1029/2018jf004790

Arriaga, J., Rutten, J., Ribas, F., Falqués, A., & Ruessink, G. (2017, 3). Modeling the long-term diffusion and feeding capability of a mega-nourishment. *Coastal Engineering*, *121*, 1-13. doi: 10.1016/j.coastaleng.2016.11.011

Ashton, A. D., & Murray, A. B. (2006a, 12). High-angle wave instability and emergent shoreline shapes: 2. wave climate analysis and comparisons to nature. *Journal of Geophysical Research: Earth Surface*, *111*(F4). Retrieved from `https://agupubs.onlinelibrary.wiley.com/doi/abs/10.1029/2005JF000423` doi: 10.1029/2005JF000423

Ashton, A. D., & Murray, A. B. (2006b, dec). High-angle wave instability and emergent shoreline shapes: 1. modeling of sand waves, flying spits, and capes. *Journal of Geophysical Research: Earth Surface*, *111*(F4). Retrieved from `http://dx.doi.org/10.1029/2005JF000422` doi: 10.1029/2005jf000422

Ashton, A. D., Nienhuis, J., & Ells, K. (2016). On a neck, on a spit: controls on the shape of free spits. *Earth Surface Dynamics*, *4*(1), 193–210. Retrieved from `https://esurf.copernicus.org/articles/4/193/2016/` doi: 10.5194/esurf-4-193-2016

Athanasiou, P., Van Dongeren, A., Giardino, A., Vousdoukas, M., Gaytan-Aguilar, S., & Ranasinghe, R. (2019, 10). Global distribution of nearshore slopes with implications for coastal retreat. *Earth System Science Data*, *11*, 1515-1529. doi: 10.5194/essd-11-1515-2019

Barkwith, A., Hurst, M. D., Thomas, C. W., Ellis, M. A., Limber, P. L., & Murray, A. B. (2014). Coastal vulnerability of a pinned, soft-cliff coastline, ii: assessing the influence of sea walls on future morphology. *Earth Surface Dynamics*, *2*(1), 233–242. doi: 10.5194/esurf-2-233-2014

Barnard, P. L., van Ormondt, M., Erikson, L. H., Eshleman, J., Hapke, C., Ruggiero, P., ... Foxgrover, A. C. (2014, Nov 01). Development of the coastal storm modeling system (cosmos) for predicting the impact of storms on high-energy, active-margin coasts. *Natural Hazards*, *74*(2), 1095-1125. Retrieved from `https://doi.org/10.1007/s11069-014-1236-y` doi: 10.1007/s11069-014-1236-y

Beiboer, L. J. O. (2022, 9). *Coastline of San Antonio, Chile.*

Bhattacharyya, S., Abraham, J. P., Cheng, L., & Gorman, J. (2021). *Introductory chapter: A brief history of and introduction to computational fluid dynamics* (S. Bhattacharyya, Ed.). Rijeka: IntechOpen. Retrieved from https://doi.org/10.5772/intechopen.97235 doi: 10.5772/intechopen.97235

Blatná, D. (2006). Outliers in regression. *Trutnov*, *30*, 1–6. doi: https://statistika.vse.cz/konference/amse/PDF/Blatna.pdf

Boak, E. H., & Turner, I. L. (2005, 7). Shoreline definition and detection: A review. *Journal of Coastal Research*, *21*, 688-703. doi: 10.2112/03-0071.1

Bolle, A., Mercelis, P., Roelvink, D., Haerens, P., & Trouw, K. (2011, 1). Application and validation of xbeach for three different field sites. *Coastal Engineering*, *1*. doi: 10.9753/icce.v32.sediment.40

Bosboom, J., & Stive, M. J. (2021). *Coastal dynamics*. TU Delft Open. doi: 10.5074/T.2021.001

Bruun, P. (1962, 2). Sea-level rise as a cause of shore erosion. *Journal of the Waterways and Harbors Division*, *88*(1), 117-130. Retrieved from https://ascelibrary.org/doi/abs/10.1061/JWHEAU.0000252 doi: 10.1061/JWHEAU.0000252

Bulleri, F., & Chapman, M. G. (2010, 2). The introduction of coastal infrastructure as a driver of change in marine environments. *Journal of Applied Ecology*, *47*(1), 26-35. Retrieved from https://besjournals.onlinelibrary.wiley.com/doi/abs/10.1111/j.1365-2664.2009.01751.x doi: 10.1111/j.1365-2664.2009.01751.x

Castelle, B., Ritz, A., Marieu, V., Lerma, A. N., & Vandenhove, M. (2022, 9). Primary drivers of multidecadal spatial and temporal patterns of shoreline change derived from optical satellite imagery. *Geomorphology*, *413*. doi: 10.1016/j.geomorph.2022.108360

Centre, B. O. D. (2023). *Gebco gridded global bathymetry data.* https://www.gebco.net/. ([Accessed 11-10-2023])

Coelho, C., Silva, R., Veloso-Gomes, F., & Rodrigues, L. (2011, 1). Artificial nourishment and sand by-passing in the aveiro inlet, portugal - numerical studies. *Coastal Engineering Proceedings*, *1*(32), sediment.99. Retrieved from https://icce-ojs-tamu.tdl.org/icce/article/view/1186 doi: 10.9753/icce.v32.sediment.99

de Schipper, M. A., de Vries, S., Ruessink, G., de Zeeuw, R. C., Rutten, J., van Gelder-Maas, C., & Stive, M. J. (2016). Initial spreading of a mega feeder nourishment: Observations of the sand engine pilot project. *Coastal Engineering*, *111*, 23-38. Retrieved from https://www.sciencedirect.com/science/article/pii/S037838391500188X doi: https://doi.org/10.1016/j.coastaleng.2015.10.011

de Boer, G., & den Heijer, K. (2016, Nov). *Jarkus.* Retrieved from https://publicwiki.deltares.nl/display/OET/Dataset+documentation+JarKus

Deltares. (2023a). *Delft3d.* https://oss.deltares.nl/web/delft3d/about. ([Accessed 13-10-2023])

Deltares. (2023b). *Unibest-cl+.* https://www.deltares.nl/en/software-and-data/products/unibest-cl. ([Accessed 13-10-2023])

Deltares. (2023c). *Xbeach.* https://oss.deltares.nl/web/xbeach/. ([Accessed 13-10-2023])

Do, A. T., de Vries, S., & Stive, M. J. (2019, 1). The estimation and evaluation of shoreline locations, shoreline-change rates, and coastal volume changes derived from landsat images. *Journal of Coastal Research*, *35*, 56-71. doi: 10.2112/JCOASTRES-D-18-00021.1

Duncan, E. W., & Mengersen, K. L. (2020). Comparing bayesian spatial models: Goodness-of-smoothing criteria for assessing under-and over-smoothing. *PloS one*, *15*(5), e0233019. doi: http://dx.doi.org/10.1371/journal.pone.0233019

ECMWF. (2023). *Era5.* https://confluence.ecmwf.int/display/CKB/ERA5%3A+data+documentation. ([Accessed 13-10-2023])

Egbert, G. D., & Erofeeva, S. Y. (2002, 2). Efficient inverse modeling of barotropic ocean tides. *Journal of Atmospheric and Oceanic technology*, *19*(2), 183–204. doi: https://doi.org/10.1175/1520-0426(2002)019⟨0183:EIMOBO⟩2.0.CO;2

Elmoustapha, A. O., Levoy, F., Monfort, O., & Koutitonsky, V. G. (2007, 12). A numerical forecast of shoreline evolution after harbour construction in nouakchott, mauritania. *Journal of Coastal Research*, *23*, 1409-1417. doi: 10.2112/04-0423.1

ESA. (2023). *Sentinel 2.* `https://www.esa.int/Applications/Observing_the_Earth/Copernicus/Sentinel-2`. ([Accessed 13-10-2023])

Google. (2024). *Google Earth.* Retrieved from `https://www.google.com/earth/` (Accessed on 2024-05-04)

Gorelick, N., Hancher, M., Dixon, M., Ilyushchenko, S., Thau, D., & Moore, R. (2017). Google earth engine: Planetary-scale geospatial analysis for everyone. *Remote Sensing of Environment*, *202*, 18-27. Retrieved from `https://www.sciencedirect.com/science/article/pii/S0034425717302900` (Big Remotely Sensed Data: tools, applications and experiences) doi: https://doi.org/10.1016/j.rse.2017.06.031

Güner, H. A., Yüksel, Y., & Çevik, E. Ö. (2013, 3). Longshore sediment transport-field data and estimations using neural networks, numerical model, and empirical models. *Journal of Coastal Research*, *29*, 311-324. doi: 10.2112/JCOASTRES-D-11-00074.1

Hagenaars, G., de Vries, S., Luijendijk, A. P., de Boer, W. P., & Reniers, A. J. (2018). On the accuracy of automated shoreline detection derived from satellite imagery: A case study of the sand motor mega-scale nourishment. *Coastal Engineering*, *133*, 113-125. Retrieved from `https://www.sciencedirect.com/science/article/pii/S0378383917302399` doi: https://doi.org/10.1016/j.coastaleng.2017.12.011

Hagenaars, G., Luijendijk, A., de Vries, S., & de Boer, W. (2017). Long term coastline monitoring derived from satellite imagery. , 1551–1562. Retrieved from `https://pure.tudelft.nl/ws/portalfiles/portal/27445169/122_Hagenaars_Gerben.pdf`

Hallermeier, R. J. (n.d.). Uses for a calculated limit depth to beach erosion. , 1493-1512. Retrieved from `https://ascelibrary.org/doi/abs/10.1061/9780872621909.090` doi: 10.1061/9780872621909.090

Harley, M. D., Kinsela, M. A., Sánchez-García, E., & Vos, K. (2019). Shoreline change mapping using crowd-sourced smartphone images. *Coastal Engineering*, *150*, 175-189. Retrieved from `https://www.sciencedirect.com/science/article/pii/S0378383918304551` doi: https://doi.org/10.1016/j.coastaleng.2019.04.003

Hincks, A. T. (2022). *A quote by anthony t. hincks.* Goodreads. Retrieved from `https://www.goodreads.com/quotes/11266318-sand-leads-me-to-the-shores-of-new-discoveries`

Hodge, V., & Austin, J. (2004). A survey of outlier detection methodologies. *Artificial intelligence review*, *22*, 85–126. doi: http://dx.doi.org/10.1023/B:AIRE.0000045502.10941.a9

Hoekstra, R., Walstra, D., & Swinkels, C. (2012, 12). Pilot project sand groynes delfland coast. *COASTAL ENGINEERING*, *1*(33), 2. Retrieved from `https://icce-ojs-tamu.tdl.org/icce/article/view/6968` doi: 10.9753/icce.v33.sediment.128

Huisman, B., & Dagalaki, V. (2020). *Unibest user manual.* Deltares.

Ibaceta, R., Harley, M. D., Turner, I. L., & Splinter, K. D. (2023). Interannual variability in dominant shoreline behaviour at an embayed beach. *Geomorphology*, *433*, 108706. Retrieved from `https://www.sciencedirect.com/science/article/pii/S0169555X23001265` doi: https://doi.org/10.1016/j.geomorph.2023.108706

Janssen, V. (2009, 1). Understanding coordinate reference systems, datums and transformations. doi: https://hdl.handle.net/102.100.100/586681

Kahl, D. T., Vulis, L. M., Schubert, J. E., & Sanders, B. F. (2024). Characterizing longshore transport potential and divergence of drift to inform beach loss trends. *Coastal Engineering*, *189*, 104473. Retrieved from `https://www.sciencedirect.com/science/article/pii/S0378383924000218` doi: https://doi.org/10.1016/j.coastaleng.2024.104473

Kew, S. F., Selten, F. M., Lenderink, G., & Hazeleger, W. (2013). The simultaneous occurrence of surge and discharge extremes for the rhine delta. *Natural Hazards and Earth System Sciences*,

*13*(8), 2017–2029. Retrieved from https://nhess.copernicus.org/articles/13/2017/2013/ doi: 10.5194/nhess-13-2017-2013

Knorr, E. M., Ng, R. T., & Tucakov, V. (2000). Distance-based outliers: algorithms and applications. *The VLDB Journal*, *8*(3), 237–253. doi: https://doi.org/10.1007/s007780050006

Kraus, N. C., Larson, M., & Wise, R. A. (1998, 3). Depth of closure in beach-fill design. *Coastal Engineering Tech. Note CETN II-40*. doi: https://apps.dtic.mil/sti/tr/pdf/ADA578584.pdf

Kunte, P. D., Alagarsamy, R., & Hursthouse, A. S. (2013, Jun 01). Sediment fluxes and the littoral drift along northeast andhra pradesh coast, india: estimation by remote sensing. *Environmental Monitoring and Assessment*, *185*(6), 5177-5192. Retrieved from https://doi.org/10.1007/s10661-012-2934-0 doi: 10.1007/s10661-012-2934-0

Larson, M., Hanson, H., & Kraus, N. C. (1987). Analytical solutions of the one-line model of shoreline change.
doi: https://hdl.handle.net/11681/12401

Luijendijk, A. P., Hagenaars, G., Ranasinghe, R., Baart, F., Donchyts, G., & Aarninkhof, S. (2018, 12). The state of the world's beaches. *Scientific Reports*, *8*. doi: 10.1038/s41598-018-24630-6

Luijendijk, A. P., Ranasinghe, R., de Schipper, M. A., Huisman, B. A., Swinkels, C. M., Walstra, D. J., & Stive, M. J. (2017, 1). The initial morphological response of the sand engine: A process-based modelling study. *Coastal Engineering*, *119*, 1-14. doi: 10.1016/j.coastaleng.2016.09.005

Manchuk, J. G., & Deutsch, C. (2009). Conversion of latitude and longitude to utm coordinates. *Paper 410, CCG Annual Report*, *11*. Retrieved from https://citeseerx.ist.psu.edu/document?repid=rep1&type=pdf&doi=f0180ea6f8fab77b53381c7cff3c610f7a9df64b

Marchand, M., Bucx, T., & Mulder, J. (2009, 2). The conscience project: Bridging the knowledge gap for sustainable coastline management. *IOP Conference Series: Earth and Environmental Science*, *6*, 352030. doi: 10.1088/1755-1307/6/5/352030

McAllister, E., Payo, A., Novellino, A., Dolphin, T., & Medina-Lopez, E. (2022, 6). Multispectral satellite imagery and machine learning for the extraction of shoreline indicators. *Coastal Engineering*, *174*. doi: 10.1016/j.coastaleng.2022.104102

Miller, J. K., & Dean, R. G. (2004). A simple new shoreline change model. *Coastal Engineering*, *51*(7), 531-556. Retrieved from https://www.sciencedirect.com/science/article/pii/S0378383904000614 doi: https://doi.org/10.1016/j.coastaleng.2004.05.006

Miranda, I. M., Toldo Jr, E. E., da Fontoura Klein, A. H., da Silva, G. V., & Strauss, D. (2022, 3). Sediment budget of a cuspate shoreline and its influence on spit development—lagoa dos patos, brazil. *Geo-Marine Letters*, *42*. doi: 10.1007/s00367-021-00724-5

Nakagawa, S., & Schielzeth, H. (2013, 2). A general and simple method for obtaining r2 from generalized linear mixed-effects models. *Methods in Ecology and Evolution*, *4*(2), 133-142. Retrieved from https://besjournals.onlinelibrary.wiley.com/doi/abs/10.1111/j.2041-210x.2012.00261.x doi: 10.1111/j.2041-210x.2012.00261.x

NASA. (2023a). *Landsat 5 — landsat.gsfc.nasa.gov.* https://landsat.gsfc.nasa.gov/satellites/landsat-5/. ([Accessed 11-10-2023])

NASA. (2023b). *Landsat 7 — landsat.gsfc.nasa.gov.* https://landsat.gsfc.nasa.gov/satellites/landsat-7/. ([Accessed 11-10-2023])

NASA. (2023c). *Landsat 8 — landsat.gsfc.nasa.gov.* https://landsat.gsfc.nasa.gov/satellites/landsat-8/. ([Accessed 11-10-2023])

Oh, J.-E., Chang, Y. S., Jeong, W. M., Kim, K. H., & Ryu, K. H. (2020). Estimation of longshore sediment transport using video monitoring shoreline data. *Journal of Marine Science and Engineering*, *8*(8). Retrieved from https://www.mdpi.com/2077-1312/8/8/572 doi: 10.3390/jmse8080572

OpenStreetMap. (2024). *OSMCoastline - OpenStreetMap retrieved from https://wiki.openstreetmap.org/wiki/OSMCoastline.*

Otsu, N. (1979). A threshold selection method from gray-level histograms. *IEEE Transactions on Systems, Man, and Cybernetics*, *9*(1), 62-66. doi: 10.1109/TSMC.1979.4310076

Pinto, C. A., Taborda, R., Andrade, C., Baptista, P., Silva, P. A., Mendes, D., & Pais-Barbosa, J. (2022, jan). Morphological development and behaviour of a shoreface nourishment in the portuguese western coast. *Journal of Marine Science and Engineering*, *10*(2), 146. Retrieved from http://dx.doi.org/10.3390/jmse10020146 doi: 10.3390/jmse10020146

Pontee, N. (2013). Defining coastal squeeze: A discussion. *Ocean and Coastal Management*, *84*, 204-207. Retrieved from https://www.sciencedirect.com/science/article/pii/S0964569113001786 doi: https://doi.org/10.1016/j.ocecoaman.2013.07.010

Radermacher, M., De Schipper, M., Price, T., Huisman, B., Aarninkhof, S., & Reniers, A. (2018, 7). Behaviour of subtidal sandbars in response to nourishments. *Geomorphology*, *313*, 1-12. doi: 10.1016/j.geomorph.2018.04.005

Randazzo, G., Barreca, G., Cascio, M., Crupi, A., Fontana, M., Gregorio, F., ... Muzirafuti, A. (2020, 5). Analysis of very high spatial resolution images for automatic shoreline extraction and satellite-derived bathymetry mapping. *Geosciences*, *10*, 172. doi: 10.3390/geosciences10050172

[Rijkswaterstaat], M. (1980). *Jarkusraaien.* Retrieved 2024-06-07, from https://maps.rijkswaterstaat.nl/dataregister-publicatie/srv/api/records/b6a80ed7-ef50-46e6-b967-aeaa631ff1eb

Roelvink, D., Huisman, B., Elghandour, A., Ghonim, M., & Reyns, J. (2020, 7). Efficient modeling of complex sandy coastal evolution at monthly to century time scales. *Frontiers in Marine Science*, *7*. doi: 10.3389/fmars.2020.00535

Salgado, C. M., Azevedo, C., Proença, H., & Vieira, S. M. (2016). *Missing data.* Cham: Springer International Publishing. Retrieved from https://doi.org/10.1007/978-3-319-43742-2_13 doi: 10.1007/978-3-319-43742-2_13

Samou, M. S., Bertin, X., Sakho, I., Lazar, A., Sadio, M., & Diouf, M. B. (2023). Wave climate variability along the coastlines of senegal over the last four decades. *Atmosphere*, *14*(7). Retrieved from https://www.mdpi.com/2073-4433/14/7/1142 doi: 10.3390/atmos14071142

Sedrati, M., & Anthony, E. J. (2014, 10). Confronting coastal morphodynamics with counter-erosion engineering: the emblematic case of wissant bay, dover strait. *Journal of Coastal Conservation*, *18*, 483-494. doi: 10.1007/s11852-013-0300-1

Shore Monitoring & Research. (2023). *Survey data cross-shore.* Retrieved from https://www.shoremonitoring.nl

Silva, A. N., Taborda, R., Bertin, X., & Dodet, G. (2012, 11). Seasonal to decadal variability of longshore sand transport at the northwest coast of portugal. *Journal of Waterway, Port, Coastal, and Ocean Engineering*, *138*(6), 464-472. Retrieved from https://ascelibrary.org/doi/abs/10.1061/%28ASCE%29WW.1943-5460.0000152 doi: 10.1061/(ASCE)WW.1943-5460.0000152

Silva, F., & Duck, R. (2001). Historical changes of bottom topography and tidal amplitude in the ria de aveiro, portugal–trends for future evolution. *Climate Research*, *18*, 17–24. Retrieved from http://dx.doi.org/10.3354/cr018017 doi: 10.3354/cr018017

Thyrsted, T. (1986, 12). Remote sensing - a new tool in exploration geology. *Rapport Grønlands Geologiske Undersøgelse*, *128*, 135–146. Retrieved from https://geusjournals.org/index.php/rapggu/article/view/7930 doi: 10.34194/rapggu.v128.7930

Tonnon, P. K., Huisman, B., Stam, G., & Van Rijn, L. (2018, 1). Numerical modelling of erosion rates, life span and maintenance volumes of mega nourishments. *Coastal Engineering*, *131*, 51-69. doi: 10.1016/j.coastaleng.2017.10.001

Toure, S., Diop, O., Kpalma, K., & Maiga, A. S. (2019, 2). Shoreline detection using optical remote sensing: A review. *ISPRS International Journal of Geo-Information*, *8*. doi: 10.3390/ijgi8020075

Uh Zapata, M., Itzá Balam, R., & Montalvo-Urquizo, J. (2018, 3). High-order implicit staggered-grid finite differences methods for the acoustic wave equation. *Numerical Methods for Partial Differential*

*Equations*, *34*(2), 602-625. Retrieved from https://onlinelibrary.wiley.com/doi/abs/10.1002/num.22217 doi: 10.1002/num.22217

Vafaei, S., Soosani, J., Adeli, K., Fadaei, H., Naghavi, H., Pham, T. D., & Tien Bui, D. (2018). Improving accuracy estimation of forest aboveground biomass based on incorporation of alos-2 palsar-2 and sentinel-2a imagery and machine learning: A case study of the hyrcanian forest area (iran). *Remote Sensing*, *10*(2). Retrieved from https://www.mdpi.com/2072-4292/10/2/172 doi: 10.3390/rs10020172

Valiente, N. G., Masselink, G., Scott, T., Conley, D., & McCarroll, R. J. (2019, 1). Role of waves and tides on depth of closure and potential for headland bypassing. *Marine Geology*, *407*, 60-75. doi: 10.1016/j.margeo.2018.10.009

Van Rijn, L. (2011, 12). Coastal erosion and control. *Ocean and Coastal Management*, *54*, 867-887. doi: 10.1016/j.ocecoaman.2011.05.004

van Slobbe, E., de Vriend, H. J., Aarninkhof, S., Lulofs, K., de Vries, M., & Dircke, P. (2013, Apr 01). Building with nature: in search of resilient storm surge protection strategies. *Natural Hazards*, *66*(3), 1461-1480. Retrieved from https://doi.org/10.1007/s11069-013-0612-3 doi: 10.1007/s11069-013-0612-3

Vitousek, S., Barnard, P. L., & Limber, P. (2017, 4). Can beaches survive climate change? *Journal of Geophysical Research: Earth Surface*, *122*, 1060-1067. doi: 10.1002/2017JF004308

Vitousek, S., Barnard, P. L., Limber, P., Erikson, L., & Cole, B. (2017, 4). A model integrating longshore and cross-shore processes for predicting long-term shoreline response to climate change. *Journal of Geophysical Research: Earth Surface*, *122*, 782-806. doi: 10.1002/2016JF004065

Vitousek, S., Buscombe, D., Vos, K., Barnard, P. L., Ritchie, A. C., & Warrick, J. A. (2023). The future of coastal monitoring through satellite remote sensing. *Cambridge Prisms: Coastal Futures*, *1*, e10. doi: 10.1017/cft.2022.4

Vitousek, S., Vos, K., Splinter, K. D., Erikson, L., & Barnard, P. L. (2023, 7). A model integrating satellite-derived shoreline observations for predicting fine-scale shoreline response to waves and sea-level rise across large coastal regions. *Journal of Geophysical Research: Earth Surface*, *128*. doi: 10.1029/2022JF006936

Vos, K., Splinter, K. D., Harley, M. D., Simmons, J. A., & Turner, I. L. (2019, 12). Coastsat: A google earth engine-enabled python toolkit to extract shorelines from publicly available satellite imagery. *Environmental Modelling and Software*, *122*. doi: 10.1016/j.envsoft.2019.104528

Vousdoukas, M. I., Ranasinghe, R., Mentaschi, L., Plomaritis, T. A., Athanasiou, P., Luijendijk, A., & Feyen, L. (2020, 3). Sandy coastlines under threat of erosion. *Nature Climate Change*, *10*, 260-263. doi: 10.1038/s41558-020-0697-0

Walton, T. L., & Dean, R. G. (1973). *Application of littoral drift roses to coastal engineering problems.* Sydney, N.S.W.: Institution of Engineers, Australia. Retrieved from https://search.informit.org/doi/10.3316/informit.971740437615016

Walton, T. L., & Dean, R. G. (2010). Longshore sediment transport via littoral drift rose. *Ocean Engineering*, *37*(2), 228-235. Retrieved from https://www.sciencedirect.com/science/article/pii/S0029801809002595 doi: https://doi.org/10.1016/j.oceaneng.2009.11.002

Weisse, R., von Storch, H., Niemeyer, H. D., & Knaack, H. (2012, 11). Changing north sea storm surge climate: An increasing hazard? *Ocean and Coastal Management*, *68*, 58-68. Retrieved from https://www.sciencedirect.com/science/article/pii/S0964569111001451 (Special Issue on the Wadden Sea Region) doi: 10.1016/j.ocecoaman.2011.09.005

Wijnberg, K. M. (2002). Environmental controls on decadal morphologic behaviour of the holland coast. *Marine Geology*, *189*(3), 227-247. Retrieved from https://www.sciencedirect.com/science/article/pii/S0025322702004802 doi: https://doi.org/10.1016/S0025-3227(02)00480-2

Windarni, V. A., Setiawan, A., & Rahmatalia, A. (2023, nov). Comparison of the karney polygon method and the shoelace method for calculating area. *MATRIK Jurnal Manajemen, Teknik Informatika dan Rekayasa Komputer*, *23*(1), 39–52. Retrieved from http://dx.doi.org/10.30812/matrik.v23i1.2929 doi: 10.30812/matrik.v23i1.2929

Wölfl, A.-C., Snaith, H., Amirebrahimi, S., Devey, C. W., Dorschel, B., Ferrini, V., ... others (2019). Seafloor mapping–the challenge of a truly global ocean bathymetry. *Frontiers in Marine Science*, *6*, 434383. doi: https://doi.org/10.3389/fmars.2019.00283

Zhao, Q., Yu, L., Li, X., Peng, D., Zhang, Y., & Gong, P. (2021, 9). Progress and trends in the application of google earth and google earth engine. *Remote Sensing*, *13*. doi: 10.3390/rs13183778

# A

# Elaboration Methodology

## A.1 From Ellipsoidal to UTM

In Section 3.3, the average distance between transects is determined. However, this is done using the coordinate system of Universal Transverse Mercator (UTM). First, an explanation is provided to distinguish between the latitude and longitude coordinate systems (ellipsoidal model) and the Northing and Easting coordinate system (UTM). Then, the method for converting the shoreline position from longitude and latitude to Easting and Northing will be offered.

### A.1.1 Ellipsoidal model

According to Manchuk & Deutsch (2009), map projections are beneficial for presenting and simplifying distance, area and volume computations. These calculations can be complex in the Earth's ellipsoidal coordinate system. The ellipsoidal coordinates define the Earth with longitude, latitude and height axe coordinates. On the other hand, there is the Universal Transverse Mercator (UTM) projection, which shows a map in a cylindrical coordinate system that is discretised into a set of zones, each being an approximate Cartesian system with East and North coordinates (Manchuk & Deutsch, 2009).

The latitude and longitude data are projected onto an ellipsoidal model of the Earth. The so-called World Geodetic Systems of 1984 (WGS84), which is utilised in (GPS) systems. Figure A.1 (Manchuk & Deutsch, 2009) shows that this model matches the Earth, or Geoid, with low height error. The ellipsoidal model is aligned with the Earth's poles and includes an equator from which latitude is measured. Finally, a reference meridian must be selected from which longitude is measured. This is the zero line in longitude, located in Greenwich, UK (Manchuk & Deutsch, 2009; Janssen, 2009).

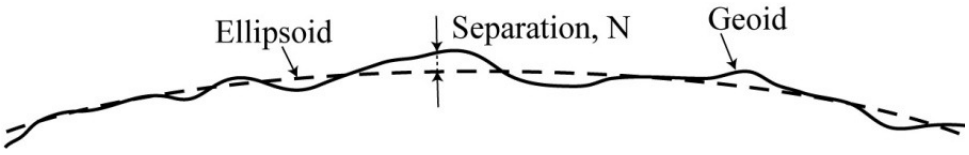


Figure A.1: This figure shows the Earth's surface, the Geoid, with the ellipsoidal model of the Earth. Where $N$ is the difference between the model and reality. Source: Manchuk & Deutsch (2009)

### A.1.2 UTM

Using UTM coordinates rather than latitude and longitude coordinates has various advantages. One significant advantage is that UTM coordinates provide a more localised and precise representation of a specific location on Earth. UTM coordinates use a grid method to split the Earth's surface into zones, enabling exact placement within each zone (Manchuk & Deutsch, 2009; Janssen, 2009). According to Manchuk & Deutsch (2009), Transverse Mercator (TM) projections are made by placing a cylinder in contact with a line of equal longitude, commonly known as a meridian illustrated in Figure A.2 and projecting the Earth's surface onto it. Such projections are suitable for portions of the Earth that are not next to the Equator, as opposed to the normal Mercator projection, which uses a cylinder in contact with the Equator.

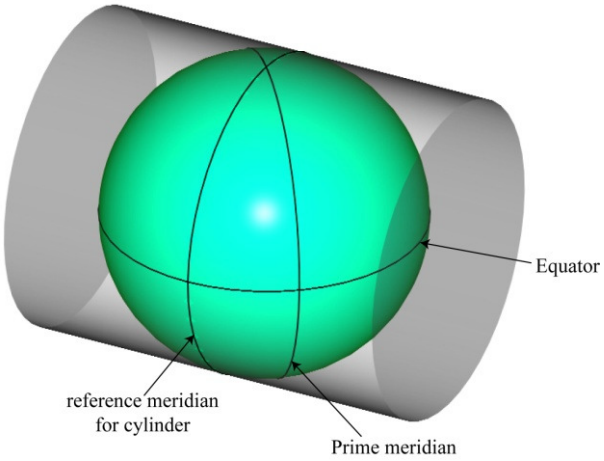


Figure A.2: This image shows the ellipsoidal model inside a cylinder. The cylinder shows the world in the Transverse Mercator projection. Source: Manchuk & Deutsch (2009)

The world can be divided into zones for the UTM coordinate system. Figure A.3 shows all the zones around the world. In each UTM zone, the projected grid coordinates, i.e. Easting and Northing, are initially referenced to the origin defined by the intersection of the Configuration and Management (CM) and the Equator, resulting in negative Easting coordinates west of the CM and negative Northing coordinates in the southern hemisphere. In order to ensure positive coordinate values across the entire zone, the UTM system applies false coordinates to the origin by adding 500,000 m to the true Easting and, in the southern hemisphere, 10,000,000 m to the true Northing (Janssen, 2009).

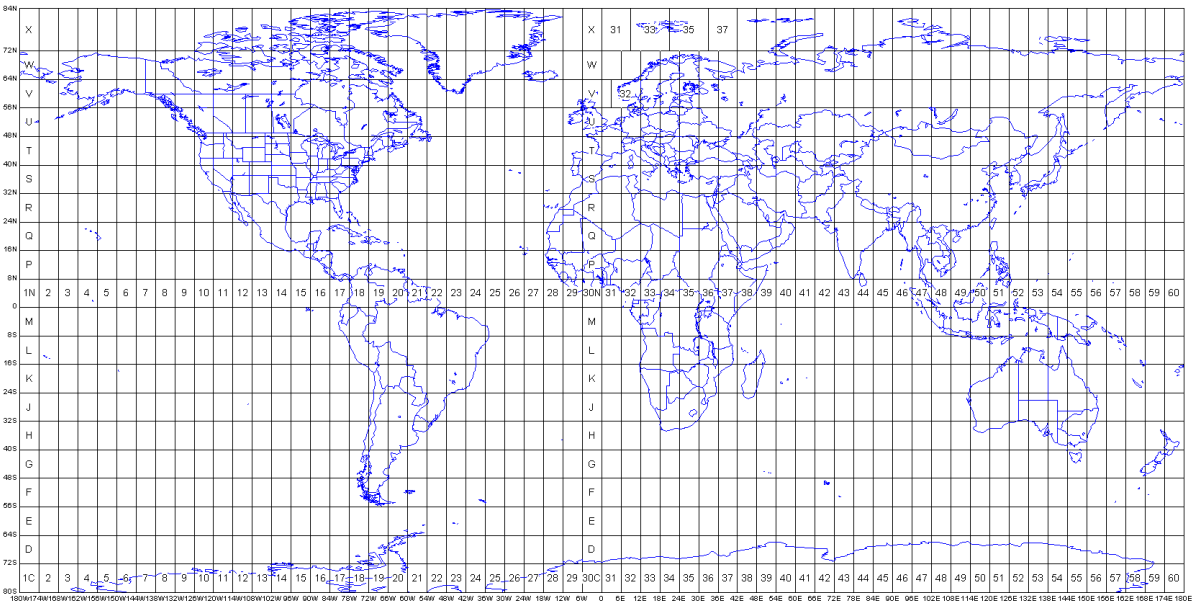

Figure A.3: This image shows all the UTM zones with numbers and letters worldwide. Source: (Janssen, 2009), `https://www.dmap.co.uk/utmworld.htm`.

### A.1.3 Ellipsoidal to UTM

Using the UTM coordinates system, as described in Section A.1.2, provides more precise coordinates, which is more valuable in the littoral transport process. First, the latitude and longitude of the transect are transformed. An important step is to pick a UTM zone, as shown in Figure A.3. Using the Python package "pyproj" (`https://pyproj4.github.io/pyproj/stable/index.html`), latitude and longitude may be transformed into UTM coordinates. The input data include the WGS84 coordinate system and the selected UTM zone. The output consists of Northing and Eastern coordinates.

After converting the transects, the same can be done with the coastline positions. Because the transects are converted to Easting and Northing coordinates, the shoreline position from Satellite-derived Shoreline can be directly turned into UTM coordinates. However, SDS gives the distance from the starting point of the transect. An interpolation method is utilised to determine the shoreline's location. The length between the start point from the transect and the coastline position, as well as the location of the start point of the transect in $x$ and $y$ coordinates, can be used to calculate the shoreline position in $x$ and $y$ coordinates. Equation A.1 illustrates the steps for calculating the shoreline position in UTM.

$$\begin{aligned} L_{transect} &= \sqrt{(x_2 - x_1)^2 + (y_2 - y_1)^2} \\ \text{Ratio} &= \frac{d}{L_{transect}} \\ P_x &= x_1 + \text{Ratio} * (x_2 - x_1) \\ P_y &= y_1 + \text{Ratio} * (y_2 - y_1) \end{aligned} \tag{A.1}$$

$L_{transect}$ represents the length of the transect ($T_{start}(x_1, y_1)$ and $T_{end}(x_2, y_2)$). This length is based on the Pythagoras equation ($a^2 + b^2 = c^2$). The Ratio is calculated as the length of the transect divided by the distance ($d$) between the coastline position and the start of the transect. $P_x$ and $P_y$ are the Easting and Northing coordinates in metres from the seashore point.

## A.2 Reorder Transects

Following the methodology, the acquired coastal cell will go through an initial reordering process to ensure proper alignment of all the transects. The initial step involves converting the longitude and latitude data of the Satellite-derived Shoreline into Easting ($X$) and Northing ($Y$) coordinates, as detailed in Appendix A.1. Subsequently, the transect located at the bottom left in the coastal cell can be identified as the most southern transect. Once the southernmost transect is determined, the distances between the other transects can be calculated. This calculation involves measuring the distance between the centre points of each transect. To find the centre point, the $X$ and $Y$ coordinates of a transect's start and end locations are divided by two, as demonstrated in Equation A.2.

$$\begin{aligned} \text{Midpoint}_x &= (\text{end point}_x - \text{start point}_x)/2 \\ \text{Midpoint}_y &= (\text{end point}_y - \text{start point}_y)/2 \end{aligned} \tag{A.2}$$

Upon identifying the centre point of each transect, the distance between these points can be calculated using a variation on the Pythagoras equation ($a^2 + b^2 = c^2$) as shown in Equation A.3. These distances will then be compiled into a data frame alongside the corresponding transect ID. It is important to note that the southern transect will have a zero distance ($D = 0$). Table A.1 provides an example of this data frame.

$$D = \sqrt{(x_T - x_{T0})^2 + (y_T - y_{T0})^2} \tag{A.3}$$

Where $D$ is the computed distance, $T$ is one of the transects in the dataset and $T0$ is the most southern transect. The $x$ and $y$ components are the Easting and Northing coordinates.

Table A.1: A visualisation of the south transect data frame

| **transect_id** | **distance [m]** |
|---|---|
| transect_1 | 0 |
| transect_2 | 5 |
| transect_3 | 10 |
| ⋮ | ⋮ |
| transect_N-1 | M-1 |
| transect_N | M |

The next step involves arranging the data frame in ascending order based on the distance values, with the southern transect positioned at the top. Once the dataset is sorted, it can be merged with the Satellite-derived Shoreline dataset using the transect ID order from the southern transect data frame (Table A.1). This ensures that all the data follows the newly ordered transect sequence. Figure A.4 shows a diagram illustrating all the steps.


Figure A.4: An overview of all the steps to reorder the transect into a south-to-north sequence.

## A.3 Nourishment Detection

In Section 3.3.1, it is outlined that it is essential to identify potential nourishments within the dataset before conducting outlier detection. The algorithm for detecting nourishment is developed based on the characteristics of the Delfland coast, which is known for its significant nourishment content and is well-documented, as shown in Appendix D.

### Identifying

One way to analyse the Satellite-derived Shoreline data is to determine the presence of nourishments in the selected coastal cell or identify outliers. An evaluation will be conducted on the transects' shoreline positions in the temporal domain to distinguish between outliers, nourishments and genuine shoreline positions. To classify a shoreline position as a nourishment, it is crucial to understand the impact of nourishment on the shoreline. When nourishment is placed along the shoreline, there is a significant seaward migration of the shoreline position. Typically, nourishments are placed in areas experiencing structural erosion along the coast.

Consequently, after the placement of nourishments, erosion occurs, and sediment spreads along the coast or disappears (Bosboom & Stive, 2021). Furthermore, nourishment is placed along a certain part of the coast. This indicates that the shoreline migrates significantly seawards within a particular width. This width is essential to achieve a specific shape, such as the Sand Engine (Luijendijk et al., 2017; de Schipper et al., 2016). These effects of nourishments can serve as criteria to identify nourishments in the Satellite-derived Shoreline data. Therefore, two criteria can be established:

1. The shoreline position should exhibit a significant seaward migration over a certain distance.
2. A certain number of adjacent shoreline positions should shift by the same distance.

Four different shoreline position migrations between two years are considered to determine the optimal shoreline shift for the Delfland coastal cell: 30, 40, 45, and 50 meters. These shifts represent the minimum distance the shoreline should migrate between two years. The results of the nourishment identification for each shift are shown in Figures A.5a-d. In these figures, the shoreline position is coloured green-blue if it migrates the set amount and yellow if five adjacent transects migrate with the same amount or more. This second criterion is used to identify significant nourishment. Specifically, five SDS transects correspond to a distance of 2500 meters. It is important to note that the matrix plots are based on the difference in shoreline position between two years. Figure A.5f illustrates the difference plot for the Delfland coast obtained from the SDS data, where the blue colour indicates the seaward movement of the shoreline and the red colour represents erosion.

The comparison of the detected shoreline movements using different criteria with the actual nourishment data obtained from Appendix D reveals that more nourishments have been placed (Figure A.5e) than those identified in Figures A.5a-d. It is worth mentioning that the nourishment on the left side of the matrix in Figure A.5e is not present in the other matrices. This suggests that these nourishments were too small to be detected by the SDS. Upon closer examination of Figure A.5a in comparison to Figures A.5b-d, it is evident that the 30-meter criterion also identifies numerous shoreline positions as nourishments, which cannot be linked to the actual nourishments in Figure A.5e. Considering that the shoreline migrations of 40, 45, and 50 meters align more closely with Figure A.5e, a shoreline migration of 40 meters is chosen. The selection of 40 meters instead of a higher value ensures the identification of as many nourishments as possible while minimising noise.

Other methods of identifying nourishment involve assessing the initiation of a new trend. In the event of structural erosion along the shoreline, a downward trend line will be evident in a time series. Following the addition of nourishment, the shoreline will extend further into the sea before eroding once more. Two distinct slopes are visible in the time series data: one before nourishment and one after. However, indicating these regression lines within a fluctuating time series can pose a challenge.

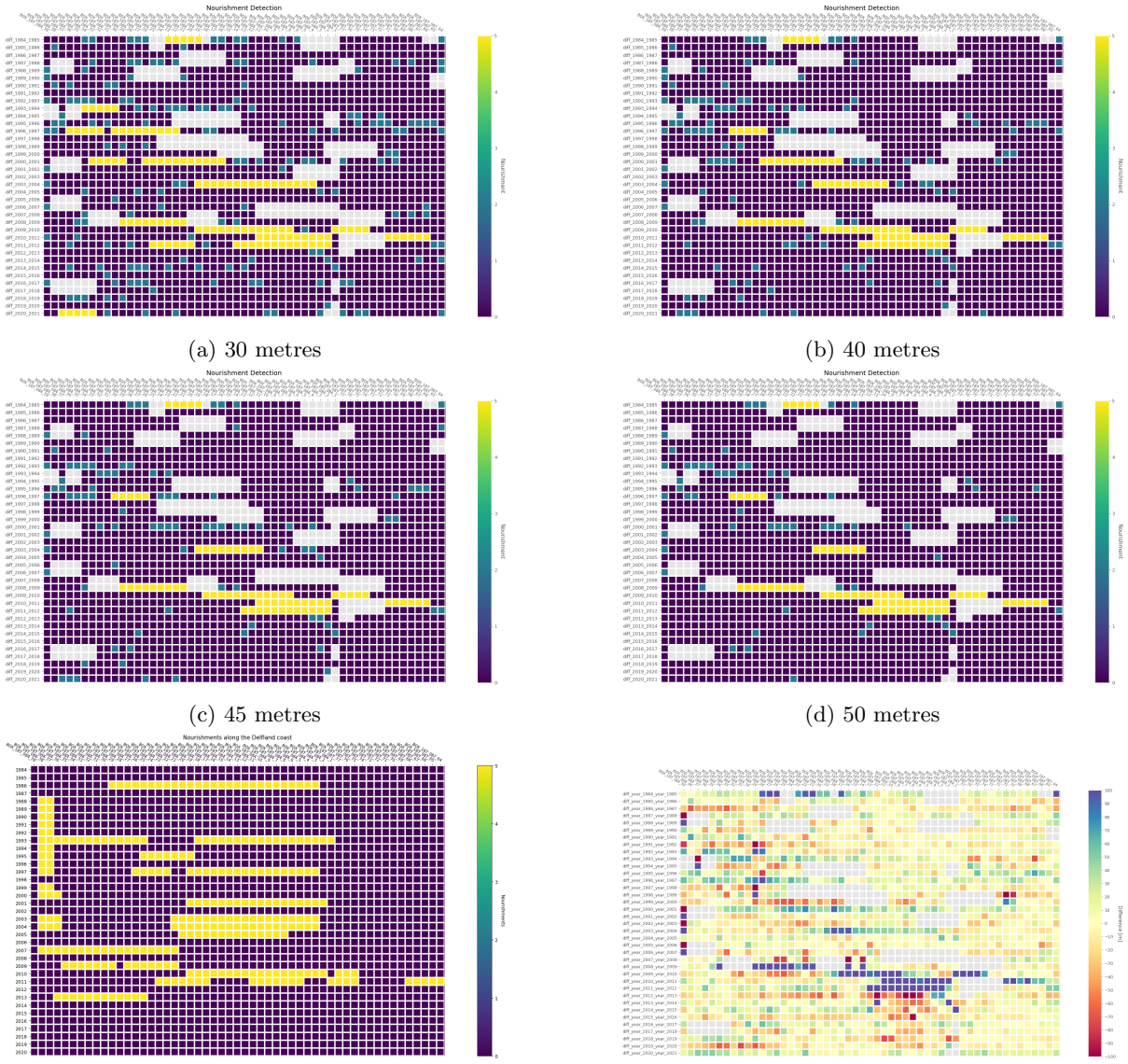


(a) 30 metres

(b) 40 metres

(c) 45 metres

(d) 50 metres

(e) Nourishment RWS

(f) Shoreline difference

Figure A.5: There are six different matrices shown here. Figures a–d show the detected nourishment with varying migration limitations. Figure a illustrates nourishment at 30 metres, b at 40 metres, c at 45 metres, and d at 50 metres shoreline position shift. The blue-green colour indicates shoreline alterations, although there are no five transects adjacent to one another. Figure e depicts the documented nourishment according to de Boer & den Heijer (2016). Figure f depicts the difference in coastline location for the Delfland instance. The white spots are cells with no data.

Nevertheless, the spatial requirement for detecting nourishment would still be five transects, although this value can be adjusted higher or lower. Figure A.5e illustrates instances where nourishments are distributed across two or three sections. Since these nourishments are not depicted in Figure A.5f, the spatial domain value of five transects remains unchanged.

Upon comparing the nourishment data from Rijkswaterstaat, as shown in Figure A.5e (Appendix D), with the shoreline change shown in Figure A.5f, it is clear that not all nourishments are reflected in the data. Over the period spanning from 1985 to 2020, three types of nourishments were implemented along the Delfland coast: Beach, Shoreface, and Dune nourishment. Particularly noteworthy is the visibility of beach nourishments in the SDS data, indicating that these nourishments are likely to be identified by the nourishment detection algorithm compared to the other types of nourishments.

# B

# Expansion Result Cases

This section will provide a more comprehensive analysis of the outcomes of the treated cases discussed in Chapter 4. It aims to offer additional background information and present a detailed overview of the steps involved in the SHORECAST model, as explained in Chapter 3. The treatment of the Nouakchott cases is covered in Sections B.1 and B.2. Section B.3 contains the results of Aveiro, while Section B.4 focuses on the Delfland coast.

## B.1 Results - Nouakchott North

The Nouakchott North coastal cell contains 27 transects starting from the harbour in the south to the north (*BOX_142_001_51* to *BOX_142_001_25*), as shown in Figure 4.3a. The shoreline between the southern and northern transects is roughly 13 km long and was determined with the mean distance between transects described in Section 3.3.4. The period used to achieve the Longshore Sediment Transport is from 1984 to 2021. Figure B.2 shows the coordinate system along the shoreline of the Nouakchott North case. At the origin, the harbour is positioned. This coordinate system will be used in this Nouakchott North study. Because of this coordinate system, sediment transport flows positively from left to right and negatively from right to left.

In an optimal situation, this research area should contain 1026 coastline points (38 years of shoreline positions along 27 transects) obtained by SDS. However, there are 172 empty spots, indicating that 16.76% of the dataset is missing. This is illustrated in a matrix format as displayed in Figure B.3a, where the empty spots are the grey cells. These empty spots are the result of the lack of data. One of the reasons could be due to not having enough clear satellite images to set up an annual composite and to extract the shoreline position, as described in Section 2.3. A closer look at Figure B.3a shows the spatial range between $-50$ and 1050 metres. In Figure B.3, the 1984 shoreline position is used as a reference point. The 1984 shoreline position was set to zero, and all subsequent years' coastal positions were calculated using the 1984 shoreline position. In 1986 and 1987, the shoreline is retreated at some transects, as shown with the dark red spots in Figure B.3b.

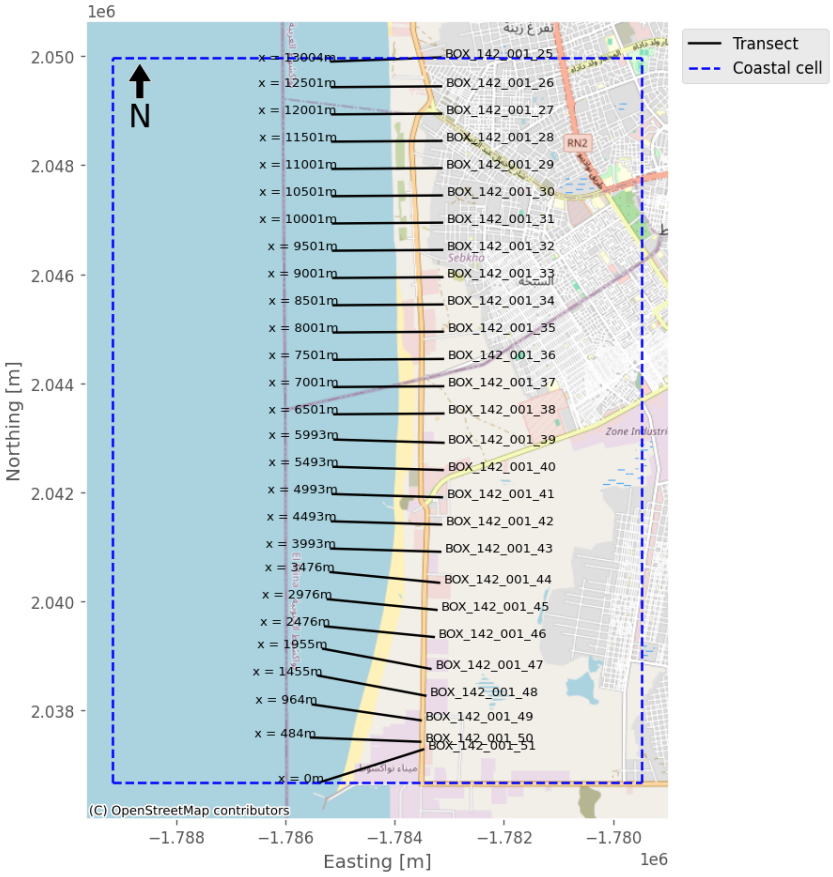


Figure B.1: Coastal cell for Nouakchott case. Inside the blue dashed line, the transects can be found as provided by the SDS dataset. Aside from the transect ID, the average measured distance from the south (the harbour) to the most northern transect is provided.

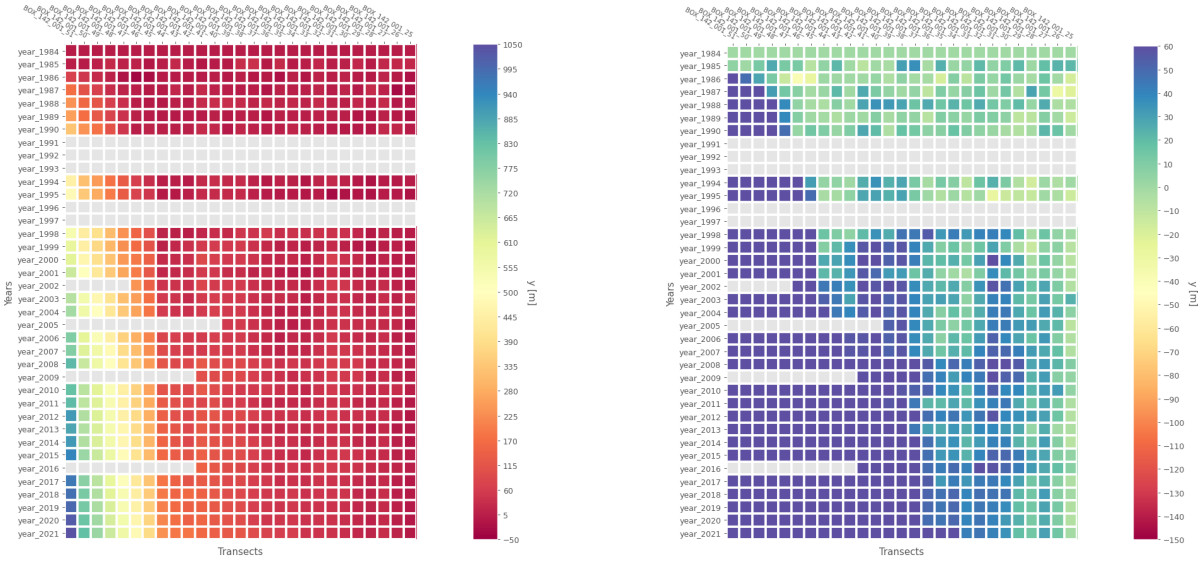


(a) (b)

Figure B.3: These two matrices represent the shoreline's position over time and space. In both images, the shoreline position from 1984 is set to zero, and all subsequent positions are based on this baseline. The left matrix (a) displays the SDS data before outliers are identified and removed. The right matrix (b) displays the same, but the spatial range is shorter than in Figure a. The spatial range is set from −50 to 210 metres.


Figure B.2: An visualisation of the coordinate system utilised along the Nouakchott North shoreline. Source: Google (2024).

### Outliers

Before applying the outlier methods as described in Section 3.3.1, a nourishment check will be executed to see if the data contains nourishments. No nourishments are detected in the Nouakchott North case. Next, two outlier methods (Standardised Residual and Shoreline Shift Detection methods) will be applied to the dataset to improve the accuracy of the still-to-be-derived Longshore Sediment Transport. The result of this method is presented in Figure B.4. Due to the outlier methods, more shoreline positions are missing because a shoreline position identified as an outlier will be removed from the data. The Shoreline Shift Detection algorithm is the most aggressive technique and has removed forty-one shoreline positions compared to the Standardised Residuals method, which has removed seven shoreline positions. As a result, 220 shoreline positions are missing in the dataset, which is 21.4 % of the data.

### Interpolation

The empty spots in the transects where the shoreline position is unknown must be filled to derive the LST. As mentioned in Section 3.3.2, linear interpolation is used to fill these gaps. Before interpolation, each transect's first and last year is checked to see if it contains a shoreline position. Otherwise, the linear interpolation will not fill up all the missing shoreline positions. If any shoreline position is missing from the first and last years of the matrix, they will be filled using spatial intersection. Figure B.4 illustrates the removed shoreline position of 1984 at transect *BOX_142_001_45*. In Figure B.5a, spatial intersections are used to fill the gap. Now that the start and last years of the matrix are complete, the gaps in the middle can be added by linear interpolation. Figure B.5b shows the results.

The fully interpolated matrix (Figure B.5b) shows that the shoreline gradually shifts towards the sea because red is less than blue. In addition to accretion in the cross-direction of the shoreline, sand accumulates in the longshore direction. The seashore position is gradually migrating to the right in these figures. The harbour's location is on the left side of the matrix (transect number *BOX_142_001_51*), indicating that sand is gradually accumulating in a northward direction.

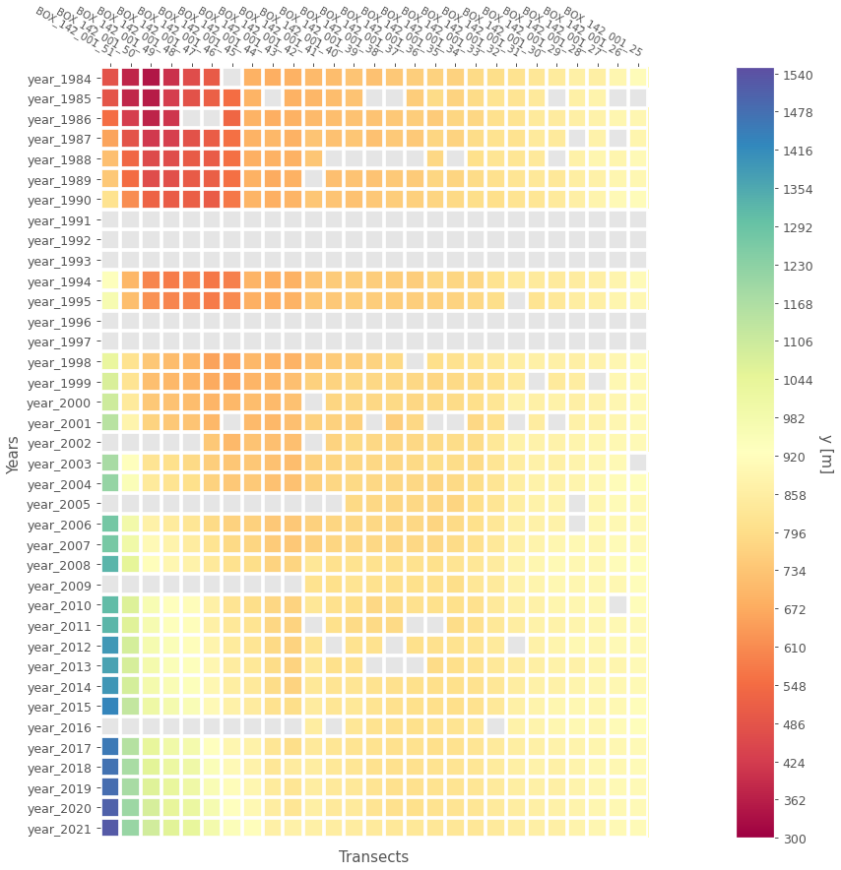


Figure B.4: The results of the outlier detection algorithms from Section 3.3.1 applied on the dataset visualised in a matrix format.

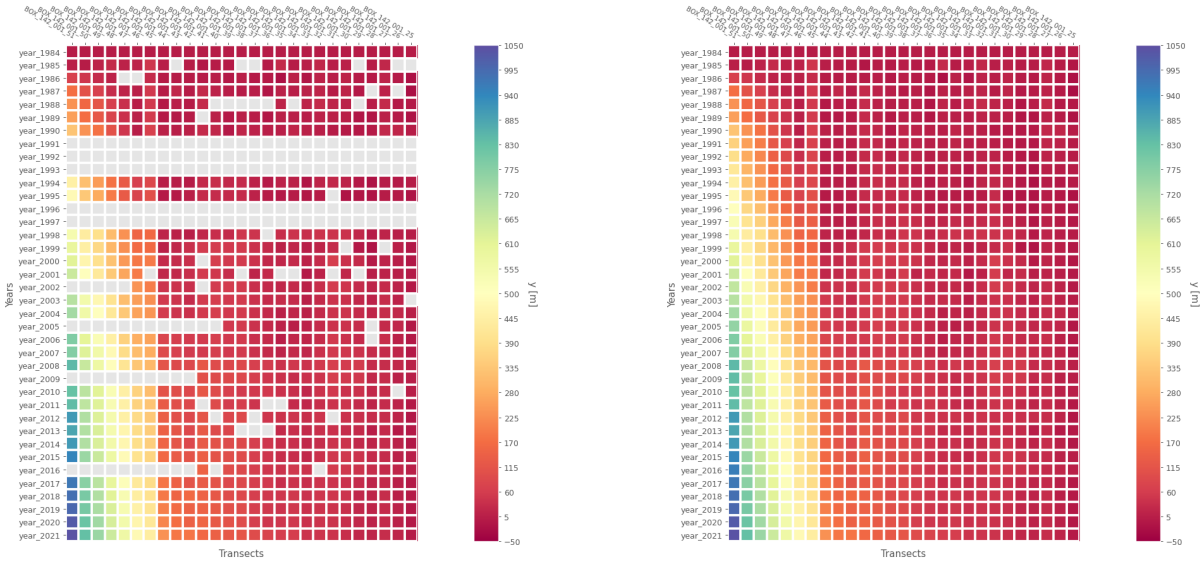


(a) (b)

Figure B.5: These two matrices depict the shoreline's position in time and space. In both images, the shoreline position from 1984 is set to zero and all following positions are based on the shoreline position of 1984. The left matrix (a) shows the shoreline locations following spatial intersection, whereas the right picture (b) displays the matrix with all shoreline positions after linear interpolation.

### Smoothing

Using the improved rolling mean method discussed in Section 3.3.3 on the interpolated data results in a more gradual migration of the shoreline position. However, the first year (1984) and last year (2021) will be absent due to the smoothing factor $N = 5$ as indicated in Section 3.3.3. Figure B.6a shows the smoothing results. Another technique to observe the smoothing process is comparing the growth between years of the shoreline positions along the same transect. The results of these differences are illustrated in Figure B.6b, where the difference is marked with $\Delta y$. The shoreline is accreting on the left side of Figure B.6b, as shown in blue. This left side is also the location of Nouakchott's harbour. The spatial range of the right matrix is $-30$ to 30. On the right side of Figure B.6b, the shoreline is not eroding or accreting significantly, which could mean the shoreline is stable in the north.

Figure B.7 illustrates the movement of the shoreline through time along the Nouakchott shoreline from 1985 (blue) to 2020 (red). This figure illustrates that the shoreline is accreting at the harbour in the south. In contrast to the north, where the shoreline might be presumed to be stable because it migrates slowly. This is also visible in Figure B.6b.

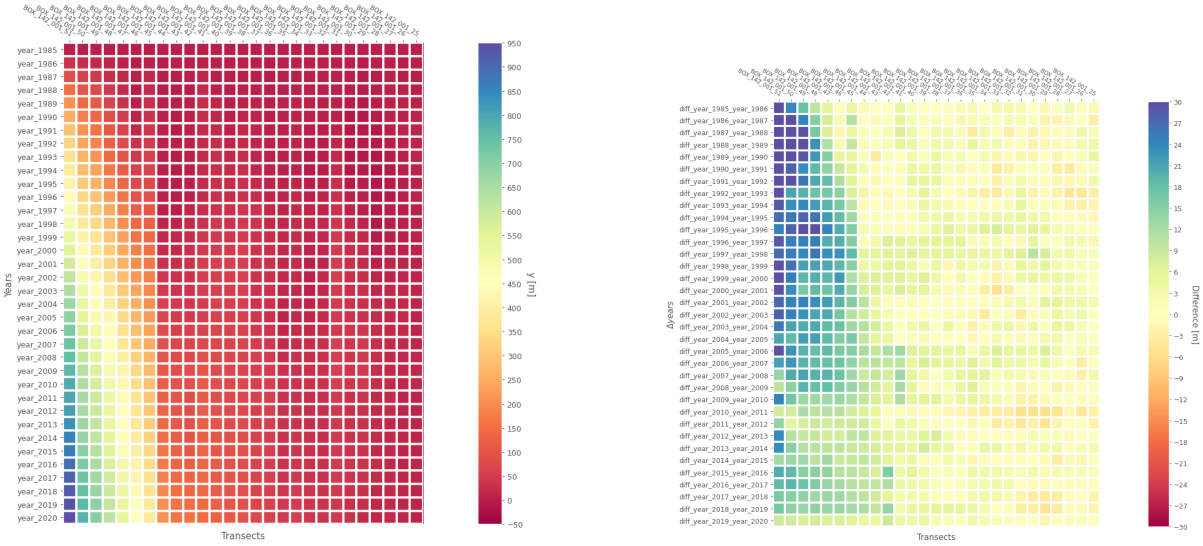


(a) (b)

Figure B.6: Here are two matrices shown. The left matrix (a) represents the result of smoothing the shoreline locations ($y$) with 1985 as the reference shoreline point. The right matrix (b) depicts the difference in coastline positions from the smooth shoreline matrix throughout the years ($\Delta y$).

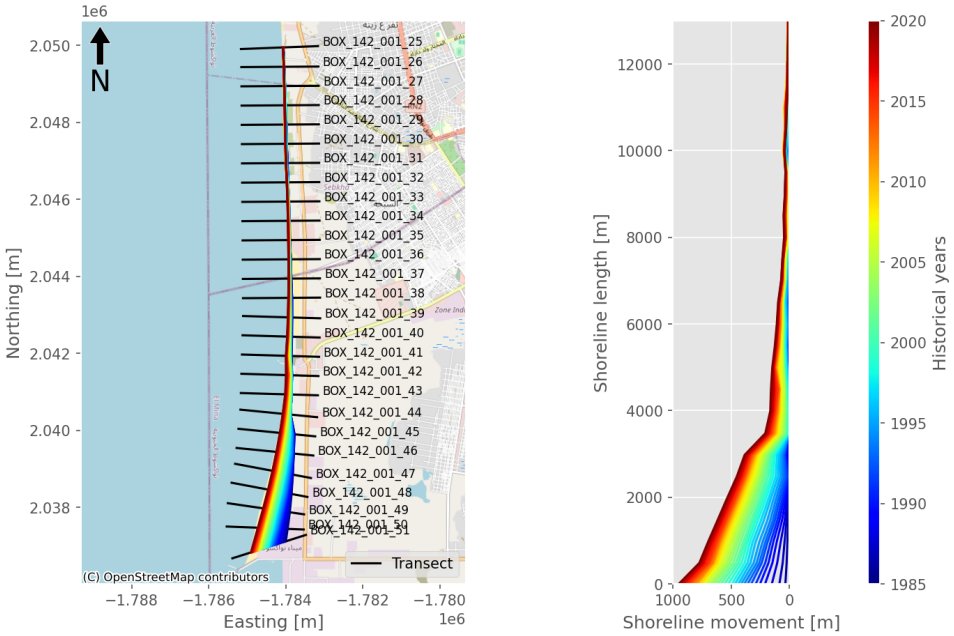


Figure B.7: The result of the smoothing procedure along the Nouakchott coastline, where blue represents the oldest year (1985) and red represents the most recent year (2020).

### Longshore Sediment Transport gradient

The Longshore Sediment Transport gradient is computed by multiplying the surface gradient ($\Delta A$) by the active height, as described in Section 3.3.6. The active height consists of two values: the depth of closure and the mean spring tidal range. The depth of closure may be obtained from Athanasiou et al. (2019) dataset (Figure 3.16). As a result, the closure depth near Nouakchott is 7.76 metres and the Mean Spring Tidal Range is 0.95 metre (Mirco-tidal regime), as illustrated in Figure B.8. The tide was determined using the model TPXO9 by Egbert & Erofeeva (2002). Furthermore, the figure shows a semi-diurnal tide pattern, which aligns with Elmoustapha et al. (2007). An active height of 8.71 metres is used to determine the littoral transport gradient.

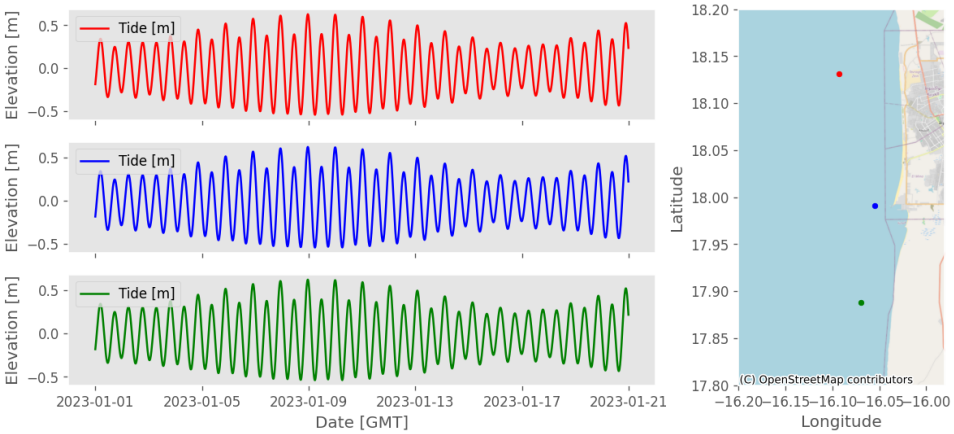


Figure B.8: The tidal cycle in Nouakchott at three locations for 20 days.

The surface change ($\Delta A$) is calculated between transects every two years. Figure B.9 depicts the accumulated surface gradient over two years across all transects. The figure illustrates a significant amount of accretion in the first 26 years. The accumulation surface gradient between 2010 and 2011 is relatively minimal compared to the rest. In addition, the highest accretion occurred between 1994 and 2010 compared to the other years. This is also visible in Figure B.6b.

The volume gradient ($\Delta V$) will be determined using two assumptions, as discussed in Section 3.3.6. These

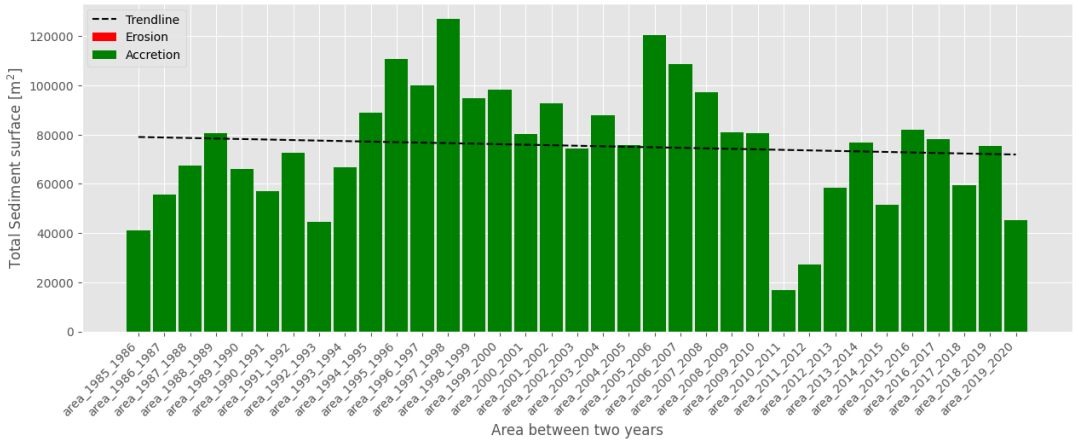


Figure B.9: The accumulative surface gradient over all transects between two years.

assumptions include that the shoreline's shape remains constant and moves horizontally. Multiplying the active height with the surface gradient yields the result shown in Figure B.10, graph C. Graph A displays the coastline gradient over two years, while graph B shows the surface gradient along the shoreline. The distance $X$ represents the mean distance (Section 3.3.4). The average over five years is shown for clarity. The harbour is located at point $X = 0$.

A considerable amount of sand accumulates between $X$=0 and 5000 metres. From 6000 metres to 13 km, the beach becomes more constant. However, it continues to accumulate because the values are above zero, but compared to the first 5 kilometres, the shoreline can be considered stable. This finding is consistent with Figure B.7. A simple test to see if the volume gradient is calculated appropriately is to compare the shapes of graphs B and C. These two graphs should look similar because each $\Delta A$ value is multiplied by a constant (active height), but the value on the y-axis is different. Both graphs appear identical in this example, indicating that the volume gradient has been calculated appropriately. On the other hand, graphs A and B should appear identical, but this is not the case. This is due to the placement of the SDS transect. The transects are not parallel, particularly those near the port ($X = 0$).

**Littoral transport**

As noted in Section 3.3.7, some boundary conditions are required to derive littoral transport from the LST gradient ($\Delta V$). Table 4.1 indicated that the Nouakchott case would have a single boundary condition. Figure B.11 shows the boundary situation at the Nouakchott harbour, where the breakwater is anticipated to prevent sediment bypassing.

Calculating sediment transport from $X$ at zero to $X$ at 13 km yields the result shown in Figure B.12. This chart illustrates a five-year average of sediment transport to enhance visualization. Figure B.12 indicates that the average sediment transport into the system is roughly $-0.66$ million m$^3$. Between 1987 and 1998, Elmoustapha et al. (2007) reported an annual sediment transport of -0.8 million m$^3$. As illustrated in the graph, the five-year average sediment transport has been decreasing over the years.

The sediment flow rate at $X$ = 13km ranges from 0.4 to 0.85 million m$^3$. Figure B.12 shows a shift in sand accumulation to the right. This is obvious because the slope of the lines between $X$ is zero and 6 km is becoming more gentle. This indicates that the shoreline accumulates from south to north.

In addition to determining Longshore Sediment Transport by shoreline movements throughout the years, the total surface area between the shoreline position of 1985 and 2020 can be computed and multiplied by the active height. Figure B.13 shows the volume change from 1985 to 2020, 23.01 million m$^3$ in 35 years, or approximately 0.66 million m$^3$ per year. This is consistent with the results in Figure B.12.

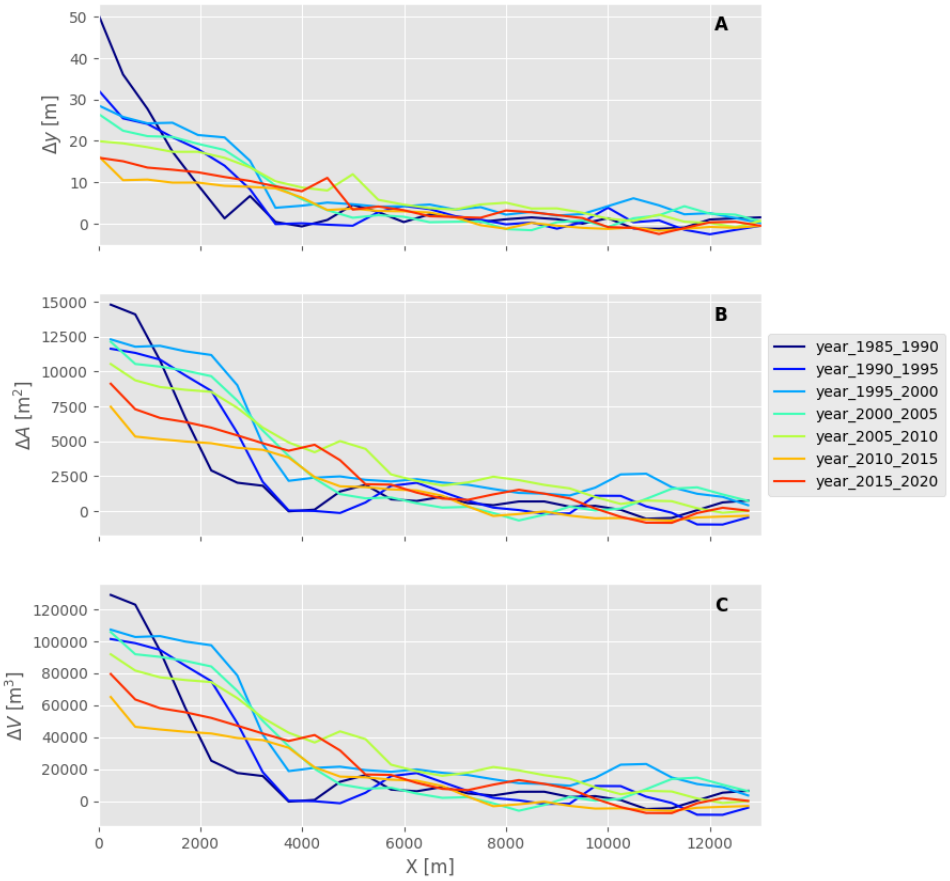


Figure B.10: Three graphs are presented along the same X-axis. The lines represent a five-year average. The first graph (A) displays the difference in shoreline ($\Delta y$). The second graph (B) exhibits the surface gradient ($\Delta A$), while the final graph (C) displays the littoral transport gradient ($\Delta V$).

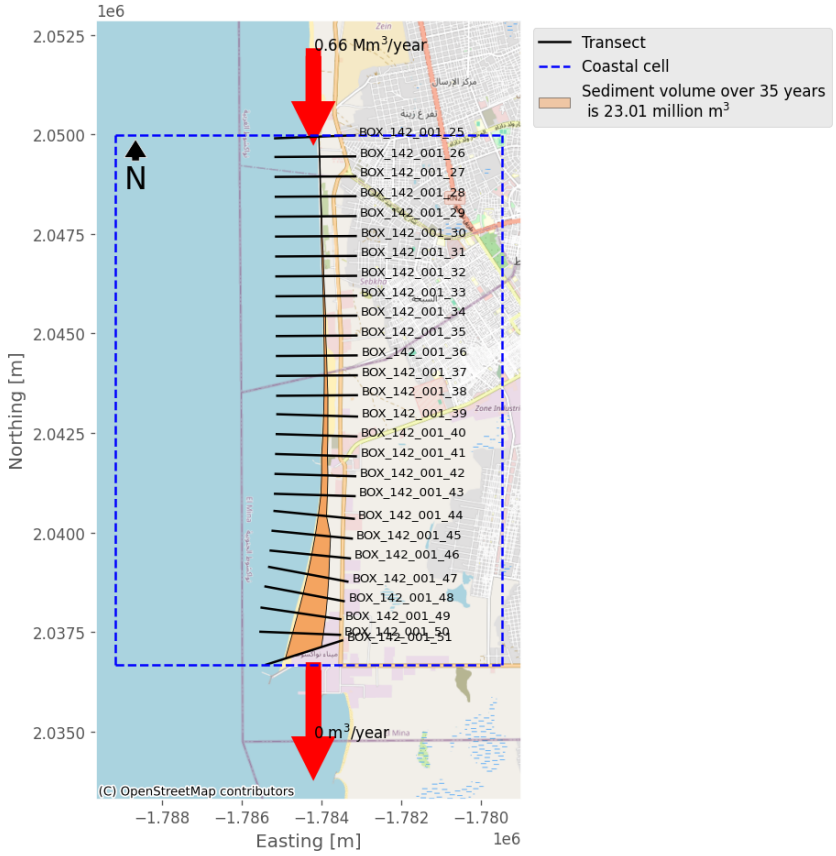


Figure B.13: The result of the sediment balance of the Nouakchott north coastal cell. The assumption is that there is no sediment transport at the bottom.

Figure B.11: A satellite image (March 2024) of the breakwater at Nouakchott Harbour. Assumed is no bypassing of sediment. Source: Google (2024).

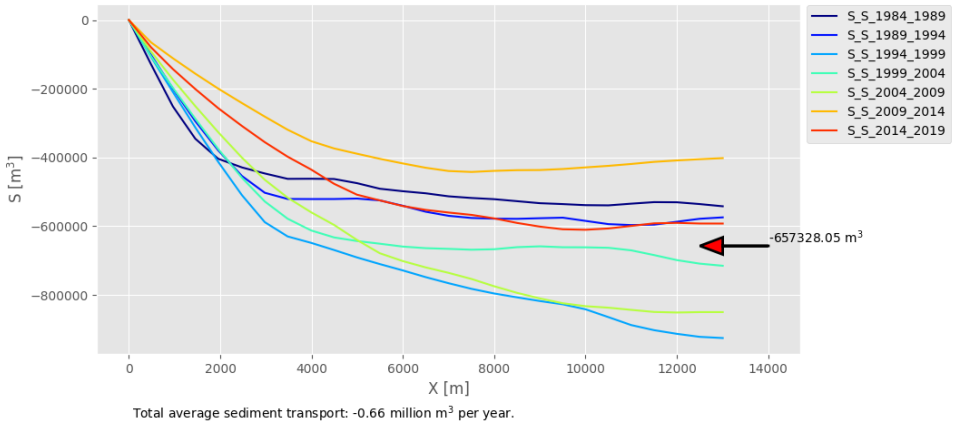


Figure B.12: The average five-year sediment transport at Nouakchott north, where $S = 0$ and $X = 0$ metres. At $X = 13000$ metres, the system receives approximately 0.66 million m3 of sediment yearly.

### Shoreline orientation

Besides deriving the historical littoral transport, the historical shoreline orientation can also be obtained. From the historical shoreline orientation, it is possible to see how it has migrated through time and whether the shoreline is stable. Applying the shoreline orientation method described in Section 3.4.1 on the Nouakchott North case gives the following result as shown in Figure B.14. The distances along the x-axis represent the mean distance between transects (Section 3.3.4). The port is located at $X$ is zero in this figure. The graphic illustrates that the shoreline orientation rapidly changes in the $0 < X < 5000$ metres range. This is also the accumulating zone. However, the shoreline orientation changed faster between 1985 and 2000 than in the recent decade. This is consistent with the visualisation in Figure B.7. The shoreline orientation is consistent throughout the $8000 < X < 13000$ metres range. The coastal orientation remains between 265 and 270 degrees. The shoreline orientation shows that the shoreline has become smoother over time. This is due to sediment accumulation at $X = 0$ (near the port) and movement along the shore to the north.

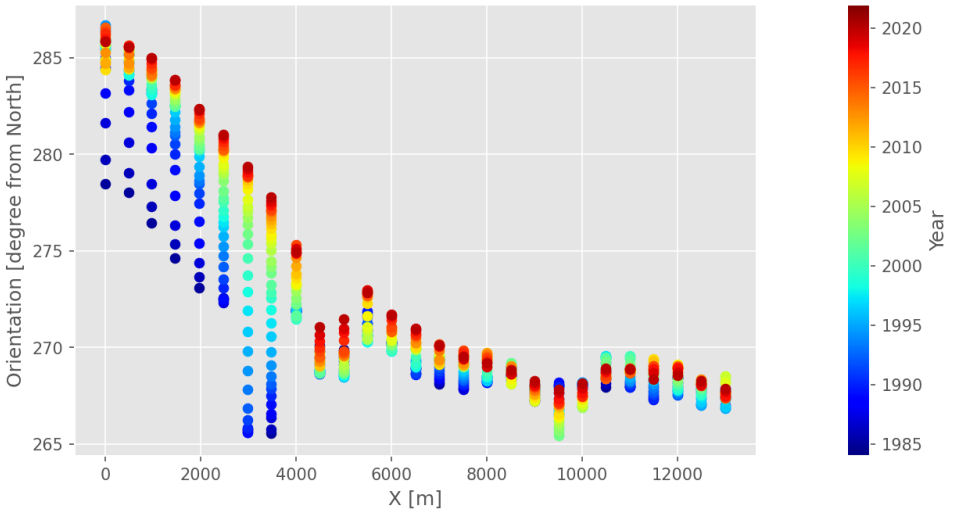


Figure B.14: A visualisation of coastline orientation of the Nouakchott North case from 1985 (blue) to 2020 (red). The port is located at $X = 0$.

### S-$\varphi$ relation

Combining the Longshore Sediment Transport with the shoreline orientation allows for investigating the relationship between the two. This is the so-called S-$\varphi$ relationship as explained in Section 3.4.2. Figure B.15a illustrates how the orientation affects sediment movement. It is feasible to see that sediment transport is high in some orientations but low in others. Higher orientations have a lower LST, which is consistent with Figures B.12 and B.14. Furthermore, Figure B.15a contains many dots between 265 and 270 degrees. These shoreline orientations correspond to the orientations in Figure B.14 between $X$ is 6 and 13 kilometres. However, the Longshore Sediment Transport range is more significant at this shoreline area as shown in Figure B.12. As a result, the wide spreading in Figure B.15a.

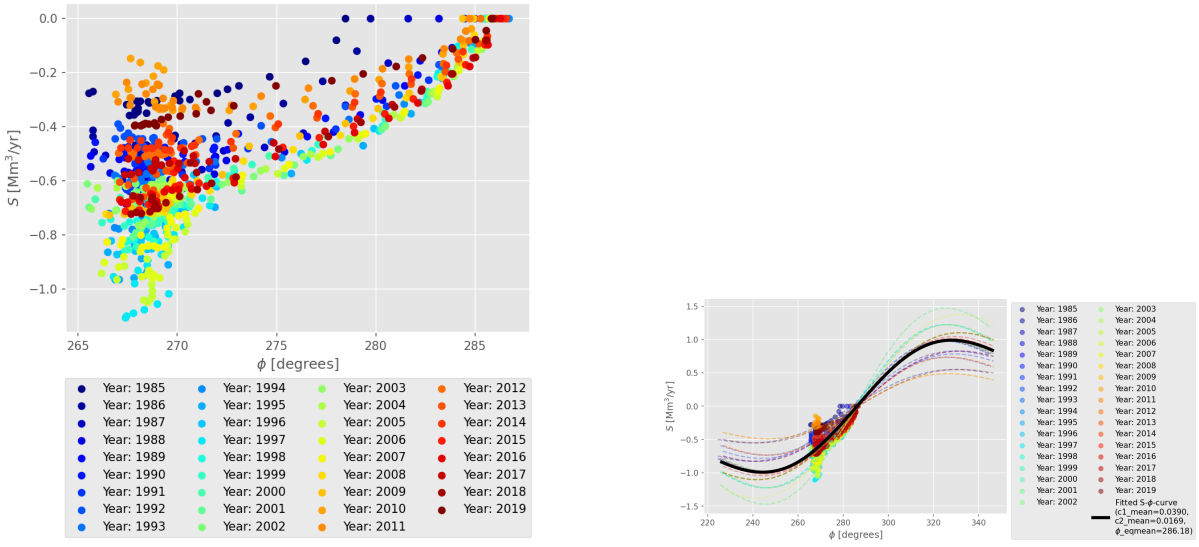


(a) (b)

Figure B.15: These two images demonstrate the shoreline orientation relative to the Longshore Sediment Transport. The left image (a) shows the shoreline orientation associated with the LST, whereas the right image (b) shows the fitted S-$\varphi$ relation per year and the mean (the black line).

To establish a connection between the Longshore Sediment Transport and the shoreline orientation, the data of Figure B.15a will be fitted through Equation 3.19. As discussed in Section 3.4.2, this equation includes three variables: $c_1$, $c_2$, and $\theta_{eq}$. The function uses yearly shoreline orientation and the

corresponding LST. The lowest RMSE value selects the best fit per year.

The black line in Figure B.15b represents the average fit across all fitted years. Equation B.1 determines the variables of Equation 3.19 by calculating their mean. This function's RMSE across the entire data is 0.06.

$$\begin{aligned} S(\theta) &= 0.0390 \cdot \theta_r e^{-(0.0169 \cdot \theta_r)^2} \\ \theta_r &= \theta - 286.18 \end{aligned} \tag{B.1}$$

Where $\theta$ represents the coastline orientation and $S$ represents the littoral transport. A check that can be done is to see if the amount of sediment at $X = 13000$ metres obtained with the formula (Equation B.1) is the same as what is found in Figure B.12. The littoral transport obtained as shown in Figure B.12 is -0.66 million $m^3$. The average shoreline orientation of the last three transects over 38 years is 267.96 degrees. Filling in this value into Equation B.1 gives a littoral transport of $-0.65$ million $m^3$, which aligns with each other.

### Future shorelines

With the acquired S -$\varphi$ relationship, as explained above, it can now anticipate how the coastline might evolve. It is assumed that the sediment transport inflow flux remains constant and that no sediment leaves the area externally, such as by humans digging up sand. Figure B.16 illustrates the projected coastline for the next 20 years beginning in 2020, using the approach given in Section 3.5 and Equation B.1. The prediction is made with a time step of half a year to be able to have a stable result, which is in line with the Courant number (3.21 in section 3.5).

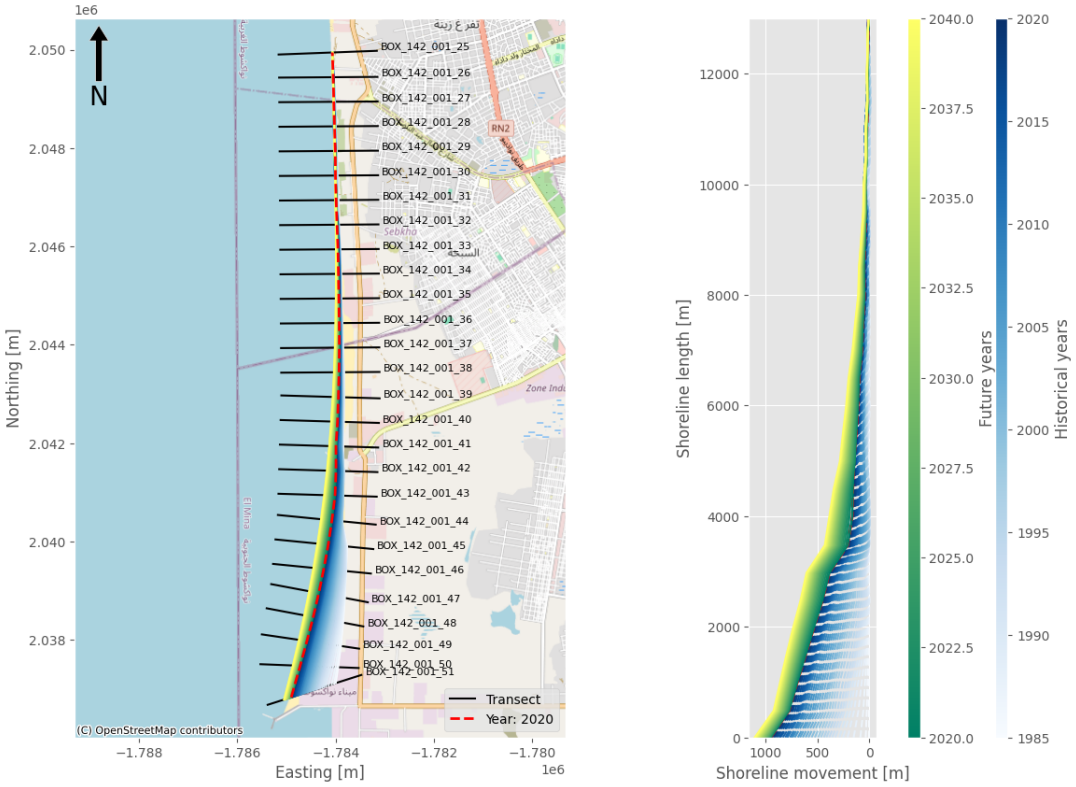


Figure B.16: The shoreline prediction for Nouakchott North. The historical movement (white to blue range) and the predicted shoreline position (green to yellow range).

One observation is that the shoreline will accumulate closer to the harbour during the next two decades. Furthermore, the sediment deposit migrates northwards, this is also visible in Figure B.17. Where the yellow line moves more to the left. It is important to note that this model does not account for sediment

bypassing at the harbour. There will be no sediment bypassing when the shoreline advances further out to sea. Another observation is that the shoreline remains in the same position as it has been throughout history. As a result, the northern shoreline remains steady over the last two kilometres.

Based on the results above, the future shoreline positions can be estimated in the Nouakchott North case. Therefore, sub-question three is answered as was formulated in Section 1.3.

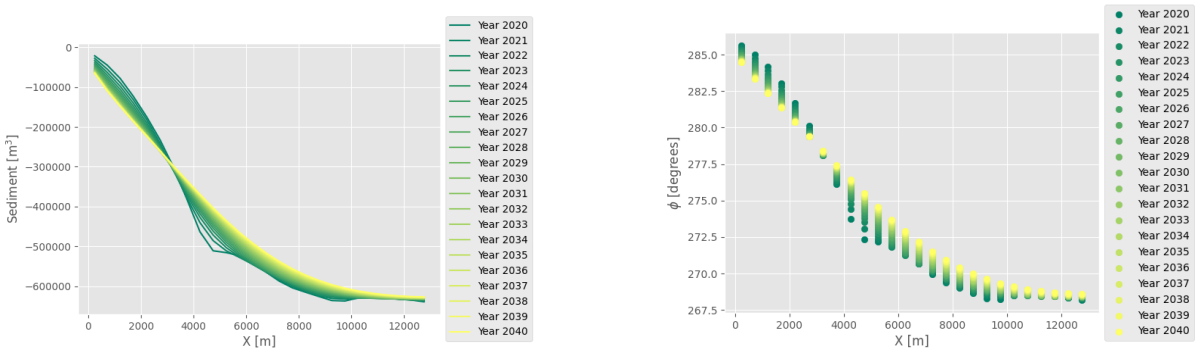


(a) (b)

Figure B.17: The two figures display the expected Longshore Sediment Transport (a) and shoreline orientation (b).

## B.2 Results - Nouakchott South

In the Nouakchott South coastal cell the shoreline has the same length as the North coastal cell. Starting from the south at transect *BOX_142_000_17* to *BOX_142_001_54*. The Nouakchott's harbour in the north is next to transect *BOX_142_001_54* as shown in Figure B.18. Along these 13 kilometres, 27 transects are placed as provided from the SDS dataset (Section 2.3) and contains shoreline positions from 1984 to 2021. The 13-kilometre shoreline was determined with the mean distance between transects described in Section 3.3.4. The coordinate system used for the Nouakchott south case is shown in Figure B.19, where the harbour is positioned at $X$ is 13 km. Because of this coordinate system, sediment transport flows positively from left to right and negatively from right to left.

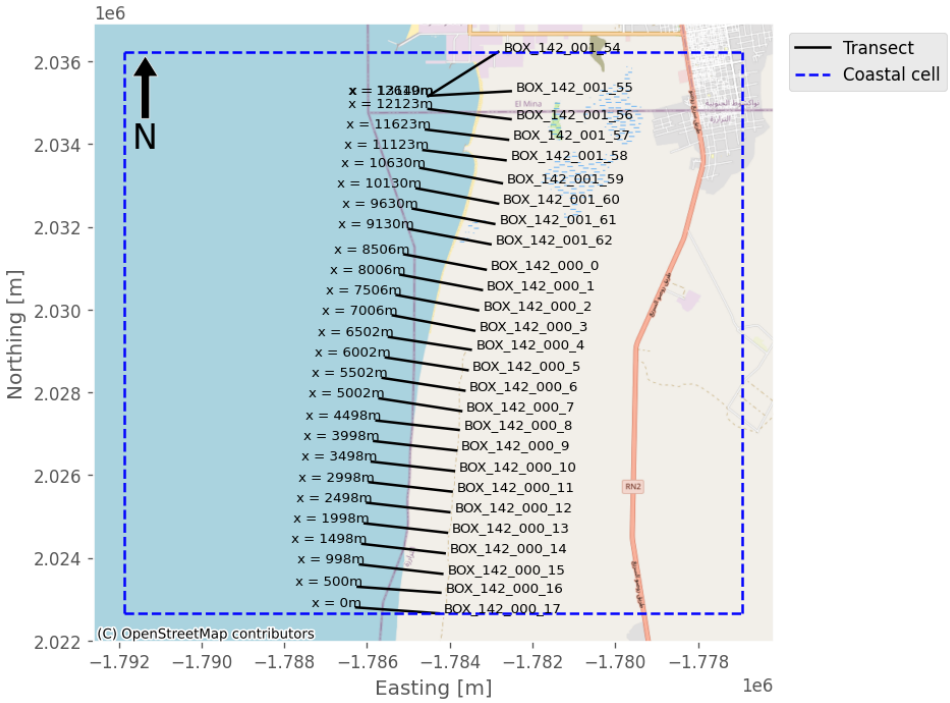


Figure B.18: A visualisation of the Nouakchott sourth coastal cell with the transects provided by the SDS dataset inside the cell. Aside from the transect ID, the average distance from the south to the most northern transect (the harbour) is provided.

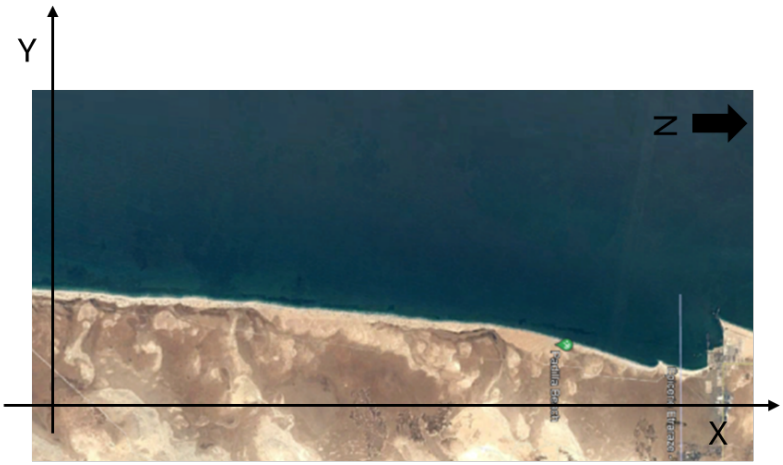


Figure B.19: The coordinate system utilised along the Nouakchott North shoreline. Source: Google (2024).

Ideally, this research area should include 1026 shoreline positions obtained by SDS. However, there are 217 blank locations, indicating that 21.15% of the dataset is missing. Figure B.20a shows the obtained and blank shoreline positions in a matrix format. Section 2.3 explains that a lack of good data causes empty spaces. The spatial range in Figure B.20a ranges from -750 to 90 metres, with the shoreline position from 1984 to zero. All shoreline positions after 1984 utilise the 1984 position as a reference. Looking at both matrices in Figure B.20 shows that the shoreline is retreating quite a lot near the harbour (the right side of the matrix) and that this erosion is steadily migrating to the left, as the red colour is spreading more to the left.

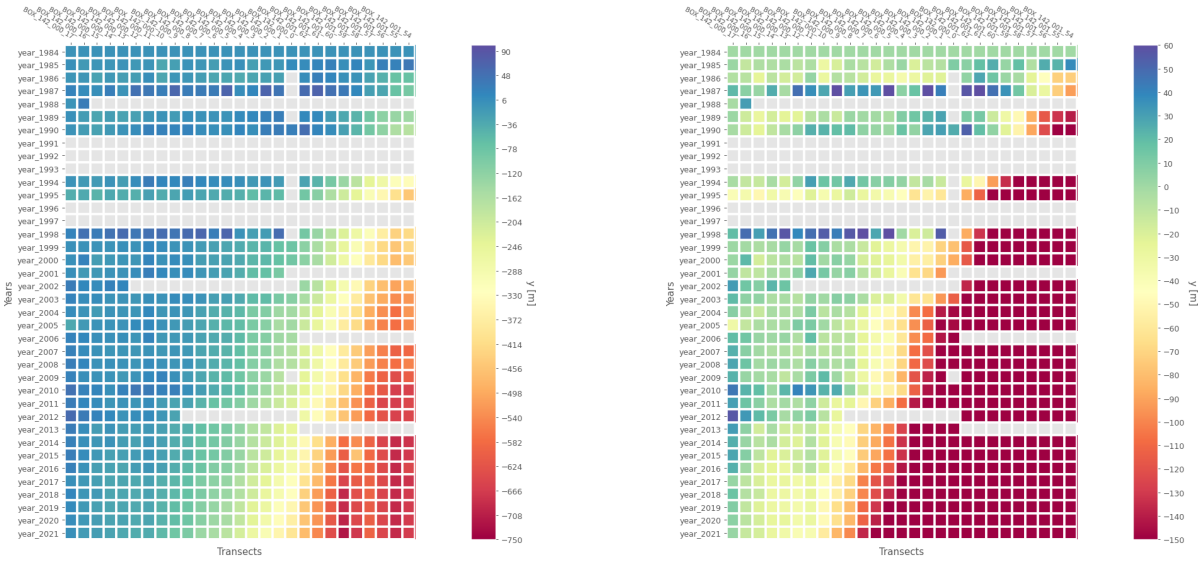


(a) (b)

Figure B.20: These two matrices represent the shoreline's position over time and space. In both images, the shoreline position from 1984 is set to zero, and all subsequent positions are based on this baseline. The left matrix (a) displays the SDS data before outliers are identified and removed. The right matrix (b) displays the same, but the spatial range is shorter than Figure a. It has been set from −150 to 60 meters.

### Outliers

Figure B.20 shows that the shoreline is retreating significantly. Therefore, the government could have taken anthropological measures to reduce erosion, such as nourishment. Using the nourishment algorithm shows that no measures have been taken, as visualised in Figure B.21a. However, between 1986 and 1987, the shoreline position increased by more than 40 meters, as shown by the blue-green colour in multiple places. However, there were no five transects next to each other to qualify it as nourishment. Therefore, the colour is not yellow.

Two methods for detecting outliers on the Nouakchott South dataset will be applied. The results of this analysis is presented in Figure B.21b. Due to the outlier method, Figure B.21b shows more empty spots than Figure B.20. Due to the outlier method, two shoreline positions from 1984 have been deleted. In total, 16 shoreline positions are detected as outliers and are removed from the dataset. Two hundred thirty-three shoreline positions are blank, representing a 7.4% increase. It is worth noting that this increase is less than that observed in the Nouakchott North case, which had a 21.4% increase in empty spots.

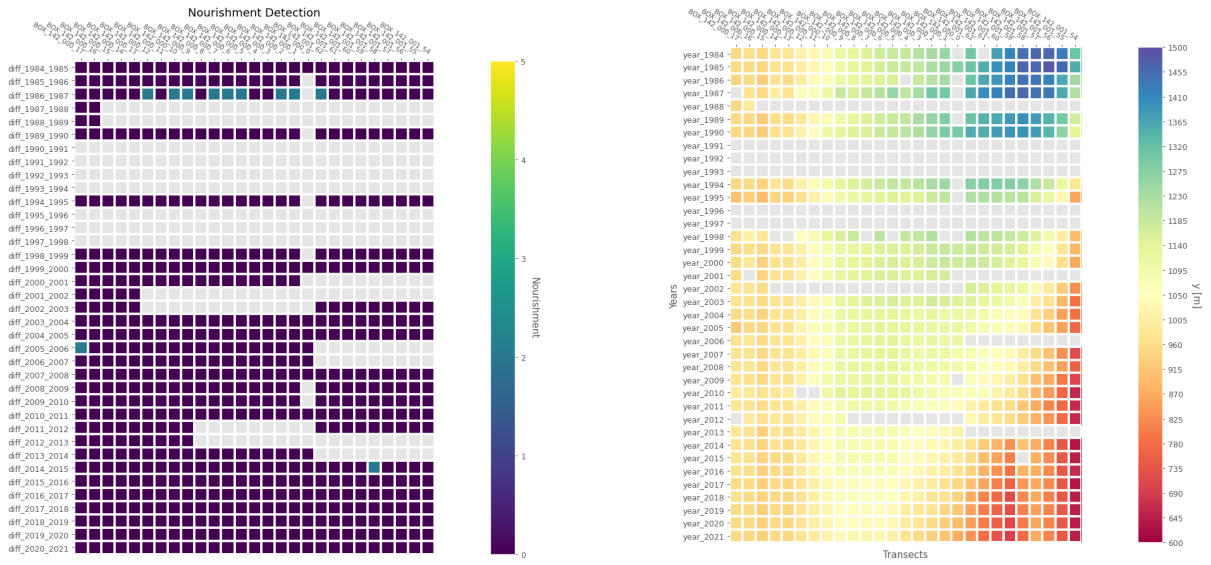


(a) (b)

Figure B.21: The left matrix short the result of the nourishment algorithm. The right image shows the result after the outlier method was applied.

### Interpolation

As in the Nouakchott North case, the blank places will be filled using linear interpolation. Spatial intersections will fill gaps between transects *BOX_142_000_0* and *BOX_142_001_61* in 1984. Figure B.22a displays the results of the spatial intersection approach of shoreline positions in 1984. Now that the first and last year are known, the blank spots in the middle of the matrix (Figure B.22a) can be filled. The right matrix in Figure B.22 shows the outcome after linear interpolation. In addition, the shoreline position in both matrices is based on the shoreline position in 1984. Figure B.22b depicts an erosion pattern over time (from top to bottom, the colour changes from blue to red), with erosion moving to the left. The port is positioned on the right side of these matrices.

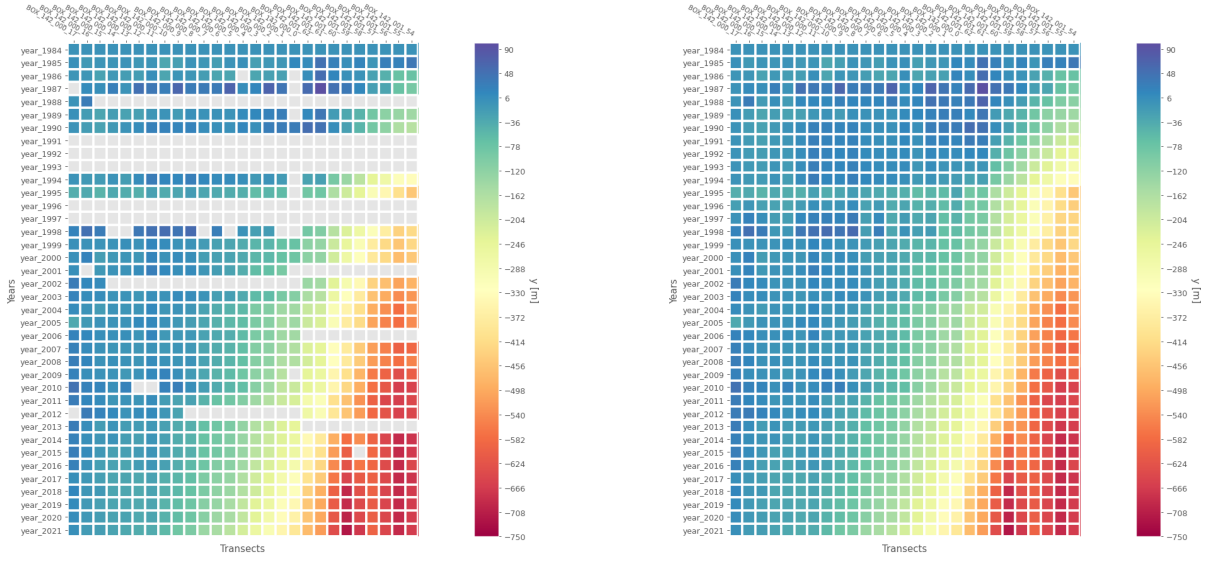


(a) (b)

Figure B.22: These two matrices depict the shoreline's position in time and space. In both images, the coastline position from 1984 is set to zero, and all following positions are based on that baseline. The left matrix (a) depicts the shoreline locations following spatial intersection, whereas the right picture (b) displays the matrix with all shoreline positions after linear interpolation.

### Smoothing

Applying the smoothing method on the interpolated data leads to a more gradual shoreline migration. However, the first year (1984) and the last year (2021) will be missing due to the smoothing factor $N = 5$. Figure B.23a shows the smoothing result. Another method for observing the smoothing process is to compare annual growth rates. This can be accomplished by calculating the difference between the coastline positions. Figure B.23b shows the results. The spatial range of the right matrix is $-30$ to 30 metres. Figure B.23 illustrates severe erosion on the right side of the matrix. Furthermore, the left side of the matrix does not appear to degrade or accrete. As a result, the southern shoreline (the matrix's left side) is considered stable.

Figure B.23b shows that the difference between the shoreline positions at the last four transects on the right side of the matrix suddenly became yellow. This yellow colour means that the shoreline is not eroding or accreting. As a result, it could be indicated that the shoreline at these four transects became stable after 2013. This is also visible in Figure B.24. However, Figure B.23b shows significant erosion after four transects from right to left. Figure B.24 displays the movement of the shoreline over time along the Nouakchott south shoreline. The blue in this image illustrates 1985, and the red represents 2020. The figure shows how the shoreline is eroding at the harbour. In contrast, the southern shoreline may be assumed to be stable because it moves slowly.

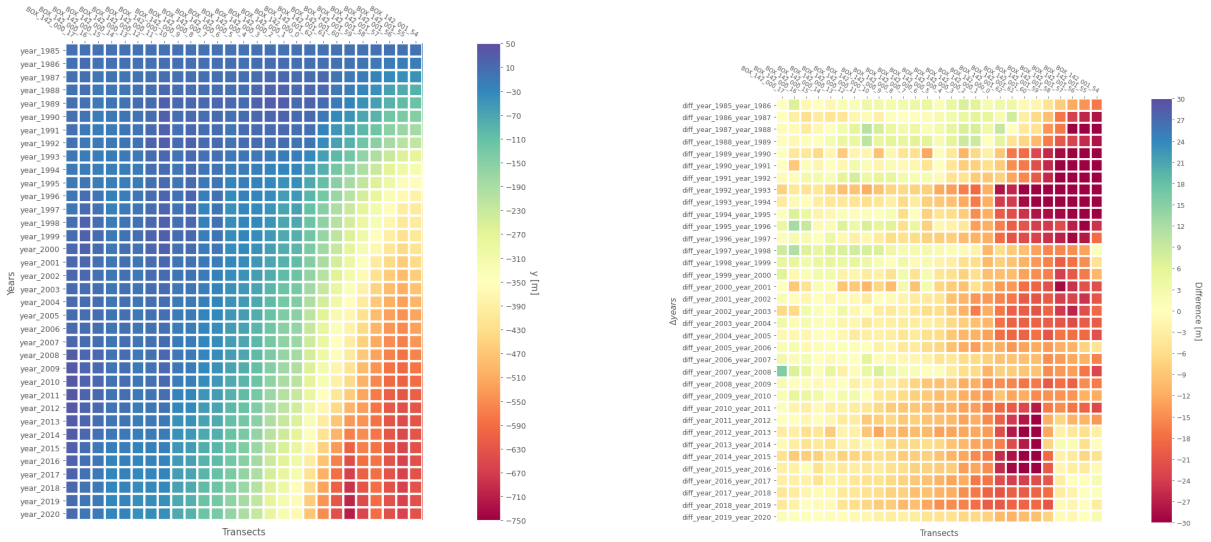


(a) (b)

Figure B.23: Here are two matrices shown. The left matrix (a) represents the result of smoothing the shoreline locations ($y$) with 1985 as a reference. The right matrix (b) shows the difference in coastline positions from the smooth shoreline matrix throughout the years ($\Delta y$).

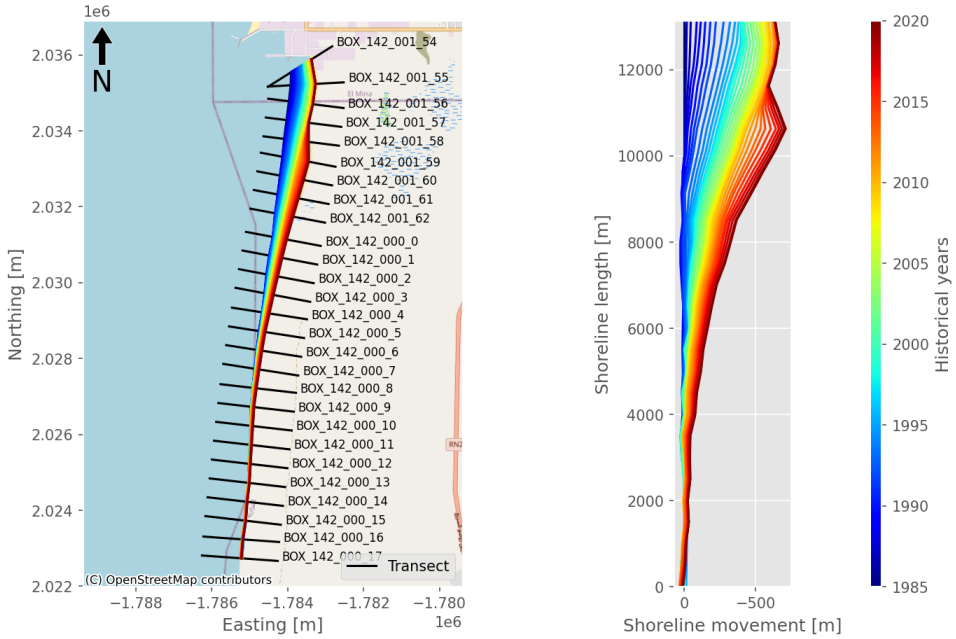


Figure B.24: The result of the smoothing procedure may be seen along the Nouakchott coastline, where blue represents the oldest year (1985) and red represents the most recent (2020).

### Longshore Sediment Transport gradient

The Longshore Sediment Transport gradient is computed by multiplying the surface gradient ($\Delta A$) by the active height. The active height consists of the depth of closure and the mean spring tidal range. The depth of closure obtained from the dataset of Athanasiou et al. (2019) (illustrated in Figure 3.16) along this coast is 7.76 metres. The mean spring tidal range is 0.95 metres (micro-tidal regime) as obtained from the TPXO9 model (Egbert & Erofeeva, 2002) and is illustrated in Figure B.8. All in all, the active height is 8.71 metres.

The surface gradient ($\Delta A$) is computed between the transects every two years. Figure B.25 shows the erosion surface gradient over two years across all transects. It is noteworthy little amount of erosion that occurs throughout the first four years. After that, the erosion gradient accelerates dramatically. The erosion gradient was lower in the first four years since the harbour was not fully developed. Hence, sand was still present in the system. Since 1991, the Groyne has been constructed immediately south of the harbour. This could be a significant rise in the surface gradient (Elmoustapha et al., 2007).

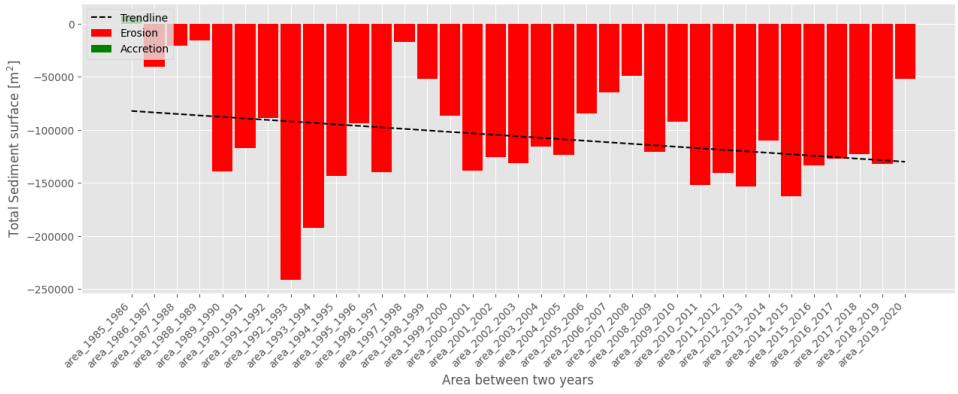


Figure B.25: The erosion surface gradient over all transects between two years.

Section 3.3.6 discusses how two assumptions can be used to calculate the volume gradient ($\Delta V$). These assumptions include the shoreline's consistent shape and horizontal migration. Graph C in Figure B.26 shows the volume gradient obtained by multiplying the active height ($H$) by the surface gradient ($\Delta A$).

Graph A illustrates the coastal gradient over two years, while graph B displays the surface gradient along the beach. The distance $X$ represents the average distance (Section 3.3.4). To make the graph easier to interpret, an average of five years is shown from 1985 to 2020. The harbour is located at $X = 13000$ metres.

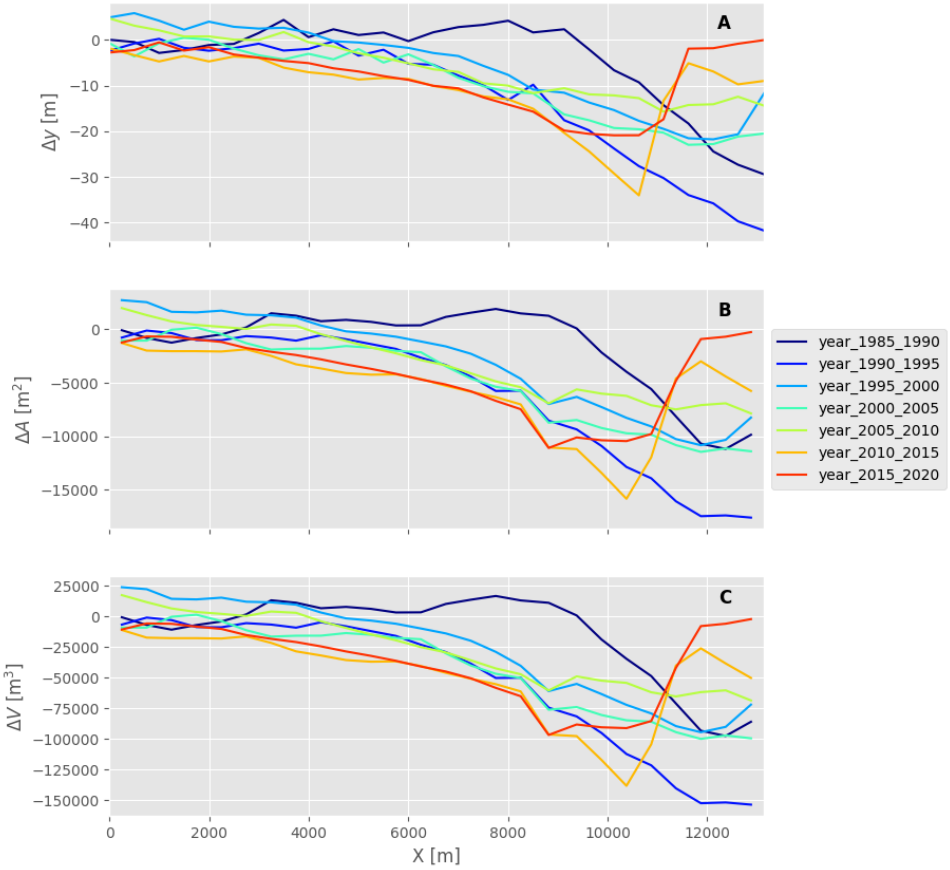


Figure B.26: Three graphs are presented. Graph A shows the shoreline difference between two years ($\Delta y$). The second graph (B) displays the surface gradient ($\Delta A$), while the final graph (C) displays the littoral transport gradient ($\Delta V$). $X$ is the cumulative mean distance between transects.

Figure B.26 shows three graphs with the same line but different values along the y-axis. The difference between $\Delta y$ and $\Delta A$ is due to the different lengths of the transects. The active height's multiplication factor is the difference between $\Delta A$ and $\Delta V$. During the first 25 years of the harbour, the right side saw considerable erosion at 10000 and 13000 metres. The pace of erosion has dropped since 2012, and it has been almost zero for the last five years. The build revetment between transects *BOX_142_001_58* and *BOX_142_001_57* prevents further erosion near the harbour, as illustrated in Figure B.27. The revetment was built in 2012.

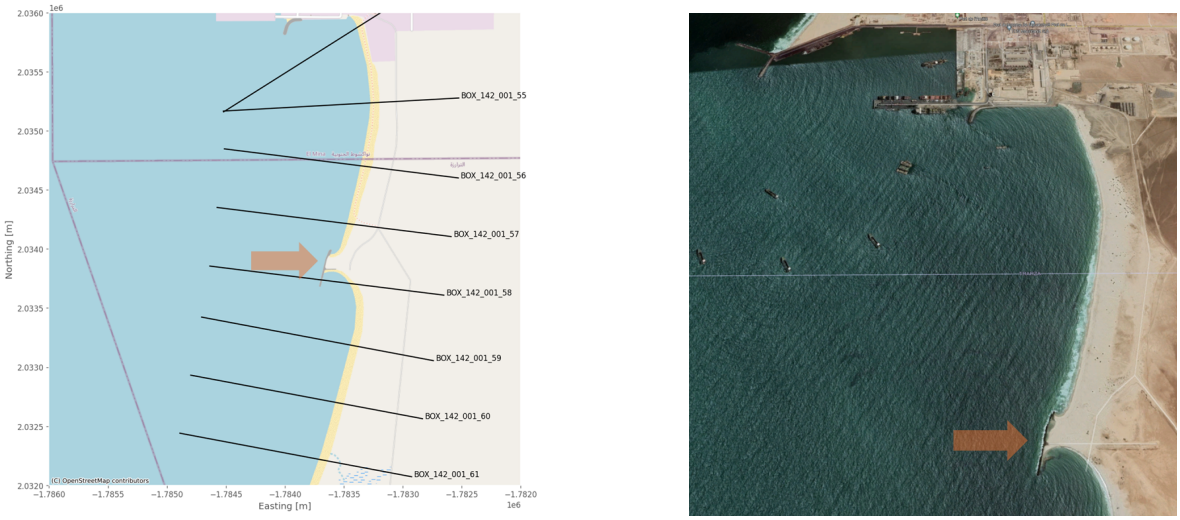


(a) (b)

Figure B.27: A visualisation of the shoreline revetment. The revetment is positioned between the transects *BOX_142_001_58* and *BOX_142_001_57*, as shown by the brown arrow in both images. Source figure b: Google (2024).

The small revetment created in 2012 parallel to the shoreline significantly impacts the beach between it and the port. In Figure B.26, the area between 11 and 13 kilometres has become stable due to this revetment. However, this same revetment caused significantly more erosion at the shoreline between 8 and 11 kilometres. Figures B.24 and B.26 illustrate the evolution of the shoreline over time. Furthermore, Figure B.23b shows that since 2013, the difference matrix has turned yellow at four transects near the port instead of red due to this build revetment.

### Littoral transport

As stated in Section 4.2.2, some boundary conditions are necessary to derive littoral transport from the volume gradient ($\Delta V$). According to Table 4.1, the Nouakchott case will have only one boundary condition. Figure B.11 shows the boundary condition of the Nouakchott harbour, which is the breakwater. The breakwater is assumed that it will prevent sediment bypassing from north to south. Determining littoral transport begins at the seaport in the north and progresses south. Figure B.28 shows the derived littoral transport along the southern part of the Nouakchott harbour.

With the harbour at $X = 13$km and $S = 0$, the annual sediment that leaves the system at $X = 0$ metres is approximately 0.92 million $m^3$ of sand. However, the amount of sediment moving out of the system at $X = 13$km fluctuates between -0.38 and -1.4 million $m^3$ in 38 years. In addition, the image illustrates the revetment constructed along the shoreline near the harbour. The revetment is visible because the sediment transport rate is almost zero at $X = 12$ kilometres. Furthermore, at $X = 0$, the lines are almost horizontal. This suggests the shoreline is stable, with no significant erosion or accretion.

In addition to determining Longshore Sediment Transport by shoreline movements throughout the years, the total surface area between the shoreline position of 1985 and 2020 can be computed and multiplied by the active height. Figure B.29 shows the volume change from 1985 to 2020, 32.36 million $m^3$ in 35 years, or approximately 0.92 million $m^3$ per year. This is consistent with the results in Figure B.28.

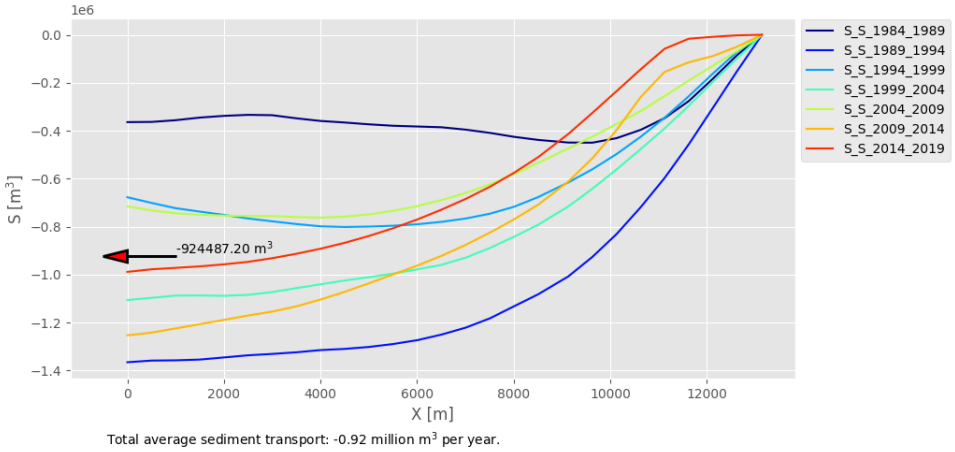


Figure B.28: The graphic depicts the average five-year sediment transport, where $S = 0$ and $X = 13$km. At $X = 0$ metres, approximately 0.92 million m3 of sediment leaves the system yearly.

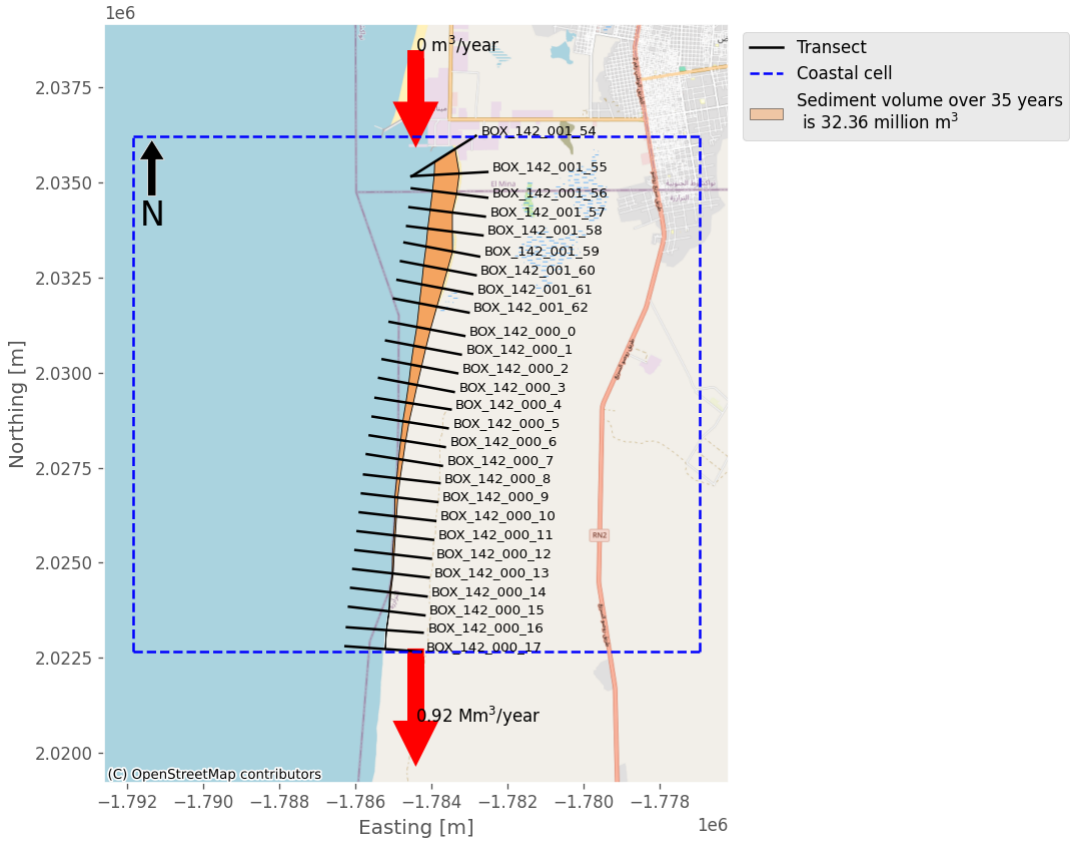


Figure B.29: The result of the sediment balance of the Nouakchott South's coastal cell. The assumption is that no sediment transport is at the top, but 0.92 million m$^3$ is leaving the coastal cell.

### Shoreline orientation

In addition to historical littoral transport, the historical shoreline orientation can be determined. Figure B.30 shows the result of applying the shoreline orientation method on the Nouakchott South case. Where the harbour is positioned at $X = 13000$ metres. Figure B.30 illustrates that the shoreline orientation decreases at a few kilometres starting at $X = 13$ km but increasing again after $X = 10$ km. The decrease occurs because the port's shoreline location is stationary, but the erosion is moving inland and towards the harbour, as seen in Figure B.24. The deepest erosion point has been achieved at around 10 km,

and the beach erodes less along the shoreline in the direction of $X = 0$. Furthermore, the water is more southwest of the shoreline for the first three kilometres, then northwest for the next ten to five kilometres.

Figure B.28 shows that the build revetment is also visible in the shoreline orientation. Because the orientation of the last five years is almost similar between $X$ is 12 and 13 km. Another clear sign of the presence of the revetment can be found at $X$ is 11 kilometres. The coastline orientation first rose before but drastically decreased after 2012 (as seen by the substantial space between the points). This quick change is due to a gap that forms shortly following the revetment. Figures B.24 and B.27 demonstrate these implications.

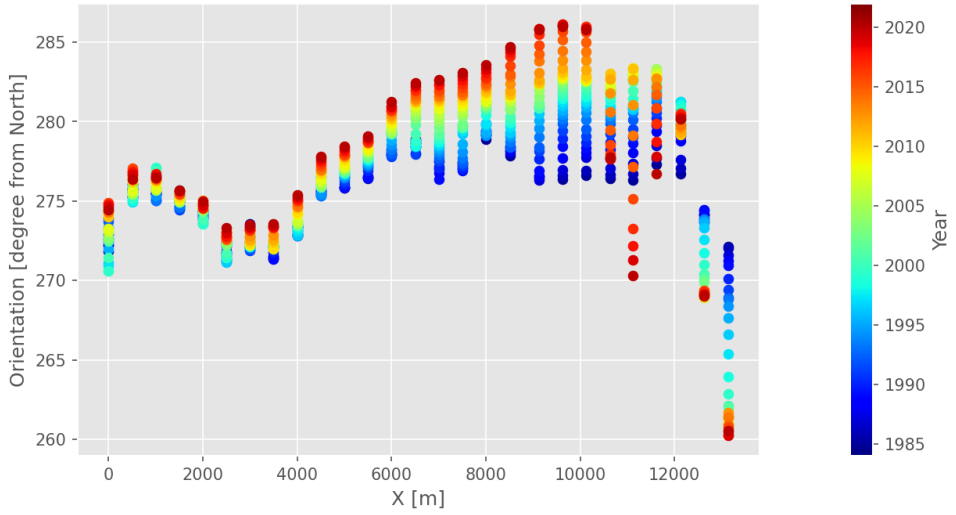


Figure B.30: A visualisation of coastline orientation of the Nouakchott South case from 1985 (blue) to 2020 (red). The port is located at $X = 13$ km.

### S-$\varphi$ relation

Combining the Longshore Sediment Transport with the shoreline orientation allows for investigating the relationship between the two. Figure B.31a illustrates the result where the orientation is plotted relative to the LST. Analysis of Figure B.31a reveals that a significant portion of the coastline orientation is between 270 and 290 degrees. However, there are some dots where $S$ is almost zero and the orientation is less than 270 degrees. These dots are related to the shape of the transect *BOX_142_001_54*. Aside from this transect, the dots reveal a little curving movement. As the shoreline orientation rises, the LST decreases and vice versa. This could be a sign that there is a relation between the orientation and LST.

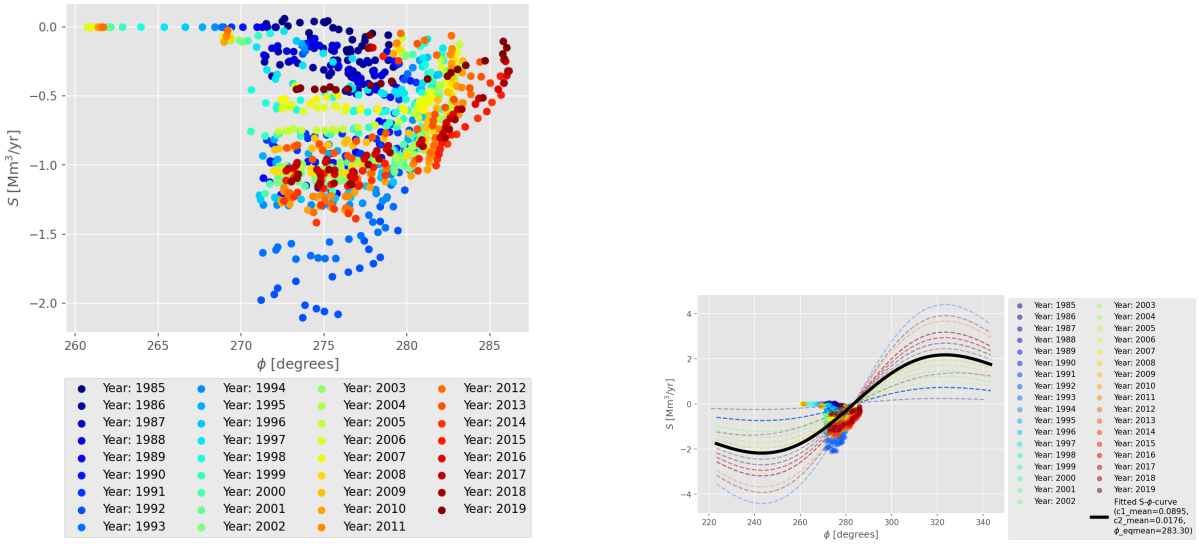


(a) (b)

Figure B.31: These two images demonstrate the shoreline orientation relative to the Longshore Sediment Transport. The left image (a) shows the shoreline orientation associated with the LST, whereas the right image (b) shows the fitted S-$\varphi$ relation per year and the mean (the black line).

To establish a connection between the Longshore Sediment Transport and the shoreline orientation, the data of Figure B.31a will be fitted by Equation 3.19. As outlined Section 3.4.2, this equation has three variables: $c_1$ $c_2$ and $\theta_{eq}$. The equation uses yearly shoreline orientation and the corresponding LST. The lowest RMSE value selects the best fit per year. The black line in Figure B.31b is the mean of all the fits. The result of these variables is shown in Equation 4.2. The function's RMSE across the entire data is 0.09 from the black line.

$$\begin{aligned} S(\theta) &= 0.0392 \cdot \theta_r e^{-(0.0171 \cdot \theta_r)^2} \\ \theta_r &= \theta - 299.49 \end{aligned} \tag{B.2}$$

$\theta$ represents the coastline orientation and $S$ represents the littoral transport. To validate the S-$\varphi$ curve, compare the sediment leaving the system on the left (Figure B.28) to the sediment transport determined by Equation B.2. The average shoreline orientation over the last three transects is 275.04 degrees, resulting in sediment transport of $-0.65$ million m$^3$. This value is lower than the $-0.92$ million m$^3$ seen in Figure B.28. This lower value could be attributed to revetment and the assumption of the active height.

To determine if the sediment transport from the S-$\varphi$ relation is equal, add the total LST gradient over 35 years and divide by 35 to calculate the yearly sediment transport gradient. As a result, the sediment transport gradient is $-0.92$ million m$^3$ year. This value is more consistent with the acquired value from Figure B.28 than the S-$\varphi$ relation value by an orientation from the last three transects.

### Future shorelines

With the acquired S-$\varphi$ relationship, as discussed above, it can now anticipate how the coastline might evolve. It is assumed that the sediment transport inflow flux remains constant and that no sediment leaves the area externally, such as by humans digging up sand. Figure B.32 shows the anticipated coastline over the next 20 years starting in 2020, based on the approach described in Section 3.5 and Equation B.2. The prediction uses a quarter-year time step ($\Delta t = 0.25$) to provide a stable outcome consistent with the Courant number (Equation 3.21 in Section 3.5).

According to the historical analysis, a revetment was built between the transects *BOX_142_001_58* and *BOX_142_001_57* as shown in Figures B.27. While making the prediction, it is assumed that the revetment will remain in its current position and will not be extended or removed. As a result, the shoreline

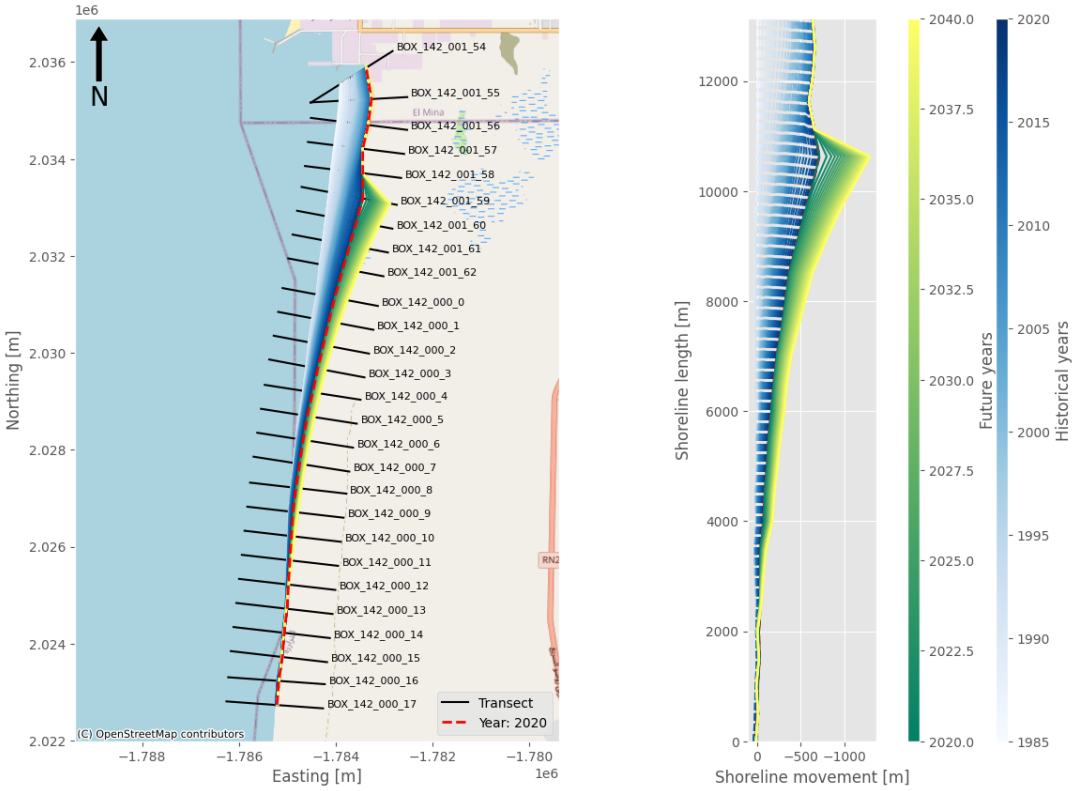


Figure B.32: The prediction of the Nouakchott South shoreline for the next 20 years. The historical movement (white to blue range) and predicted shoreline position (green to yellow range).

position along these two transects remains unchanged. However, the shoreline changes along the transect after the revetment (from north to south). This observation is also visible in Figure B.33a.

After the revetment, there will be a significant erosion just behind the revetment. This spit form causes the shoreline to erode more in the following transect until transect *BOX_142_000_12*, where the shoreline becomes more stable again. This is evident because the historical and prediction lines overlap each other. Figure B.33a illustrates that sediment movement approaches equilibrium around $X = 0$. This is also noticeable in the coastline orientation, as shown in Figure B.33b.

Figure B.33b shows four shoreline orientations that appear random. The four yellow dots represent coastline orientation in the stable region between the harbour and the revetment. These four points correspond to the coastline orientation in recent years, as illustrated in Figure B.30.

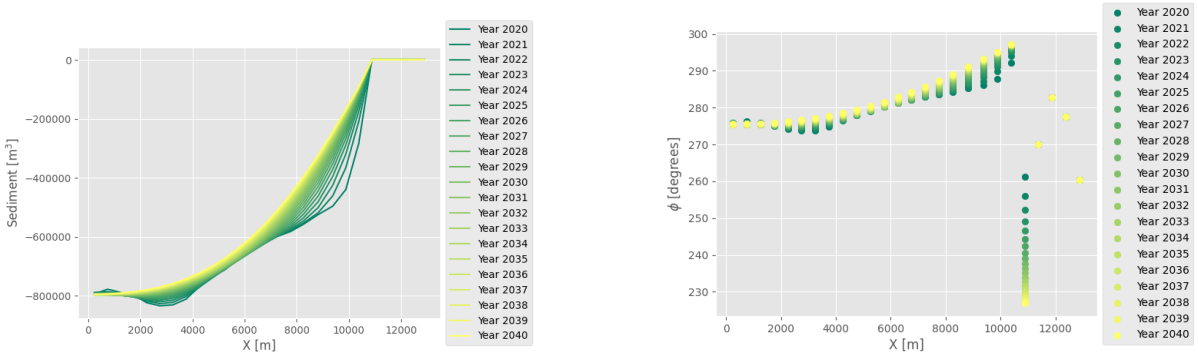


(a) (b)

Figure B.33: A visualisation of the predicted Longshore Sediment Transport (a) and shoreline orientation (b).

Based on the prediction model, the shoreline is expected to erode further. To reduce this erosion, anthropogenic measures can be applied. Such as a nourishment or a groyne to reduce erosion. More details regarding these interventions are provided in Appendix C.

## B.3 Results - Aveiro

Similar to Nouakchott, Aveiro can also be seen as a coastal cell. The shoreline in the coastal cell of Aveiro is approximately 10 km long, starting from the port in the south at transect *BOX_164_124_17* and ending at *BOX_164_126_18*, as displayed in Figure B.34. Along these 10 km stretch, 26 transects were placed based on the coastline position from OpenStreetMap (OSM) 2016. The dataset includes shoreline positions from 1984 to 2021. Figure B.35 shows the coordinate system along the shoreline of the Aveiro case. At the origin, the harbour is positioned. This coordinate system will be used in this Aveiro study. Because of this coordinate system, sediment transport flows positively from left to right and negatively from right to left.

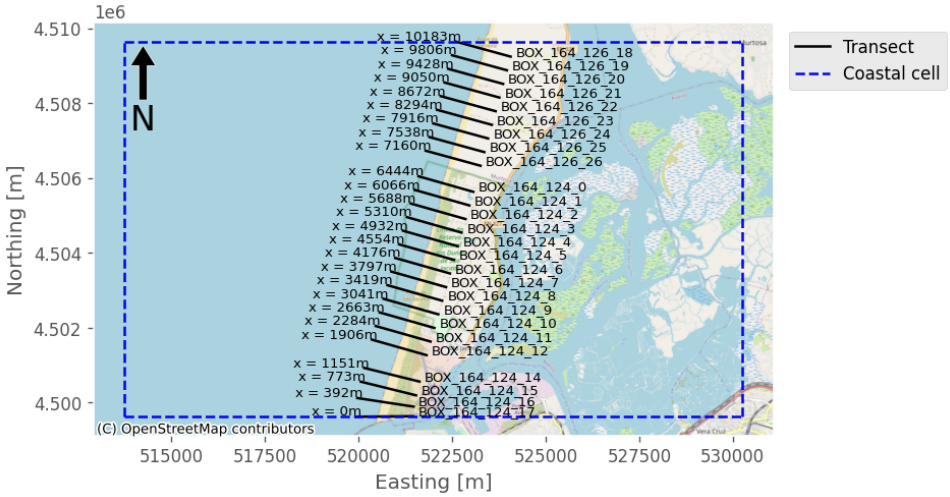


Figure B.34: A visualisation of the coastal cell of Aveiro with the transect inside the cell provided by the SDS dataset. Aside from the transect ID, the average measured distance from the south (the harbour) to the most northern transect is provided.

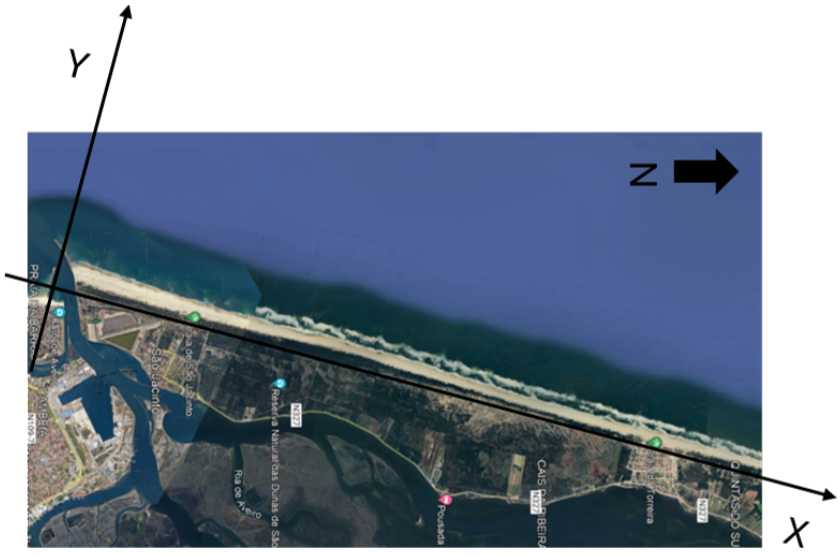


Figure B.35: The coordinate system utilised along the Aveiro shoreline. Source: Google (2024).

Ideally, this research area would have 988 shoreline points, representing 38 years of shoreline positions along 26 transects, obtained by SDS. Unfortunately, there are 194 missing spots, which means that 19.64% of the dataset is missing. This is illustrated in a matrix format, as displayed in Figure B.36a, where the empty spots are the grey cells. These empty spots are the result of the lack of data. A closer look at Figure B.36a shows the spatial range between $-150$ and 250 metres. The 1984 shoreline position

was set to zero, and all subsequent years' coastal positions were calculated using the 1984 shoreline position.

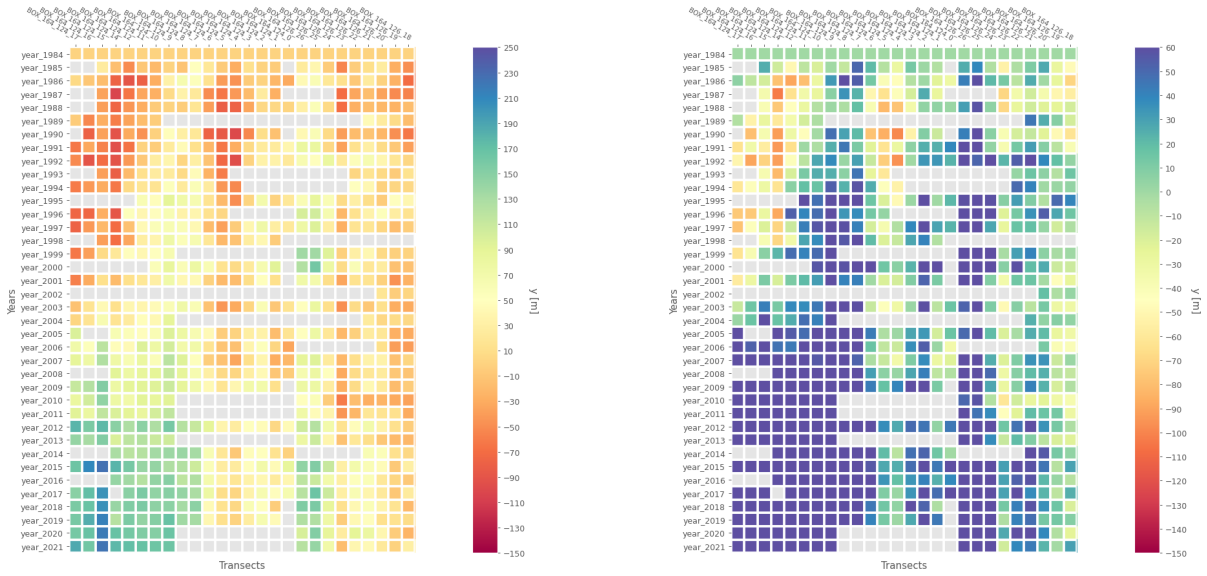


(a) (b)

Figure B.36: These two matrices represent the shoreline's position over time and space. In both images, the shoreline position from 1984 is set to zero, and all subsequent positions are based on this baseline. The left matrix (a) displays the SDS data before outliers are identified and removed. The right matrix (b) displays the same, but the spatial range is shorter than Figure a. It has been set from −150 to 60 meters.

In addition, Figure B.36a illustrates that the shoreline migrates seaward because the colour changes from red to green/blue. However, this occurs on the matrix's left side, adjacent to the harbour.

### Outliers

The two outlier methods (Standardised Residual and Shoreline Shift Detection) will be applied to the dataset to improve the accuracy of still-to-be-derived LST. Applying the two outlier methods on the dataset gives the following result as illustrated in Figure B.37. Due to the outlier methods, more shoreline positions are missing because a shoreline position identified as an outlier will be removed from the data. The Shoreline Shift Detection algorithm is the most aggressive technique and has removed thirty-nine shoreline positions compared to the Standardised Residuals method, which has removed five shoreline positions. As a result, 238 shoreline positions are missing in the dataset, which is an increase of 22.68 %.

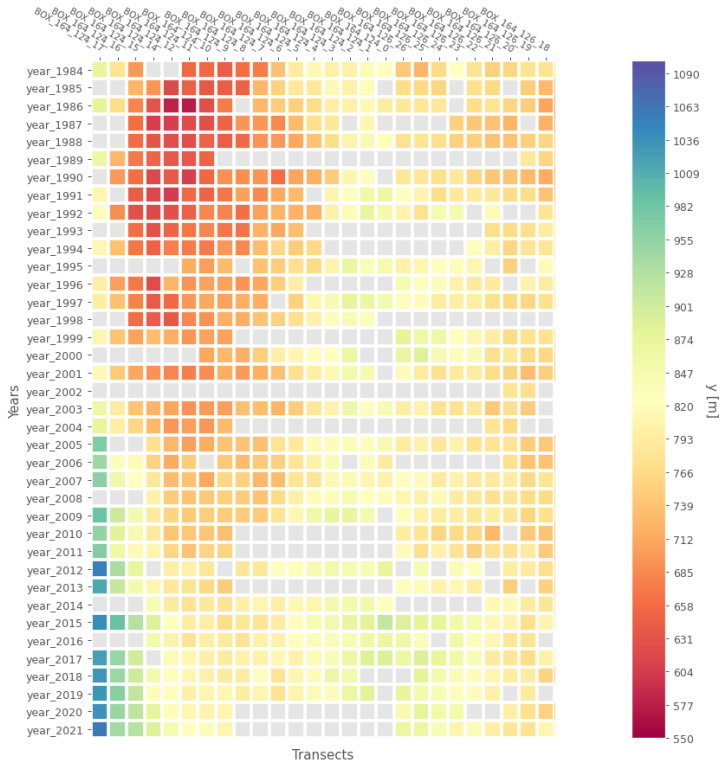


Figure B.37: The result of the outlier methods in a matrix format.

### Interpolation

Upon comparing Figure B.36 with Figure B.37, it becomes visible that shoreline positions are also missing in Figure B.37 for the year 1984. This implies that both matrices suffer from missing shoreline positions in the last year of observation. Filling in the blank spots is necessary to derive the littoral transport (Section 3.3.2). The transects that will be filled with spatial intersections are *BOX_164_124_16*, *BOX_164_124_14*, *BOX_164_124_12*, and *BOX_164_124_7* until *BOX_164_124_0*. Figure B.38a shows the spatial intersection results. Now that the first and last years of the matrix (Figure B.38a) are complete, the gaps in the middle can be added by linear interpolation. Figure B.38b shows the results.

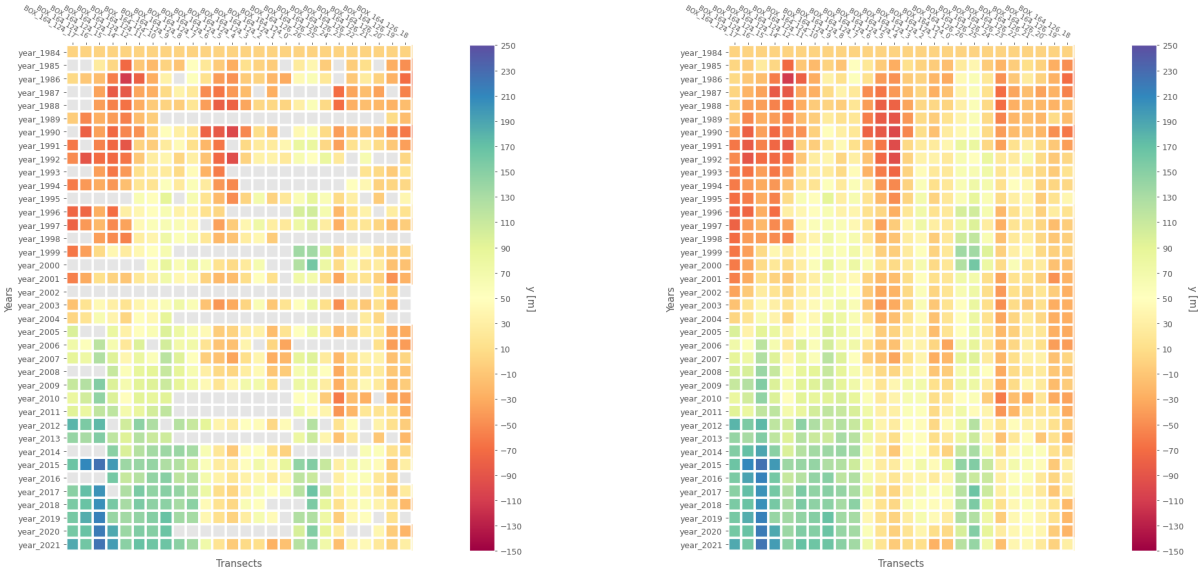


(a) (b)

Figure B.38: These two matrices depict the shoreline's position in time and space. In both images, the coastline position from 1984 is set to zero, and all following positions are based on that baseline. The left matrix (a) depicts the shoreline locations following spatial intersection, whereas the right picture (b) displays the matrix with all shoreline positions after linear interpolation.

Figure B.38b shows a gradual shift of the shoreline towards the sea, as the red colour is lower than the blue. In addition to accretion in the cross-direction of the shoreline, sand accumulates also in the longshore direction. The shoreline migrates northwards. The harbour's location on the left side of the matrix (transect number *BOX_164_124_17*) suggests that sand accumulation is migrating into the sea and northward over time.

Because the coastline location of 1984 was used as reference year, both matrices demonstrate that the shoreline retreats in the first few years before accumulating over the last 15 years. Significant erosion occurred along transect *BOX_164_124_16* between 1987 and 2001.

### Smoothing

Using the improved rolling mean method on the interpolated data results in a more gradual migration of the shoreline position. Due to the smoothing factor of $N = 5$, the first year (1984) and last year (2021) will be absent from the results. Figure B.39a shows the smoothing results. Besides showing the smoothing shoreline positions ($y$) to observe the result of the smoothing, it is also possible to show the difference between the shoreline positions ($\Delta y$) to obtain a smooth growing or decreasing gradient through time. The difference between the shoreline positions along the same transect is shown in Figure B.39b. Figure B.39b has a spatial range of $-30$ to 30 meters difference.

Figure B.39a illustrates that the shoreline retreats in the first few decades. Erosion also occurs close to the harbour in this period. The harbour is located on the left side of transect *BOX_164_124_17*. Furthermore, the entire shoreline experiences erosion for several years before it starts accumulating sand.

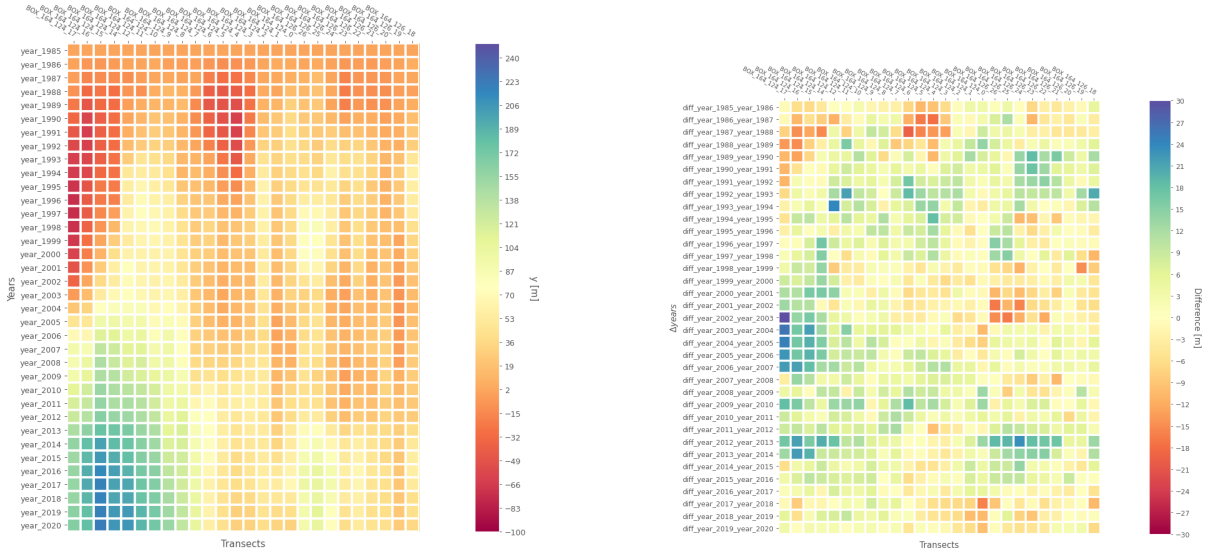


(a) (b)

Figure B.39: The left matrix (a) represents the result of smoothing the shoreline locations ($y$) with the year 1985 as reference. The right matrix (b) depicts the difference in coastline positions from the smooth shoreline matrix throughout the years ($\Delta y$).

The matrix visualisation can likewise be transformed into a visualisation along the Aveiro coastline. Figure B.40 shows how the Aveiro shoreline has changed, where blue is the oldest shoreline and red is the most recent shoreline. Figure B.39a shows that the shoreline at the harbour has been accreting over the last decade. The north shoreline appears more steady because the lines from different years are stacked on each other. This observation can also be seen in Figure B.40. In addition, the shoreline almost reaches a stable point at transect *BOX_164_124_1*.

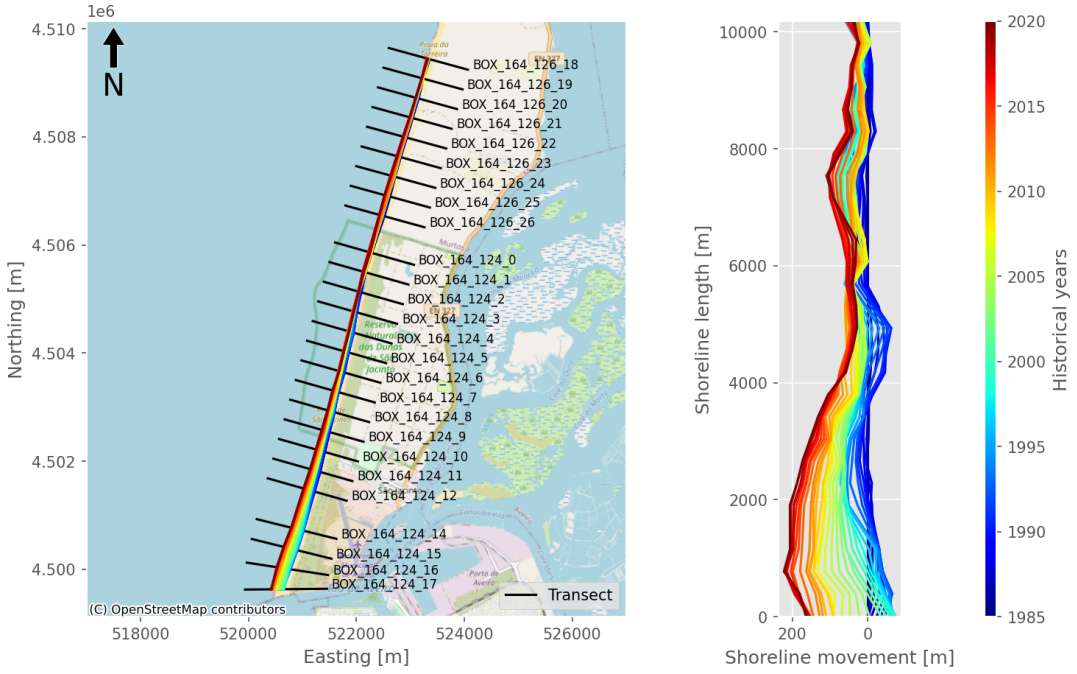


Figure B.40: The result of the smoothing procedure along the Aveiro coastline, where blue represents the oldest year (1985) and red represents the most recent (2020).

### Longshore Sediment Transport gradient

The Longshore Sediment Transport gradient is computed by multiplying the surface gradient ($\Delta A$) by the active height($H$). The active height consists of the depth of closure and the Mean Spring Tidal Range. The depth of closure may be obtained from Figure 3.16 by Athanasiou et al. (2019). As a result, the closure depth near Aveiro is 15.43 metres and the Mean Spring Tidal Range is 2.23 metres (Meso-tidal regime), as illustrated in Figure B.8. The tide was determined using the model TPXO9 by Egbert & Erofeeva (2002). Furthermore, the figure shows a semi-diurnal tide pattern. Combining the depth of closure and the Mean Spring Tidal Range gives an active height of 17.66 meters.

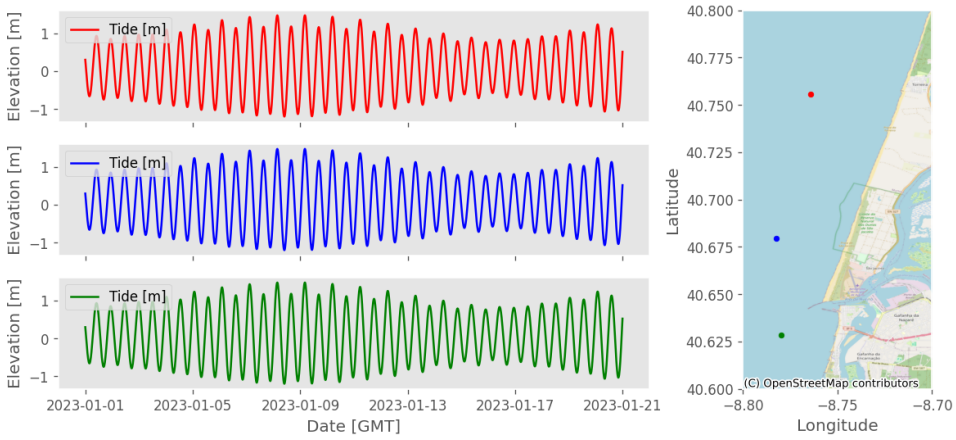


Figure B.41: The tidal cycle at three locations for 20 days in front of the Aveiro shoreline.

The surface change ($\Delta A$) is calculated between transects every two years. Figure B.42 shows the surface gradient over two years across all transects. As shown in Figure B.39a, there is significant erosion in the first several years. This erosion is also noticeable in Figure B.42. After some years of erosion, there is a period of accretion, followed by more erosion and another accretion period. It has a pattern of a wave. However, significant erosion has occurred across transects over the recent three years. All in all, the trend in the bar plot is positive, which means that the shoreline is moving seaward.

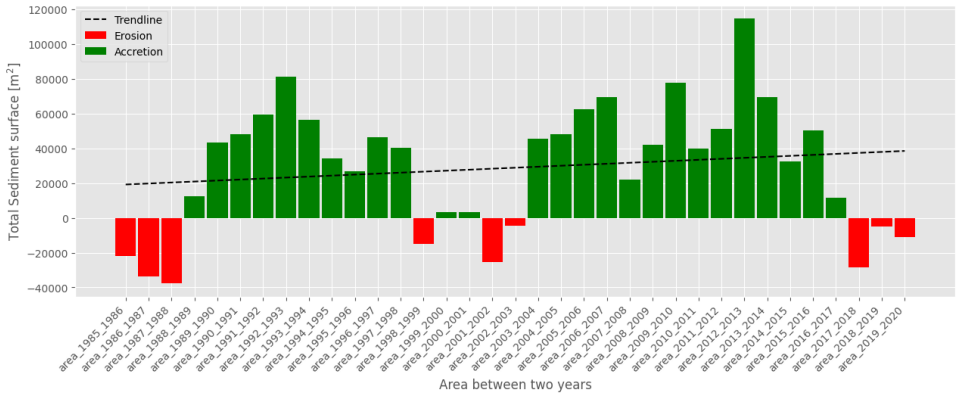


Figure B.42: The cumulative result of the surface gradient across all transects between two years from 1985 to 2020.

The volume gradient ($\Delta V$) can be determined using two assumptions. These assumptions include that the shoreline's shape remains constant and moves horizontally. Multiplying the active height with the surface gradient gives the following result shown in Figure B.43, Graph C. Graph A shows the shoreline gradient between two years, whereas Graph B shows the surface gradient along the shoreline. The distance $X$ reflects the mean distance (Section 3.3.4). An average for five years is shown from 1985 to 2020 to make the graph more understandable. The harbour is located at $X = 0$.

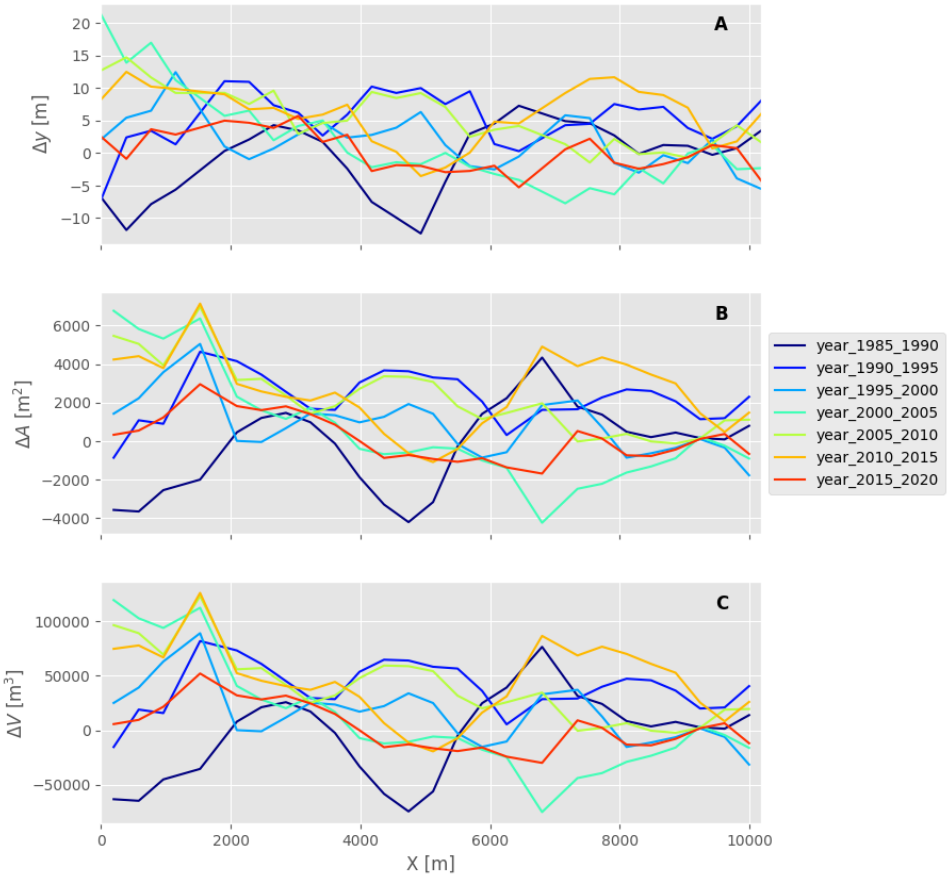


Figure B.43: Three graphs are presented. Graph A shows the shoreline difference between two years ($\Delta y$). The second graph (B) displays the surface gradient ($\Delta A$), while the final graph (C) shows the littoral transport gradient ($\Delta V$).

Figure B.43 shows the effect of the breakwater placement at the Ria de Aveiro entrance, resulting in a significant accretion between $X = 0$ and 3 km over the last 20 years. However, between 1985 and 1990, there was substantial erosion near $X$=0 to 2 km. Further along the x-axis, severe erosion followed by years of accretion can be seen between $X = 0$ and 6 km.

Figure B.40 demonstrates that the coastline stabilizes at a specific location, transect *BOX_164_124_1*, which is 6.4 kilometres away from the origin. This point is visible in Figure B.43. Over the years, there have been instances of both accretion and erosion around this point. Despite these changes, the shoreline position has remained steady. Additionally, the beach at $X$ is 10 kilometres also experienced erosion and accretion throughout its history. Nevertheless, the result is a stable shoreline, which can also be seen in Figure B.40.

### Littoral transport

As noted in Section 3.3.7, some boundary conditions are required to derive littoral transport from the LST gradient ($\Delta V$). Table 4.1 indicated that the Aveiro case would have one boundary condition. Figure B.44 shows the boundary, which is the breakwater of the Ria de Aveiro entrance. Thereby, it is assumed that this breakwater prevents sediment transport from North to South. So, Longshore Sediment Transport ($S$) is zero at this point.

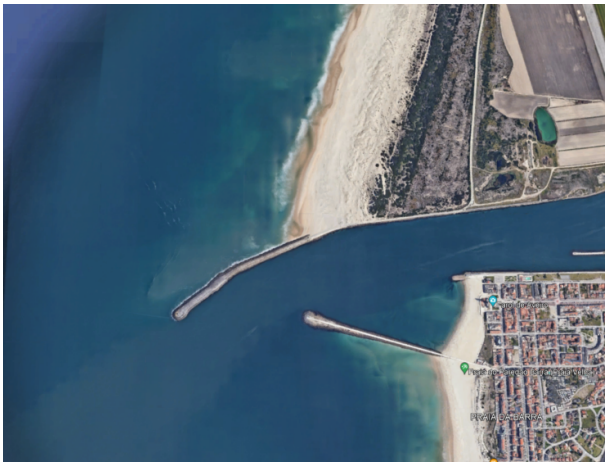

Figure B.44: This satellite image (March 2024) illustrates the breakwater at the entrance of the Aveiro's harbour and from the Ria de Aveiro. Thereby, it is assumed that there is no bypassing of sediment. Source: Google (2024).

Determining the Longshore Sediment Transport along the shoreline results in an average sediment transport per year of $-0.51$ million m$^3$, as shown in Figure B.45. This image illustrates a five-year average of sediment transport to enhance visualisation. The sediment flow rate at $X = 10$ kilometres ranges from 0.18 to -1.2 million m$^3$. According to Pinto et al. (2022), the LST is around 1 million m$^3$ per year from north to south.

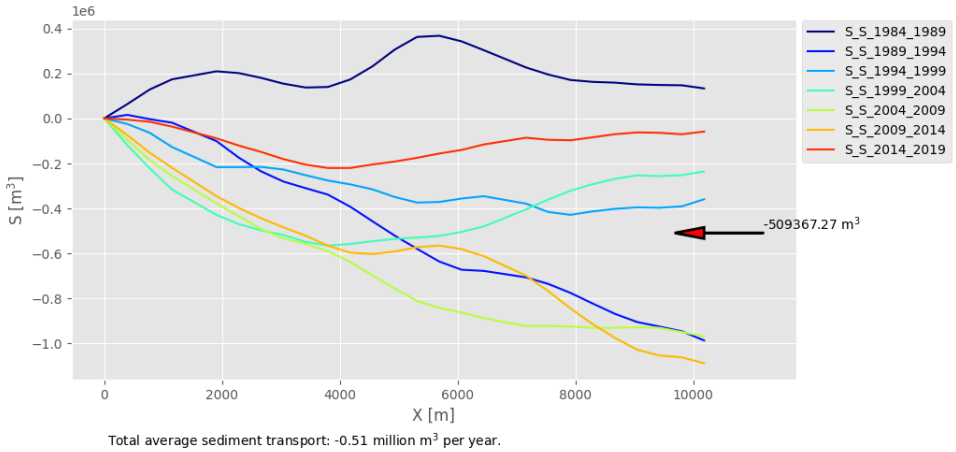


Figure B.45: The derived Longshore Sediment Transport of Aveiro starting from the breakwater in the south, where $S = 0$ and $X = 0$ metres. At $X = 10$ kilometres, the system receives approximately 0.51 million m3 of sediment yearly.

In addition to determining Longshore Sediment Transport by shoreline movements throughout the years, the total surface area between the shoreline position of 1985 and 2020 can be computed and multiplied by the active height. Figure B.46 shows the volume change from 1985 to 2020, 17.83 million m$^3$ in 35 years, or approximately 0.51 million m$^3$ per year. This is consistent with the results in Figure B.45.

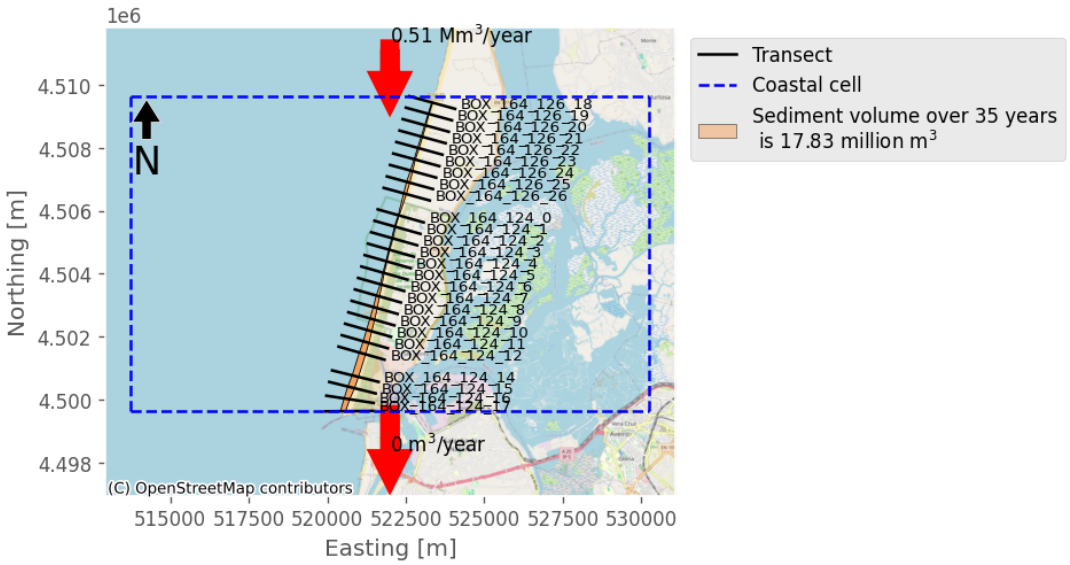


Figure B.46: The sediment balance in the selected coastal cell of the Aveiro. Given the assumption is that there is no sediment transport at the bottom, 0.51 million $m^3$ is leaving the coastal cell.

### Shoreline orientation

Besides deriving the historical littoral transport, the historical shoreline orientation can also be obtained. From the historical shoreline orientation, it is possible to see how the shoreline has migrated through time and whether it is stable. Applying the shoreline orientation method on the Aveiro case gives the following result, as shown in Figure B.47. The distances along the x-axis represent the mean distance between transects. The breakwater from Figure B.44 is located at X is zero in this Figure B.47. Figure B.47 shows an orientation range of 278 to 294 degrees north. Furthermore, the orientations between 1985 and 2020 do overlap much. Therefore, no substantial evidence exists of the shoreline rotating in a specific direction. This is consistent with the observations in Figure B.43.

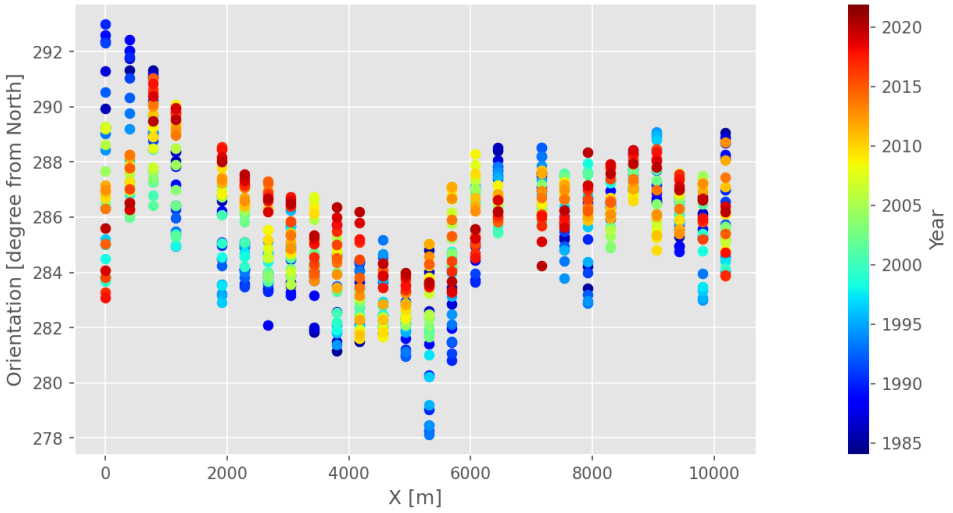


Figure B.47: A visualisation of shoreline orientation of the Aveiro case from 1985 (blue) to 2020 (red). The port is located at $X = 0$.

### S-$\varphi$ relation

Combining the Longshore Sediment Transport with the shoreline orientation allows for investigating the relationship between the two. Figure B.48a show the orientation affects sediment movement. The image demonstrates a tiny orientational range of roughly 10 degrees compared to an extensive sediment

transport range. Most points are between 0.5 and −1 million $m^3$ sediment. This indicates that there is quite some sediment transport flowing along the coast. On the other hand, an orientation higher than 290 gives almost a zero Longshore Sediment Transport.

This small orientation range in Figure B.48a is also visible in Figure B.47. Furthermore, the shoreline orientations in Figure B.47 also overlap each other, resulting in a small spread in Figure B.48a.

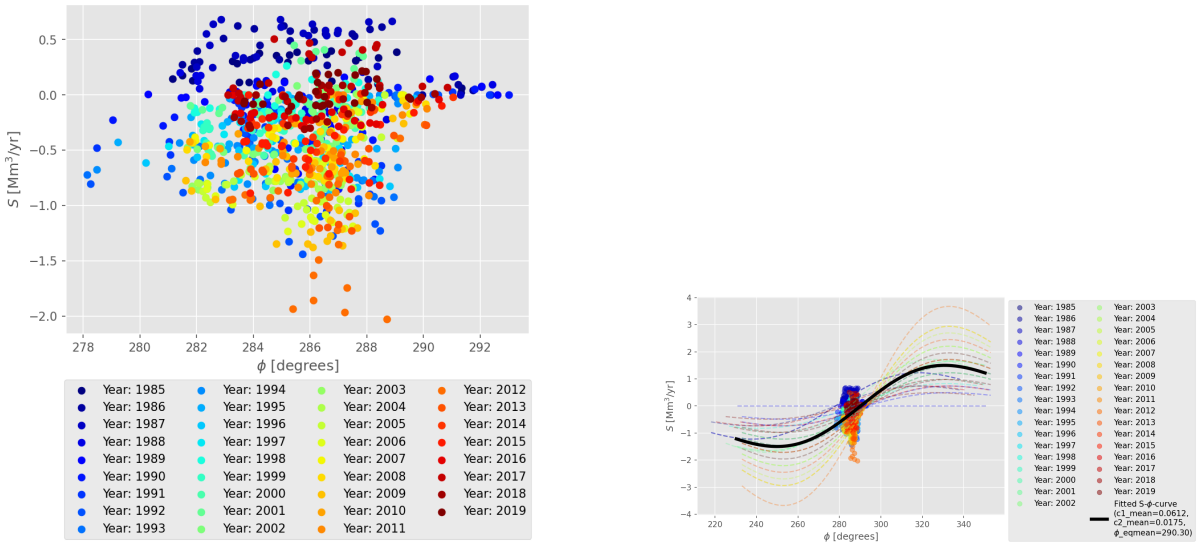


(a) (b)

Figure B.48: These two images demonstrate the shoreline orientation relative to the Longshore Sediment Transport. The left image (a) shows the shoreline orientation associated with the LST, whereas the right image (b) shows the fitted S-$\varphi$ relation per year and the mean (the black line).

To establish a connection between the Longshore Sediment Transport and the shoreline orientation, the data of Figure B.48a will be fitted through Equation 3.19. Outlined in Section 3.4.2, this equation includes three variables: $c_1$, $c_2$ and $\theta_{eq}$. The function uses yearly shoreline orientation and the corresponding Longshore Sediment Transport. The lowest RMSE value selects the best fit per year. The black line in Figure B.48b represents the average fit across all fitted years. Equation B.3 determines the variables of Equation 3.19 by calculating their mean. This function's RMSE across the entire data is 0.11. $\theta$ denotes the coastal orientation, while $S$ represents littoral transport.

$$\begin{aligned} S(\theta) &= 0.0612 \cdot \theta_r e^{-(0.0175 \cdot \theta_r)^2} \\ \theta_r &= \theta - 290.30 \end{aligned} \tag{B.3}$$

A deeper look at Figure B.48b indicates that the yearly S-$\varphi$ relation (the dashed lines) is scattered significantly over the data set. The range of the equilibrium shoreline orientation is 255 to 305. This is due to the modest orientation spread versus the big LST spread. In some years, sediment transport can reach over 2 million $m^3$.

A check that can be done is to see if the amount of sediment at $X$ is 10 kilometres obtained with the formula (B.3) is the same as what is found in Figure B.45. The littoral transport obtained as shown in Figure B.45 is −0.51 million $m^3$. The average shoreline orientation of the last three transects over 38 years is 286.11 degrees. Filling this value into Equation B.3 gives a littoral transport of −0.25 million $m^3$, which is the almost the half of the acquired littoral transport in Figure B.45.

**Future shorelines**

With the acquired S-$\varphi$ relationship, as outlined above, it is possible to determine how the shoreline will evolve. It is assumed that the sediment transport inflow flux remains constant and that no sediment leaves the area externally, such as by humans digging up sand. Figure B.49 illustrates the projected

shoreline for the next 20 years beginning in 2020, using the approach given in Section 3.5 and Equation B.3.

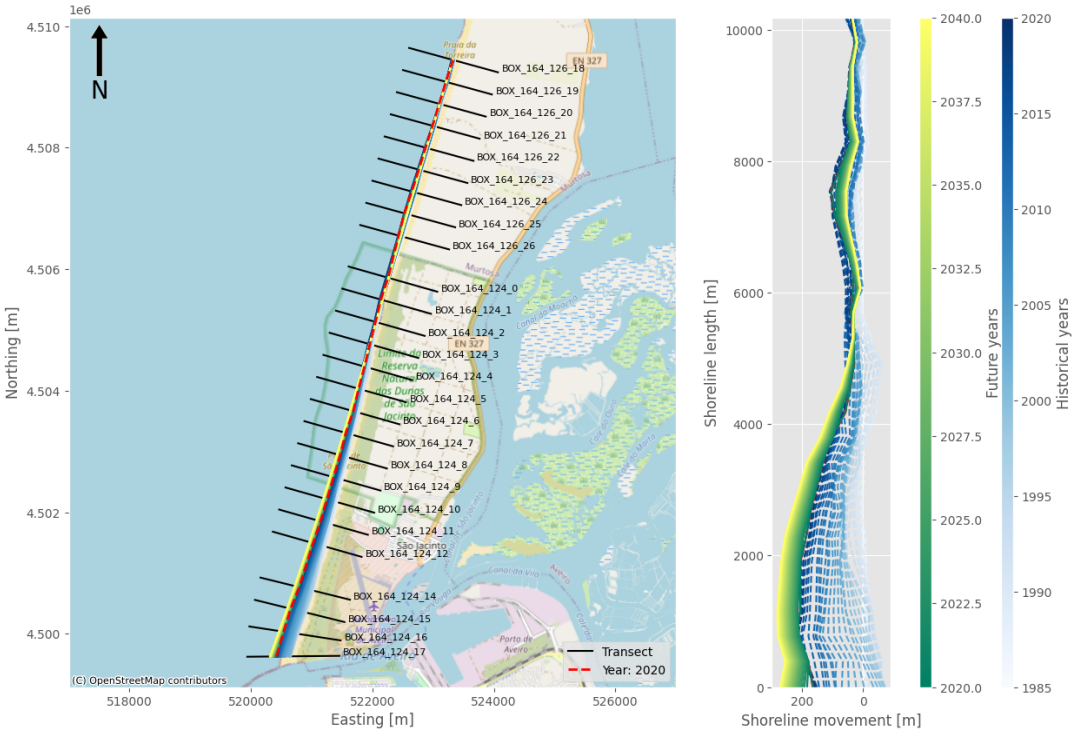


Figure B.49: The results of the shoreline prediction from 2020 to 2040. The historical movement (white to blue range) and prospective shoreline position (green to yellow range) of the Aveiro coastline.

Figure B.49 shows that the shoreline is accreting more in the south (near the port entrance), assuming no bypassing of sediment in the future. Furthermore, the accumulating sand is slowly moving northwards, as seen in Figure B.50a, because the lines between X are 0 and 2 kilometres are moving to the right. Aside from the predicted sediment transport, the shoreline orientation changes more in the first few kilometres after $X$ is zero. Figures B.50a and B.50b show a 7.5-kilometer-long rapid change around $X$ (transect *BOX_164_126_25*). Which is not directly visible in the historical analysis, Figure B.43.

Figure B.50a shows significant movement in the first few years in the predicted sediment transport. This is related to the model's spin-up time. This spin-up time can also be seen in Figure B.50b, where the orientation is placed a bit randomly in the first few years.

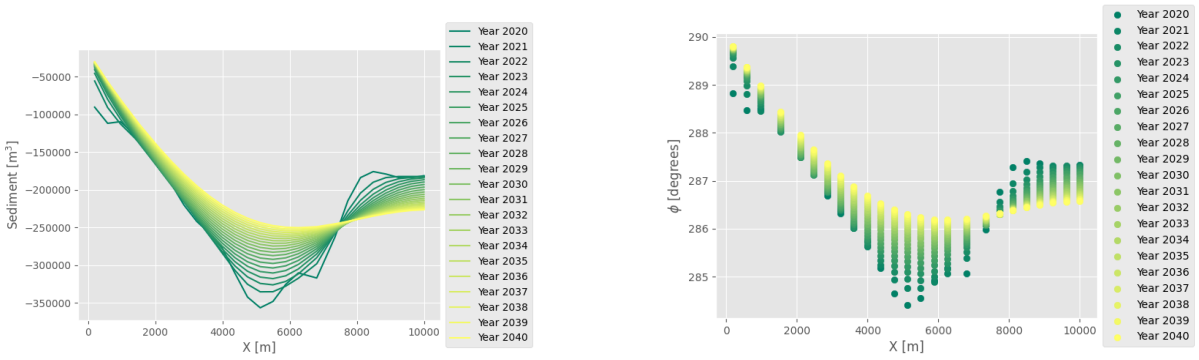


(a) (b)

Figure B.50: A visualisation of the predicted Longshore Sediment Transport (a) and shoreline orientation (b) for Aveiro.

## B.4 Results - Delfland

In the Delfland coastal cell is the shoreline approximately 16.5 km, starting from the harbour in the south at transect *BOX_187_084_39* and ending at *BOX_187_087_64*, as displayed in Figure B.51. Along these 16.5 km stretch, 53 transects are placed based on the coastline position from OpenStreetMap (OSM) 2016. The dataset includes shoreline positions from 1984 to 2021. Figure B.52 shows the coordinate system along the shoreline used in the Delfland case. At the origin, the Rotterdam's harbour is positioned. Because of this coordinate system, sediment transport flows positively from left to right and negatively from right to left.

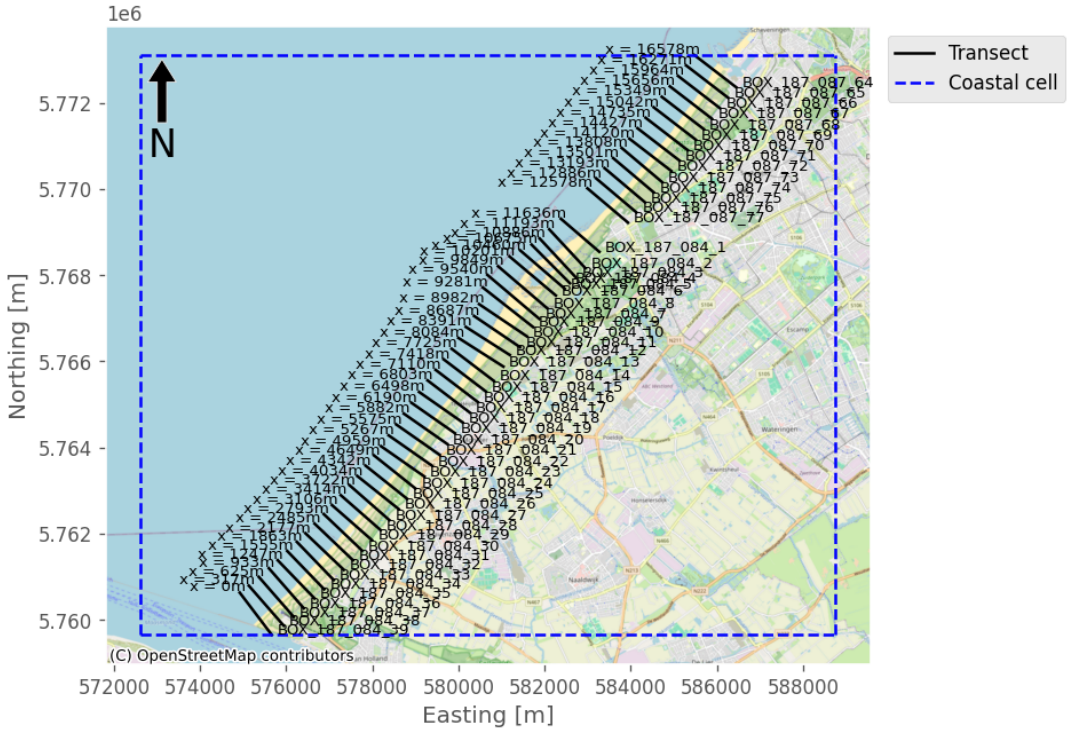


Figure B.51: The visualisation of the Delfland's coast cell with inside the position of the transects along the shore provided by the SDS dataset. Aside from the transect ID, the average measured distance from the south to the most northern transect is provided.


Figure B.52: The coordinate system utilised along the Delfland shoreline. Source: Google (2024).

In an ideal scenario, the research area would have 2014 shoreline points representing 38 years of shoreline positions along 53 transects obtained by SDS. Unfortunately, there are 133 missing spots, which is 6.6%

of the dataset. Figure B.53a illustrates the missing spots in a matrix format. These gaps occurred due to a lack of data, explained in Section 2.3. A closer look at Figure B.53a shows the spatial range between 50 and 1350 metres.

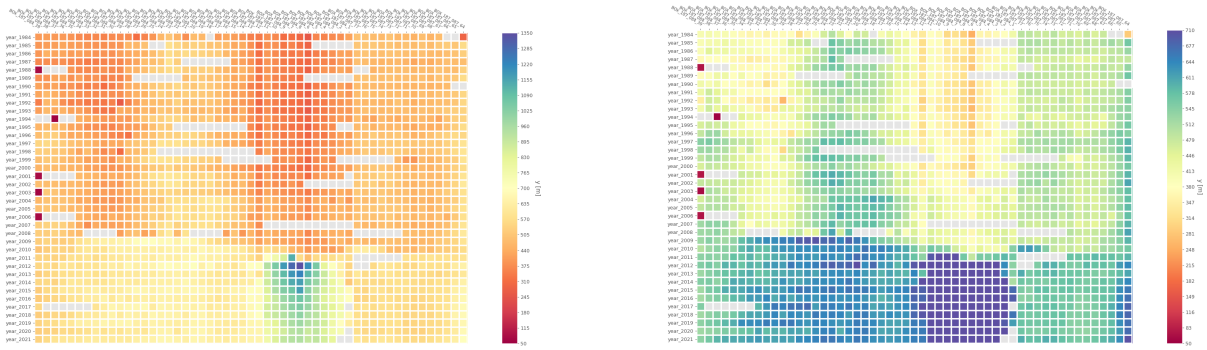

(a) (b)

Figure B.53: These two matrices show the shoreline's position over time and space. The Rotterdam Harbour is on the left, and the Scheveningen harbour is on the right in both matrices. The left matrix (a) shows the SDS data before outliers are detected and deleted. The right matrix (b) shows the same results, but the spatial range is shorter than in Figure a. It has been set between 50 to 710 per metre.

### Nourishments

Figure B.53a demonstrates a considerable rise in coastline position across numerous transects during 2009. Furthermore, in 2012, the shoreline position increased significantly. Both increases are attributed to nourishment. The growth in shoreline around 2011 is due to the Sand Engine. As mentioned in the introduction (Section 4.4.1), anthropogenic measures, such as nourishments, have significantly impacted the Delfland shore over the last 20 years. Therefore, the nourishment detection technique will be applied. Table B.1 provides the outcome of the years and transect labelled as nourishment. Figure B.54 shows the nourishment in a spatial domain through time.

Table B.1: The detected nourishment along the Delfland coast using the nourishment algorithm explained in Section 3.3.1.

| **Years** | **Start transect** | **End transect** |
|---|---|---|
| 1984 - 1985 | BOX_187_084_23 | BOX_187_084_19 |
| 1996 - 1997 | BOX_187_084_30 | BOX_187_084_26 |
| 2000 - 2001 | BOX_187_084_26 | BOX_187_084_16 |
| 2003 - 2004 | BOX_187_084_19 | BOX_187_084_10 |
| 2008 - 2009 | BOX_187_084_29 | BOX_187_084_21 |
| 2009 - 2010 | BOX_187_084_18 | BOX_187_084_8 |
| 2009 - 2010 | BOX_187_084_1 | BOX_187_087_74 |
| 2010 - 2011 | BOX_187_084_11 | BOX_187_084_2 |
| 2010 - 2011 | BOX_187_087_71 | BOX_187_087_66 |
| 2011 - 2012 | BOX_187_084_13 | BOX_187_084_2 |

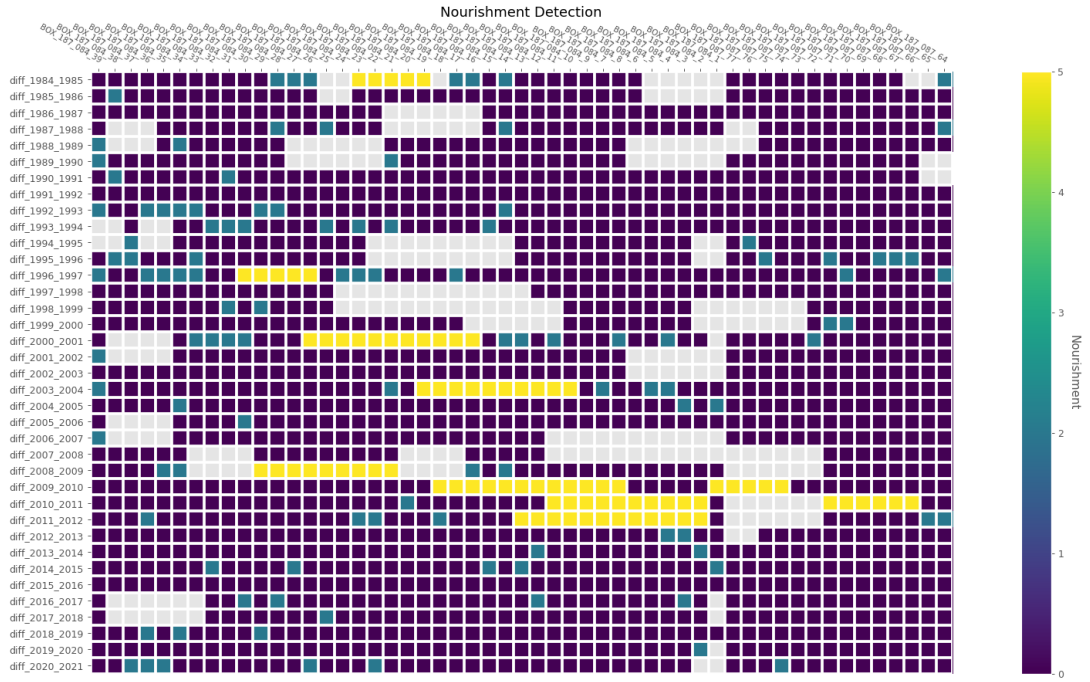


Figure B.54: The identified nourishments along the Delfland coast, with yellow indicating detected nourishment, blue-green indicating no nourishment but a shoreline position shift of more than 40 metres and dark blue indicating no nourishment and no shoreline shift of 40 metres.

### Outliers

Once the nourishments are determined, the outlier method can be applied. Figure B.55 shows the results of applying the outlier approach to the SDS dataset. This figure shows that more shoreline positions are missing than in Figure B.53. The Shoreline Shift Detection technique employs the most aggressive approach of the two outlier identification approaches. This technique eliminates 35 shoreline positions. The other technique, Standardised Residuals, removes 14 shoreline points from the data. As a result, there are currently 175 blank spaces, an increase of 31.6 %.

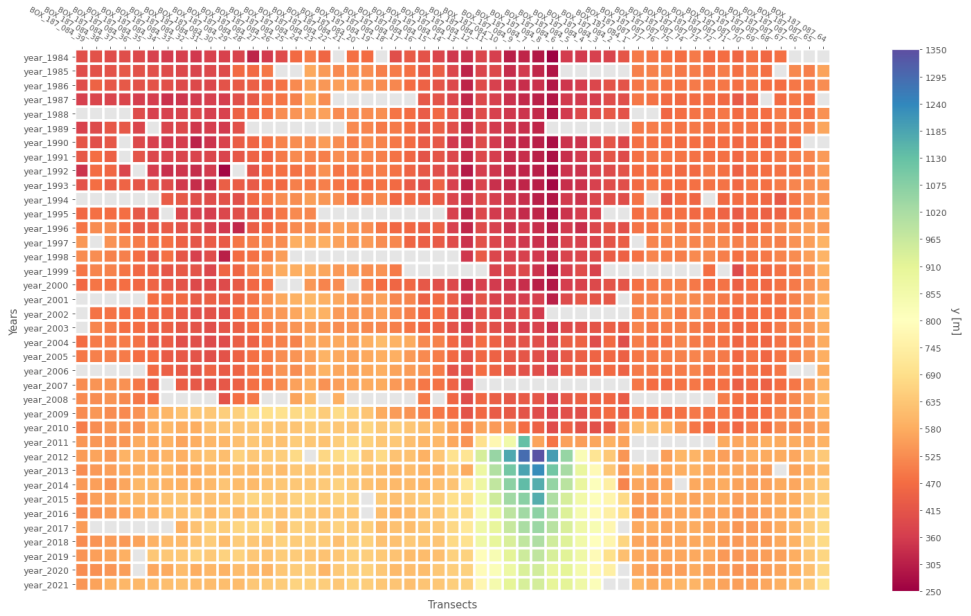


Figure B.55: This matrix shows the results of the outlier detection algorithms from Section 3.3.1.

### Interpolation

Outlier approaches deleted several shoreline sites from the SDS dataset. Figure B.55 demonstrates that in the first row (the year 1984), many coastline positions are missing in the middle and near the harbour of Scheveningen. Because the coastline position for the last three transects is unclear, locating them using spatial intersections is difficult. Therefore, the shoreline position in the top right corner, transect *BOX_187_087_64*, will get the shoreline position of next year (1985). With this assumed shoreline position, spatial intersection will derive other shoreline positions in 1984 and 2021. The following transects will be filled up by spatial intersection: *BOX_187_084_21*, *BOX_187_084_18*, *BOX_187_084_2*, *BOX_187_084_1*, *BOX_187_087_66* and *BOX_187_084_65*. The result is shown in Figure B.56a. The remaining years will be filled via linear interpolation. Figure B.56b illustrates the linear interpolation results.

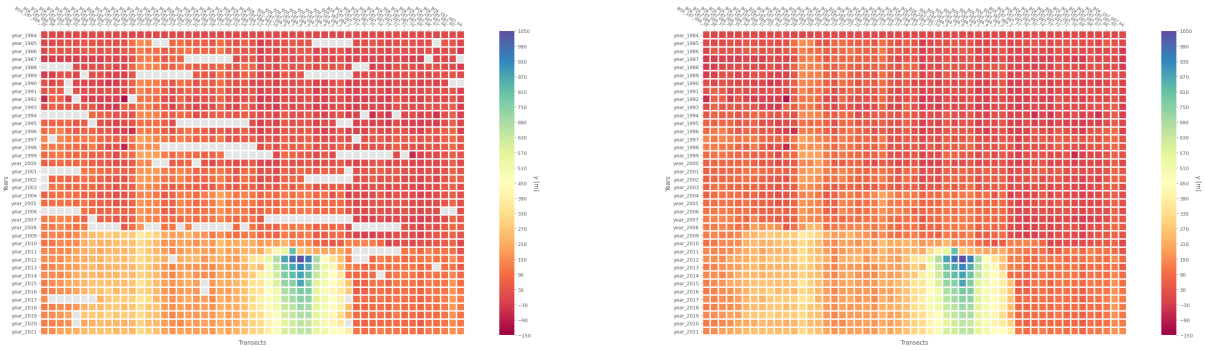

(a) (b)

Figure B.56: These two matrices depict the shoreline's position in time and space. In both images, the coastline position from 1984 is set to zero, and all following positions are based on that baseline. The left matrix (a) depicts the shoreline locations following spatial intersection, whereas the right picture (b) displays the matrix with all shoreline positions after linear interpolation.

Upon closer examination of Figure B.56b, a significant pattern of nourishments emerges, as presented and discovered in Figure B.54. Additionally, the Sand Engine stands out from the data due to the marked increase in the coastline location, indicated by blue and green colours in the right matrix. Consequently, the progressive erosion caused by the Sand Engine is visible as the shoreline erodes after 2012. Apart from the Sand Engine, the change from red to orange indicates more nourishments along the Delfland shore before the Sand Engine's construction. This is visible in 2009 between Rotterdam Harbour and the Sand Engine's location.

### Smoothing

A smoothing procedure will be avoided because of the extensive nourishment along the Delfland shore. This is primarily due to the mega-nourishment in 2011, so the smoothing would no longer be realistic because the smoothing algorithm will affect the shoreline position before the mega-nourishment is constructed. The shoreline positions before the nourishment will increase significantly and the shoreline position of the nourishment itself will decrease significantly. This also holds for the years after the mega-nourishment. Figure B.56b illustrates how the data from the linear interpolation is used in the subsequent parts of the process. Figure B.57 illustrates the shoreline, with blue indicating the earliest and red indicating the most recent year. In addition, the Sand Engine is a substantial standard distribution form created in 2012 (Arriaga et al., 2017).

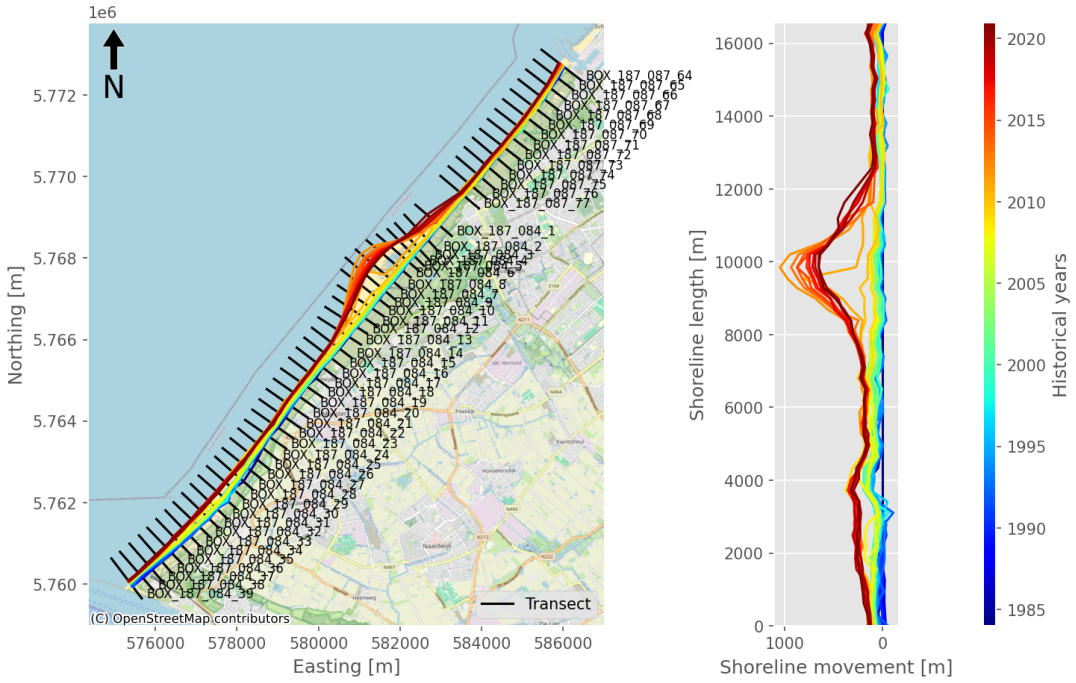


Figure B.57: The result of the interpolation procedure along the Delfland coastline, where blue represents the oldest year (1984), and red represents the most recent (2021).

### Longshore Sediment Transport gradient

The gradient of the Longshore Sediment Transport is calculated by multiplying the changes in surface between transects by the active height. The active height includes the depth of closure and the Mean Spring Tidal Range. The closure depth is obtained from Figure 3.16 by Athanasiou et al. (2019). For the Delfland coast, the depth of closure is 9.07 meters, while the Mean Spring Tidal Range is 1.56 meters, indicating a Micro-tidal regime, as shown in Figure B.58. The tide was determined using the TPXO9 model by Egbert & Erofeeva (2002) and is consistent with the study by Luijendijk et al. (2017); Wijnberg (2002). Additionally, the figure displays a semi-diurnal tide pattern (Wijnberg, 2002). Combining the depth of closure and the Mean Spring Tidal Range gives an active height of 10.63 meters. According to Wijnberg (2002), the Delfland coast is a wave-dominated coast.

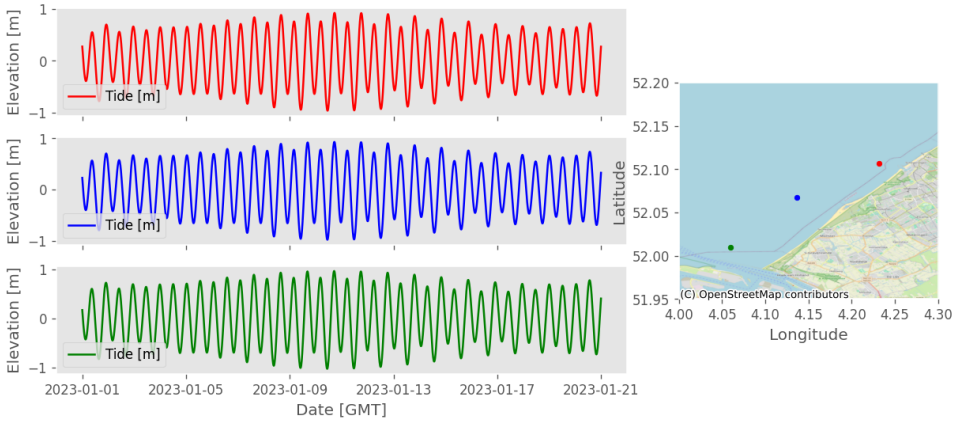


Figure B.58: An illustration of the 20-day tidal cycle along the Delfland coast at three locations.

The surface change ($\Delta A$) is calculated between transects every two years. Figure B.59 displays the surface gradient over two years across all transects. The graph shows years with significant accretion (the green bars) and years with erosion (the red bars). The years with significant accretion could be due to nourishment because the shoreline has migrated seawards significantly. Comparing nourishment

identification findings from Table B.1 with Figure B.59 reveals that most detected nourishment is evident in the bar plot. The most major one is from 2011 to 2012. This is the Sand Engine nourishment. However, the detected nourishment from 2003 to 2004 fades slightly in the barplot compared to the other recognised nourishments.

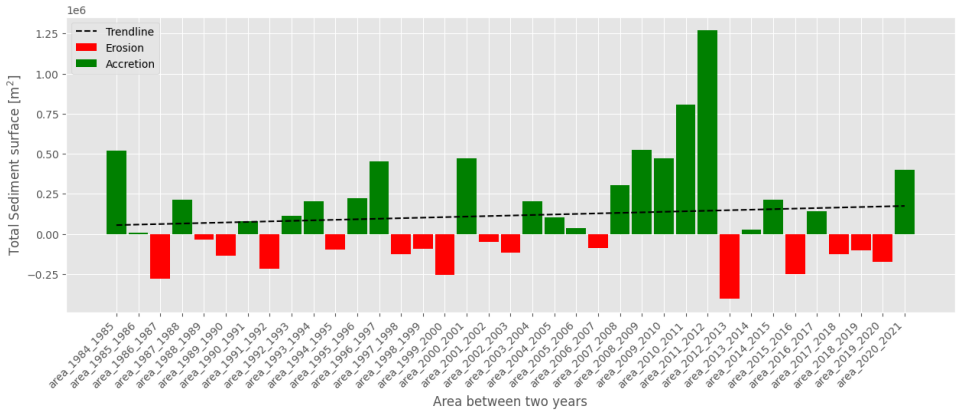


Figure B.59: The surface gradient cumulative across all transects between two years from 1984 till 2021.

The volume gradient can be determined by assuming that the coastline form remains constant in shape and shifts horizontally with erosion and accretion. Graph C in Figure B.60 shows the volume gradient obtained by multiplying the active height by the surface gradient. Graph A shows the coastal gradient over two years, whereas graph B shows the surface gradient along the shoreline. The distance $X$ reflects the mean distance. An average for five years is shown from 1984 to 2021 to make the graph more understandable. The harbour of Rotterdam is located at $X = 0$ and Scheveningen at $X = 16.5$ kilometres.

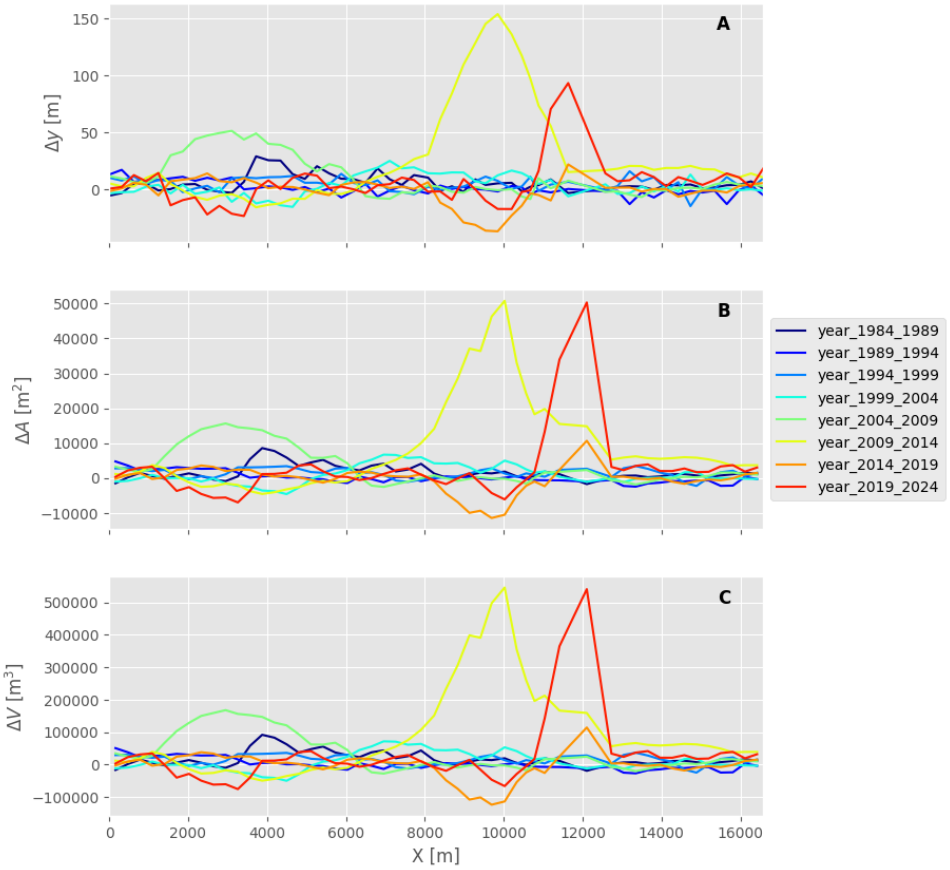


Figure B.60: Three graphs are presented. Graph A shows the shoreline difference between two years ($\Delta y$). The second graph (B) displays the surface gradient ($\Delta A$), while the final graph (C) shows the littoral transport gradient ($\Delta V$).

Figure B.60 shows the average over five years. The line increases swiftly in years with Sand Engine nourishment (orange). The erosion caused by mega-nourishment is also obvious, as seen by the red line. Aside from these lines, the coastline appears very stable, as the lines in all three graphs ($\Delta y$, $\Delta A$, $\Delta V$) lie around the origin of the y-axis. In other words, the artificial measures implemented along the Delfland shore considerably impact the coast.

### Littoral transport

As outlined in Section 3.3.7, some boundary conditions are required to derive the littoral transport from Longshore Sediment Transport gradient ($\Delta V$). Table 4.1 indicates that the Delfland case has two boundary conditions. Figure B.61 illustrates the harbours of Rotterdam and Scheveningen. Figure B.61a shows the massive breakwater from the entrance of Rotterdam's harbour at Hoek van Holland, while Figure B.61b depicts the breakwater from the entrance of the harbour of Scheveningen. Both breakwaters are assumed to have no sediment bypassing.

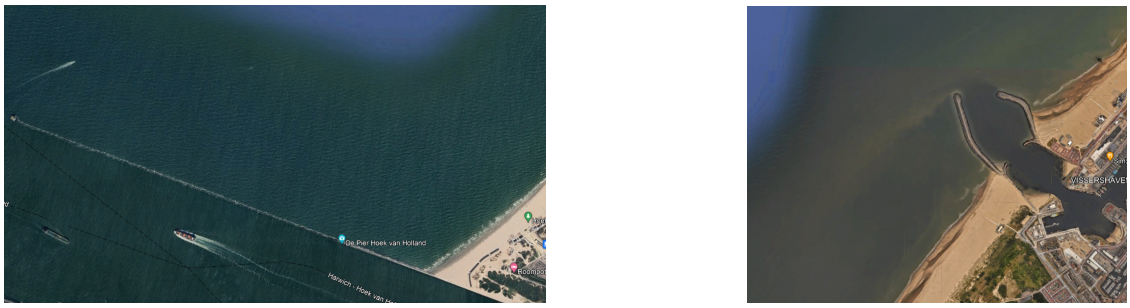

(a) (b)

Figure B.61: The two breakwaters are assumed to have no bypassing of sediment. The left image shows Hoek van Holland's breakwater and the right image shows Scheveningen's breakwater.

The sediment transport is calculated from both sides. First, from Rotterdam harbour to Scheveningen, where $S$ is zero at Rotterdam harbour (Figure B.62 A). Second, from Scheveningen to Rotterdam's harbour, where $S$ is zero at Scheveningen harbour (Figure B.62B). Graph C in Figure B.62 shows sediment transport under the assumption that at both ends the transport is zero and no bypassing occurs. This sediment is computed using Equation B.4. $\alpha$ is a number between 0 and 1 calculated from the distance $X_n$ divided by the maximum distance $X_{max}$. The letters A and B are the Longshore Sediment Transport from Graph A and B. In addition, the years with the nourishments have been removed. These years are detected by the nourishment algorithm and shown in Table B.1. This is done to get a more realistic image of the LST.

$$\begin{aligned} \alpha &= X_n / X_{max} \\ LST &= (1-\alpha) \cdot A + \alpha \cdot B \end{aligned} \tag{B.4}$$

Graph C in Figure B.62 shows that the highest sediment transport was 0.75 million $m^3$ from 1999 to 2004 from Hoek van Holland ($X$ is 0 km) to Scheveningen ($X$ is 16.5 km). Between 2019 and 2021, sediment transport from Scheveningen to Hoek van Holland reached 0.75 million $m^3$. This transport to the left is caused by the amount of erosion at the Sand Engine.

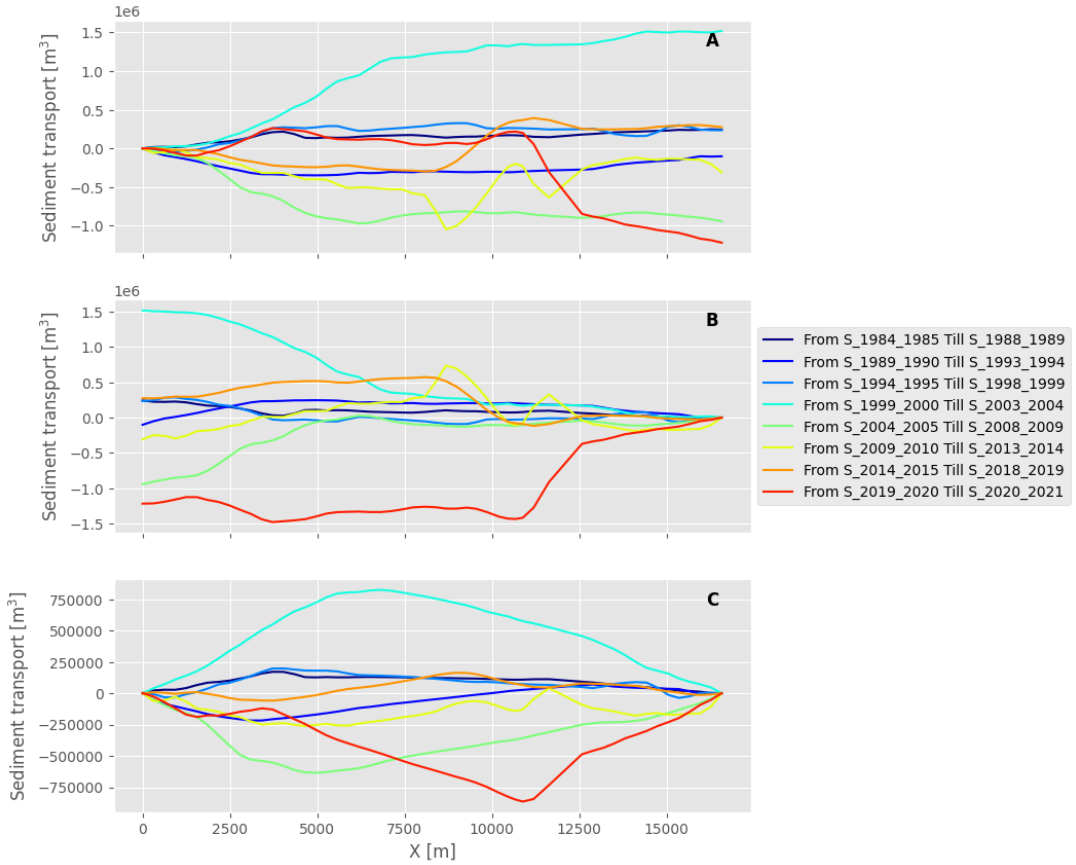


Figure B.62: The average five-year sediment transport along the Delfland coast. Graph A assumes minimal sediment transport in Rotterdam harbour. Graph B depicts sediment transport, assuming zero sediment transport at Scheveningen harbour. Equation B.4 is used to combine Graph A and B, resulting in Graph C.

In addition to determining Longshore Sediment Transport by shoreline movements throughout the years, the total surface area between the shoreline position of 1985 and 2020 can be computed and multiplied by the active height. Figure B.63 shows the volume change from 1984 to 2021, 45.55 million $m^3$ in 37 years. Thereby, at both boundaries, the assumption is that there is no bypassing of sediment. In the derived volume, the nourishment has been taken into account as far as they are visible between the shoreline position of 1984 and 2021

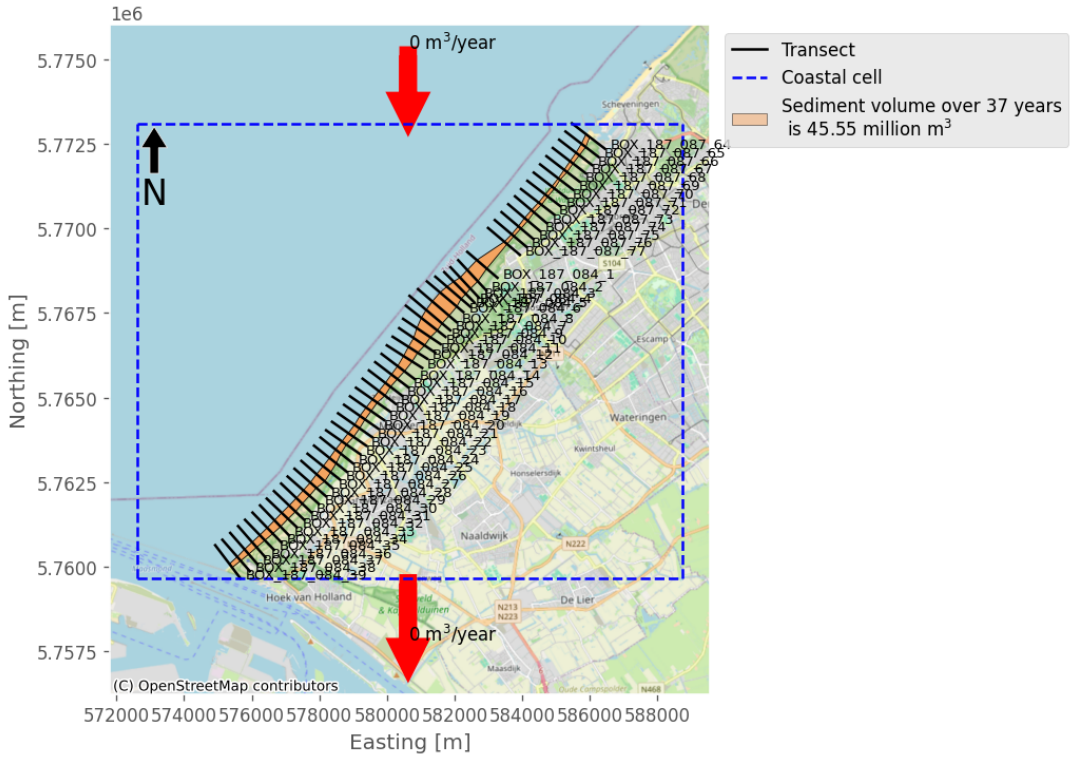


Figure B.63: The sediment balance in the selected coastal cell of the Delfland. The assumption is that there is no sediment transport at both sides.

### Shoreline orientation

Besides deriving the historical littoral transport, the historical shoreline orientation can also be obtained. From the historical shoreline orientation, it is possible to see how the shoreline has migrated through time and whether it is stable. Applying the shoreline orientation method on the Delfland coast gives the following result, as shown in Figure B.64. The Rotterdam harbour is at $X$ is zero and the harbour of Scheveningen at $X$ is 16.5 kilometres. Figure B.64 shows that the shoreline remains steady for the first 26 years starting from 1984 due to its 300-330 degrees north orientation domain. However, erosion caused by the shoreline's direction is declining.

Since 2011, there has been a significant change in shoreline orientation between $X0$ and $X = 13$ kilometres. The orientation shifts downward between 7.5 and 10 kilometres and upward between 10 and 13 kilometres. The creation of the Sand Engine (de Schipper et al., 2016), a mega-nourishment, resulted in these jumps. Furthermore, the erosion of this mega-nourishment is evident as the orientation returns to the 300 and 330-degree domains as previously.

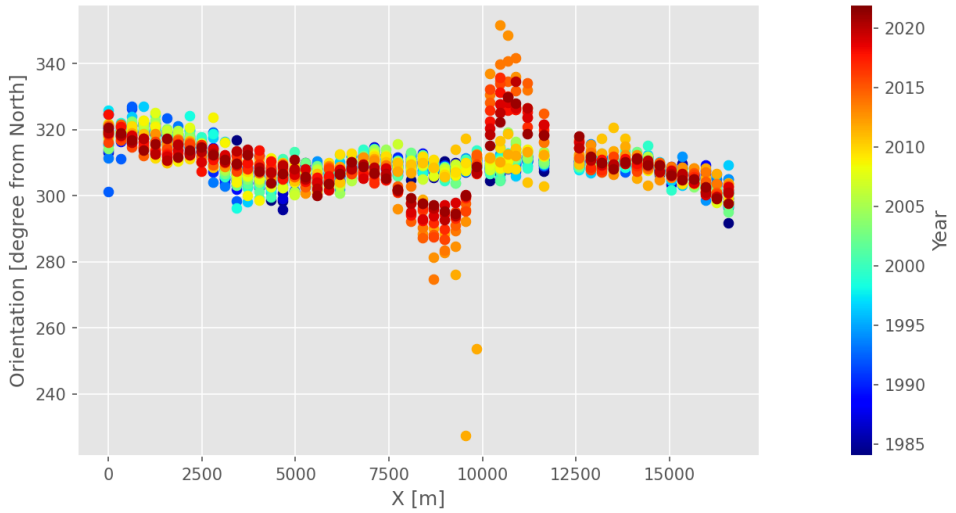


Figure B.64: A visualization of the shoreline orientation of the Delfland case from 1984 (blue) to 2021 (red). The harbour of Rotterdam is located at $X = 0$ km, and the harbour of Scheveningen is located at $X = 16.5$ km.

### S-$\varphi$ relation

Combining the Longshore Sediment Transport with the shoreline orientation allows for investigating the relationship between the two. Figure B.65a illustrates how the shoreline orientation is corresponding with the sediment transport. In addition, the nourishment years have been removed from the shoreline orientation and sediment transport dataset because those were years where sediment was brought into the coastal cell and did not represent the normal Longshore Sediment Transport along the coast. The removed years are 1996, 2003, 2008, 2009, 2010, 2011 and 2012.

A closer look at Figure B.65a shows that most orientations are spread between 300 and 320 degrees North. The corresponding sediment transport is between -2 million $m^3$ and 1.5 million $m^3$. However, in recent years, the red and orange colours have spread more due to significant shoreline change due to mega-nourishment. This is also visible in Figure B.64, where the shoreline orientation is suddenly between 240 and 350 degrees and moves back to 300 and 320 degrees North. Since sediment transport is widely spread compared to shoreline orientation, it is more challenging to fit an excellent S-$\varphi$ relationship through the data.

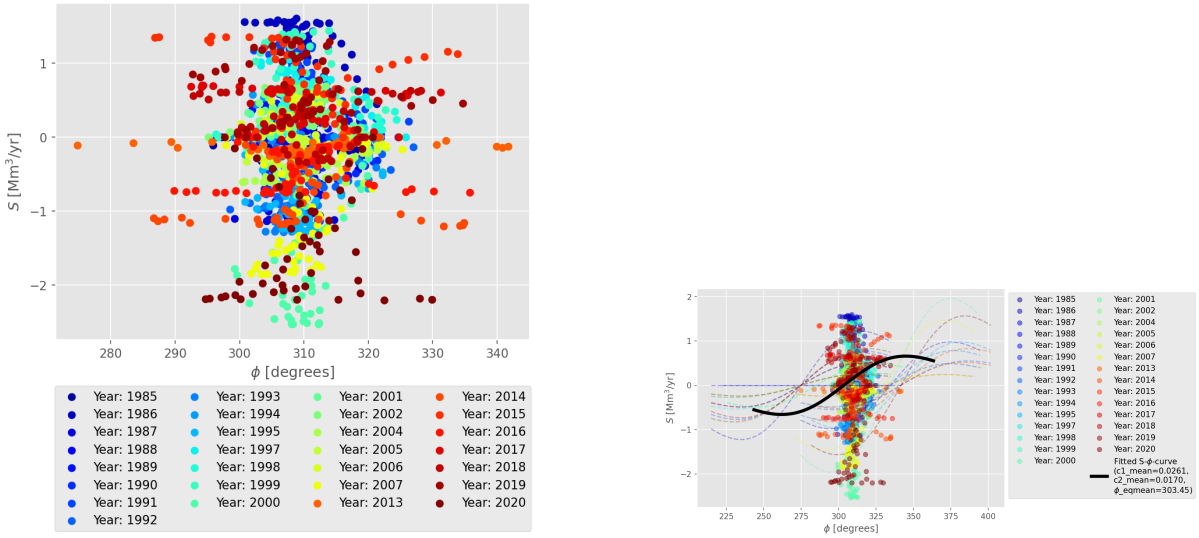


(a) (b)

Figure B.65: These two images demonstrate the shoreline orientation relative to the Longshore Sediment Transport. The left image (a) shows the shoreline orientation associated with the LST, whereas the right image (b) shows the fitted S-$\varphi$ relation per year and the mean (the black line).

To establish a connection between the Longshore Sediment Transport and the shoreline orientation, the data of Figure B.65a will be fitted through Equation 3.19. This equation includes three variables: $c_1$, $c_2$, and $\theta_{eq}$. The function uses yearly shoreline orientation and the corresponding LST. The lowest RMSE value selects the best fit per year.

The black line in Figure B.65b represents the average fit across all fitted years. Equation B.5 determines the variables of Equation 3.19 by calculating their mean. This function's RMSE across the entire data is 0.73.

$$\begin{aligned} S(\theta) &= 0.0261 \cdot \theta_r e^{-(0.0170 \cdot \theta_r)^2} \\ \theta_r &= \theta - 304.18 \end{aligned} \tag{B.5}$$

Where $\theta$ represents the coastline orientation and $S$ represents the littoral transport. To check if Equation B.5 agrees with the results from Figure B.63, the minimum and maximum sediment transport is computed from Equation B.5. The highest sediment transport is 0.59 million m$^3$ at 342.97 degrees north. The minimal sediment movement is -0.59 million m$^3$ at 258.97 degrees North. Combining these values results in yearly sediment volume movement on the coast, similar to the obtained value in Figure B.63. The yearly sediment volume movement is 1.2 million m$^3$.

### Future shorelines

With the acquired S -$\varphi$ relationship, as explained above, it can now anticipate how the coastline might evolve. It is assumed that the sediment transport inflow flux remains constant and that no sediment leaves the area externally, such as by humans digging up sand. Figure B.66 illustrates the projected coastline for the next 20 years beginning in 2020, using the approach given in Section 3.5 and Equation B.5. The prediction is made with a time step of a quarter year to be able to have the stable result, which is in line with the Courant number (Equation 3.21 in section 3.5).

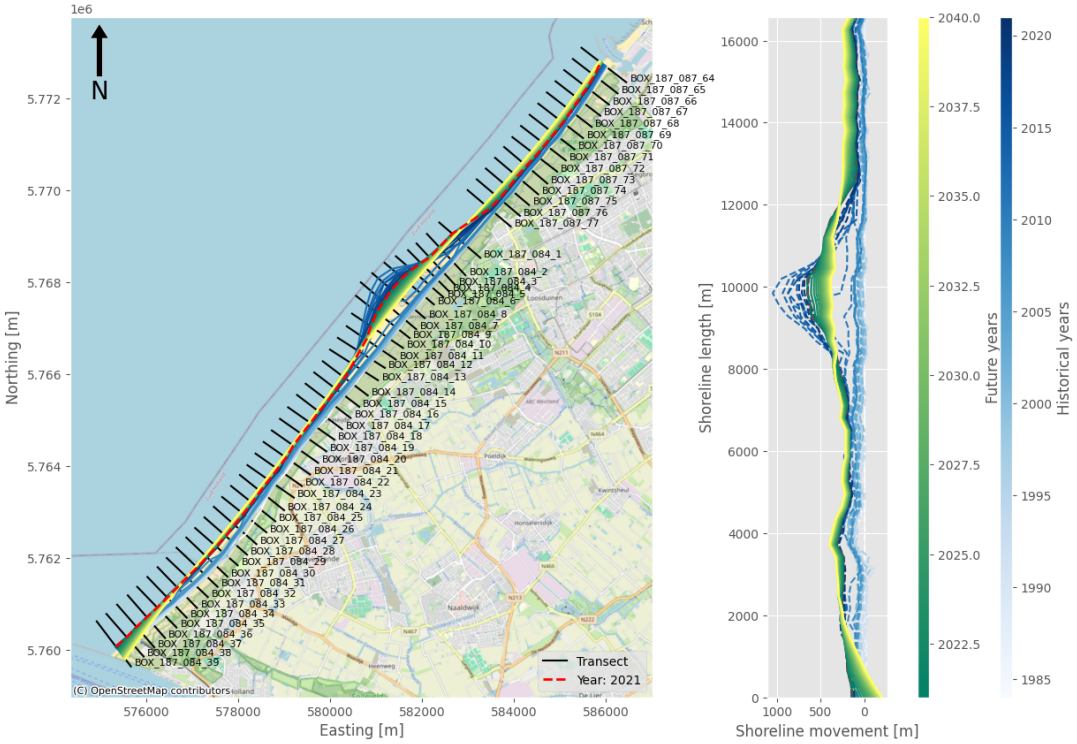


Figure B.66: This image shows the historical movement (white to blue range) and the predicted shoreline position (green to yellow range) along the Delfland coastline.

Figure B.66 illustrates that the Sand Engine built in 2011 is eroding at the top and accumulating at the sides of the nourishment. This is consistent with a Gaussian curve, as described by Arriaga et al. (2017). According to Arriaga et al. (2017), the Sand Engine is migrating towards the northeast. This is also visible in Figures B.66 and B.67.

Since the sediment transport at the boundaries of the Delfland coastal cell has been assumed to be zero, this effect is also visible in the prediction shown in Figure B.66. This figure illustrates that the shoreline in Scheveningen will accrete, while at Hoek van Holland in the south, the shoreline will retreat significantly. Furthermore, the Sand Engine will erode during the next 20 years, and this sediment will be deposited between the Sand Engine and Scheveningen. As a result, the shoreline accretes dramatically. The sediment migrates from Hoek van Holland to Scheveningen, as seen in Figure B.68a. The sediment transport is above zero, indicating a left-to-right movement (Figure B.52).

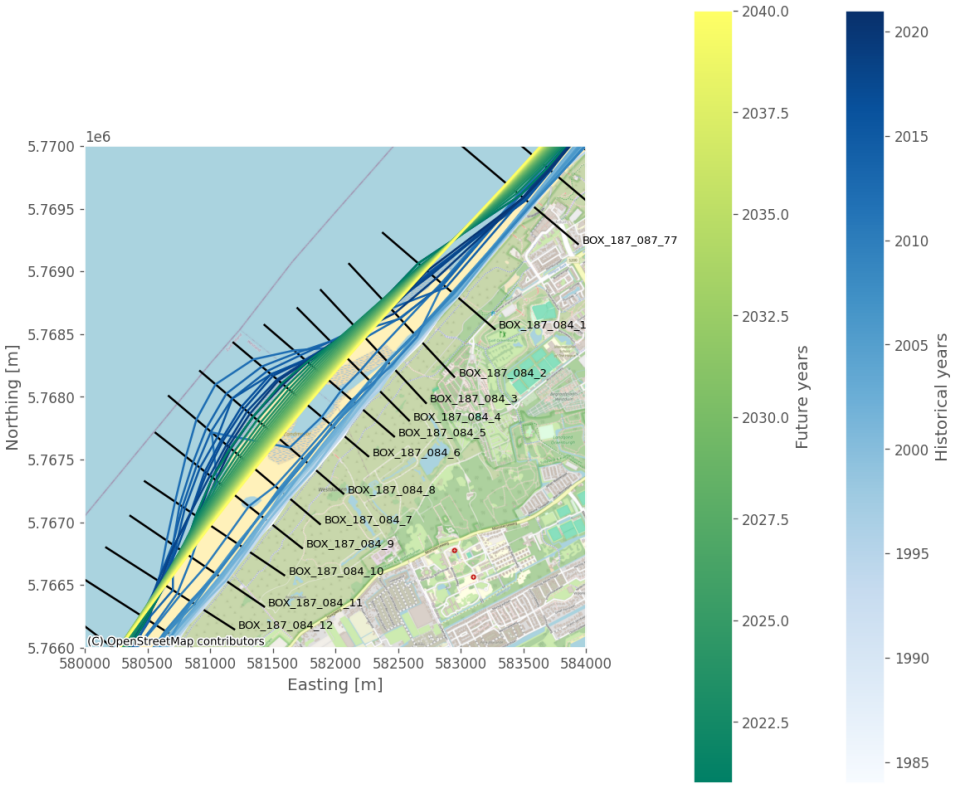


Figure B.67: The result of the shoreline prediction for the Delfland coast from 2020 to 2040. Figure B.66 shows the same result but is zoomed in at the Sand Engine nourishment.

A closer look at both figures in Figure B.68 indicates that the sediment transport is aiming to go to zero at both ends, which is due to the boundary conditions, and the sediment transport range is decreasing with time. Figure B.68b demonstrates this trend as the shoreline orientation range decreases. At the borders, the shoreline orientation is migrating to the equilibrium orientation of the S-$\varphi$ relationship in Figure B.65b and Equation B.5.

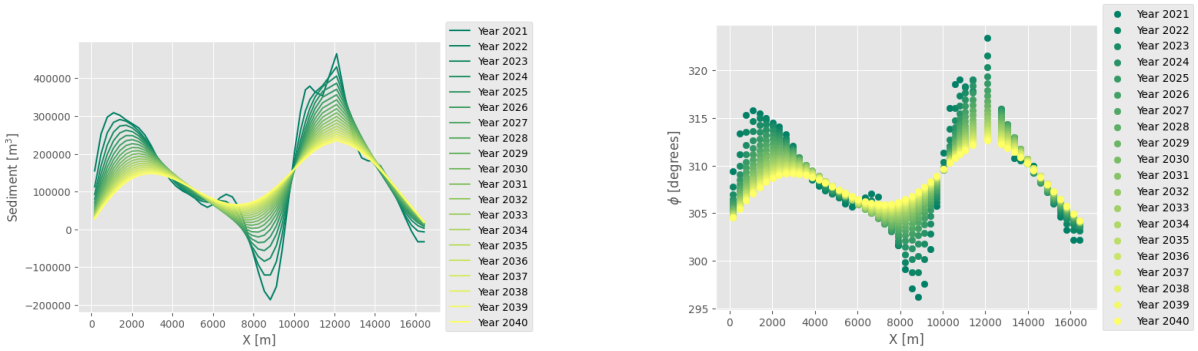


(a) (b)

Figure B.68: The two figures display the expected Longshore Sediment Transport (a) and shoreline orientation (b).

# C

# Future Scenarios

In the southern coastal cell of Nouakchott, there is a noticeable shoreline retreat due to structural erosion. Coastal management typically employs two approaches to address this issue. One method utilizes hard measures like groynes, which are artificial coastal structures. In contrast, the other method involves soft measures such as nourishment, a natural solution. This natural solution follows the principles of Building with Nature (van Slobbe et al., 2013). Both strategies can be applied in Nouakchott South to prevent further erosion. The soft measure is discussed in Section C.1, while the hard measure is explained in Section C.2.

## C.1 Nourishment

An extensive nourishment was implemented along the shoreline for the Nouakchott south case. The nourishment is constructed based on a normal distribution. The purpose is to evaluate the response of the SHORECAST model to a significant sudden change in shoreline position. The prediction, as discussed in Section 3.5, is made considering the most recent shoreline orientation and the S-$\varphi$ relation provided in Equation C.1. The nourishment is scheduled to be completed by the year 2025, with the model starting its prediction from 2020.

$$\begin{aligned} S(\theta) &= 0.0392 \cdot \theta_r e^{-(0.0171 \cdot \theta_r)^2} \\ \theta_r &= \theta - 299.49 \end{aligned} \tag{C.1}$$

The normal distribution parameters utilized can be found in Table C.1. In order to ensure visibility on the map and enable the SHORECAST model to respond, the input values for the normal distribution have been slightly exaggerated. Following the updated shoreline position calculation, a smoothing process is applied to enhance realism, as illustrated in Figure C.1. The nourishment area, indicated by the grey region between the red and purple dashed lines, contains a sediment volume of 17.48 million $m^3$.

Table C.1: The parameters used to create a nourishment in the coastal cell of Nouakchott South follow a normal distribution.

| Terms | Values |
|---|---|
| Central transect | BOX_142_001_60 |
| Standard deviation | 600 |
| Scaling factor | 2 million |
| Construction year | 2025 |

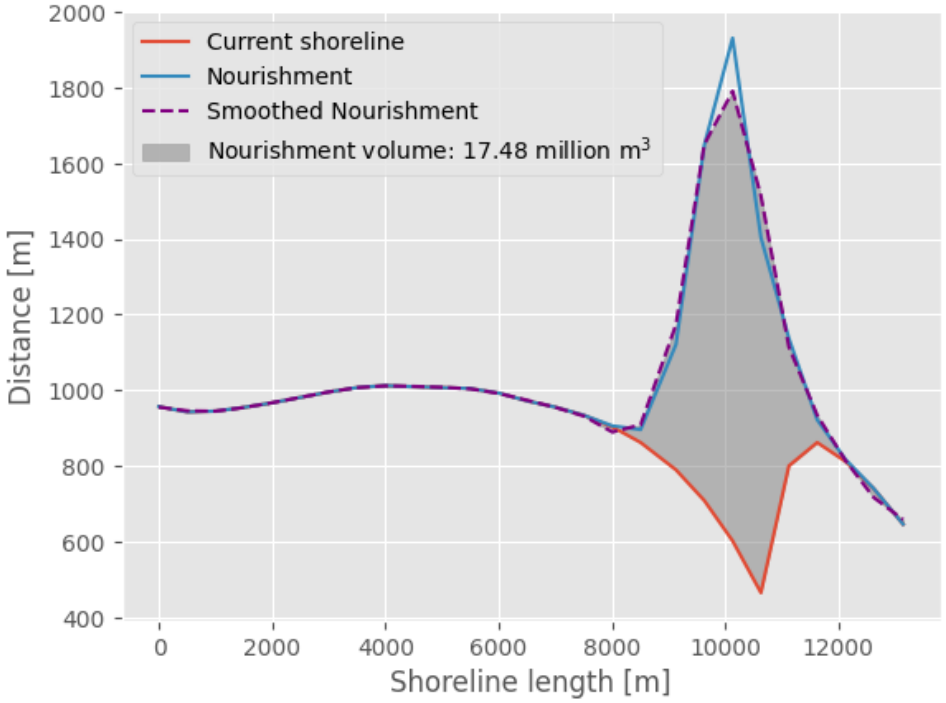


Figure C.1: The current shoreline, along with the planned nourishment, is determined using the normal distribution and subsequently refined.

Figure C.2 illustrates the placement of nourishment along the Nouakchott South coastal cell in 2025. Additionally, it illustrates the changes of the nourishment between 2025 and 2040. Erosion occurs at the top of the nourishment, causing sediment to spread further south. Moreover, the space behind the revetment is now filled. The findings from Figure C.2 indicate that the SHORECAST model can handle future nourishment scenarios and accurately predict the evolution of nourishment over time.

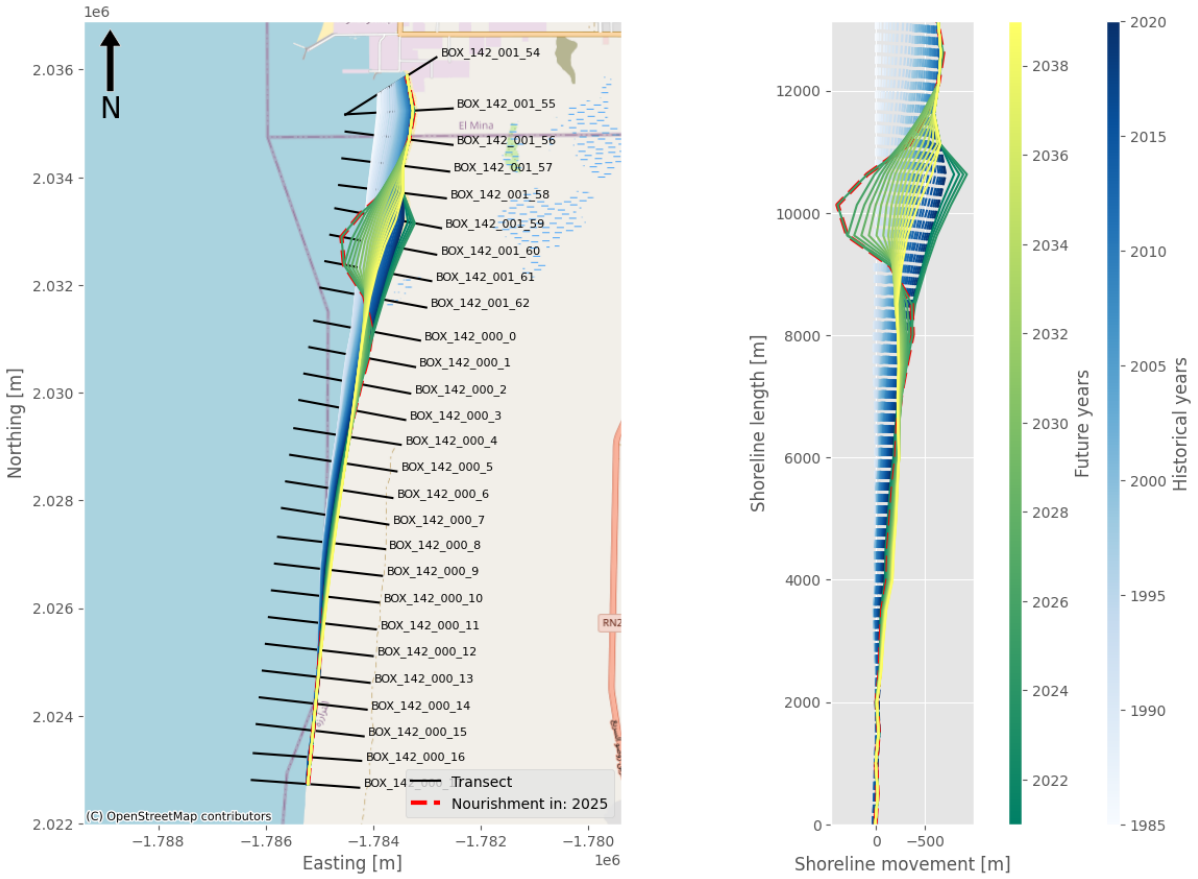


Figure C.2: The evolution of the nourishment placed in the Nouakchott South coastal cell to reduce the erosion along the shoreline.

## C.2 Groyne

Besides the soft solution, the nourishment and hard solution can also be implemented along the shoreline. Such as one or more groynes along the shoreline can help reduce erosion in the coastal area of Nouakchott South. Figure C.3 displays the coastal region of Nouakchott South with two groynes. These groynes are positioned at transects *BOX_142_000_0*, and *BOX_142_000_7*. Upon initial observation, it is evident that the SHORECAST model can effectively account for the presence of groynes along the shoreline in its predictions. As anticipated, accretion occurs on the windward side, while erosion is observed on the leeward side of the groyne.

Nonetheless, the SHORECAST model determines the new shoreline position by considering sediment supply from the previous transect and the calculated Longshore Sediment Transport value from the S-$\varphi$ relationship. Consequently, substantial erosion is expected on the leeward side. As discussed in Section 5.3.3, a different equilibrium in shoreline orientation will occur just behind the littoral barrier. Therefore, the erosion displayed in Figure C.3 may be more evident than in reality.

The comparison between the outcomes of the nourishment (Figure C.2) and the groynes (Figure C.3) reveals that the mega-nourishment demonstrates to be a more efficient approach in reducing erosion within the coastal cell of Nouakchott South.

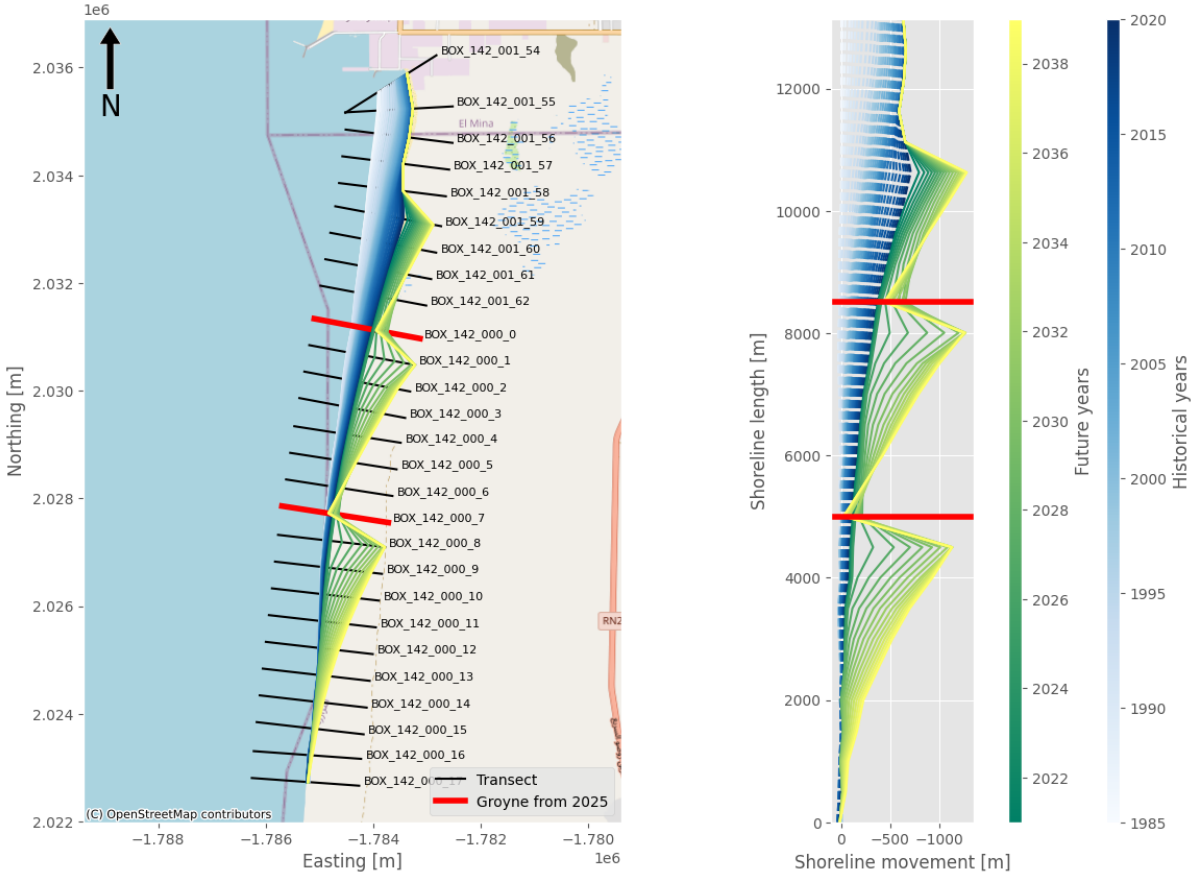


Figure C.3: The evolution of the shoreline when two groynes are built along the shoreline in the Nouakchott South coastal cell to reduce the erosion along the shoreline.

# D

# Nourishment Delfland

In the past 37 years, many anthropogenic activities have been conducted along the Delfland coast in the Netherlands because of the structural erosion that is occurring in this coastal area. Since the early 1980s, various sand nourishments have been carried out along the coast to reduce shoreline erosion. Rijkswaterstaat, the Dutch government agency responsible for water management and infrastructure, monitors these activities off the Dutch coast. The nourishment measures from 1984 to 2021 are illustrated in Figure D.1. During this period, three types of nourishment were utilized: Beach, Shoreface and Dune, with beach nourishment being the most common. The distribution of these types of nourishment along the Delfland coast is detailed in figure D.2, providing a comprehensive overview of the strategies used.

Over 37 years, 55.99 million $m^3$ of nourishment has been applied to the coastal area. Out of this overall volume, 46.51 million $m^3$ is attributed to the Beach, while the Shoreface accounts for 9.49 million $m^3$. Notably, the nourishment carried out in 2011 is considered a mega-nourishment known as the Sand Engine. Additionally, the most recent nourishment took place in 2013. Moreover, a significant amount of nourishment has been implemented near the breakwater of Hoek van Holland, indicating that this area's structural erosion is more severe than the rest of the coast.

The nourishment along the Delfland coast is distributed across various transects, as described in Chapter 3. Rijkswaterstaat utilizes Jarkusraaien ([Rijkswaterstaat], 1980), which are lines placed by Rijkswaterstaat but do not align with the Satellite-derived Shoreline transects. Therefore, aligning the nourishment with the SDS transects is necessary. Figure D.3 illustrates the placement of nourishments along the SDS transects in yellow. Additionally, the nourishment is placed in the matrix based on the year of realisation.

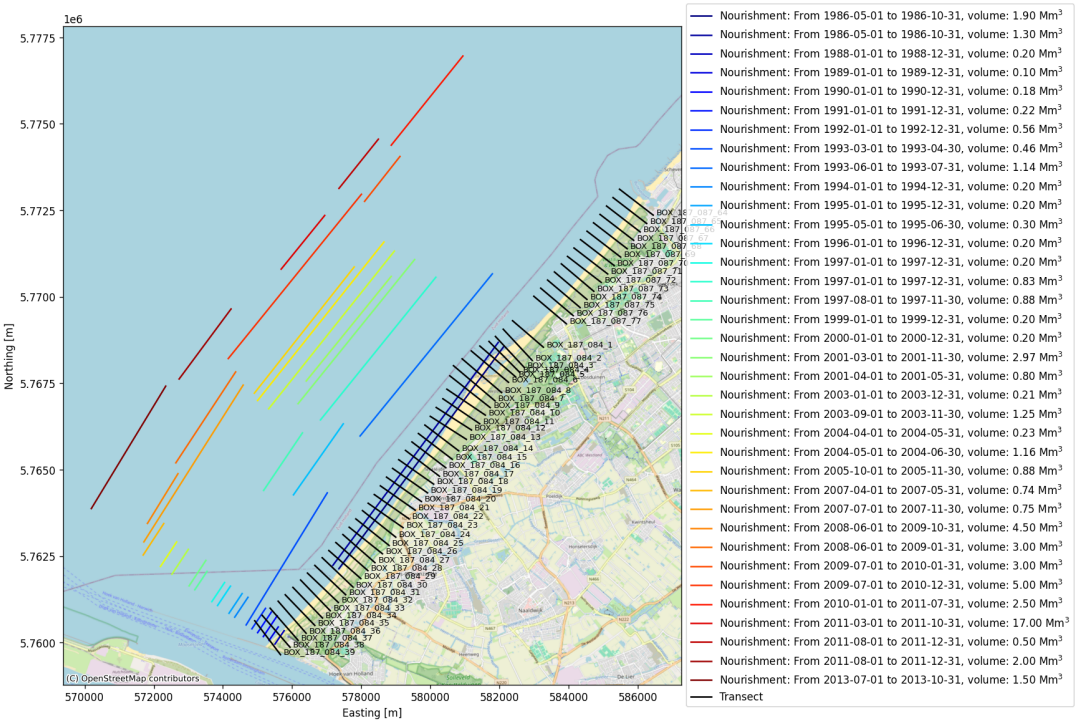


Figure D.1: The nourishment executed at the Delfland coast along the Jarkus Raaien from 1984 to 2021. Thereby, the volume per nourishment is provided.

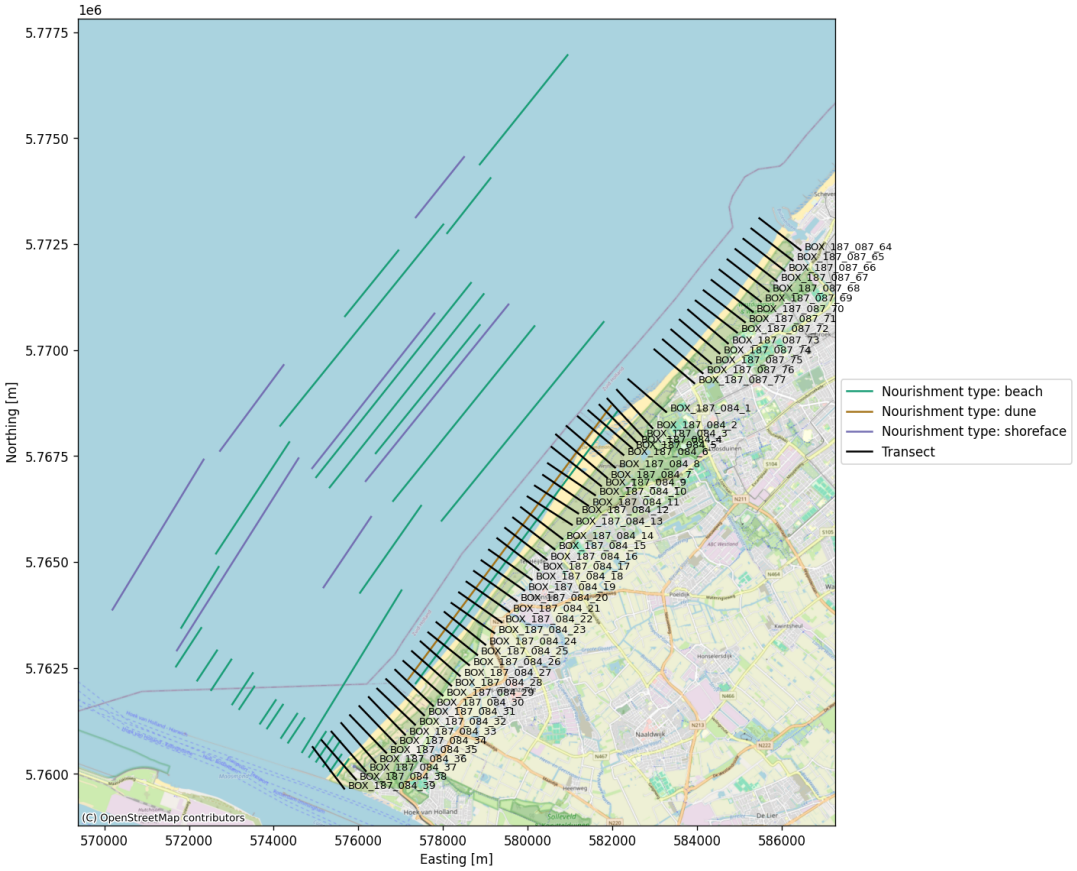


Figure D.2: The nourishment executed at the Delfland coast along the Jarkus Raaien from 1984 to 2021. Thereby, the nourishment types are provided.

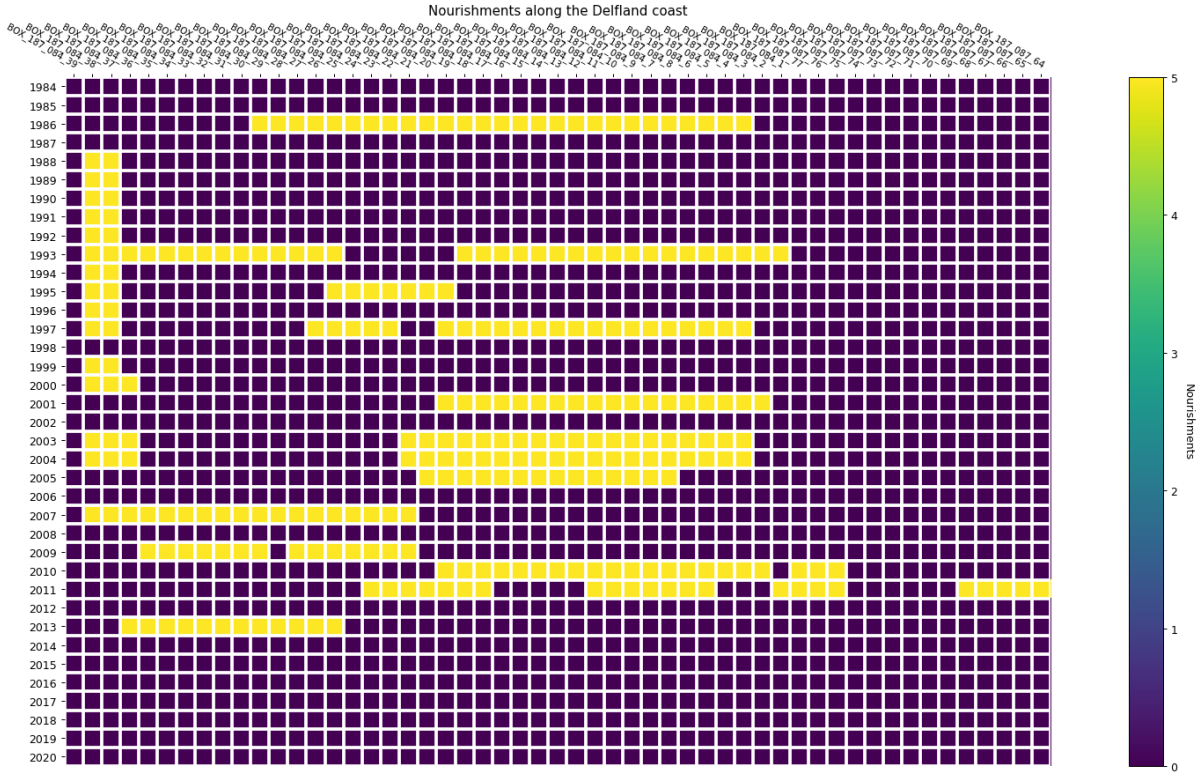


Figure D.3: The nourishment along the Delfland coast on the Satellite-derived Shoreline transects.